9.18 Iron Formations: Their Origins and Implications for Ancient Seawater Chemistry

A Bekker, University of Manitoba, Winnipeg, MB, Canada
NJ Planavsky, Division of Geological and Planetary Sciences, Caltech, Pasadena, CA, USA
B Krapež and B Rasmussen, Curtin University, Perth, WA, Australia
A Hofmann, University of Johannesburg, Johannesburg, South Africa
JF Slack, US Geological Survey, Reston, VA, USA
OJ Rouxel, IFREMER, Centre de Brest, Plouzané, France
KO Konhauser, University of Alberta, Edmonton, AB, Canada

9.18.1 Introduction

Giant hematite and martite–goethite iron ores (≥56% Fe) hosted in iron formations (IFs) are the principal source of iron for the global steel industry. Given their economic importance, IFs have been extensively studied, but many aspects of their origin remain enigmatic because modern analogues are unknown. IFs were deposited, albeit intermittently, for more than 3 billion years, but as the Earth system changed fundamentally, so did the style of IF deposition. Aspects of, and changes in, the Earth system that are most relevant to the deposition of IF include volcanism, evolution of the biosphere, and ocean composition (e.g., Bekker et al., 2010; Holland, 2005; Huston and Logan, 2004). In this chapter, interplays among these factors and their respective links to the deposition of IF are discussed. The late-stage alteration processes responsible for the transition of IFs to economic-grade iron ore are not discussed (for recent reviews of these processes see Beukes et al., 2008; Clout and Simonson, 2005; Evans et al., 2013; Morey, 1999; Rasmussen et al., 2007; Taylor et al., 2001).

The abundance of IFs in Precambrian successions was used in early studies to argue for a largely anoxic atmosphere and ocean system (e.g., Cloud, 1973; Holland, 1984). It is generally accepted that accumulation of such large masses of iron required the transport of Fe(II), because Fe(III) is essentially insoluble at circumneutral pH values in the presence of even traces (<1 μM) of dissolved oxygen. Although earlier studies invoked a continental source of iron for IFs (Borchert, 1965; James, 1954; Lepp and Goldich, 1964), the discovery of modern seafloor-hydrothermal systems shifted emphasis to the hydrothermal processes in the deep ocean as the most likely source (e.g., Isley, 1995). Although a biological role in iron precipitation was suggested over a century ago (e.g., Gruner, 1922; Harder, 1919; Leith, 1903), the importance of microorganisms began to receive greater acceptance only with the discovery of microfossils present in Paleoproterozoic IFs in the Animikie Basin of the Lake Superior region (e.g., Barghoorn and Tyler, 1965; Cloud, 1965) and, more recently, as the understanding of their significance in the modern iron cycle increased dramatically. Cloud (1965, 1973) further suggested that the redox state of the atmosphere was buffered at low levels of free oxygen, primarily by the reducing potential of the oceans and continents, including continuous IF deposition. Subsequently, it was ascertained that the Animikie IFs were deposited at ~1.88 Ga, well after the Great Oxidation Event (GOE) at ~2.32 Ga (e.g., Bekker et al., 2004), and that many of the Gunflint-type microfossils, interpreted earlier as oxygenic photosynthesizers, were instead likely metabolic iron oxidizers (Golubic and Lee, 1999; Planavsky et al., 2009) on the basis of their morphology and geochemical data for host rocks.

Acquisition of precise geochronologic constraints for Precambrian sedimentary successions also helped challenge the earlier assumption that IFs were continuously deposited before the rise of atmospheric oxygen (e.g., James, 1983). It is now believed that deposition of large, economically important IFs was instead restricted in time and coincided with mantle plume breakout events, as recorded by the secular distribution of large igneous provinces (LIPs), dike swarms, and submarine-emplaced mafic volcanic rocks (e.g., Isley and Abbott, 1999). These events not only provided the dissolved ferrous iron for IF, but also tempered the oceanic redox state and its chemistry by increasing the seafloor-hydrothermal flux of reductants such as H_2 and H_2S. In addition, associated with the deposition of IF, higher oceanic spreading rates, increased submarine and subaerial volcanic activity, high sea level, greenhouse conditions, and an enhanced production of volcanogenic massive sulfide (VMS) deposits are predicted consequences of mantle plume breakout events (e.g., Barley et al., 2005; Condie et al., 2001; Isley and Abbott, 1999). Considering that the typical duration for emplacement of LIPs is on the order of 10 My (Ernst and Buchan, 2001), a similar duration for the deposition of individual IFs should be expected unless a number of unrelated LIPs were emplaced closely in time (superplume breakout event).

Emerging age constraints provide further insights into IF genesis. For example, if the oceanic and atmospheric redox states are a major control on iron transport and deposition, why then were a number of giant IFs deposited at ~2.45 Ga? Deposition of these IFs occurred shortly before the first significant rise in atmospheric oxygen – GOE, thus suggesting a genetic link. Tectonically, it also coincides with a time of supercontinent assembly (e.g., Barley et al., 2005). If atmospheric oxygen rose during the early Paleoproterozoic, then what factors gave rise to a second prominent peak in IF deposition at ~1.88 Ga after a significant gap in large IF deposition? This pulse of IF deposition seemingly occurred during a mantle plume breakout event and supercontinent assembly (Bekker et al., 2010; Ernst and Bell, 2010; Hamilton et al., 2009), again suggesting a link.

The disappearance of IFs at ~1.8 Ga has historically been explained by either complete ocean oxidation (Holland, 1984) or development of sulfidic conditions in the deep ocean (Canfield, 1998). Neither of these models fully addresses the mechanism(s) that caused the ocean redox state prior to 1.88 Ga to change back to anoxic ferruginous conditions, and, subsequently after ~1.88 Ga, to either oxygenated or sulfidic conditions. A suboxic redox state of the deep ocean after ~1.85 Ga was proposed by Slack et al. (2007, 2009) on the basis of Ce anomalies and abundant hematite and magnetite in VMS-related, deep-water, oxide-facies exhalites of late Paleoproterozoic and Mesoproterozoic age. A variable, both geographically and temporally, deep-ocean redox state, including the presence of anoxic but nonsulfidic waters, in the mid-Proterozoic has also been recently proposed (Planavsky et al., 2011; Poulton et al., 2010).

It has long been argued that Archean and Paleoproterozoic (e.g., 1.88 Ga) IFs were deposited in entirely different settings and have different mineral compositions and textures (e.g., Klein and Beukes, 1992). Almost all Archean IFs consist predominantly of interbanded iron- and silica-rich layers and were generally, but not universally, deposited in relatively deep-water settings, as they typically lack evidence for wave or storm action. A large portion of the ~1.88 Ga IFs was, in contrast, deposited close to, or above, storm- and fair-weather wave base, and commonly has granular textures. These differences reflect not only distinctions in depositional settings but also different mechanisms for Fe(II) oxidation and Fe(III) precipitation.

Following a gap between ~1.85 and 0.7 Ga, when only small IFs were deposited, large IFs reappeared at the end of the Neoproterozoic, apparently related to snowball Earth

events (Kirschvink, 1992). These are mineralogically simple iron and silica oxide deposits that, in some places, are also stratigraphically associated with economic phosphorus and manganese deposits (Klein and Beukes, 1992). These Neoproterozoic IFs and Phanerozoic IFs, termed ironstones, are not typically voluminous, relative to the much larger Archean and Paleoproterozoic deposits. Ironstones appear to be temporally linked to marine anoxic events in many cases and comprise iron silicates and oxides without the chert enrichment, which is characteristic of Precambrian deposits, but generally with appreciable phosphorus contents. Significantly, Archean, Paleoproterozoic, and Phanerozoic IFs and ironstones are temporally associated with organic matter-rich black shales (e.g., Simonson, 2003; Van Houten and Arthur, 1989). Other Phanerozoic examples of Fe-rich rocks, commonly termed umber and jasper, developed above volcanic rocks and likely formed through either diffuse seafloor-hydrothermal venting or direct precipitation from seawater as fallout from hydrothermal plumes (Alt, 2003; Elderfield et al., 1972; Grenne and Slack, 2005). A modern analogue of umber deposits has recently been described in relation to ultradiffuse hydrothermal venting at the base of Loihi Seamount, at 5000 m below sea level (Edwards et al., 2011a,b).

Recent research has also highlighted that tectonic processes, in addition to mantle plume events and changes in iron oxidation mechanisms through time, imposed a major control over the deposition and preservation of IFs. The growth of continents created crucial shallow-water depositories and enhanced preservation of IFs in the geological record (Simonson, 2003). Before large landmasses developed considerable freeboard, IFs were likely deposited in close association with volcanic edifices and were often recycled into the mantle by subduction. Certain tectonic settings, such as isolated to semi-isolated back-arc, rift, and foreland basins, have been invoked to explain the iron source to, and basin-scale water column redox stratification in, basins, in which IFs were deposited (e.g., Beukes and Gutzmer, 2008; Ohmoto et al., 2006). Further, it is now possible with high-precision geochronology not only to correlate IFs of similar ages in different basins but also to establish that IF deposition in one basin coincided with the lack of iron enrichment in another. Nonetheless, it remains difficult in the case of Precambrian basins to separate basin and paleogeographic controls from those determined by ocean circulation and upwelling processes. Exhalites that formed distal to deep-water VMS deposits in open-marine settings help in evaluating ancient ocean redox states (Slack et al., 2007, 2009). This information can be directly compared with inferences from correlative IFs in order to constrain the redox conditions of the coeval global ocean.

Although tectonic processes exert a first-order control on Fe flux to the ocean, the marine redox state as established by oxygen content and oxidation state of sulfur and nitrogen determines whether iron and manganese can be transported in solution within the ocean. In addition, secular changes in seawater silica concentrations influenced the composition of IFs, specifically their silica and trace element contents. It is generally accepted that seawater silica contents were high during the Precambrian, but it is unclear whether silica in seawater declined dramatically at the beginning of the Phanerozoic (Siever, 1992), or if silica concentrations remained high until the Cretaceous when the emergence of diatoms removed most silica from seawater (Grenne and Slack, 2003).

In this chapter, we place the deposition of IFs in a framework of broader changes in tectonics, mantle plume activity, and oceanic and atmospheric redox states in order to assemble a new integrated model for their deposition. It is highlighted that no single parameter is solely responsible for IF deposition. Rather, complex give-and-take relationships among all of these parameters determined the time intervals and settings in which IFs were deposited throughout Earth history, as well as changes in their mineralogy and composition. **Figure 1** shows the global distribution of large IFs ($\geq$1000 Gt) and selected smaller deposits discussed below.

9.18.2 Definition of IF

The term 'iron formation' has often been restricted to stratigraphic units composed of layered, bedded, or laminated rocks (**Figures 2–5**) that contain 15 wt% or more iron, and where the iron minerals are commonly interlayered with quartz, chert, or carbonate (Gross, 1980; James, 1954). James (1954) defined four facies of IF: silicate, carbonate, oxide, and sulfide. Sulfide-facies IFs are pyritic carbonaceous shales or slates, and, as such, not typically considered IF in the strictest sense. Barren or mineralized, seafloor-hydrothermal, iron-rich exhalites and sulfidic cherts are in some cases also assigned to the IF category and host some important gold deposits in Archean terranes. The former, in many cases, represent facies of VMS deposits, whereas the latter could be either exhalites or hydrothermally replaced IF (Groves et al., 1987). As a result, many Archean (sulfide-facies) IFs described in the literature are not true IFs (Hofmann et al., 2003). All other facies are generally interbedded with variably recrystallized chert (Simonson, 2003). Oxide-facies IF consists predominantly of magnetite or hematite, whereas carbonate-facies varieties contain siderite or ankerite as major constituents. The mineralogy of silicate-facies IFs is more complex and depends to a large extent on the degree of metamorphism. Under relatively low-grade metamorphic conditions, at the biotite zone and below, greenalite, minnesotaite, stilpnomelane, chamosite, ripidolite (Fe-chlorite), riebeckite, and ferri-annite may be present. At higher grades, cummingtonite, grunerite, pyroxene, garnet, and fayalite can occur.

On the basis of interpreted depositional settings, IFs have classically been subdivided into Superior type and Algoma type (Gross, 1980; see also discussion in Bekker et al., 2012). Superior-type IFs were regarded as having been deposited in nearshore continental-shelf environments, because they typically are interbedded with carbonates, quartz arenite, and black shale, but only with minor amounts of volcanic rocks (Gross, 1980). Algoma-type IFs are generally hosted within volcanic rocks, and, in some cases, in graywacke, and apparently formed by exhalative-hydrothermal processes close to volcanic centers. Barrett et al. (1988a) argued, on the basis of geochemical signatures, that some Algoma-type deposits formed within restricted basins like the modern Red Sea. Algoma-type IFs are present in volcano-sedimentary sequences of greenstone belts ranging in age from Eoarchean to Phanerozoic (Goodwin, 1973; Huston and Logan, 2004; Isley and Abbott, 1999; James, 1983; Peter, 2003; Peter et al., 2003).

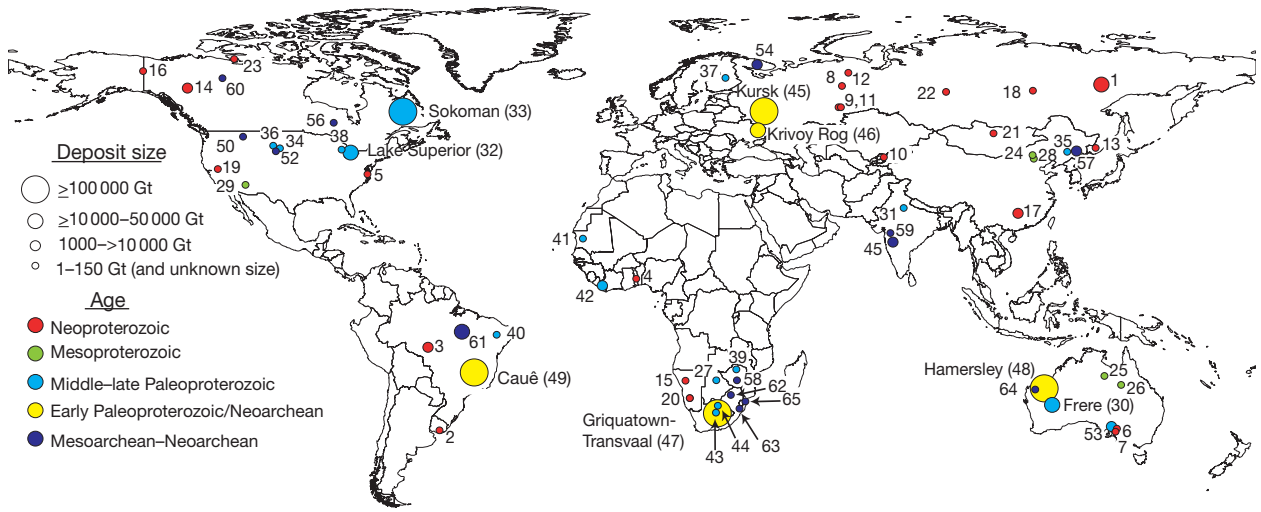

Figure 1 Major sediment-hosted iron formations of the world discussed in the text. 1, Maly Khinghan Formation; 2, Yerbel Formation; 3, Jacadigo Group (Urucum district); 4, Bisokpabe Group; 5, Chestnut Hill Formation; 6, Holowilena Ironstone; 7, Braemar Iron Formation; 8, Vil'va and Koyva formations; 9, Bakeevo (Tolparovo) Formation; 10, Dzhetymtau Suite; 11,Uk Formation; 12, Yamata Formation; 13, Lake Khanka Formation; 14, Rapitan Formation; 15, Chuos Formation; 16, Tindir Group; 17, Fulu Formation; 18, Medvezhevo Formation; 19, Kingston Peak Formation; 20, Numees Formation; 21, Mugur Formation; 22, Nizhne-Angara Formation; 23, Aok Formation (Shaler Supergroup); 24, Xiamaling Formation; 25, Roper Group (Corcoran & McMinn formations); 26, South Nicholson Group (Mullera Formation); 27, Shoshong Formation; 28, Chuanlinggou Iron Formation; 29, Pike's Peak Iron Formation; 30, Frere Formation; 31, Alwar Group (North Delhi fold belt); 32, Lake Superior region (Gunflint Iron Formation, Negaunee Iron Formation, Biwabik Iron Formation, Ironwood Iron Formation, Riverton Iron Formation); 33, Sokoman Iron Formation; 34, Rochford Formation; 35, Liaohe Group; 36, Estes Formation; 37, Pääkkö Iron Formation; 38, Glen Township Formation; 39, Lomagundi Group; 40, Caldeirão belt; 41, Ijil Group; 42, Nimba Itabirite; 43, Hotazel Iron Formation; 44, Timeball Hill Formation; 45, Kursk Supergroup; 46, Krivoy Rog Supergroup; 47, Transvaal Province (Griquatown Iron Formation, Kuruman Iron Formation, Penge Iron Formation); 48, Hamersley basin iron formations (Boolgeeda Iron Formation, Weeli Wolli Formation, Brockman Iron Formation (Joffre Mbr), Brockman Iron Formation (Dales Gorge Mbr), Mt. Sylvia Formation, Marra Mamba Iron Formation); 49, Cauê Formation; 50, Indian Creek Metamorphic Suite; 51, Ruker Series; 52, Benchmark Iron Formation; 53, Hutchison Group (Middleback Ranges); 54, Nemo Iron Formation; 55, Chitradurga Group; 56, Beardmore-Geraldton assemblage; 57, Anshan Iron Formation; 58, Manjeri Iron Formation; 59, Bababudan Group; 60, Central Slave Cover Group; 61, Carajás Formation; 62, West Rand Group; 63, Pongola Supergroup; 64, Jack Hills belt; 65, Moodies Group.

Although common in Superior-type IF, granular iron formations (GIFs) are generally absent within Algoma-type deposits, which are typically banded with chert and Fe oxide, silicate, or carbonate pairs on various scales (**Figure 2(a)**). IFs older than 3.0 Ga appear to be predominantly of the Algoma type, which likely reflects the scarcity of preserved cratonic successions prior to this time. Mineralogically, Algoma- and Superior-type IFs are similar.

Algoma-type IFs are generally thinner and smaller in lateral extent relative to Superior-type IFs and rarely exceed 10^7 Mt (Huston and Logan, 2004), although the former are more abundant in terms of numbers of deposits and geographic distribution (Beukes and Gutzmer, 2008). Typically Algoma-type IFs are less than 50 m thick and rarely extend to more than 10 km along strike. However, these characteristics do not indicate that all Algoma-type IFs were originally smaller, as most had been affected by deformation and tectonic dismemberment, implying that their original size and extent are likely underestimated (Gole and Klein, 1981). By contrast, Superior-type IFs are typically laterally more extensive and thicker than Algoma-type IF. Some major, Superior-type sedimentary deposits (not orebodies) initially contained an estimated 10^8 Mt at 15 wt% Fe (Isley, 1995; James, 1983).

Clear differentiation between Superior and Algoma types of IF is difficult in Archean successions affected by strong deformation and shearing that produced tectonic dismemberment or imbrication of genetically unrelated sequences. For example, IFs interbedded with quartz arenite and carbonate are locally interlayered with thick packages of mafic–ultramafic extrusive rocks. Although some of these sequences may represent primary stratigraphic units that were deposited in extensional continental or arc settings (e.g., Srinivasan and Ojakangas, 1986), others could have formed by the tectonic imbrication of cratonic cover sequences and overlying piles of mafic–ultramafic rocks (e.g., Dirks et al., 2002).

This distinction is further complicated by the full gradation between Superior- and Algoma-type IFs that emerged as studies advanced. For example, bimodal volcanic rocks, tuff beds, and stilpnomelane-rich shale are commonly associated with IFs in the Animikie basin of North America and the Hamersley Group of Western Australia, both being typical examples of Superior-type IFs. On the other hand, some Paleoarchean and younger IFs in greenstone belts occur in sedimentary successions containing minimal recognizable volcanic material. However, the geochemistry and lithology of IFs and host rocks clearly indicate that both Algoma- and Superior-type IFs were deposited contemporaneously with submarine volcanism and intense hydrothermal activity. Therefore, the two types of IF can be considered as idealized end-members for precipitates ranging from proximal hydrothermal deposits to distal hydrogenous deposits that all precipitated from seawater coeval with seafloor-hydrothermal activity.

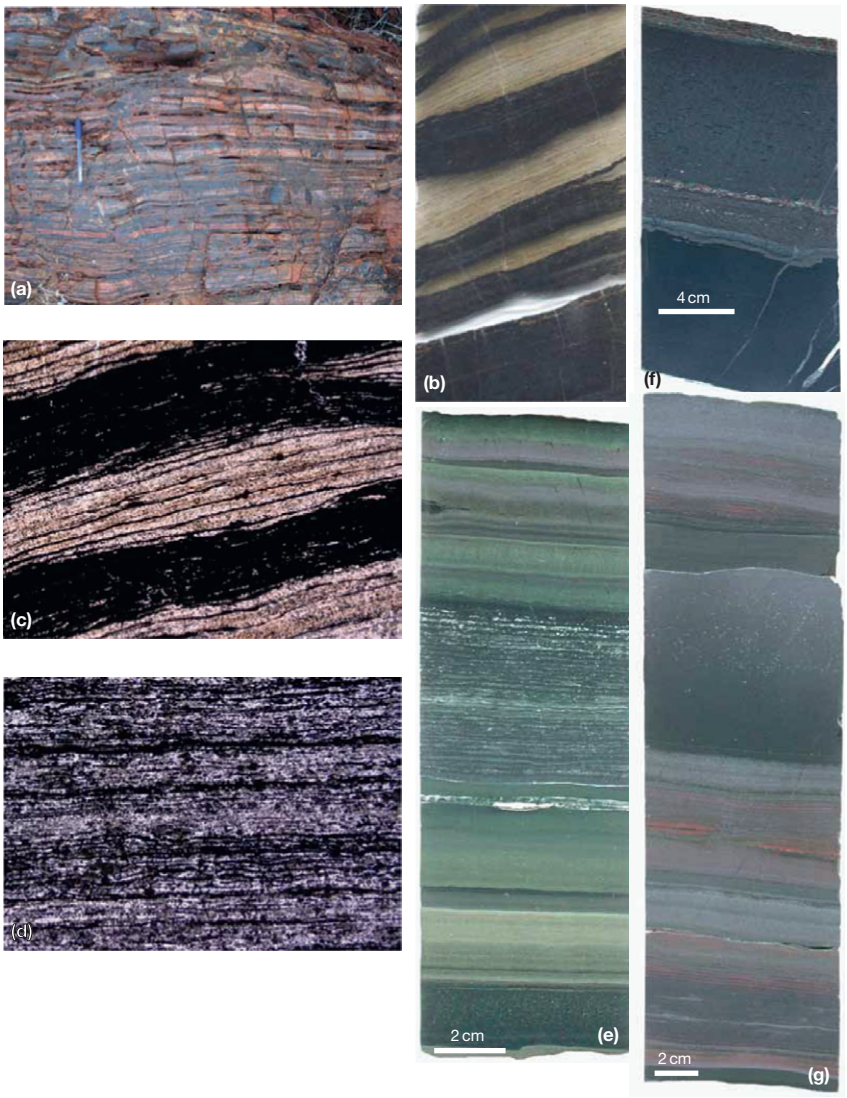

Figure 2 (a) Typical appearance of jaspilitic iron formation from the Early Archean Nimingarra Iron Formation of the Gorge Creek Group in the North Pilbara. A network of fractures introduces ore-grade specular hematite into the iron formation, and although distal to any known iron ores, this kind of alteration is virtually background for all banded iron formations (BIFs) in the Pilbara, showing that BIFs everywhere have experienced the ore-forming events to some degree. The degree of alteration casts doubts on the myth that BIFs are virtually unmodified from their sedimentary precursor. (b) Alternating layers of magnetite–hematite and chert in BIF. The magnetite bands are laminated to vaguely laminated to massive and even at the small scale truncate laminations (primary layering) in the chert. Field of view is 2 cm. (c) Close-up of BIF in (b) showing regularly spaced laminae of hematite in chert bands and erosional truncation of lamination in bedded chert. Field of view is 6 mm. (d) Finely laminated hematite–chert bands. Field of view is 6 mm. (e) Rhythms in BIF resembling thinly bedded density-current deposits (cf. turbidites), the lowest (dark) unit contains detrital grains. The green color is ferrostilpnomelane. Coarse structure in the chert interval is typical of early (precompaction) diagenetic chert and comprises irregular laminae of chert and relict laminae of ferric-stilpnomelane, obscured by rhombic carbonate. (f) Massive, graded bed from BIF composed of detrital grains of shale in a cherty matrix with euhedral grains of magnetite. The blue color is due to fine-grained, metamorphic riebeckite. (g) Graded massive to plane-laminated bed of stilpnomelane-rich tuffaceous siltstone–mudstone within BIF. The lower part of the section is similar to the rhythmic bedding in (e), but ferrostilpnomelane (green) has been oxidized to ferricstilpnomelane (dark), and magnetite euhedra have been replaced by hematite (red), although much magnetite remains. White-speckled appearance of the tuffaceous bed is due to fine-grained, diagenetic rhombic ankerite-ferroan dolomite. (b–d and f) Dales Gorge Member of the Brockman Iron Formation, Hamersley Province, Western Australia; (e and g) Joffre Member of the Brockman Iron Formation, Hamersley Province, Western Australia.

The gradient in hydrothermal influence on IF is also reflected in their geochemistry. Compositions of the Algoma-type end-member typically record local volcanic or hydrothermal conditions, rather than being representative of the large-scale chemistry of the oceans during their formation. In contrast, the deposition of Superior-type end-member reflects processes that probably acted on a global scale, and thus they are likely more representative of seawater composition (Huston and Logan, 2004). However, the potential influences by nearby cratonic areas also need to be considered (e.g., Alexander et al., 2009). In general, for discerning whether the geochemistry of IF reflects local or global seawater

compositions, a simple distinction between Algoma and Superior types is insufficient. Instead, one has to constrain the tectonic setting and degree of isolation of the basin in which IFs were deposited, relative to the global ocean, before any inferences regarding composition and redox state of ancient seawater can be made.

9.18.3 Mineralogy of IF

IFs are defined by their unusual mineralogy, which includes mostly silica and a wide range of Fe-rich and Al-poor minerals. Most IFs comprise layers containing magnetite and/or hematite, which alternate on the scale of several millimeters with bands of microcrystalline silica, forming microbands (Figures 2 and 3). Well-banded IFs (Figures 2 and 3), known as banded iron formations (BIFs), are mostly restricted to Archean and early Paleoproterozoic sequences. Large portions of late Paleoproterozoic IFs from the Superior and Slave cratons in North America and the Capricorn Orogen in Western Australia comprise sand-sized grains that commonly are cross-bedded and lack the finely laminated textures of BIF; these are generally referred to as GIFs (Figure 5). GIFs are typically intercalated with well-laminated IFs, Fe-rich mudstone, mafic and felsic volcanic rocks, and carbonate and sandstone.

The mineralogy of BIF and GIF from the best preserved sequences is remarkably uniform, comprising mostly silica, magnetite, hematite, Fe-rich silicate minerals (stilpnomelane, minnesotaite, greenalite, and riebeckite), carbonate minerals (siderite, ankerite, calcite, and dolomite), and, less commonly, sulfides (pyrite and pyrrhotite).

Chert (and crystalline quartz in metamorphosed IFs) is ubiquitous in all types of IF. In BIF, chert layers are commonly banded, alternating with millimeter-thick laminae of Fe-rich silicate and carbonate minerals. Individual laminae are wavy to wrinkly and, locally, appear to truncate against overlying laminae. In places, chert forms precompaction nodules draped by compacted laminae, suggesting an early paragenesis for the nodular chert. In GIF, the chert 'peloids' show open packing, indicating precompaction lithification.

Magnetite is widespread in IFs, where it occurs as euhedral, fine- to coarse-grained crystals (Figures 2 and 3). It is particularly abundant in cherty Fe-rich layers as laminae comprising dense clusters of intergrown euhedra (Figure 3(a)–3(c)). Magnetite commonly is replaced by hematite (termed martite) and locally replaces carbonate minerals. Magnetite is clearly a secondary mineral that formed mostly during the late history of the

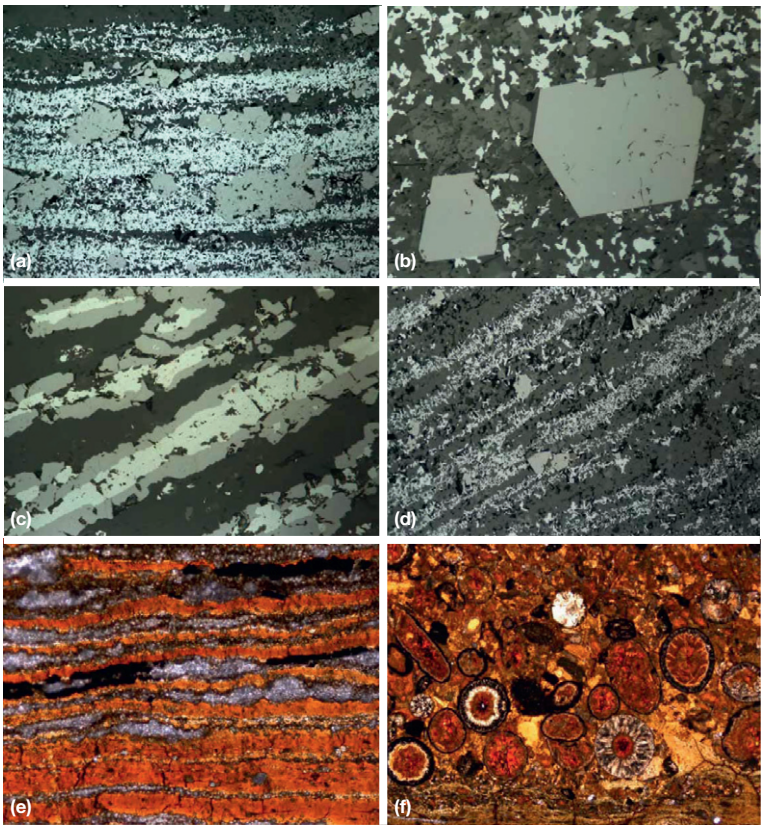

Figure 3 Photomicrographs from the Dales Gorge Member of the Brockman Iron Formation, Hamersley Province, Western Australia. (a) Banded iron formation comprising several larger clusters of magnetite euhedra in a band of laminated hematite. Field of view is 2.5 mm. (b) Two magnetite euhedra in a matrix of hematite, silica and carbonate. Field of view is 1.25 mm. (c) Alternating laminae of silica and iron oxides. Hematite cores are surrounded by magnetite. Field of view is 0.3125 mm. (d) Laminae of fine-grained hematite alternating with bands of chert. Field of view is 0.625 mm. (e) Band of laminated stilpnomelane and fine-grained siderite. Field of view is 0.625 mm. (f) Impact ejecta layer in the Dales Gorge S-band #4 containing melt spherules largely replaced by stilpnomelane. Field of view is 6 mm.

iron ore formation associated with metamorphism and deformation (Ayres, 1972; Ewers and Morris, 1981; LaBerge, 1964).

Hematite is the most common Fe-oxide mineral in IFs, where it typically occurs with magnetite in millimeter- to centimeter-thick layers (**Figure 3**). Together with magnetite, hematite defines the lamination in most chert layers. Hematite may also be present in some intercalated mudstones, but in this case, it is much less abundant than magnetite (or pyrite). The timing of hematite growth is texturally ambiguous, although rare hematite spheroids (Ayres, 1972) likely represent some of the earliest components of IFs (**Figure 4(e)** and **4(f)**). If they did form very early, then the precursor phase probably was a form of ferric oxyhydroxide, such as ferrihydrite.

Stilpnomelane is an Fe- and K-rich, Al-poor, hydrous silicate mineral, with a composition that is similar to that of sedimentary nontronite, an iron-rich, alumina-poor smectite. Stilpnomelane is diagnostic of lower greenschist facies metamorphic conditions. It is the most common Fe-silicate in many IFs, where it occurs as highly pleochroic plates and fibers, forming solid bands interlaminated with secondary carbonate (**Figure 3(e)**), and as irregular mattes and sheaves. Stilpnomelane is the main constituent of most mudstones associated with IFs, and is also a common component of chert and tuff layers and impact ejecta layers (**Figure 3(f)**) intercalated with IFs. For example, it replaces volcanic glass in felsic tuff beds and, locally, fine-grained stilpnomelane-filled spheres occur in laminated chert beds (Ayres, 1972; **Figure 4(a)**). At higher temperatures (>400 °C), stilpnomelane is replaced by biotite.

Minnesotaite is an Fe- and Mg-rich hydrous silicate that typically is less abundant than stilpnomelane, although there are some exceptions in sections of the late Paleoproterozoic IFs in the Superior craton. Minnesotaite occurs as radiating plates

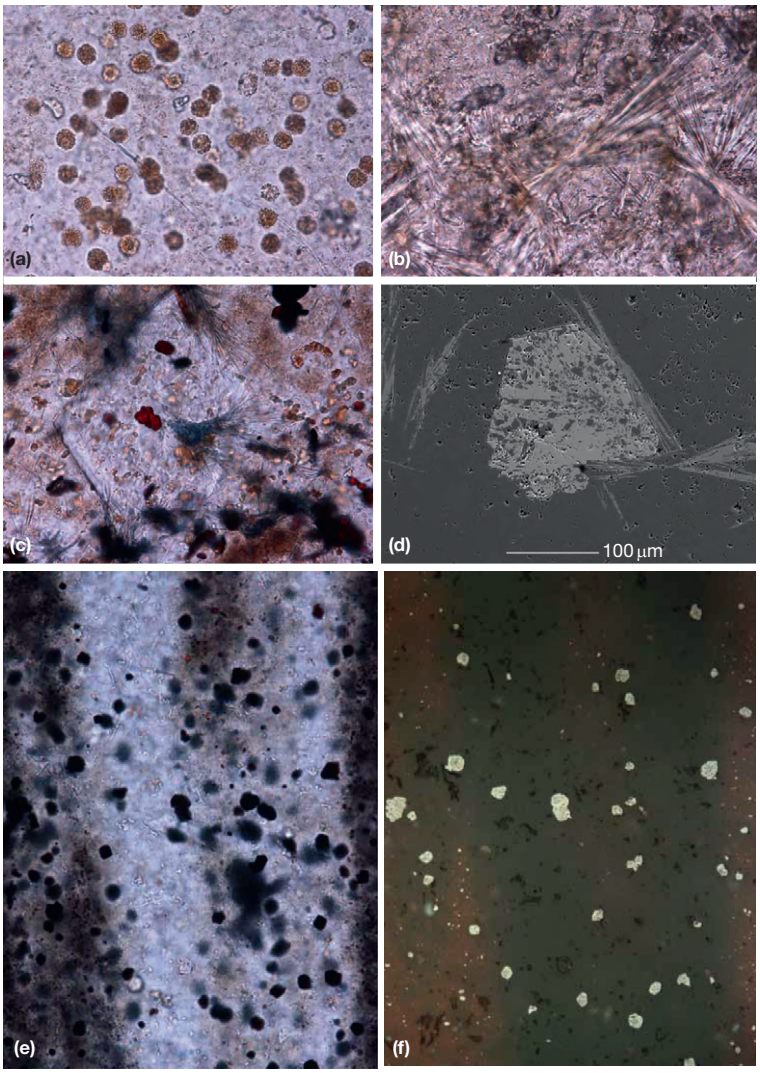

Figure 4 Samples from the Dales Gorge Member of the Brockman Iron Formation, Hamersley Province, Western Australia. (a) Numerous spherical structures composed of stilpnomelane in a chert matrix. Field of view is 0.625 mm. (b) Fine-grained sprays of minnesotaite needles arranged in typical 'bow-ties.' Field of view is 0.3125 mm. (c) Coarse euhedral ankerite rhomb enclosing crystals of hematite and riebeckite in a chert matrix. Field of view is 0.625 mm. (d) Back-scattered electron image of inclusion-rich apatite in a chert band. (e) Plane-polarized light image of numerous minute hematite crystals (opaque) preserved in a chert–hematite layer. Field of view is ~0.3 mm. (f) Reflected light image of (e) showing hematite crystals (white) containing numerous minute inclusions (speckled) in a matrix of chert (dark gray). Field of view is ~0.3 mm.

and needles, forming common 'bow-tie' texture (Figure 4(b)) and forms during metamorphism and late-stage hydrothermal alteration.

Riebeckite is a Na-rich amphibole that occurs in most BIFs from the Hamersley region in Western Australia and in the Kaapvaal craton of South Africa (Beukes, 1973; Klein and Gole, 1981). Riebeckite-rich layers are characteristically blue in hand specimen. Riebeckite forms clusters of randomly oriented fibers, which locally may be aligned to define a structural fabric. Paragenetic relations indicate that riebeckite formed late in the history of IFs. The fibrous form of riebeckite (crocidolite) forms veins that are a source of asbestos; these are overpressure veins that formed during regional folding (Krapež et al., 2003).

Greenalite is a pale green Fe-silicate that occurs in many IFs but typically is less abundant than stilpnomelane and minnesotaite. Greenalite is rare in the Hamersley and Transvaal BIFs, but where present occurs as a late-stage, secondary mineral. However, in GIF from the Superior craton, greenalite is more abundant and appears to be among the earliest minerals to have formed (Klein, 2005). Nevertheless, greenalite is not an original sedimentary mineral.

Siderite is the most common carbonate in BIFs, typically occurring as minute, single, rhomb-shaped crystals or massive layers of microcrystalline crystals. In some beds, siderite may comprise >50% of the rock. Small siderite nodules are common in some layers, where they display evidence of differential compaction, thus indicating that the nodules probably formed before deep burial. The texturally earliest siderite is present as minute (<20 μm) spheroids, which occur in some IFs and intercalated mudstone from the Hamersley Province (Ayres, 1972). This siderite appears to have replaced or overgrown an earlier phase, which occurs in the core of some crystals, indicating a diagenetic origin for the siderite. Sideritic BIF in many cases is not a primary sedimentary facies, because it can be closely linked to near-ore alteration.

Ankerite and ferroan dolomite occur in many chert layers typically as coarse, euhedral rhombs that overgrow and contain inclusions of chert, hematite, magnetite, and Fe-silicate minerals (Figure 4(c)), indicating that these carbonates were among the last minerals to form.

Trace minerals include pyrite, apatite, monazite, xenotime, zircon, ilmenite, and K-feldspar. Trace amounts of apatite have been reported from most IFs, forming euhedral crystals containing abundant inclusions of silica and other matrix minerals (Figure 4(d)). Apatite, even from very low metamorphic grade IFs, lacks significant carbonate and fluorine substitution into the crystal structure (e.g., Li et al., 2011), which would be expected if the mineral had formed during early marine diagenesis. Therefore, apatite is likely a burial diagenetic and metamorphic product. Apatite formation is probably associated with phosphorus exclusion during recrystallization of iron oxides or oxidation of buried organic matter (Li et al., 2011). Apatite is the most abundant phosphate mineral, but monazite and xenotime are also present in some IFs. Monazite forms minute (typically <100 μm), inclusion-rich aggregates in mudstone, whereas xenotime occurs mostly as overgrowths on zircon grains, which are likely diagenetic in origin. Zircon is rare in IFs, but can be locally abundant in millimeter- to centimeter-thick layers of felsic tuff (Pickard, 2002, 2003). Xenotime overgrowths can be dated in situ by the U–Pb SHRIMP method to obtain ages for IF upgrading (e.g., Rasmussen et al., 2007).

In conclusion, no unambiguously original sedimentary minerals occur even in the best-preserved IFs that only underwent very low-grade metamorphism. Microspherical and nodular textures appear to be among the earliest features of the IFs; however, it is highly unlikely that the minerals associated with those textures are original.

9.18.3.1 Precursor Sediments

Since all IFs have undergone significant modifications even during diagenesis and prehnite–pumpellyite facies metamorphism, their mineralogy reflects a combination of factors, including the original bulk composition of the precursor sediment, diagenetic and metamorphic conditions, and postdepositional fluid flow. Effects of increasing temperature and pressure have yielded a progressive change in mineralogy through replacement and recrystallization, increase in grain size, and obliteration of primary textures (Klein, 2005).

The alternating layers of magnetite and hematite are commonly interpreted to have formed from a ferric iron oxyhydroxide rain to the sediment pile. During early diagenesis, the ferric oxyhydroxide was apparently converted to hematite. It is possible that ferric iron and dissolved/absorbed ferrous iron combined to form a mixed-valence iron phase that later was converted to magnetite during late diagenesis and metamorphism. However, the magnetite could have also formed entirely during metamorphism, in cases with organic matter acting as the reductant (e.g., Perry et al., 1973; Tompkins and Cowan, 2001). Although the texture of most of the magnetite and hematite grains indicates a secondary, postdepositional origin, rare spheroids of hematite, about 5–20 μm in diameter, as mentioned above, have been considered to be among the earliest textures known in BIFs (Ayres, 1972). The spheroids are interpreted to represent original iron oxyhydroxides that were converted to hematite during diagenesis or regional metamorphism. Similar spheroidal textures comprising solid stilpnomelane and siderite are also present (Figure 4(a); Ayres, 1972).

Silica is widely considered to have been delivered to the sediments absorbed on iron oxyhydroxides, scavenged with organic matter, and precipitated from the water column at the sediment–water interface in colloidal form (e.g., Fischer and Knoll, 2009; Krapež et al., 2003; Grenne and Slack, 2005). An alternative interpretation is that the chert formed largely beneath the sediment–water interface as a replacement of a precursor sediment (Krapež et al., 2003).

Recently, Rosing et al. (2010) proposed that the ubiquitous coexistence of magnetite and siderite in Archean and Paleoproterozoic IFs could be used to constrain early Earth's atmospheric composition. They suggested that atmospheric CO_2 and CH_4 concentrations have been consistently overestimated in modeling early Earth's energy balance to explain the presence of liquid water on Earth at the time when, in the Sun's youth, solar luminosity was greatly reduced. Rosing et al. (2010) suggested that the coexistence of siderite and magnetite in IFs represents an assemblage that is close to thermodynamic equilibrium with the atmosphere, thus constraining the partial pressures of CO_2 and H_2. However, both these minerals are of diagenetic and metamorphic origins. Further, even in the

unlikely case that IF mineral assemblages formed during early diagenetic conditions in an environment close to chemical equilibrium with seawater, they cannot be used to constrain atmospheric carbon dioxide levels. For instance, dissimilatory iron-reducing bacteria have been observed to generate magnetite even at very high aqueous ΣCO_2 concentrations (~50 mM; Behrends and Van Cappellen, 2007) and headspace pCO_2 (~0.2 atm; Roh et al., 2003). Therefore, pCO_2 values greatly elevated above modern levels do not preclude the formation of magnetite at any stage in IF evolution. IF mineral assemblages thus cannot be used to place constraints on past atmospheric CO_2 concentrations. More broadly, since almost all Fe-bearing minerals in IFs formed at different times during diagenesis or metamorphism, their chemical and isotopic compositions are unlikely to reflect chemical equilibrium with seawater. Accordingly, the use of mineral assemblages to infer composition of the environment in which they formed, or extrapolations regarding composition of the atmosphere–ocean system, is typically plagued with uncertainties.

9.18.3.1.1 Secular trend in Fe mineralogy of GIFs

The secular change in the mineralogy of the same sedimentary facies may, however, provide insight into environmental change. Specifically, the mineralogy of GIFs may record atmosphere–ocean redox state and evolution leading to deposition of IFs. GIFs first appear at ~2.6–2.5 Ga in South Africa, Western Australia, and Brazil (Beukes and Klein, 1990; Simonson and Goode, 1989; Spier et al., 2007). However, most granules and sand-sized grains in these older GIFs consist of minerals having reduced and mixed-valence iron (e.g., magnetite, Fe-silicates, and carbonates); only rarely have hematite granules been observed and never as coated grains or oolites (Beukes and Klein, 1990; Simonson and Goode, 1989; Spier et al., 2007). In contrast, the extensive GIFs of the Animikie basin that were deposited at ~1.9 Ga contain oolites, coated grains, and granules made of minerals having predominantly oxidized iron (e.g., hematite), although reduced or mixed-valence coated grains, and granules are also present. Similar to the Animikie basin, younger Proterozoic IFs and Phanerozoic ironstones having coated grains are predominantly composed of ferric iron.

The secular trend in the distribution of mixed-valence iron silicates is poorly established. Early work suggested that glauconite did not form in open-marine, shallow-water settings until the Phanerozoic (Cloud, 1955). However, this view was rebutted by Kimberley (1989), who described Proterozoic examples including the ~2.3 Ga Gordon Lake Formation (Chandler, 1986) and emphasized that Archean examples are missing from the rock record. Indeed, mixed-valence iron silicate minerals such as berthierite, chamosite, and glauconite are absent in shallow-water Archean successions, even though they became abundant during the GOE (e.g., ironstone of the Timeball Hill Formation; Dorland, 1999). We infer that the lack of these minerals in shallow-water, Archean settings reflects low oxygen concentration that inhibited formation of mixed-valence Fe-silicates. In contrast, in Archean deep-water settings, mixed-valence Fe-silicates such as the precursors to stipnomelane and greenalite are common, indicating an upside-down redox profile similar to that documented in the Transvaal basin by combined sedimentary facies and mineralogical study (Beukes and Klein, 1990). Walker (1984) linked this counterintuitive redox structure to decreasing organic carbon fluxes offshore. Thus, the study of iron oxidation in mixed-valence Fe-silicate minerals holds potential to reveal information about ocean oxidation in the past. Specifically, the marked absence of mixed-valence iron minerals prior to ~2.3 Ga is one of several lines of evidence pointing to the lack of a discrete redoxcline and predominantly anoxic marine conditions in the Archean.

9.18.4 Depositional Setting and Sequence-Stratigraphic Framework

Depositional environments of IFs range from deep water, beyond or above a continental slope for BIF to shallow water, above storm- and fair-weather wave base for GIF. Both BIF and GIF were deposited during periods of high or rising sea level (cf. Fralick and Pufahl, 2006; Krapež et al., 2003; Simonson and Hassler, 1996).

Detailed sedimentologic studies of IFs have been conducted in the Hamersley Province of Western Australia, and in the Transvaal and Griqualand West structural basins of South Africa. There is no evidence from these studies that depositional environments were restricted. For instance, in the Hamersley Province, basin architecture did not change conclusively during the deposition of BIF and associated non-BIF facies, but rather the change that did occur involved a higher hydrothermal flux of reduced iron (Fe^{2+}) to the basin (Krapež et al., 2003). It is therefore likely that increased hydrothermal activity rather than changes in basin architecture was the first-order control on that flux.

Studies of BIF of the Hamersley Province have documented the presence of iron minerals and chert in paired layers that vary from 0.2- to 2.0-mm-thick microbands to 10- to 50-mm-thick mesobands. Initially, Trendall and Blockley (1970) (see also Trendall, 1990) suggested that such microbands and mesobands could be correlated basin-wide, which led to the inference that BIFs are chemical varves (Morris and Horwitz, 1983; Trendall, 1973). More recent studies, however, have shown that only the chert mesobands can be correlated (Krapež et al., 2003).

Through facies and sequence-stratigraphic analyses, Krapež et al. (2003) and Pickard et al. (2004) concluded that all chert in BIF is diagenetic in origin. Moreover, they concluded that chert mesobands are siliceous equivalents of modern-day seafloor hardgrounds (**Figure 2**), in which silica replaced precursor sediment at or below the sediment–water interface. Three-dimensional and microscale lenticularity of chert and relics of precursor sediment within lamina sets and discontinuous bands (**Figure 2(b)** and **2(c)**), as well as erosion surfaces on bedded cherts, show that chert has a replacement origin and formed during early diagenesis, prior to compaction.

Minute spheroids (~10 μm diameter) documented in the Brockman Iron Formation (Hamersley Group) were interpreted to record paragenetically early textures (Ayres, 1972). The spheroids are distributed along laminae in bedded chert, and along the chert laminae of BIF. Assuming that lamina sets in BIF originated from a process similar to that responsible for the lamina sets in lithofacies interbedded with BIF, they can be assumed to have a density current origin (Krapež et al., 2003). This density current interpretation is supported by the presence in BIF of two bedding styles of mesobands: microbanded and

tabular-bedded (**Figure 2**); the latter typically is massive or weakly laminated (Ewers and Morris, 1981; Morris, 1993). Massive mesobands grading upwards into microbanded mesobands resemble density-current intervals, and are preserved at various scales (**Figure 2(e)** and **2(f)**); some of those massive intervals are internally graded and contain tabular, mm-scale detrital fragments of shale. Occurrences of erosional truncation of draped laminae (Krapež et al., 2003) also support the density-current interpretation (**Figure 2(b)** and **2(c)**). Resedimentation occurred either by bottom currents or gravity-driven turbidity currents, and the resulting sediment bodies may have been contourite drifts (Krapež et al., 2003). The precursor sediments to BIFs were therefore microgranular in texture. Krapež et al. (2003) concluded that the precursor sediments could have been granular hydrothermal muds, composed of iron-rich smectite and particles of iron oxyhydroxide and siderite that were deposited on the flanks of submarine volcanoes.

The sequence architecture of formations containing BIF is identical to that of clastic sedimentary rocks that accumulated beyond the continental slope, comprising lowstand fans of shelf-derived sediment overlain by condensed sections of pelagites, hemipelagites, or intrabasinal clastic sediment (e.g., Haq, 1991). Depositional sequences in the Dales Gorge Member of the Hamersley Province, documented by Krapež et al. (2003), comprise lowstand density-current deposits (dolostone, graded shale, and rare conglomerate) overlain by a condensed section of BIF. Bedded chert defines the top of each depositional sequence by showing: (1) sharp, erosional contacts with overlying dolostone or mudstone; and (2) gradational contacts into underlying BIF. In contrast, the contacts from lowstand mudstone to condensed-section BIF are transitional (Krapež et al., 2003).

Lowstand deposits change from dolostone-shale to shale-only toward the southwest in the Hamersley Province, indicating a paleoslope to the southwest (Simonson et al., 1993); an overall thinning of lowstand deposits accompanies this down-paleoslope change. Lowstand deposits in distal sections contain BIF units that are identical to BIF in the condensed sections. This pattern suggests that the precursor sediments to BIF characterized basin sedimentation not only during rising and high sea level, but also during some lowstands, beyond the limits of shelf-derived resedimented sediments. Isopachs of BIF presented by Trendall and Blockley (1970) show that thickness variations define mounds elongated across the paleoslope. These trends, combined with the sequence architecture, indicate that the source of precursor sediments for BIF was within the basin realm and that the depositional system was some form of contourite current. A contourite drift is a sedimentary deposit that accumulates along the continental slope, from density currents that follow the contours of the basin floor, possibly entering the basin from a distal submarine canyon. For the precursor sediments to BIF, the deep-sea currents may have traveled down canyons headed in volcanic complexes. The implication is, therefore, that some precursor sediments to BIF were hydrothermal clays or clays derived by submarine weathering of basalts that accumulated on the slopes of, and among, submarine volcanoes (Krapež et al., 2003).

This model for deposition of the Dales Gorge BIF is applicable to other deep-water BIF such as those in the correlative Transvaal (South Africa), Krivoy Rog (Ukraine), Kursk Magnetic Anomaly (KMA, Russia), and Quadrilátero Ferrífero (Brazil) successions (**Appendix 1**). It is, however, not applicable to shallow-water IFs, such as those in the Pongola and Witwatersrand supergroups (Beukes and Cairncross, 1991), where responses to rising and falling sea levels differed according to sequence stratigraphy. Detailed sedimentological models for the Algoma-type IFs or thin BIF interbedded with shallow-water deposits, which integrated a basin-scale and sequence-stratigraphic approach, are not available and therefore it is premature at this point to discuss their sedimentological setting relative to the predictive architecture of deep- or shallow-water depositional environments.

GIFs are clastic sedimentary rocks that are largely restricted, at least in terms of preservation, to continental basins of Paleoproterozoic age. Paleoproterozoic basins surrounding the Superior craton of North America constitute the type area, where two lithofacies were recognized for a long time: slaty and cherty GIF (Ojakangas, 1983). The so-called slaty lithofacies is iron-rich shale comprising alternating, millimeter-scale, parallel- and wavy-laminated layers of iron-oxides or -silicates and chert, interbedded with lenses of grainstone. Lamina sets are similar to those in BIF, being made up of a basal layer rich in iron oxides and an upper chert-rich layer; gently-dipping erosive truncations draped by mudstone are also present (Pufahl and Fralick, 2004).

The cherty lithofacies is a grainstone with a cherty cement; in situ and reworked stromatolites are common (Ojakangas, 1983; Planavsky et al., 2009; Pufahl and Fralick, 2004). This lithofacies comprises interconnecting lenses of trough cross-stratified grainstone. The largest lenses typically have a basal layer of intraformational breccia derived from reworking of the underlying iron-rich mudstone.

Millimeter- to centimeter-scale, grain-size grading in iron-rich shale indicates that the depositional process was gravity settling. Occurrence of a siliciclastic component to the mudstone/shale supports suspension deposition from density currents. Density-current settling is common along current-, wave-, and storm-dominated shores, such that micrograded sets of mudstone are essentially the ambient sedimentary style. Traction currents likely were key in the deposition of granular beds within the mudstone sequences. Sets are channel-shaped, showing internal trough cross-stratification. Evidence of wave- and current-formed sedimentary structures and hummocky cross-stratification is abundant (e.g., Ojakangas, 1983; Pufahl and Fralick, 2004), establishing that the depositional environment was a shallow-water shelf disturbed by storms and influenced by significant sea-level changes. The environment also was coeval with bimodal volcanism, indicating almost certainly a volcano-tectonic influence. In general, the stratigraphic pattern is one of alternating packages of storm-influenced event beds and background density-current deposits, passing upwards into shallow-water grainstones of the cherty lithofacies (**Figures 5** and **6(a)**). The sequence-stratigraphic architecture therefore is upwards thickening and coarsening, reflecting deposition during rising and high sea level on a shelf. In the shallowest parts of the Animikie basin, these shallow-water facies can be capped by exposure surfaces, indicating IF filled the accommodation space. Although contrasting with the sequence architecture of BIF of the Hamersley

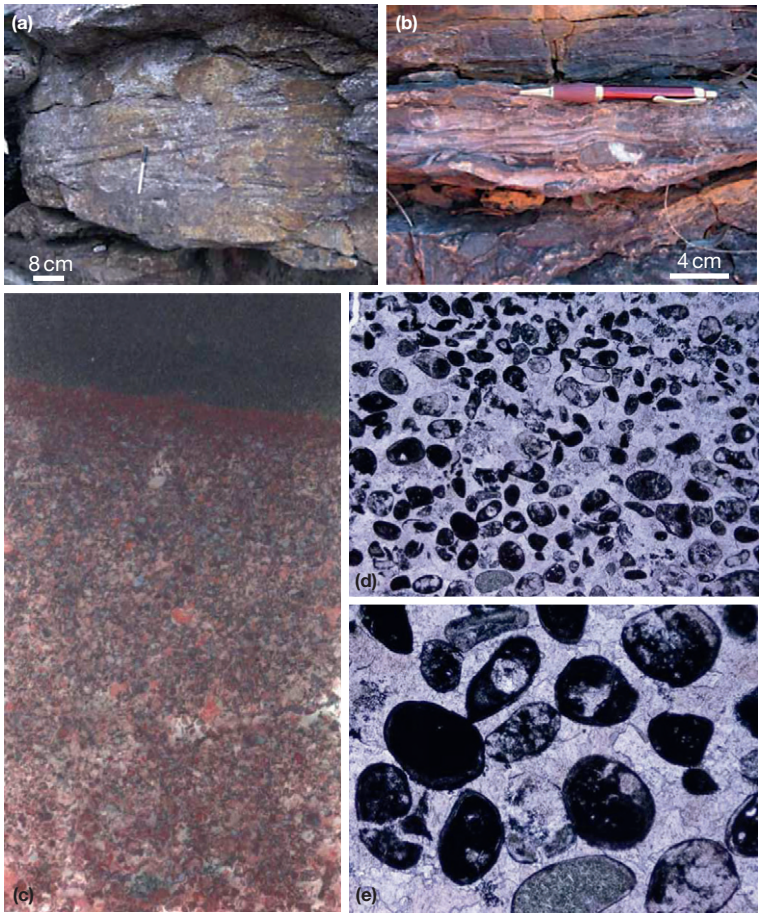

Figure 5 Middle Proterozoic GIFs. (a) Trough cross-bedded GIF of the *c*.1.88 Ga Temiscamie Iron Formation, Mistassini basin, Quebec. (b) Quartz-rich sandstone overlying ooidal ironstone and containing large rounded clasts of cemented ooidal ironstone and wavy heavy mineral bands composed of hematite; Train Range Member of the Mullera Formation, Constance Range, Northern Territory–Queensland border, Australia. (c) Graded bed comprising granules and ooides. Field of view is 2 cm. (d and e) Rounded granules comprising hematite, magnetite, chlorite, chert, and carbonate 'floating' in a matrix of carbonate cement. Field of view is 6 mm in (d) and 2.5 mm in (e). (c–e) ~1.88 Ga Frere Formation, Earaheedy Group, Western Australia.

basins (Krapež et al., 2003), the two styles are linked and are in agreement with a classic sequence-stratigraphic profile, defined by GIF on the shelf and BIFs on the deep-water basin floor. For GIF of the Superior craton, the transition between pairs of slaty and cherty lithofacies is a unit of convolute IF (**Figure 6(a)**).

Sequence-stratigraphic models for Phanerozoic (and some Mesoproterozoic) GIFs (ironstones) are slightly different because they comprise thin and locally discontinuous lithofacies within siliciclastic depositional sequences. Maynard and Van Houten (1992) suggested that oolitic ironstones were deposited after the peak of regression and prior to the peak of transgression (**Figure 6(b)**). The ironstones are capped by a hardground, which in the Mesoproterozoic oolitic IFs of northern Australia, is recognized by ooids, granules, and intraclasts floating in an early diagenetic chert matrix/cement (Harms, 1965). Cherty hardground records the peak of siliciclastic sediment starvation on the shelf, thereby representing a maximum flooding surface (**Figure 6(b)**; cf. Fürsich et al., 1992; Pope and Read, 1997). Oolitic IF within siliciclastic depositional sequences therefore formed during transgression rather than still-stand. Not only would peak flooding be the time of high organic productivity and anoxia on the shelf, but it likely would also be the period of maximum ingress of basinal waters, again suggesting that a basinal supply of Fe(II) was a key aspect of IF.

9.18.4.1 Basin-Type Control on IF Deposition

After the rise of atmospheric oxygen during the GOE, isolated to semi-isolated basins favored the development of conditions necessary for Fe(II) transport. Restriction commonly results in less vigorous circulation and limits exchange between oxygenated surface waters and bottom waters. Additionally, a smaller flux of reductants was required to induce anoxia. Under these conditions during the Phanerozoic, small IFs and exhalites formed in arc-related basins in association with volcanic successions. Some Phanerozoic ironstones also likely formed in redox-stratified epicontinental seas. Before the GOE, ocean redox state was not a limiting factor for the deposition of IFs. However, large hydrothermal fluxes were required to deliver iron from the site where it was released from volcanics to the

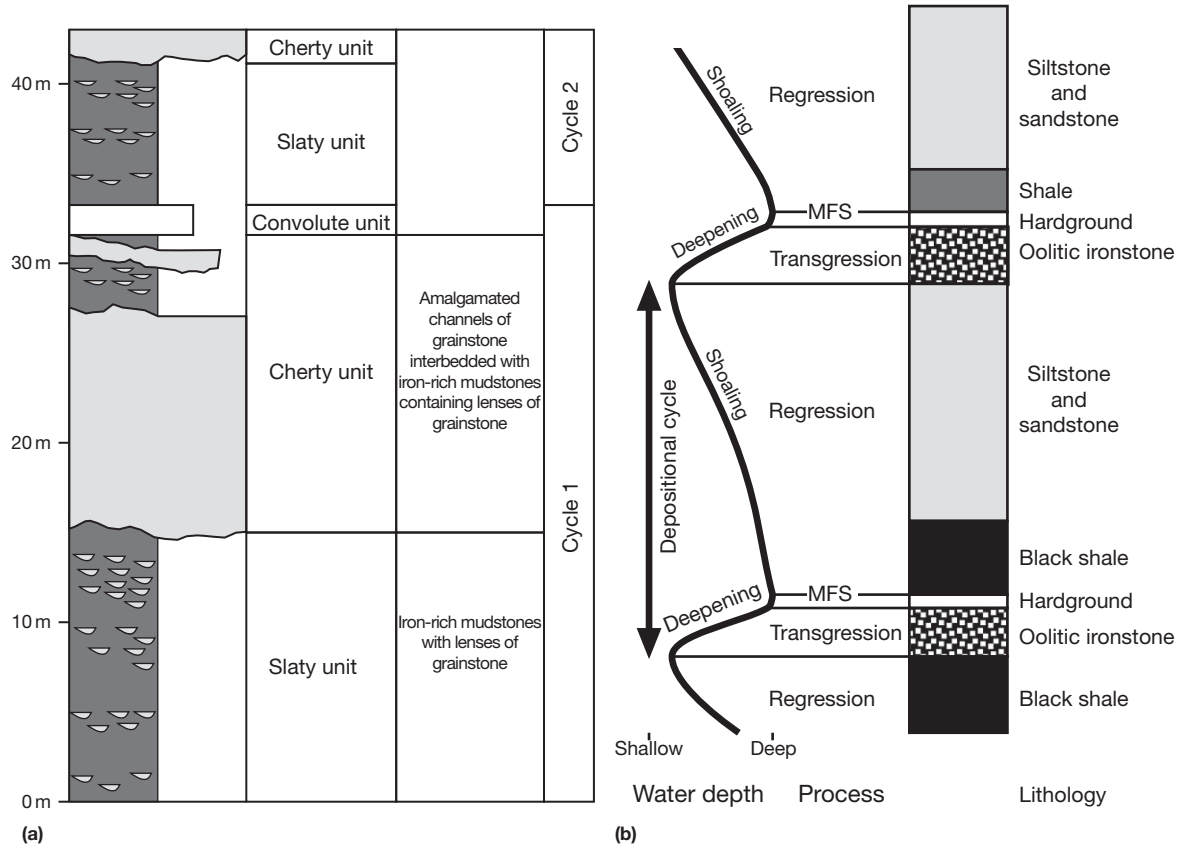

Figure 6 (a) Stratigraphic profile showing facies composition of depositional cycles in granular iron formations of the Lake Superior area. Each cycle shallows upwards from laminated iron-rich mudstone to amalgamated channel fills of grainstone, with convoluted units present at the top of each sequence. Modified from Pufahl PK and Fralick PW (2004) Depositional controls on Palaeoproterozoic iron formation accumulation, Gogebic Range, Lake Superior region, USA. *Sedimentology* 51: 791–808. (b) Generalized sequence-stratigraphic model for Phanerozoic oolitic ironstones. Rather than oolitic ironstones forming during still-stand at the peak of regression, they probably formed during transgression prior to maximum flooding. Modified from Maynard JB and Van Houten FB (1992) Descriptive model of oolitic ironstones. In: Bliss JD (ed.) *Developments in Mineral Deposit Modeling*. *US Geological Survey Bulletin 2004*, pp. 39–40. Washington, DC: US Government Printing Office.

depositional site on continental margins and oceanic plateaus, where it could survive subduction.

In addition to basin configuration and isolation, basin tectonic setting also is a critical factor in the formation of large IFs. A large Fe flux to the basin is needed to overwhelm background siliciclastic sedimentation and result in deposition of IF rather than Fe-enriched shale. Although sedimentation rates of IFs were likely high (see below), IFs are confined to depositional sites having low rates of terrigenous sediment delivery such as during rising and high sea level (cf. Krapež et al., 2003). In this sense, IFs mark condensed sections in the context of sediment delivered from the continents. Considering this sequence stratigraphic framework, large IFs should not occur in intracratonic rift basins and on passive continental margins where a high sediment flux and a buffered redox state of the large seawater reservoir after the GOE likely hindered their development. In addition, late stages in foreland basin evolution are also not favorable for the deposition of large IFs because high sediment fluxes derived from the unroofing of fold-and-thrust belts likely overwhelmed their accumulation. By contrast, early-stage foreland, back-, and fore-arc basins were better suited for IF deposition: relatively gentle slopes, continuous subsidence, basin isolation, and submarine volcanic activity would have all favored IF development. This framework not only allows the screening of basins for their potential to have large IFs, but also justifies the use of known IFs as markers of condensed sections on a basin scale and for interbasinal correlation.

9.18.4.2 Sedimentation Rates

Knowledge of sedimentation rates of IFs is important for understanding their iron sources and mechanisms of deposition, as well as depositional settings that are favorable for their formation. There have been many geochronologic studies (e.g., Altermann and Nelson, 1998; Arndt et al., 1991; Barley et al., 1997; Barton et al., 1994; Pickard, 2002, 2003) that discuss sedimentation rates of the precursor sediments to BIF. Inferred compacted sedimentation rates range from as low as 2–6 m My^{-1} to as high as 30–33 m My^{-1}. However, there has been limited attention paid to extremely pulsed nature of IF deposition. Krapež et al. (2003) showed that each sedimentation unit of Hamersley BIF is capped by a seafloor hardground of chert, and that many of those hardgrounds were eroded prior to deposition of subsequent sets. Therefore, it is difficult to determine the significance of average depositional rates for

BIF when so much time within each sedimentation unit and depositional sequence had been taken up by non-depositional processes such as erosion and subseafloor silica replacement. Clearly, depositional rates so calculated significantly underestimate true depositional rates. Although all sedimentary rocks are characterized by pulsed deposition (Sadler, 1981), the sedimentary architecture of IFs suggests that they have experienced extreme (in frequency and duration) sedimentary hiatuses. Therefore, although previous estimates of depositional rates for IFs are similar to those for typical deep-sea sediments, there undoubtedly were pulses of rapid sedimentation similar to, or likely even more extreme than, those characteristic of near-axis, modern deep-sea sediments.

Based on the sequence analysis presented in Krapež et al. (2003), and known geochronological constraints, each depositional sequence spans an average duration of about 1.5 My, roughly equal to the duration of third-order eustatic cycles possibly driven by pulses in spreading rates of mid-ocean ridges. The thickness of each depositional sequence is not constant, and neither is the proportion of diagenetic lithofacies, further negating the meaning of IF sedimentation rates based on the ratio of averaged thickness to averaged time interval. It is therefore reasonable to infer that rates as high as 33 m My^{-1} for the maximum compacted sedimentation rate are an underestimation, and that even higher sedimentation rates should be considered in modeling IF deposition.

9.18.5 IF: A Proxy for Ancient Seawater Composition

9.18.5.1 Trace Elements

IFs, as chemical deposits, are among the most obvious lithologies to use to investigate the composition of ancient oceans. Their precursor minerals precipitated directly from, or formed by, interaction with seawater. Moreover, many IFs contain low concentrations of crustally sourced elements such as Al, Ti, Zr, Th, Nb, and Sc, which supports an authigenic origin. Hence, secular changes in IF composition have long been used as proxies for the chemical evolution of seawater over time (e.g., Bau and Dulski, 1996; Bolhar et al., 2002; Jacobsen and Pimentel-Klose, 1988), and, most recently, to evaluate the types of nutrients that were available to ancient marine life (e.g., Bjerrum and Canfield, 2002; Konhauser et al., 2007a,b; Planavsky et al., 2010a,b). Four examples of how hydrogenous trace elements can track seawater composition are provided below.

9.18.5.1.1 Rare earth elements

Analysis of rare earth element (REE) patterns is a powerful tool to understand conditions under which IFs were deposited (e.g., Alexander et al., 2008; Bau and Dulski, 1996; Bau and Möller, 1993; Derry and Jacobsen, 1990; Frei et al., 2008; Fryer, 1977; Kato et al., 2006; Klein and Beukes, 1989; Planavsky et al., 2010a,b). Given a constant ionic charge, all of the REE should generally display similar behavior, with differences being linked to ionic radius. The most notable exceptions are the redox-related anomalies shown by Ce and Eu. Ce can be oxidized from the trivalent to tetravalent state under similar redox conditions to Mn(II) oxidation. In high-temperature (>250 °C) hydrothermal systems, Eu can undergo reduction from the trivalent to divalent state (Sverjensky, 1984), resulting in positive anomalies in hydrothermal fluids relative to neighboring lanthanide series elements (Sm and Gd). Fluid pH and ligand (sulfate, chloride, and fluoride) concentrations have an effect on REE patterns of hydrothermal fluids formed in back-arc basins such as the Manus basin (Craddock et al., 2010). Additionally, certain REE (foremost La and Gd) display anomalous bonding behavior linked to their f orbital configurations in low-temperature aqueous systems. This anomalous behavior, referred to as the lanthanide tetrad effect, can be explained from a quantum mechanics perspective with refined, spin-pairing energy theory (Kawabe et al., 1999). Anomalous redox- and non-redox-controlled bonding behavior results in deviations from the pattern expected based exclusively on charge and radius-smoothed REE patterns when normalized to average shale (Byrne and Sholkovitz, 1996). Lastly, there are differences in burial fluxes of light versus heavy REE in aqueous systems. In marine systems, carbonate complexation of REE results in the light REE having a much higher sorption affinity. Therefore, deviations in REE patterns can be used to track high-temperature, hydrothermal, and low-temperature, aqueous geochemical processes.

REE studies of IFs build on the assumption that there is minimal fractionation of REE during adsorption onto ferric iron oxyhydroxide precipitates; IFs are inferred to trap an REE signature of seawater at the site of ferric iron precipitation. This assumption is based on both experimental studies and results from natural systems, and is likely valid for pH-buffered marine systems. For instance, Mn-poor hydrothermal plume particles essentially record a seawater REE pattern (e.g., Sherrell et al., 1999). REE behavior in modern seawater is relatively well understood and serves as a foundation for interpreting REE patterns of IF.

There have been two main objectives in REE studies of IFs: (1) tracing Fe sources, and (2) using the redox-dependent properties of REE to decipher oxidation mechanisms responsible for iron deposition. Europium anomalies have been central in the use of REE to trace Fe sources. Europium enrichment in chemical sedimentary rocks that precipitated from seawater indicates a strong influence of hydrothermal fluids on the seawater-dissolved REE load (Derry and Jacobsen, 1988, 1990; Klinkhammer et al., 1983). The disparate behavior of Eu from neighboring REE in hydrothermal fluids is linked to Eu (III) reduction at high temperatures (>250 °C) and low Eh conditions (Klinkhammer et al., 1983; Sverjensky, 1984). It is generally assumed that Fe and REE will not fractionate during transport from spreading ridges or other exhalative centers, and therefore a large positive Eu anomaly indicates that Fe in the protolith of IF is hydrothermally derived (e.g., Slack et al., 2007). Nd isotope data further support a hydrothermal source of Fe to Precambrian IFs (e.g., Bau and Dulski, 1996; Derry and Jacobsen, 1990; Jacobsen and Pimentel-Klose, 1988).

Secular trends in the magnitude of Eu anomalies in large sediment-hosted IFs have historically been assumed to indicate variations in hydrothermal flux (e.g., Derry and Jacobsen, 1990), possibly linked to thermal history of the mantle. However, without independent constraints it is not possible to exclude a link between a long-term decrease in the magnitude of Eu anomalies to shifts in the continental delivery of REE, potentially related to either crustal growth or crustal emergence above seawater. Large positive Eu anomalies are a common

feature in Phanerozoic and Proterozoic distal hydrothermal sediments (e.g., Peter, 2003; Slack et al., 2007), but positive Eu anomalies in post-Paleoproterozoic sediments are generally assumed to indicate a local hydrothermal flux rather than hydrothermally dominated seawater composition of the global ocean. The lack of large Eu anomalies in IFs (e.g., ~2.22 Ga Hotazel Formation in South Africa; Tsikos and Moore, 1997) or any of the Neoproterozoic IFs associated with the 'snowball Earth' glaciations (e.g., Halverson et al., 2011; Klein and Ladeira, 2004) may indicate that during deposition of these IFs the oceans were not greatly influenced by a high-temperature (>250 °C) hydrothermal flux.

REE studies have also focused on redox-controlled, water-column REE behavior in modern anoxic basins. In general, oxygenated marine settings display a strong negative Ce anomaly when normalized to shale composites ($Ce_{(SN)}$), whereas suboxic and anoxic waters lack large negative $Ce_{(SN)}$ anomalies (e.g., Byrne and Sholkovitz, 1996; German and Elderfield, 1990). Oxidation of Ce(III) to Ce(IV) greatly reduces Ce solubility, resulting in its preferential removal onto Mn–Fe oxyhydroxides, organic matter, and clay particles (Byrne and Sholkovitz, 1996). In contrast, suboxic and anoxic waters lack large negative $Ce_{(SN)}$ anomalies due to reductive dissolution of settling Mn–Fe-rich particles (Byrne and Sholkovitz, 1996; German et al., 1991). Similarly, light REE depletion and high Y/Ho ratios develop in oxygenated waters due to preferential removal of light versus heavy REE and of Ho relative to Y onto Mn–Fe oxyhydroxides and other particle-reactive surfaces. As a result, the ratio of light to heavy REE markedly increases across redox boundaries due to reductive dissolution of Mn–Fe oxyhydroxides (Byrne and Sholkovitz, 1996; German et al., 1991), whereas dissolved Y/Ho ratios decrease across redox boundaries. In many modern marine basins, the $Ce_{(SN)}$ anomaly and light to heavy REE ratio return to values near that of the shale composite across the Mn and Fe redox boundaries. In some basins, even positive $Ce_{(SN)}$ anomalies and light REE enrichment develop within anoxic and suboxic waters (e.g., Bau et al., 1997b; de Baar et al., 1988; De Carlo and Green, 2002; Schijf et al., 1995). Redox-induced shifts in REE patterns in some modern stratified basins have been directly linked to Mn-cycling in the suboxic zone (De Carlo and Green 2002; German et al., 1991).

In many Archean and early Paleoproterozoic IFs there is no deviation from trivalent Ce behavior (e.g., Alexander et al., 2008; Bau and Dulski, 1996; Bau and Möller, 1993; Bau et al., 1997a; Frei et al., 2008; Fryer, 1977; Prakash and Devapriyan, 1996), suggesting that the water column from which ferric oxyhydroxides precipitated was reducing with respect to Mn (cf. Bau and Dulski, 1996). In support of this model, in a recent survey, 18 different Paleoproterozoic and Archean IFs lack significant true Ce anomalies until after the GOE (Planavsky et al., 2010a,b; **Figure 7(a)** and **7(b)**). There are several reported cases of Ce anomalies in Archean IFs (e.g., Kato et al., 2006). However, many – if not all – of these cases can be linked to analytical artifacts or analysis of samples that were affected by supergene alteration or weathering (Bekker et al., 2010; Braun et al., 1990; Planavsky et al., 2010a,b; Valeton et al., 1997).

There also appear to be differences in trivalent REE behavior in IFs before and after the rise of atmospheric oxygen. Archean and early Paleoproterozoic IFs are characterized by consistent light REE depletion and high Y/Ho ratios (Planavsky et al., 2010a,b). This pattern contrasts markedly with data for late Paleoproterozoic IFs that show significant ranges in light to heavy REE ($Pr/Yb_{(SN)}$) and Y/Ho ratios both below and above the shale composite value (Planavsky et al., 2010a,b; **Figure 7(c)**). This range of light to heavy REE and Y/Ho ratios (**Figure 7(c)** and **7(d)**) in late Paleoproterozoic IFs likely reflects variable fractionation of REE+Y by Mn- and Fe-oxyhydroxide precipitation and dissolution. Such an interpretation implies deposition of late Paleoproterozoic IFs, at ~1.88 Ga, in basins having varying redox conditions and a strong redoxcline, which separated the upper oxic water column from the deeper-water, suboxic to anoxic waters (Planavsky et al., 2009). A similar Mn redoxcline was likely absent in the Archean oceans. Significant Ce anomalies are lacking in carbonates deposited in shallow-marine settings on Archean carbonate platforms, which is consistent with this model (Planavsky et al., 2010a,b).

Isotope ratios of some REE (e.g., Ce and Nd), in addition to REE concentrations, have been used to constrain REE and Fe sources to seawater and the time when REE systematics was established (Amakawa et al., 1996; Derry and Jacobsen, 1990; Hayashi et al., 2004; Shimizu et al., 1991; Tanaka and Masuda, 1982). Both Ce and Nd have short residence times in the modern ocean, 90–165 and 1000–1500 years, respectively, and heterogeneous isotope compositions (Amakawa et al., 1996). The Archean oceans were also likely strongly heterogeneous having $\varepsilon_{Nd}(t)$ values of +1 to +2 typical of deep waters dominated by hydrothermal Nd sources, and lower values down to −3 typical of shallow waters dominated by terrestrial Nd sources (Alexander et al., 2009). Similarly, $\varepsilon_{Ce}(t)$ values in IFs show a strong hydrothermal impact on seawater composition in the Archean (Shimizu et al., 1990, 1991). Further, the La–Ce geochronometry can be a valuable tool to constrain whether negative or positive Ce anomalies reflect seawater composition, diagenesis, or later metamorphic alteration, by dating when REE systematics was established and comparing this age with the independently known depositional age (Hayashi et al., 2004).

9.18.5.1.2 Phosphorus

IFs have the potential to track dissolved phosphate concentrations in ancient oceans (e.g., Bjerrum and Canfield, 2002). It is well established, based on work in modern hydrothermal systems, that phosphate sorption onto iron oxides follows a distribution coefficient relationship; the amount of solid-phase P in iron oxides scales with dissolved phosphate concentrations (e.g., Edmonds and German, 2004; Feely et al., 1998). Importantly, however, this does not imply that P is simply adsorbed onto ferric oxides. In fact, there is evidence that P is co-precipitated with a Fe–Ca–P phase (Lilley et al., 1995). During early diagenesis, sediment phosphorus concentrations decrease slightly, but most phosphorus will be retained during Fe oxide recrystallization and secondary apatite precipitation (e.g., Poulton and Canfield, 2006). The process will not significantly vary in different depositional settings, because it is controlled largely by the surface chemistry of iron oxides. This simple framework opens a pathway for estimating the levels of this key nutrient in the ocean through Earth history (Bjerrum and Canfield, 2002).

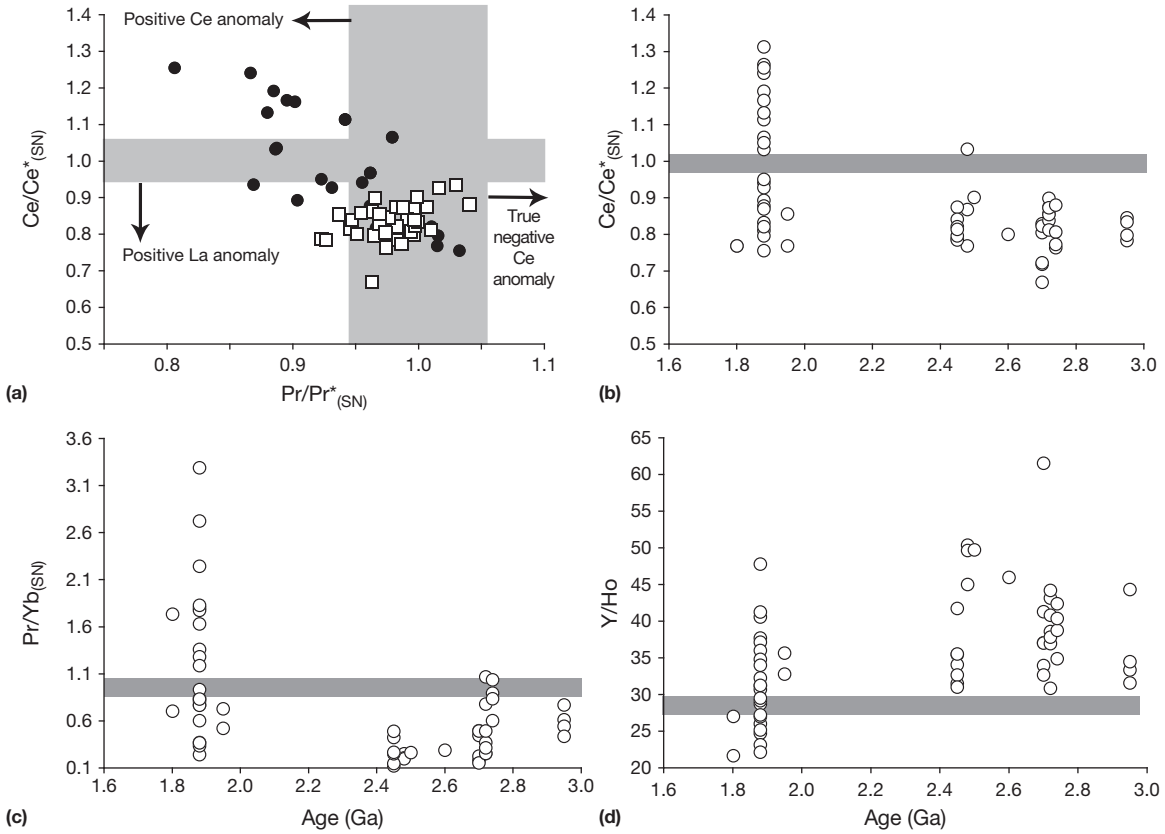

Figure 7 Secular trends in REE + Y characteristics in a set of 18 Archean and Paleoproterozoic iron formations. (a) Plot of Ce_{SN} and Pr_{SN} anomalies for a set of late Paleoproterozoic (●) and Archean and early Paleoproterozoic (□) iron formations. Positive Ce anomalies are only present in late Paleoproterozoic iron formations, whereas all iron formations shown lack true negative Ce anomalies. True negative Ce anomalies are defined by Ce/Ce^*_{SN} ($Ce_{SN}/(0.5(Pr_{SN}+La_{SN}))$) and Pr/Pr^*_{SN} ($Pr_{SN}/(0.5Ce_{SN}+0.5Nd_{SN})$) values above and below unity, respectively. This approach, first described by Bau and Dulski (1996), discriminates between positive La and true negative Ce anomalies. (b) Ce anomalies ($Ce_{SN}/(0.5(Pr_{SN}+La_{SN}))$). (c) Light to heavy REE ratios (Pr/Yb_{SN}). (d) Y/Ho ratios. Black bar indicates PAAS shale composite values. Archean iron formations are characterized by higher Y/Ho ratios and lower light to heavy REE ratios than those of the shale composite; late Paleoproterozoic iron formations have a large range of Y/Ho and light to heavy REE ratios. Observed secular trend in REE + Y characteristics is best explained by the absence of an Fe–Mn chemocline in the Archean oceans prior to the rise of atmospheric oxygen (see text for details). Modified from Planavsky NJ, Bekker A, Rouxel OJ, Knudsen A, and Lyons TW (2010) Rare earth element and yttrium compositions of Archean and Paleoproterozoic iron formations revisited: New perspectives on the significance and mechanisms of deposition. *Geochimica et Cosmochimica Acta* 74: 6387–6405; Planavsky NJ, Rouxel OJ, Bekker A, et al. (2010). The evolution of the marine phosphate reservoir. *Nature* 467: 1088–1090.

A complicating factor of this seemingly simple approach is that distribution coefficients can vary with different solution chemistry, potentially leading to dramatically different P/Fe ratios in IFs. Fortunately, phosphate outcompetes most anions for sorption sites on iron oxides. However, dissolved Si, at high concentrations, will outcompete phosphate for such sites (e.g., Konhauser et al., 2007a,b). Additionally, metal-silica coprecipitation should diminish the resulting particle's point of zero net charge, rendering it less reactive to dissolved anions (e.g., Konhauser et al., 2007a,b). Therefore, higher dissolved Si levels should yield lower P/Fe ratios in iron oxides, at constant phosphate concentrations. This process is significant because the marine Si cycle and dissolved Si concentrations have changed dramatically through time with the proliferation of enzymatic Si precipitation, foremost with the radiation and evolution of diatoms in the Cretaceous (Maliva et al., 2008; Siever, 1992). More generally, dissolved Si concentrations in seawater have decreased through the Phanerozoic as the Si cycle became increasingly biologically controlled. A decrease in dissolved Si concentrations through time is likely to have affected the abundance of a wide range of elements in iron oxide-rich rocks, not just P concentrations.

Interestingly, at low levels, variations in Si concentration appear to have little effect on anion sorption to iron oxides. In the North Atlantic, bottom-water Si is about 40 μM whereas in the Pacific the concentrations are much higher, ~170 μM (e.g., WOCE, 2002). One might expect the slope between dissolved P concentrations and P/Fe ratios to be different between the Atlantic and the Pacific oceans; in the Pacific, the particles should adsorb much less P. However, the trends in both oceans are similar (Edmonds and German, 2004; Feely et al., 1998). In the modern ocean, Si has no obvious influence on P/Fe ratios for the concentration range of 40–170 μM Si. This is not surprising, since at these relatively low Si concentrations, negligible Si becomes incorporated into ferric-oxyhydroxide plume particles. Importantly, the range of variation in modern

dissolved Si concentrations is small compared to changes in seawater Si concentrations envisaged during biomineralization evolutionary events in the late Precambrian and Phanerozoic (100s–1000s of micromolar Si shifts; Maliva et al., 2005; Siever, 1992). However, this potential discrepancy warrants additional experimental work on phosphate sorption onto iron oxides at lower silica concentrations. It is possible that a threshold value exists at which the inhibitory effect becomes pronounced.

Additionally, iron-rich particles in modern, neutrally buoyant plumes and rising plumes contain P-rich organic matter and Fe as sulfides (Edmonds and German, 2004; Feely et al., 1998). The P/Fe ratios of hydrothermal plume particles are likely to be affected by these organic P and Fe(II) phases (even though the Fe(II) phases are oxidized to Fe(III) phases relatively rapidly). However, these effects are small enough that a single global phosphorus–Fe-oxide K_d value can be delineated from modern hydrothermal particles (Feely et al., 1998). In summary, P/Fe ratios in modern hydrothermal plume particles are primarily controlled by the phosphate concentration in coeval seawater.

When viewed in light of the evolution of the Si cycle, P/Fe ratios in IFs offer a perspective on dissolved P concentrations in the oceans through time (e.g., Planavsky et al., 2010a,b; **Figure 8**). It appears that a relatively narrow range of variation existed in dissolved phosphate concentrations throughout the Phanerozoic, consistent with models of global biogeochemical cycles (e.g., Arvidson et al., 2006). In contrast, during the Precambrian, phosphate concentrations may have been significantly elevated relative to those of modern oceans. Foremost, Neoproterozoic IFs have very high P/Fe ratios, despite the high dissolved Si concentrations at that time, which would have inhibited phosphate sorption onto iron oxides. Similarly, in Archean and Paleoproterozoic IFs, P/Fe ratios are suggestive of elevated marine phosphate concentrations. This hypothesis is a deviation from the prevailing view of the early Precambrian phosphorus cycle (Bjerrum and Canfield, 2002). A large amount of phosphorus is currently removed from seawater during the oxic alteration of seafloor basalts by absorption of P onto basalt-derived iron oxyhydroxide particles (see **Chapter 10.13**). In largely anoxic early Precambrian oceans, however, this phosphorus flux would have been shut off, which likely partly

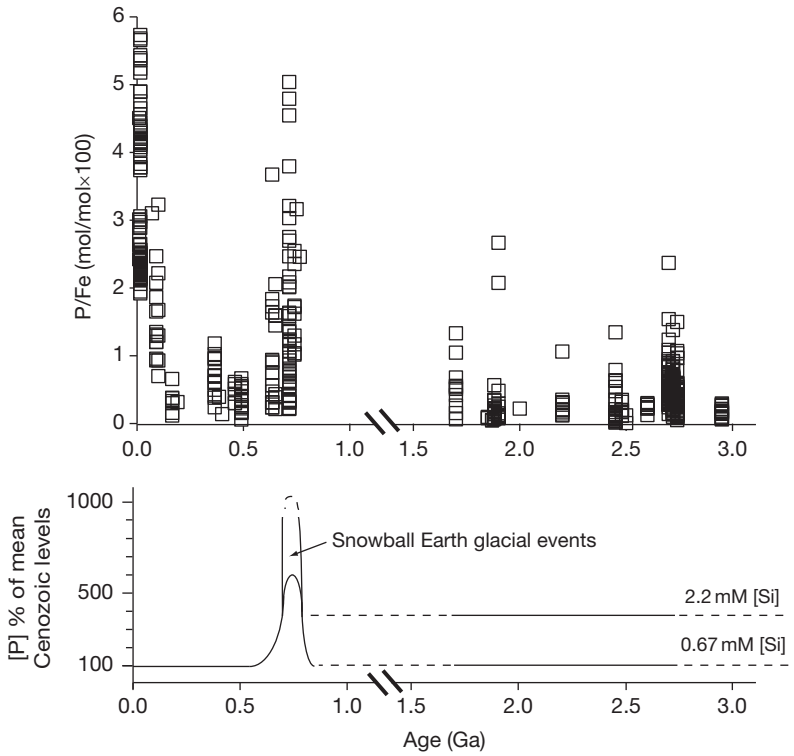

Figure 8 (a) P/Fe molar ratios through time in iron oxide-rich distal hydrothermal sediments and iron formations with low amounts of siliciclastic input. Open squares are individual samples. The P/Fe ratio reflects the size of the marine phosphate reservoir; phosphate sorption onto ferric oxyhydroxides follows a distribution coefficient relationship. The ratio is also influenced by the concentration of dissolved silica, because phosphate and silica hydroxides compete for sorption sites on ferric oxyhydroxides. (b) Phosphate concentrations were extrapolated from average P/Fe ratios for individual formations at dissolved seawater silica concentration of 0.67 mM (cristobalite saturation) and 2.2 mM (amorphous silica saturation). The compilation of P/Fe data suggests that there were elevated seawater phosphate concentrations in the Precambrian and a peak in phosphate level associated with the Neoproterozoic snowball Earth glaciations. This late Precambrian increase in dissolved phosphorus concentration may have stimulated high rates of organic carbon burial and a corresponding increase in atmospheric oxygen levels – paving the way for the metazoan diversification. Modified from Planavsky NJ, Rouxel OJ, Bekker A, et al. (2010). The evolution of the marine phosphate reservoir. *Nature* 467: 1088–1090.

explains elevated Precambrian phosphate concentrations in seawater. If this interpretation is quantitatively important, it provides an underappreciated feedback that may help constrain ocean productivity and, indirectly, surface oxidation from overly high levels. The Neoproterozoic IFs are closely tied temporally to snowball Earth glaciations, suggesting that glaciations or deglaciations could have played a complementary role to the high P levels inferred for Neoproterozoic seawater (cf. Hoffman and Schrag, 2002; Planavsky et al., 2010a,b).

9.18.5.1.3 Nickel

Nickel concentrations similar to those of phosphate follow a distribution coefficient relationship during precipitation of ferric oxyhydroxides. Therefore, the amount of Ni in oxide-facies IFs with limited contribution of detrital materials can be used to track first-order trends in dissolved Ni concentrations in seawater (Konhauser et al., 2009). Ni is also of special interest because it is a bioessential nutrient that in the modern ocean follows a nutrient-type profile. The nickel content (expressed as molar Ni/Fe) in IFs has changed dramatically over time, beginning with a drop in Ni availability in the oceans at ~2.7 Ga (Konhauser et al., 2009; **Figure 9**). Iron-normalized Ni concentrations in ~3.8–2.7 Ga IFs are greater than 0.0004 M, were about half that value between 2.7 and 2.5 Ga, and subsequently slowly approached modern values (<0.0001) by 0.55 Ga. This drop in seawater Ni availability would have had profound consequences for microorganisms that depended on it, particularly methane-producing bacteria – methanogens (Konhauser et al., 2009). These bacteria have a unique Ni requirement for their methane-producing enzymes, and a deficiency in this metal could have decreased their population. Crucially, these bacteria have been implicated in controlling oxygen levels on ancient Earth because the methane they produced was reactive with oxygen and kept atmospheric oxygen levels low (Zahnle et al., 2006). Methanogenic bacteria preferentially take up light Ni isotopes, driving residual Ni in seawater to positive Ni isotope values. This isotopic shift has been interpreted as a unique biological fractionation mechanism specific to methanotrophs (Cameron et al., 2009). However, recent studies by Gueguen et al. (in press) show that nonbiological and even high-temperature magmatic processes equally fractionate Ni isotopes, thus challenging the original interpretation of large biological fractionations in Ni isotopes.

9.18.5.1.4 Chromium

The enrichment of the redox-sensitive trace metal Cr can be used to track the terrestrial Cr flux to the oceans (Frei et al., 2009; Konhauser et al., 2011). Data for nearshore IFs cannot be used to infer bulk seawater composition, but they do offer insights into the supply and composition of continental drainage waters, and, by extension, the physical and chemical weathering processes on land at the time of their deposition. In a recent compilation of Cr concentrations in IFs (**Figure 10(a)** and **10(b)**), Konhauser et al. (2011) argued that Cr was largely immobile on land until ~2.5 Ga. After that time, Cr enrichments started to increase in shallow-water IFs and peaked essentially synchronous with the permanent loss at ~2.32 Ga of mass-independent fractionation of sulfur isotopes that defines the GOE (Bekker et al., 2004; Guo et al., 2009). This indicates that Cr was solubilized at a scale unrivaled in Earth history, yet muted Cr isotope fractionations at that time (Frei et al., 2009; see **Figure 10(c)**) argue against extensive oxidative Cr(VI) transport during the GOE. Instead, Cr must have been mobilized predominantly in reduced Cr(III) form and supplied to the oceans in solution, or adsorbed onto authigenic weathering products. Crucially, it is likely that

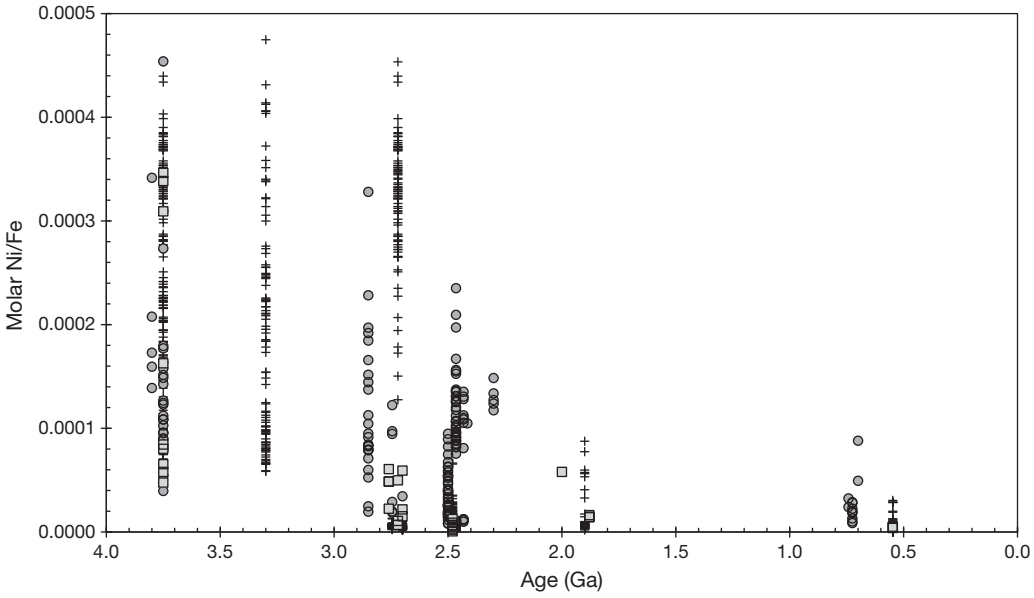

Figure 9 Ni/Fe mole ratios for iron formations versus age. Ni/Fe ratios are proposed to track marine Ni reservoir, suggesting a significant decline in marine Ni concentrations after ~2.7 Ga. The figure contains 1214 measurements, including literature data (circles), bulk (squares) and grain-by-grain laser ablation analyses (crosses). Modified from Konhauser KO, Pecoits E, Lalonde SV, et al. (2009) Oceanic nickel depletion and a methanogen famine before the Great Oxidation Event. *Nature* 458: 750–753.

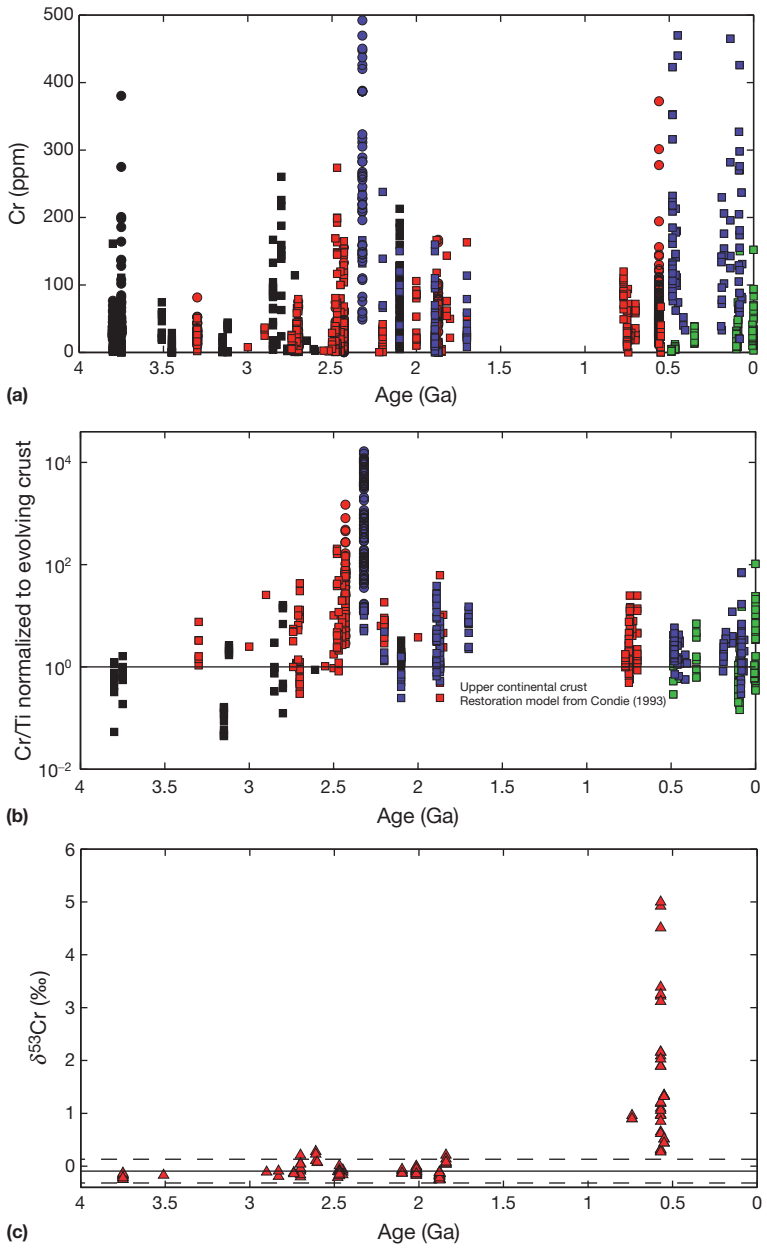

Figure 10 Chromium in iron formations and ironstones through time. (a–c) Show secular trends in Cr concentrations (a), authigenic enrichment in Cr relative to Ti (b), and Cr isotope values replotted from Frei et al., 2009 (c). Increasing enrichments in Cr in iron formations near the Archean–Proterozoic boundary suggest a change in Cr cycling. However, muted Cr isotope fractionations during this time suggest transport of reduced rather than oxidized Cr to marine environments. In (a) and (b), squares denote bulk analyses, circles are laser-ablation analyses, black represents volcanic-hosted iron formations, red denotes sediment-hosted iron formations, blue indicates Proterozoic oolitic iron formations and Phanerozoic ironstones that formed in shallow marine waters, and green represents Phanerozoic hydrothermal and exhalative deposits. In (b), Cr/Ti ratios have been normalized to the evolving Cr/Ti ratio of upper continental crust (solid line) according to the restoration model of Condie (1993). In (c), solid and dashed lines represent the mean and 2σ values, respectively, for Archaean and Paleoproterozoic Cr isotope compositions from Frei et al. (2009). Modified from Konhauser KO, Lalonde S, Planavsky NJ, et al. (2011) Aerobic bacterial pyrite oxidation and acid rock drainage during the Great Oxidation Event. *Nature* 478: 369–373, with additional data from Rye and Holland (2000).

only microbially catalyzed oxidation of crustal pyrite could have generated the degree of acidity required for appreciable Cr(III) solubilization (Rai et al., 1989). Today, aerobically respiring bacteria are essential to this process, catalyzing the continued oxidation of Fe(II) as pH values drop below the threshold for inorganic Fe(II) oxidation. Based on these constraints, it was suggested that the Cr(III) pulse beginning at ~2.48 Ga and peaking at ~2.32 Ga indicates that such bacteria began utilizing O_2 for the first time to oxidize a previously stable and abundant crustal pyrite reservoir (Konhauser et al., 2011). Sulfuric acid generated by this metabolism ultimately leached Cr from ultramafic source rocks and residual soils. This profound shift in weathering regimes constitutes Earth's first acid continental drainage system (cf. Bekker and Holland,

2012), and accounts for independent evidence of increased supply of sulfate (Bekker et al., 2004) and sulfide-hosted trace elements to the oceans at that time (Scott et al., 2008).

9.18.5.2 Stable Isotope Studies of IF

Light stable isotopes of oxygen and carbon and, to a lesser extent, hydrogen, sulfur, and nitrogen have been used widely to understand the genesis of IFs, fundamental constraints on Precambrian paleoenvironments, and the evolution of life (e.g., Baur et al., 1985; Beaumont and Roberts, 1999; Becker and Clayton, 1972; Goodwin et al., 1976; Hren et al., 2009; Shen et al., 2006; Thode and Goodwin, 1983; Walker, 1984). Following analytical advances in stable isotope geochemistry, new isotope tracers are now available, including for the two major elements in IFs, iron and silicon, as well as for trace elements such as chromium, nickel, molybdenum, germanium, and uranium. Although still in its infancy, the growing field of non-traditional stable isotope geochemistry will certainly open new avenues for investigations of IFs.

9.18.5.2.1 Traditional light stable isotopes

Carbon isotopes have long been used as a tool to understand the genesis of IFs. Most carbon isotope studies have focused on the carbonate fraction, due in part to the generally low organic carbon content in IFs. The most extensive studies have been undertaken on the low metamorphic grade deposits of the late Neoarchean to early Paleoproterozoic Transvaal Supergroup in South Africa (e.g., Beukes and Klein, 1990; Fischer et al., 2009) and the ~2.5 Ga Brockman IF in Western Australia (e.g., Baur et al., 1985; Becker and Clayton, 1972; Kaufman et al., 1990), as well as the ~1.88 Ga Biwabik and Gunflint IFs in the United States and Canada (Perry et al., 1973; Winter and Knauth, 1992). Numerous siderite-rich IFs also have been analyzed for carbonate carbon isotopes (e.g., Ohmoto et al., 2004). Based on a recent compilation by Johnson et al. (2008a), carbonates associated with IFs tend to be isotopically light, with $\delta^{13}C$ values ranging from −20.0 to +2.4‰ against Vienna Pee Dee Belemnite (V-PDB) and the majority of values clustered around −8 to −6‰ (Heimann et al., 2010). Organic carbon isotope values also are ^{13}C-depleted, with values as low as −41.4‰. Studies of carbonates from the Brockman IF (Baur et al., 1985) show that isotopically light carbon and oxygen isotope values correlate with concentrations of iron. The negative carbonate carbon isotope values have been interpreted as evidence for direct carbonate (siderite) precipitation from an iron-rich water column, stratified with respect to carbon isotope composition of total dissolved inorganic carbon and influenced by a deep-water, hydrothermal flux associated with submarine magmatic activity (e.g., Beukes and Klein, 1990; Winter and Knauth, 1992). Although a stratification of several per mil in the carbon isotope composition of dissolved inorganic carbon is present in the modern ocean (e.g., Kroopnick, 1985), a much smaller gradient is preserved in the early Precambrian rock record and is expected under the high pCO_2 conditions required to compensate for a lower solar luminosity during early Earth history (Hotinski et al., 2004). As another caveat on those interpretations, petrographic evidence (e.g., Ayres, 1972) indicates that almost all iron-rich carbonates in IFs formed during burial diagenesis and, therefore, are unlikely to have precipitated within the water column (see, e.g., how iron-rich carbonate in **Figures 2(e)**, **2(g)**, and **3(e)** occludes laminae). Consistent with these petrographic observations, some Fe-rich carbonates, in particular those in oxide and silicate facies IFs, tend to have more negative oxygen isotope values than coeval calcite and dolomite that precipitated from seawater (Heimann et al., 2010), suggesting that the Fe-rich carbonates formed during late diagenesis in sediments, possibly at several kilometers depth. Formation of ^{13}C-depleted Fe-rich carbonates also is commonly linked with a fermentative metabolism and anaerobic respiration in the anoxic water column and sediments. This interpretation was first suggested by Perry et al. (1973) and, later, by Walker (1984), who proposed that the markedly light carbon isotope values of siderite in IF reflect diagenetic precipitation of ferruginous carbonate linked to organic matter remineralization, with ferric oxides being the terminal electron acceptor. Heimann et al. (2010) placed isotopic and mass balance constraints on this model. The case of dissimilatory iron reduction (DIR) and complete C and Fe retention in sediments is described by the following equation, in which CH_2O represents the total organic carbon:

$$4Fe(OH)_3 + CH_2O + 3HCO_3^- \rightarrow 4FeCO_3 + 3OH^- + 7H_2O$$

This equation implies that three out of four carbon atoms in siderite were derived from seawater bicarbonate present in pore waters and the water column. At a lower contribution from seawater bicarbonate (e.g., at a greater depth in sediments and at a more pronounced isolation from the water column), some Fe would be lost from sediments to pore waters during DIR. A higher contribution of seawater bicarbonate would correspond to the case where the upward-diffusing iron in pore waters is bound at a higher level in sediments or at the water–sediment interface with seawater bicarbonate. Using average carbon isotope values for bicarbonate and organic carbon (0 and −30‰, respectively), the above equation requires the average carbon isotope value of siderite to be close to −7.5‰, if all iron reduced by DIR was retained in the sediments. Interestingly, as noted above, the carbon isotope values of siderite in IFs cluster close to this value, although some bias toward less-negative values is likely due to oversampling of massive beds formed at or just below the sediment–water interface. In this rather simplistic view of early diagenesis, IF carbon isotope data suggest that a significant amount, if not all, of the iron released by DIR was retained in the sediments and did not escape back into the water column.

Another plausible model links the light carbon isotope ratios in iron carbonates of IFs to iron-based methane oxidation. Recently, this process has been documented at modern marine methane seeps (Beal et al., 2009) and in an iron-rich lake (Crowe et al., 2011). These findings build from thermodynamic predictions, which suggest that bacteria are capable of linking methane oxidation to ferric iron reduction. Methanogenesis was likely a common metabolic pathway in organic matter-rich shales within iron formation-bearing sequences, and possibly in precursor sediments for Archean and Paleoproterozoic IFs (e.g., Konhauser et al., 2005). In this scenario, methane produced in sediments during early diagenesis diffused upwards and was biologically oxidized with ferric oxides,

producing both ferrous iron and bicarbonate that would then coprecipitate as iron-rich carbonate. The presence of markedly negative carbonate carbon isotope values as low as −20‰ is consistent with methane cycling having mediated carbonate precipitation, given that methane is much more isotopically depleted in ^{13}C than is typical organic matter. This process could also create organic matter having extremely depleted $\delta^{13}C$ values without aerobic involvement.

The oxygen isotope composition of chert in IFs, particularly coupled to other isotope proxies such as Si, H, and Fe, has been used to address issues such as Precambrian ocean temperatures (Hren et al., 2009; Knauth, 2005; Knauth and Lowe, 2003; Robert and Chaussidon, 2006) and seawater oxygen isotope compositions (Perry, 1967), the source of silica to IFs (Robert and Chaussidon, 2006; Steinhoefel et al., 2009; van den Boorn et al., 2007), and the degree of metamorphic overprint (Valaas Hyslop et al., 2008). Assuming that oxygen isotope values of Precambrian oceans were similar to those of ice-free recent oceans (Knauth and Lowe, 2003; Muehlenbachs, 1998) and that postdepositional isotope exchange was minimal, the bulk oxygen isotope composition of chert might be a useful paleothermometer because isotope fractionation between silica and seawater is dependent on temperature. Under this assumption, low oxygen isotope values of <+22‰ Standard Mean Ocean Water (SMOW) for 3.4–3.2 Ga cherts were interpreted as evidence for hot early oceans, implying seawater temperatures of 55–85 °C (Knauth and Lowe, 2003). This was later supported by the in situ ion microprobe study of cherts by Robert and Chaussidon (2006), revealing covariation between the silica and oxygen isotope records. Subsequent studies applying similar techniques and the modeling of diagenesis and metamorphism established that some of the ~3.5–3.3 Ga Onverwacht Group cherts in South Africa were completely equilibrated with postdepositional gold-bearing fluids and, therefore, had lost their original seawater signal (Marin-Carbonne et al., 2011). Other studies have shown that chert in the 1.88 Ga Gunflint Formation of Canada precipitated at much lower (37–52 °C) temperatures (Marin-Carbonne et al., 2012). Similarly, a study of isotope compositions of the ~3.42 Ga Buck Reef Chert in South Africa (Hren et al., 2009) questioned previously inferred temperature constraints of Knauth and Lowe (2003). Hren et al. (2009) explored the temperature dependence of oxygen and hydrogen isotope fractionations in order to calculate $\delta^{18}O$ values of ambient fluids during transformation of amorphous silica to microcrystalline quartz, finding that the Paleoarchean ocean was isotopically depleted in ^{18}O relative to the modern ocean and thus was far cooler (<40 °C) than previously envisaged. In using these and similar arguments, the assumption has generally been made that chert represents a marine chemical precipitate, and that its isotopic composition directly reflects the composition and temperature of the Archean ocean at the time of deposition. This is, however, unlikely for Paleoarchean cherts within volcano-sedimentary sequences of greenstone belts, because their origin is closely linked to syndepositional, low-temperature hydrothermal processes on the seafloor (Hofmann and Bolhar, 2007; Hofmann and Harris, 2008). Temperature estimates obtained from stable isotope paleothermometry, therefore, reflect the temperature of chert precipitation as a result of mixing of hydrothermal fluids with cold seawater. The diagenetic origin of bedded cherts in BIF of the Hamersley Group (Krapež et al., 2003) also challenges the meaning of these isotope data.

Sulfur isotope compositions of organic matter-rich and sulfidic shales interbedded with Neoarchean and Paleoproterozoic IFs have been extensively studied to constrain biological sulfur cycling, sources of sulfur, and ocean redox structure (e.g., Cameron, 1983; Goodwin et al., 1976; Grassineau et al., 2001; Thode and Goodwin, 1983). On the other hand, super-heavy S isotope values in Neoproterozoic postglacial lithologies, including Fe and Mn formations, were linked to Rayleigh fractionation during pyrite formation under low seawater sulfate conditions (Liu et al., 2006). The results were used by Habicht et al. (2002) to infer a low (<200 μM) seawater sulfate content in the Archean ocean. An increase in the range of sulfur isotope values in ~2.7 Ga black shales interbedded with IFs has been interpreted as an expression of dissimilatory bacterial sulfate reduction or redox cycling in stratified Archean oceans (Goodwin et al., 1976; Grassineau et al., 2001). Studies of multiple sulfur isotopes have shown that the range of $\delta^{34}S$ values alone in sediments deposited before the GOE cannot be used to support either of these two interpretations, because photochemical processes in an anoxic atmosphere significantly fractionate sulfur isotopes (Farquhar et al., 2000). Indeed, the same 2.7 Ga sedimentary units contain a large range of mass-independent fractionation in sulfur isotopes, thus arguing for the role of photochemical processes and against oxygenated surface environments. Although biological sulfur cycling was likely present in Archean oceans (e.g., Philippot et al., 2007; Shen et al., 2001, 2009), it is difficult to constrain its role using sulfur isotopes alone. Multiple sulfur isotope analyses of sulfur hosted in IFs also show a large range of mass-independent fractionations (Farquhar and Wing, 2005; Kaufman et al., 2007; Partridge et al., 2008), suggesting that small amounts of sulfur compounds derived from photochemically fractionated sulfur species co-precipitated with IFs.

Very little data are available for nitrogen isotope composition of IFs, mainly due to their low nitrogen contents. However, ammonium might substitute for potassium ion in the primary clay minerals (cf. Williams and Ferrell, 1991) within IFs, such as in the sedimentary precursor to stilpnomelane, making IFs at low metamorphic grade a prospective lithology for nitrogen isotope studies. From the N isotope data presently available for organic matter-rich shales, cherts, and IFs it appears as though a bimodal secular pattern exists with a change occurring across the Neoarchean–Paleoproterozoic boundary, interpreted as reflecting progressive oxidation of surface environments (Beaumont and Robert, 1999; Garvin et al., 2009; Godfrey and Falkowski, 2009; Shen et al., 2006; Thomazo et al., 2011). The older record is marked by a large range of negative and highly positive values, which are generally related to bacterial nitrogen fixation as a principal pathway for biogeochemical nitrogen cycling in anoxic oceans, where nitrification with oxygen as an electron acceptor was limited or absent (Farquhar et al., 2011). A shift to predominantly positive nitrogen isotope values in Neoarchean shales is related to an emergence of nitrification and denitrification (a process that requires dissolved nitrate), coeval with the appearance of dissolved oxygen in at least the upper part of the ocean water column (Garvin et al., 2009; Godfrey and Falkowski, 2009; Thomazo et al., 2011). Interestingly, 2.7 and 2.5 Ga

IFs, black shales, and cherts also contain nitrogen with highly positive isotope values (Beaumont and Robert, 1999; Jia and Kerrich, 2004; Shen et al., 2006). Considering that these lithologies were deposited in relatively deep-water (below storm wave-base) anoxic environments, it is highly unlikely that any nitrite or nitrate was exported into these environments from local oxygenated settings, where they could have gained positive nitrogen isotope values due to Rayleigh distillation associated with denitrification. On the other hand, it seems plausible that oxidized nitrogen species could have been produced during early diagenesis when organic matter and ammonium were biologically remineralized, with ferric iron acting as electron acceptors in the absence of oxygen. Such a process could lead to the formation of isotopically distinct nitrogen pools. There is tentative evidence for microbial ammonium oxidation to nitrite coupled to Fe(III) reduction in laboratory experiments (Sawayama, 2006) and under anaerobic conditions in wetland soils (Clement et al., 2005). Although further documentation of this process is needed, it is a thermodynamically feasible metabolic pathway, and it is likely common in modern Fe-rich systems.

9.18.5.2.2 Nontraditional stable isotopes

9.18.5.2.2.1 Fe isotopes

A number of recent iron isotope studies of IFs have been made with the aim of tracking the biogeochemical cycling of iron on early Earth (Beard et al., 1999; Craddock and Dauphas, 2011; Dauphas et al., 2004; Heimann et al., 2010; Johnson et al., 2003, 2008a,b; Planavsky et al., 2009; Rouxel et al., 2005; Steinhoefel et al., 2009). Importantly, this recent iron isotope work has bolstered evidence for a rain of ferric oxyhydroxides during IF deposition, for early diagenetic microbial iron cycling, and for a hydrothermal iron source for IFs (e.g., Anbar and Rouxel, 2007; Dauphas and Rouxel, 2006; Heimann et al., 2010; Planavsky et al., 2012). Iron isotopes are typically reported as δ^{56}Fe values with a range of 5‰ in nature. Several recent reviews provide detailed information on iron isotope systematics and fractionations (Anbar and Rouxel, 2007; Beard et al., 2003; Dauphas and Rouxel, 2006; Johnson et al., 2008b). The application of iron isotopes to understanding the ancient iron cycle is based on a foundation of extensive experimental work that determined kinetic and equilibrium fractionation factors during redox reactions and mineral precipitation (Beard et al., 1999, 2010; Bullen et al., 2001; Butler et al., 2005; Croal et al., 2004; Crosby et al., 2005; Guilbaud et al., 2011; Welch et al., 2003; Wiesli et al., 2004). In general, the largest iron isotope fractionations occur during redox reactions. For instance, during Fe(III) reduction and Fe(II) oxidation there is ~1.5‰ fractionation. The notable exception is during sulfide formation, which might be accompanied by a large (>2‰) fractionation (Guilbaud et al., 2011; Rouxel et al., 2008a,b); since IFs typically lack sulfides, this pathway for isotopic fractionation is not particularly relevant. Additionally, a sound understanding exists of the isotopic composition of iron from different sources (Dauphas and Rouxel, 2006; Johnson et al., 2008a). Most importantly, iron derived from hydrothermal sources has slightly negative or near-zero iron isotope values (e.g., Rouxel et al., 2008a,b), whereas a benthic flux (dissolved iron derived from iron reduction during early sediment diagenesis on continental shelves and supplied to deep euxinic part of the basin) is likely to have a pronounced negative iron isotope value (e.g., Severmann et al., 2008). This isotopically light benthic Fe source has also been found

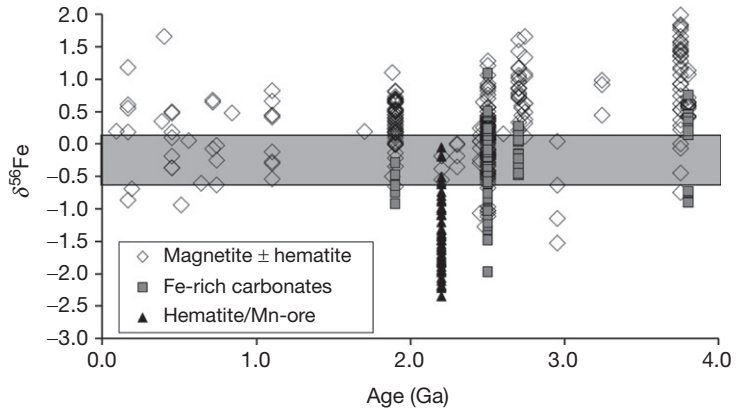

Figure 11 Secular variations in δ^{56}Fe values for Precambrian iron formations. Data for magnetite and/or hematite (open diamonds) include bulk mineral and in situ (using laser-ablation MC-ICP-MS and ion-microprobe) analyses. Data for Fe-rich carbonates (gray squares) and hematite hosted in Mn-carbonates (Hotazel Formation) correspond to bulk mineral analysis. A total of 490 datapoints is shown including 83 datapoints for the ~1.88 Ga GIF from the Animikie basin, North America (Frost et al., 2007; Planavsky et al., 2009; Valaas Hyslop et al., 2008), 138 datapoints for the ~2.5 Ga Brockman Iron Formation, Western Australia (Johnson et al., 2008a,b), 58 datapoints for the ~2.5 Ga Transvaal Supergroup IF, South Africa (Johnson et al., 2003), 27 datapoints for the ~2.7 Ga Shurugwi and Belingwe greenstone belts IF, Zimbabwe (Rouxel et al., 2005; Steinhoefel et al., 2009), 137 datapoints for the Eoarchean Isua, Akilia, and Innersuartuut IF and metamorphic rocks (Dauphas et al., 2004, 2007; Whitehouse and Fedo, 2007), 12 datapoints for the Neoproterozoic Rapitan IF (Halverson et al., 2011), 52 datapoints for IF and Mn formation from the Paleoproterozoic Hotazel Formation, Transvaal Supergroup, South Africa (Tsikos et al., 2010), and 45 datapoints for other Paleoproterozoic and Archean IFs (Planavsky et al., 2012). Gray horizontal bar represents the average δ^{56}Fe values for igneous rocks and hydrothermal sources (e.g., Beard et al., 2003; Rouxel et al., 2008a,b). For comparison, iron isotope values of jaspers and iron formations from Phanerozoic hydrothermal deposits are shown (from Planavsky et al., 2012); note that stromatolitic and oolitic-oncoidal ironstone of the Middle Eocene age from Egypt has δ^{56}Fe values ranging from +1.14 to +2.28‰ (Salama et al., 2011).

to be transferred to the water column, notably in coastal settings (Rouxel and Auro, 2010).

Bulk samples of IFs commonly contain positive or near-crustal δ^{56}Fe values (Craddock and Dauphas, 2011; Johnson et al., 2003, 2008a; Planavsky et al., 2012; Rouxel et al., 2005; Steinhoefel et al., 2009; **Figure 11**), which provide insight into iron-enrichment mechanisms. The two most commonly proposed iron sources for IFs, hydrothermal (Bau et al., 1997a,b; Bekker et al., 2010) and benthic (Raiswell, 2006; Severmann et al., 2008), have negative (subcrustal) δ^{56}Fe values. Hence, the presence of positive δ^{56}Fe values in IF must reflect a fractionation during mineral precipitation. More specifically, positive δ^{56}Fe values point toward a rain of ferric oxyhydroxides to the sediment–water interface (e.g., Dauphas et al., 2004). Ferric oxyhydroxides are fractionated by $\sim$1.5‰ relative to dissolved ferrous iron (see Johnson et al., 2008b for review). This enrichment in heavy Fe isotopes contrasts with the isotope fractionations associated with siderite, ankerite, and green rust precipitation, which are heavy iron isotope-depleted relative to the ambient $Fe(II)_{aq}$ pool (Wiesli et al., 2004); the exact fractionation during precipitation of iron silicates is unknown. In general, positive iron isotope values in IFs indicate that Fe(III) delivery was the main process driving iron enrichments. Additionally, the expression of large Fe isotope fractionations implies partial Fe(II) oxidation, pointing toward oxidation at low Eh conditions (Planavsky et al., 2012). If Fe(II) oxidation took place during mixing of anoxic Fe(II)-rich and oxygenated marine waters, as was commonly envisaged in the past (Cloud, 1973; Holland, 1984), oxidation would have been essentially quantitative given the rapid oxidation kinetics of iron at neutral to alkaline pH (e.g., Stumm and Morgan, 1995). This rapid and quantitative oxidation would have prevented any significant expression of iron isotope fractionations, which is the case with modern hydrothermal plume fallout (Severmann et al., 2004). Therefore, the presence of large iron isotope fractionations argues against oxidation having been quantitative.

The presence of positive δ^{56}Fe values in IFs dominated by reduced or mixed-valence iron minerals may also provide strong evidence for microbial Fe(III) reduction in precursor sediments to the IFs (Craddock and Dauphas, 2011; Johnson et al., 2008a,b). For example, siderite with positive δ^{56}Fe values and siderite with similar δ^{56}Fe values as coexisting iron oxides (Craddock and Dauphas, 2011) indicate a lack of isotopic equilibrium between siderite and aqueous Fe(II) in ancient anoxic oceans (Johnson et al., 2008a). Siderite that precipitated from seawater should have a negative δ^{56}Fe value, given the isotopic fractionation during siderite precipitation and expected iron isotope values for seawater. Therefore, siderite with positive δ^{56}Fe values must have been derived by reductive dissolution of iron oxyhydroxides rather than having precipitated directly from seawater. In most cases, microbial Fe(III) reduction can be assumed to be driving the reductive oxide dissolution. This also implies quantitative reduction of iron oxide precursors, which raises an important question regarding the nature of the electron donors in organic matter-starved systems of IF. Although iron isotope data for IFs may point towards microbial Fe(III) reduction in the rock record, possibly dating back to the earliest known sedimentary rocks at $\sim$3.8 Ga (Craddock and Dauphas, 2011), independent evidence is needed to exclude the possibility of siderite formation during metamorphic reaction of iron oxides and organic carbon, before positive δ^{56}Fe values in siderite can be linked with microbial Fe(III) reduction. As stressed above, petrographic evidence for siderite precipitation from seawater is generally lacking.

Positive δ^{56}Fe values in IFs are also consistent with a hydrothermal iron source. The common occurrence in bulk IF samples of δ^{56}Fe values between 0.5 and 1.0‰ (e.g., Planavsky et al., 2012) is consistent with partial oxidation of hydrothermal Fe(II), because hydrothermally sourced iron should have an initial δ^{56}Fe value between -0.5 and 0‰. These positive δ^{56}Fe values are less likely to be linked to partial oxidation of benthic and diagenetically derived iron, since the latter fluxes are typically characterized by quite negative δ^{56}Fe values (<-1.5‰). Iron isotopes do not provide definitive evidence for a hydrothermal iron source, but support this model, which is also strengthened by many other lines of geological and geochemical evidence (e.g., Bekker et al., 2010).

Iron having near-crustal or negative δ^{56}Fe values in IFs could have been sourced from either a hydrothermal or a benthic source. The degree of water-column Fe(II) oxidation is expected to vary widely in Archean and Paleoproterozoic oceans, potentially accounting for a range of iron isotope values in the particulate iron oxyhydroxide flux for a given dissolved iron isotope value. Additionally, it is likely that when reducing marine conditions prevailed, as indicated for the Archean and Paleoproterozoic oceans by REE studies (e.g., Bau and Dulski, 1996; Planavsky et al., 2010a,b), partial Fe(II) oxidation could have resulted in a dissolved iron isotope gradient. Precipitation of isotopically heavy iron oxides would leave behind an isotopically light dissolved iron pool, which also could have been transferred to the IF rock record with additional oxidation (Rouxel et al., 2005). The co-occurrence of isotopically light carbonate carbon and iron isotope values has been proposed as evidence for the reductive origin of light iron isotopes in IFs, possibly with iron being sourced from within the sediment pile (Craddock and Dauphas, 2011; Heimann et al., 2010; Johnson et al., 2008a). This model builds from the earlier interpretations outlined above that light carbonate carbon isotope values may be derived by remineralization of organic matter (e.g., Baur et al., 1985; Becker and Clayton, 1972; Kaufman et al., 1990). The light iron isotope values similarly may record partial microbial reduction of iron oxyhydroxides during early diagenesis (Johnson et al., 2008a). However, negative carbonate iron isotope values can result from direct precipitation of seawater-derived Fe(II), whereas the light carbonate carbon isotope values are linked to organic matter remineralization. Stated more simply, iron isotopes can be controlled by the flux of iron to the sediment–water interface, whereas carbon isotopes provide a signal of early diagenetic microbial processes. IF carbonates having positive δ^{56}Fe values also show markedly negative carbonate carbon isotope values (Craddock and Dauphas, 2011), consistent with the above-outlined model.

There has been extensive discussion on negative iron isotope values in IFs. Several conflicting interpretations exist for these values, such that independent geological and geochemical evidence should be used to discriminate these models (Johnson et al., 2008a; Tsikos et al., 2010). Further, light iron isotope values are not a silver bullet for DIR even if coupled with light carbonate carbon isotope values.

A compilation of bulk rock and mineral-specific δ^{56}Fe values for Archean and Paleoproterozoic IFs (**Figure 11**) shows an overall range between −2.5 and 2.7‰, which encompasses most of the natural variations in iron isotopes observed to date. Although these data reveal that many Archean and early Paleoproterozoic IFs were a sink for isotopically heavy iron, in contrast to later Proterozoic and Phanerozoic iron oxide-rich rocks, further work is needed to explore whether a secular change exists in the iron isotope composition of IF prior to the GOE. Notably, markedly low δ^{56}Fe values are common in the ~2.22 Ga Hotazel Formation of South Africa and especially in manganese-rich samples. This distinctive feature may reflect the deposition of iron and manganese from hydrothermal fluid depleted in heavy iron isotopes, by progressive Fe(II) oxidation and precipitation in the deeper part of a redox-stratified basin that had a redox state intermediate between that required for iron and manganese oxidation (Tsikos et al., 2010).

The average iron isotope composition of different types of IF is a major unresolved question. In some cases, IFs have been estimated to have a near-crustal average δ^{56}Fe value (Johnson et al., 2008a). However, as discussed above, many IFs display positive δ^{56}Fe values and thus have been interpreted as a significant sink of isotopically heavy iron (Planavsky et al., 2012; Rouxel et al., 2005). Unfortunately, previous iron isotope studies were not ideally designed to estimate the average iron isotope composition of IFs. In order to attain the most accurate average estimate possible, thick sections of randomly selected drill core intervals should be homogenized prior to analysis. Although this method is tedious, if done for several major Archean IFs it could help constrain iron isotope mass balance during that era. More specifically, this work would serve as a test for the model in which deposition of isotopically heavy IFs in the deeper parts of basins created a pool of isotopically light dissolved iron that was then buried in shallow-water environments in the Archean (Rouxel et al., 2005).

9.18.5.2.2.2 Chromium isotopes

Frei et al. (2009) measured Cr isotope values for 23 IFs ranging in age from 3.8 to 0.635 Ga (see **Figure 10(c)**). Their data revealed a pronounced difference between Archean–Paleoproterozoic and Neoproterozoic IFs. The former have Cr isotope values within a small range of −0.26 to 0.28‰, whereas the latter reach values up to +4.9‰. Based on the small positive Cr isotope excursions in IFs as old as 2.7 Ga, Frei et al. (2009) argued that Cr (VI) was mobilized from land to the oceans, where it was then quantitatively reduced to Cr(III) and incorporated into IF. The Cr (III) oxidative step that generates the Cr(VI) requires a MnO_2 catalyst, which importantly necessitates significant levels of atmospheric O_2 as much as 300 My before the GOE (e.g., Holland, 2005). However, consideration of the depositional setting questions this conclusion. The Archean IFs that display statistically significant positive δ^{53}Cr values were proximal to submarine hydrothermal centers (**Figure 10(c)**) and analyses of some modern hydrothermal vent fluids suggest hydrothermal Cr flux, likely as a reduced, organically bound Cr(III) phase (Sander and Koschinsky, 2000). Some of the solubilized Cr(III) in hydrothermal fluids is expected to be removed in the subsurface or at the sediment–water interface together with hydrothermal sulfides. Although redox-independent processes typically result in extremely small isotope fractionations, it is possible that kinetic isotope effects in hydrothermal systems were amplified, similarly to what has been observed for other transition metals (e.g., Rouxel et al., 2008a,b). The end result would be a dissolved Cr pool with small positive δ^{53}Cr values that could be recorded in some IFs proximal to volcanic centers. In this context, positive δ^{53}Cr values from ~2.7 Ga IFs (Frei et al., 2009) may provide insights into hydrothermal processes in the Archean, but are unlikely to reflect oxidative continental weathering. The currently available IF Cr isotope results are intriguing, but given the uncertainties about Cr cycling in Archean submarine hydrothermal systems, these data are not a straightforward archive of atmospheric processes.

Slightly positive Cr isotope values as reported in the upper part of the ~1.88 Ga Gunflint IF (Frei et al., 2009), are also difficult to interpret in terms of terrestrial oxidative processes, because this section of the IF experienced meteoric alteration during the ~30 My hiatus that followed deposition of this unit (Burton and Fralick, 2007). Destruction of original sedimentary features, intense silicification and carbonatization and pronounced groundwater-derived vanadium enrichment characterize the upper part of this alteration zone (Burton and Fralick, 2007). Groundwater systems, similarly to hydrothermal systems, are likely to amplify small sorption isotope effects. In fact, modeling of reactive Cr transport in a groundwater plume suggests that there can be a tenfold amplification of a Cr sorption isotope effect (Johnson and Bullen, 2004). Chromium isotopes in sedimentary rocks altered by groundwater systems are therefore equally unlikely to provide insights into atmospheric processes. By contrast, highly positive values in the Neoproterozoic IFs (Frei et al., 2009) likely reflect redox cycling, since both the partial reduction and the oxidation of Cr should create a mobile Cr(VI) reservoir with positive Cr isotope values. It would appear that the onset of a rigorous, terrestrial Mn-oxide cycle occurred sometime between the Paleo- and Neoproterozoic, but the current data gap precludes precisely defining the timing of this event.

9.18.5.2.2.3 Silicon isotopes in chert and IF bands

In order to better constrain silica sources, a growing number of studies have investigated the Si isotope composition of Precambrian IFs and cherts (Abraham et al., 2011; Andre et al., 2006; Ding et al., 1996; Jiang et al., 1993; Robert and Chaussidon, 2006; Steinhoefel et al., 2009, 2010; van den Boorn et al., 2007, 2010). Silicon isotope ratios are resistant to hydrothermal alteration and thermal effects, including high-grade metamorphism (Andre et al., 2006), due to the high abundance of Si in most rocks. Si isotope ratios are thus regarded as recording primary signatures. However, biogenic and abiogenic, low-temperature amorphous silica precipitates are significantly enriched in light Si isotopes relative to dissolved Si source (e.g., Basile-Doelsch, 2006; Ding et al., 1996; Douthitt, 1982), resulting in residual dissolved Si depleted in light isotopes. Diatoms, which preferentially incorporate light Si isotopes, dominate the modern marine silica cycle. As a result, dissolved Si in modern seawater has positive δ^{30}Si values (+0.6 to +2.2‰, **Figure 12**; De La Rocha et al., 2000; Reynolds et al., 2006). The same fractionation pattern arises from chemical precipitation of silica near seafloor

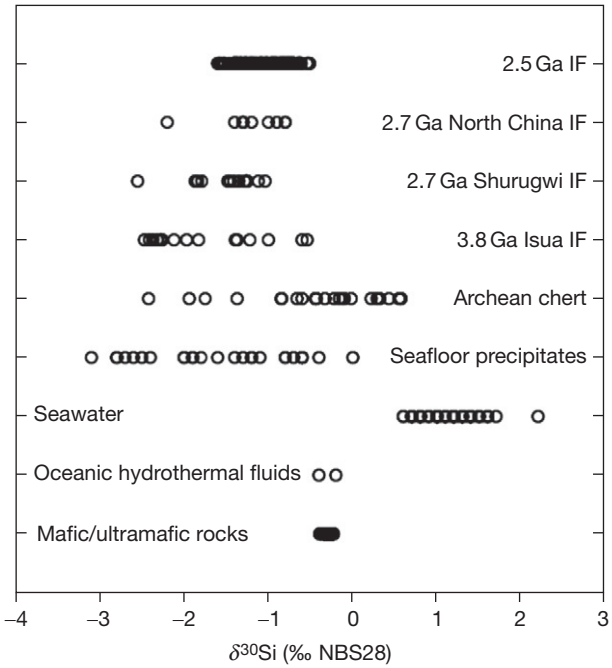

Figure 12 δ^{30}Si values of mafic to ultramafic volcanic rocks (Fitoussi et al., 2009; Savage et al., 2010), seawater and mid-ocean ridge hydrothermal fluids (De La Rocha et al., 2000), modern siliceous precipitates of seafloor hydrothermal systems (Ding et al., 1996; Wu, 1991), Paleoarchean cherts from the Pilbara craton (van den Boorn et al., 2007, 2010), the ~3.8 Ga IF from the Isua greenstone belt (André et al., 2006), the ~2.7 Ga IF from the Shurugwi greenstone belt (Steinhoefel et al., 2009) and North China craton (Ding et al., 1996; Jiang et al., 1993), and the 2.5 Ga IF from the Hamersley Group and Transvaal Supergroup (Steinhoefel et al., 2010).

hydrothermal vents. Whereas black smoker vent fluids have a Si isotope composition in the same range as mafic/ultramafic volcanic rocks (−0.4 to −0.2‰; De La Rocha et al., 2000; Fitoussi et al., 2009; Savage et al., 2010), hydrothermal seafloor precipitates typically have more negative δ^{30}Si values (as low as −3.1‰, **Figure 12**; Ding et al., 1996; Wu, 1991). Silicon isotope fractionation factors between precipitates and fluids are not well constrained, but are on the order of −1.5‰ (Basile-Doelsch et al., 2005). Owing to the absence of silica-secreting organisms during the Precambrian, Archean seawater probably was close to or at saturation with respect to amorphous silica (Siever, 1992). The removal of silica by precipitation and sorption processes probably gave rise to an Archean ocean having positive δ^{30}Si values similar to those in the modern ocean, although the values may have been higher (Robert and Chaussidon, 2006; van den Boorn et al., 2010).

δ^{30}Si values of Precambrian IFs ranging in age from 3.8 to 2.5 Ga are consistently negative (**Figure 12**). The values vary between −2.51 and −0.51‰ with an average of −1.14 ±0.84‰ (n = 165, 2σ). These negative values are consistent with a hydrothermal source of the silica and are similar to those of modern hydrothermal vent precipitates (−1.57‰, n = 26; Ding et al., 1996; Wu, 1991). The lowest average Si isotope value reported is for the ~3.8 Ga Isua IF in Greenland (−1.78‰, n = 16; Andre et al., 2006), suggesting a predominantly hydrothermal source for Si. The highest values are in ~2.5 Ga IFs of the Hamersley Group, Western Australia, and Transvaal Supergroup, South Africa (−1.02‰, n = 125; Steinhoefel et al., 2010), implying silica precipitation from a heavier Si reservoir, probably due to mixing of hydrothermal fluids with isotopically heavier seawater. The latter IFs also show the smallest spread in δ^{30}Si values, suggesting a well-mixed seawater Si reservoir. A larger spread in δ^{30}Si values may reflect pulses of hydrothermal discharge and deposition closer to the venting sites, as proposed for the ~2.7 Ga IF in the Shurugwi greenstone belt, Zimbabwe (Steinhoefel et al., 2009). Paleoarchean cherts devoid of clastic detritus and representing predominantly hydrothermal precipitates show Si isotope values that are heavier than those in IF (−0.41‰, n = 24; van den Boorn et al., 2007, 2010). The entire range of Si isotope values has been explained by mixing of hydrothermal fluids and seawater or by fractionation of hydrothermal fluids at depth (van den Boorn et al., 2010). In addition, the total range of Si isotope values in cherts and and IFs also may point to different fractionation factors involved with different mechanisms of silica precipitation and different silica phases (e.g., amorphous silica, quartz, and jasper).

9.18.6 Perspective from the Modern Iron Cycle

The modern ocean has several iron sources: (1) river and groundwater discharge, (2) continentally derived atmospheric dust, (3) remobilization from coastal and shallow-water sediments, (4) sea ice, and (5) hydrothermal fluids (Boyd and Ellwood, 2010). Oxidizing conditions in modern seawater limit dissolved iron content in open oceans to ~0.02–2 nM (average 0.5 nM; Bruland and Lohan, 2006); the present residence time of iron in the oceans is 100–200 years (Johnson et al., 1997), which is much shorter than the global ocean circulation time of ~1000 years (Boyd and Ellwood, 2010). However, even these low levels of dissolved iron are much higher than thermodynamically predicted Fe^{3+} solubility (0.08–0.2 nM). This difference reflects complexation by iron-binding ligands such as siderophores (Boyd and Ellwood, 2010). Indeed, more than 98% of dissolved iron in the deep oxic ocean is organically bound (Sander and Koschinsky, 2011).

During oxidative continental weathering, iron is retained in soils in the oxidized state. Iron-chelating and Fe(III)-reducing bacteria play an important role in iron release from soil horizons (Brantley et al., 2004). Rivers carry a significant load of iron in the form of organically bound complexes, colloids, and particulate matter. This continentally derived iron flux is largely deposited in estuaries due to flocculation of colloids induced by salinity (Boyle et al., 1977; Escoube et al., 2009). Where groundwaters are delivered into subterranean estuaries, redox change as well as pH change during seawater mixing result in near-quantitative Fe(II) oxidative precipitation (Rouxel et al., 2008a,b). Outwash in glaciated environments typically has high loads of mixed-valence silicate species and colloidal iron, but low concentrations of dissolved Fe and dissolved organic carbon (Schroth et al., 2011). In contrast, the dissolved iron flux in rivers flowing over unglaciated settings consists of organically bounded iron complexes and iron

oxyhydroxides. Therefore, rivers flowing through glaciated and unglaciated terrains deliver different Fe species to the oceans, which has important implications for Fe bioavailability in seawater.

Dissolved iron derived from aerosols amounts to $2–12 \times 10^9$ mol per year and corresponds to 30–70% of the iron flux associated with upwelling deep waters; resuspended sediments and the diagenetic flux from coastal and shallow-water sediments are other important components estimated to contribute $4.7–8.9 \times 10^{10}$ mol per year to the oceanic iron budget (Elrod et al., 2004). Anoxic to suboxic conditions in pore waters in shelf sediments can lead to an iron shuttle – the delivery of reactive iron from the shelf to the basin (Lyons and Severmann, 2006; Severmann et al., 2008). Nonsteady-state diagenesis in tropical muds deposited on the delta top and inner shelf along the Amazonia–Guianas coast of South America provides another example of an environment where Fe(III) reduction is the predominant metabolic process responsible for organic carbon oxidation. As a consequence, significant amounts of Fe are cycled between the bottom waters and surface sediments (Aller et al., 1986, 2010).

Although most base metals and some iron released from hydrothermal vents at mid-ocean ridges and in back-arc systems are precipitated at or immediately above the seawater–oceanic crust interface, as hot reducing hydrothermal fluids mix with cold oxidized seawater, iron and manganese disperse via hydrothermal plumes as far as hundreds of kilometers before deposition as metal oxyhydroxide particles, organic complexes and metal sulfide clusters and nanoparticles (e.g., Boyle et al., 2005; Sander and Koschinsky, 2011; Toner et al., 2009; Yucel et al., 2011; also see **Chapter 8.7**). Wu et al. (2011) suggested a long-range (>5000 km) transport of hydrothermal iron from the East Pacific Rise. The hydrothermal iron fluxes to the deep ocean are thought to account for 11–22% of the deep-ocean iron reservoir, with the total estimated hydrothermal iron flux being 9×10^8 mol per year (Bennett et al., 2009; Tagliabua et al., 2010). Yucel et al. (2011) estimated that nanoparticulate pyrite constitutes up to 10% of the dissolved Fe (<200 nm) flux from high-temperature (>300 °C) hydrothermal vents. In addition, Fe-rich smectite clays, such as nontronite and montmorillonite, preferentially form close to low- to moderate-temperature, hydrothermally active areas at the seafloor, where metalliferous sediments are deposited (Cuadros et al., 2011; Taitel-Goldman and Singer, 2002).

Concentrations of metals in hydrothermal fluids, including Fe and Mn, primarily increase with elevated fluid temperatures and salinity. The composition of the volcanic and plutonic host rocks as well as magma degassing and subsurface sulfide dissolution/precipitation may also affect the concentration of metals in seafloor hydrothermal fluids (Edmond et al., 1979; Mottl et al., 1979; also see **Chapter 8.7**). In contrast to mafic-hosted hydrothermal systems, those sited within ultramafic rocks developed at slow-spreading ridges tend to have high contents of dissolved reduced gases (e.g., H_2 and CH_4) and metals (Douville et al., 2002; Marbler et al., 2010). Furthermore, because ultramafic-hosted hydrothermal systems release less H_2S, a larger proportion of dissolved iron precipitates as iron oxyhydroxides (Marbler et al., 2010). Serpentinization of ultramafic rocks under submarine conditions releases H_2 from the fluids and results in partial Fe(II) oxidation to yield magnetite precipitation (Holm and Charlou, 2001).

Several submarine deeps in the Red Sea contain hot, anoxic stratified brine pools derived from rift-hosted hydrothermal systems that at depth leach Cenozoic evaporites. Metalliferous sediments containing iron oxides, silicates, sulfides, and carbonates precipitate from these brines (Taitel-Goldman and Singer, 2002). Interestingly, whereas the deep-water brine deposits are characterized by hydrothermal signals in terms of Sr and Nd isotopes and REE patterns, shallower-water deposits of the Shaban Deep have Sr, Nd, and REE patterns dominated by a seawater component (Cocherie et al., 1994), which is likely a reflection of the efficiency of REE sorption onto iron oxides and the presence of a discrete, stable redoxcline.

Modern shallow-water, iron-rich sediments are restricted to areas strongly affected by hydrothermal circulation related to active volcanism, such as within the Santorini Caldera in the Aegean Sea, where biologically mediated, ferric hydroxide and opaline silica precipitate (Hanert, 2002; Puchelt, 1973), and in Lake Malawi, eastern Africa, where nontronite mud and peloids and limonite with opal ooids are forming (Müller and Förstner, 1973). In addition, iron ooids and pisoids composed of iron oxyhydroxides admixed with amorphous silica, with volcanic rock fragments in the center, have been described by Heikoop et al. (1996) from offshore Mahengetang, Indonesia, in the photic zone; these could be modern analogues of GIF. Iron-silicate ooids and peloids were also found from Cape Mala Pascua to El Fraile Point, Venezuela, in shallow (~35–40 m depth) waters in an exhalative system connected to ultramafic rocks via a transform fault zone (Kimberley, 1994). Iron- and silica-bearing ooids also occur in the bottom sediments of Lake Chad, West Africa, off the Chari Delta (Lemoalle and Dupont, 1973).

Modern analogues comparable in scale to BIFs appear to be unknown, although evidence presented above questions whether there is a depositional rhythmicity to silica and iron banding in ancient IFs. Accordingly, we are left to speculate on the primary compositional structure of BIF.

Low-temperature Si- and Fe-rich hydrothermal deposits generally form in areas of active venting along mid-ocean ridge axes (Corliss et al., 1978; Mills, 1995), at off-axis seamounts (Alt, 1988), hot spots, and arc/back-arc submarine volcanoes (e.g., De Carlo et al., 1983). These submarine vent deposits generally do not form laterally extensive and very thick Fe–Si-rich deposits similar to IFs. Nevertheless, local but relatively thick Fe–Si-rich hydrothermal deposits have been documented in the recent rock record and on the modern ocean floor (e.g., Edwards et al., 2011a,b; Hekinian et al., 1993; Juniper and Fouquet, 1988). For example, silica- and iron-rich deposits 20 m thick occur at Ocean Drilling Program (ODP) Site 801 within Jurassic oceanic crust in the western Pacific Ocean (Alt et al., 1992; Rouxel et al., 2003). Fossil hydrothermal Si–Fe deposits, comprising umber, jasper, and IF, have been found in ophiolites as old as 490 Ma (Little et al., 2004; Robertson, 1975). Recently, a modern analogue of umber deposits has been described in relation to ultradiffuse hydrothermal venting at the base of Loihi Seamount, at

5000 m below sea level (Edwards et al., 2011a,b). This hydrothermal system is expressed as regional seafloor seepage with gelatinous iron- and silica-rich deposits, located between and over basalt pillows, in places over a meter thick. The genetic model for umbers has previously invoked deposition of iron and manganese oxides via water-column precipitation from hydrothermal fluids, followed by particle fallout and accumulation in local depressions in a ridge flank setting. However, the laminated Fe–Mn structures located between basalt pillows observed at the base of Loihi Seamount offer an alternative interpretation for umber genesis that is consistent with geological observations.

In summary, modern environments where iron deposition occurs are comparable neither in scale nor in extent to those of ancient IFs. These modern environments nevertheless do provide some insights into processes that could have operated in the Precambrian to form IFs.

9.18.6.1 Hydrothermal Pulses of Si Synchronous with Fe Addition to Seawater

There has been limited work done on the sources of silica in IF relative to iron. As such, there is still only a nascent understanding of some basic aspects of silica deposition in IFs and of the Precambrian Si cycle. IFs typically contain 34–56 wt% SiO_2 (Klein, 2005) and, potentially, represent a major sink for dissolved Si in the geological past. Prior to detailed facies and sequence-stratigraphic analyses of BIF, these deposits were long considered ambient chemogenic pelagites of the world ocean. However, it is now known that BIFs are deposits associated with pulses of reduced iron into basins. Although it is generally accepted that the source of silica in BIF was ambient seawater during most of the Precambrian, when the biological sink for seawater silica was presumably absent (Siever, 1992), the source of silica to the oceans of that time period remains uncertain. Two potential sources, similar to that for iron, have been proposed: submarine hydrothermal fluids (Mortlock et al., 1993; Wang et al., 2009) and the continents (Frei and Polat, 2007; Hamade et al., 2003). Support for the latter proposition has come mainly from the study of Ge/Si ratios in IFs, as hydrothermal fluids and rivers have very different Ge/Si ratios (Froelich et al., 1985; Mortlock et al., 1993). On the basis of covariation of Ge/Si ratios with silica content in the ~2.5 Ga Dales Gorge Member of the Brockman Iron Formation (Hamersley Group, Western Australia), Hamade et al. (2003) proposed a decoupling of Fe and Si sources, with Si being predominantly derived from riverine waters having low Ge/Si ratios due to weathering of continental landmasses. Caution is required in this interpretation, however, due to the strong Ge fractionation relative to Si by sorption onto iron oxyhydroxides (Pokrovsky et al., 2006) or by quartz precipitation (Evans and Derry, 2002). In addition, release of Ge to pore waters may also affect Ge/Si ratios (Rouxel et al., 2006). In either case, Ge/Si ratios in cherts may not reflect seawater composition but instead record multiple, unrelated, and geologically protracted processes. On the other hand, as mentioned above, Si isotopes are consistent with a hydrothermal Si source, suggesting that there were hydrothermal pulses of Si synchronous with Fe addition to seawater that in part drove IF deposition.

Ferric oxyhydroxide particles are highly reactive toward dissolved silica (e.g., Konhauser et al., 2007b), implying that drawdown of Fe from seawater was accompanied by drawdown of silica (e.g., Slack et al., 2007). It is possible that the silica component was scavenged from seawater during particle sedimentation and later was mobilized during diagenesis (see Fischer and Knoll, 2009, for additional discussion). Consistent with this interpretation, in GIF there are Fe-bearing chert peloids, deposited from suspension, and Fe-free chert cement that was deposited shortly after deposition, because the peloids have floating contacts. On the other hand, the petrographic and field evidence indicates that chert in bands in BIF was not a direct chemical precipitate from seawater, but rather a pore-filling cement and replacement of sediment; that is, chert in IFs is not a diagenetic replacement of silica that precipitated in the water column.

A relevant geological perspective to address this issue comes from occurrences of chert in sequences that record relative magmatic quiescence and that have a similar duration and sedimentation rate to those that were deposited during periods of enhanced hydrothermal activity leading to the deposition of IFs. That silica was present in seawater during deposition in all Hamersley basin sequences is shown by the universal presence within them of bedded cherts or seafloor hardgrounds. For instance, sedimentation units in black shale of the Bee Gorge Supersequence, which directly underlies the Brockman Supersequence (predominantly consisting of IF), are capped by bedded cherts in exactly the same manner as tops of sedimentation units in the overlying IFs. There are hundreds of Bee Gorge Member 'cycles' from shale to bedded chert at scales of 1 m and less. In contrast, only a few seafloor replacement chert units exist in the black shale condensed sections in the underlying Roy Hill Member of the ~2.6 Ga Jeerinah Formation, which is not associated with IFs or increased hydrothermal activity, but was deposited at a similar sedimentation rate. Monotonous shales containing rare interbedded chert only return at the base of the ~2.4 Ga Turee Creek Supersequence, just above the Boolgeeda Iron Formation.

A possible explanation for these observations is that Si concentration in the water column was much lower during deposition of the Roy Hill Member. If this interpretation is correct, it implies that sedimentary basins at the time when IFs were deposited also contained higher seawater silica concentrations. It seems likely, therefore, that the silica content of the Precambrian ocean was not constant and that secular variations existed in [Si], like in [Fe], linked with changes in hydrothermal activity.

9.18.6.2 Oxidation Mechanism: Biological versus Nonbiological

Basic conditions leading to the deposition of IFs in ancient oceans are generally agreed upon: the precursor sediments precipitated from seawater containing micromolar (<100 μmol) levels of ferrous iron (Holland, 1973, 1984). An amplified marine reservoir of dissolved iron was possible due to the presence of (1) a reducing atmosphere or one having a low oxidizing potential (Bekker et al., 2004; Holland, 1984), (2) low marine sulfate and sulfide concentrations (Habicht et al., 2002), and (3) a high hydrothermal flux of iron (Kump and Seyfried, 2005). It is generally agreed that IF deposition is linked with an oxidative

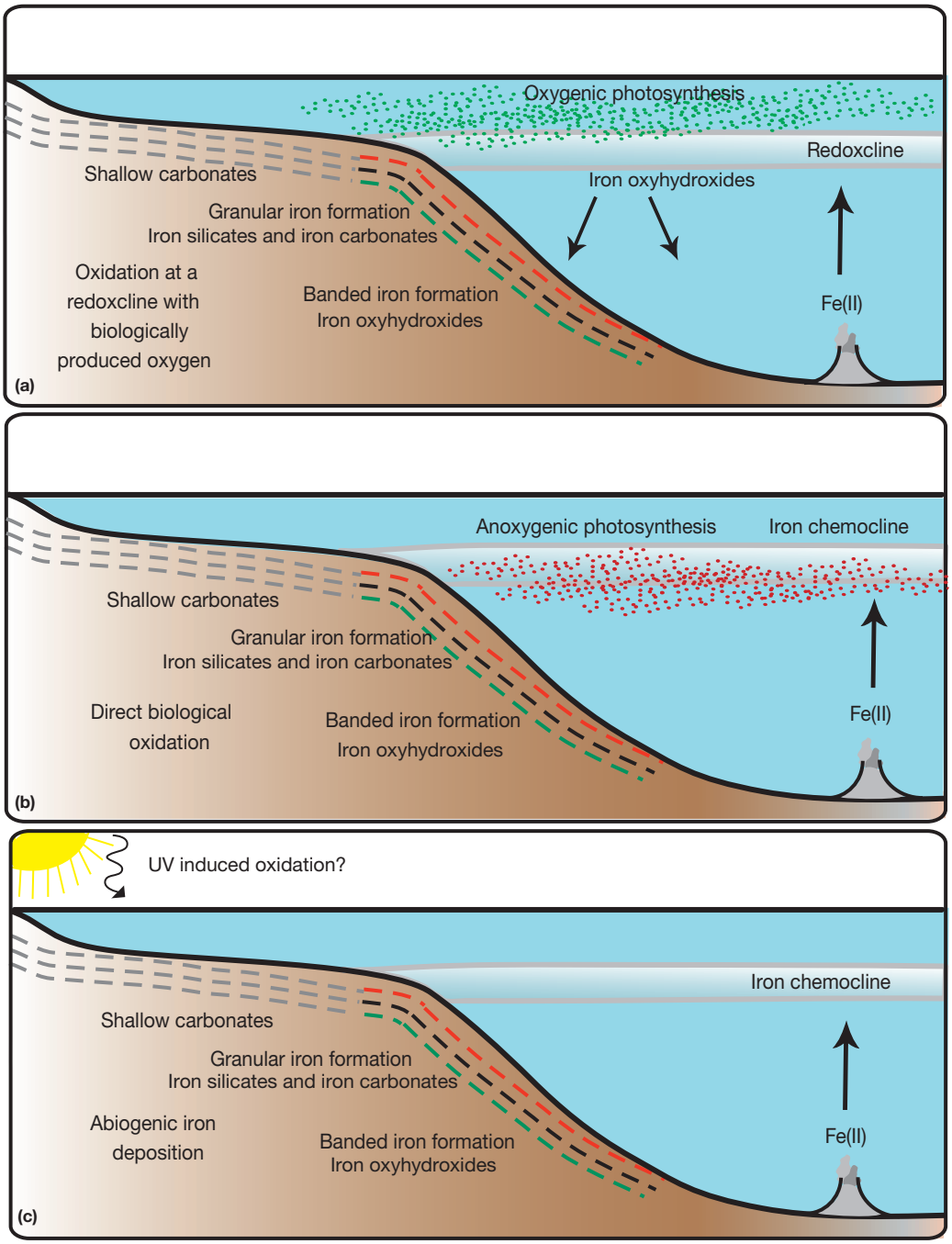

Figure 13 Simplified models for the deposition of Archean and Paleoproterozoic iron formations. Marked gradients in iron concentrations existed in both Archean and Proterozoic oceans in which iron formation deposition occurred. Oxygen oases in shallow-water environments (a), above the redoxcline, generated by oxygenic photosynthesis were originally held responsible for deposition of iron formation (e.g., Cloud, 1973). However, during the Archean even shallow-water settings may have been reducing with respect to iron. In this case, it is unlikely that oxidation with dissolved divalent oxygen was an important process; anoxygenic photosynthesis (b) was probably the dominant means of ferrous iron oxidation. Photochemical oxidation of iron was also inferred (c) highlighting the fact that iron formations can form even in a prebiotic world without microbial influence. Colored lines represent oxidation state of iron during deposition, diagenesis, and burial (red - Fe(III), black - mixed valence, and green - Fe(II)). Modified from Bekker A, Slack J, Planavsky N, et al. (2010). Iron formation: The sedimentary product of a complex interplay among mantle, tectonic, oceanic, and biospheric processes. *Economic Geology* 105: 467–508. With permission from the Society of Economic Geologists.

mechanism that converted dissolved Fe(II) into solid-phase iron oxyhydroxide particles that then settled and accumulated on the seafloor. The caveat is, however, that unequivocal original grains of ferric oxyhydroxide in IFs have not been conclusively documented.

Specific mechanisms involved in the deposition of IFs (Figure 13) remain poorly resolved despite more than a century of investigation (e.g., Beukes and Gutzmer, 2008; Harder, 1919; Klein, 2005; Ohmoto et al., 2006). Given that IF deposition spans major evolutionary changes in Earth's

surface composition, from an early anoxic atmosphere dominated by CO_2 and CH_4 to one that became partially oxygenated and CO_2-rich (e.g., Bekker and Kaufman, 2007), it is likely that IFs formed via different mechanisms during Precambrian time. The three mechanisms most widely supported in the literature are briefly summarized below.

9.18.6.2.1 Oxidation of Fe(II) by cyanobacterial O_2

The classic model for IF deposition invokes ferric iron precipitation occurring at the interface between oxygenated shallow waters and reduced upwelling iron-rich waters (Cloud, 1965, 1973; **Figure 13(a)**):

$$2Fe^{2+} + 0.5O_2 + 5H_2O \leftrightarrow 2Fe(OH)_3 + 4H^+$$

Oxygen is assumed to have been produced by planktonic oxygenic photosynthesizers. Historically, cyanobacteria were inferred to be the primary producers utilizing oxygenic photosynthesis in Archean oceans, because compelling evidence for an eukaryotic fossil record before ~1.9 Ga is absent (Han and Runnegar, 1992; Javaux, 2011; Knoll et al., 2006). Several lines of evidence tentatively suggest that oxygenic photosynthesis evolved during the Neoarchean (e.g., Buick, 1992; Buick et al., 2006; Scott et al., 2011); however, at present, direct 'smoking gun' evidence for the former existence of cyanobacteria during that time period remains lacking (e.g., Brocks, 2011).

9.18.6.2.2 Metabolic Fe(II) oxidation

Metabolic Fe(II) oxidation is the other most commonly invoked mechanism of IF deposition (**Figure 13(b)**). The potential importance of this process has been recognized for almost a century (e.g., Harder, 1919). However, it was not until a surge in the amount of interest and research on microbial iron oxidation over the past 10–20 years that this model for IF deposition became prevalent.

Three main pathways of metabolic microbial iron oxidation exist: (1) microaerophilic, (2) anoxygenic photosynthetic, and (3) nitrate-dependent. Microaerophilic bacteria, such as *Gallionella ferruginea*, *Leptothrix ochracea*, and *Mariprofundus ferrooxydans*, play an important role in Fe(II) oxidation in modern iron springs and seafloor hydrothermal vent systems. In addition to using ferrous iron as their electron donor, microaerophilic Fe(II) oxidizers use oxygen as their electron acceptor and take in carbon dioxide, which is then reduced to organic carbon through the process of chemoautorophy:

$$6Fe^{2+} + 0.5O_2 + CO_2 + 16H_2O \leftrightarrow [CH_2O] + 6Fe(OH)_3 + 12H^+$$

Presently known microaerophilic Fe(II) oxidizers belong to the phylum *Proteobacteria*, but the metabolic pathway appears to be nested within several different clades of this broad grouping of bacteria. Interestingly, microaerophilic Fe(II) oxidizers have been recently discovered to be widespread in marine systems. For example, a strain of bacteria that is morphologically indistinguishable but phylogenetically distinct from *Gallionella* was found to be abundant at the iron-rich hydrothermal vents on Loihi Seamount and other seafloor, iron-rich hydrothermal systems (Emerson and Moyer, 2002; McAllister et al., 2011). Under low oxygen conditions, microaerophilic microbial Fe(II) oxidizers can dominate the iron cycle because the rate of microbial Fe(II) oxidation can be more than 50 times faster than abiotic rates (e.g., Søgaard et al., 2000). Additionally, Fe(II)-oxidizing bacteria are present, and may be abundant, at the chemocline in ferruginous lakes, where ferric iron-rich sediments are deposited (e.g., Pavin Lake in France; Lehours et al., 2007).

Anoxygenic photosynthetic oxidation – photoferrotrophy – is another metabolic Fe(II) oxidation pathway. This pathway was predicted to be common on early Earth and linked to IF deposition (e.g., Baur, 1979; Hartman, 1984) before organisms capable of this metabolism were first cultured in the early 1990s (Widdel et al., 1993). Since then, a variety of phylogenetically diverse strains of anoxygenic Fe(II)-oxidizing phototrophs have been recognized, including strains of purple sulfur, and purple nonsulfur and green sulfur bacteria. Anoxygenic photosynthesis uses Fe(II) instead of H_2O as an electron donor, producing Fe(III) rather than dioxygen (Ehrenreich and Widdel, 1994), according to the following reaction:

$$4Fe^{2+} + 11H_2O + CO_2 \leftrightarrow [CH_2O] + 4Fe(OH)_3 + 8H^+$$

In the past two decades, a number of experimental studies have confirmed that various purple and green bacteria can use Fe(II) as a reductant for carbon dioxide fixation (e.g., Heising et al., 1999; Straub et al., 1999; Widdel et al., 1993).

More recently, organisms capable of metabolically coupling iron oxidation to nitrate reduction have been discovered (e.g., Edwards et al., 2003; Straub et al., 1996), providing another possible microbially mediated mechanism for IF deposition:

$$10Fe^{2+} + 2NO_3^- + 24H_2O \rightarrow 10Fe(OH)_3 + N_2 + 18H^+$$

Nitrate-dependent Fe(II) oxidation has been shown to be widespread in sediments (Straub and Buchholz-Cleven, 1998). Most of the described nitrate-dependent Fe(II)-oxidizing strains require an organic substrate (e.g., acetate), although lithoautotrophic, nitrate-reducing Fe-oxidizing strains (α- and γ-Proteobacteria) have been isolated in pure culture (Edwards et al., 2003). A chemolithoautotrophic Fe(II)-oxidizing, nitrate-reducing enrichment culture has been identified (Straub et al., 1996) that is capable of oxidizing Fe(II) with nitrate autotrophically. However, this culture consists of chemoheterotrophic nitrate-reducing bacteria and a novel chemolithoautotrophic Fe(II)-oxidizing bacterium (Blothe and Roden, 2009). The inability (thus far) in laboratory experiments to obtain a pure culture of nitrate-reducing iron-oxidizers suggests that a consortium of organisms is needed for nitrate-dependent Fe(II) oxidation.

There is a strong basis to believe that metabolic Fe(II) oxidation could have driven IF deposition. Simple modeling indicates that even modest populations of microaerophilic or photosynthetic iron oxidizers could account for deposition of IFs, even assuming rapid accumulation rates (Konhauser et al., 2002). Recent modeling indicates that photosynthetic Fe(II) oxidation can result in near-to-quantitative drawdown of upwelling ferrous iron under modest ocean mixing and circulation conditions (e.g., Kappler et al., 2005). Furthermore, metabolic Fe(II) oxidation is currently driving the deposition of extremely iron-rich sediments in ferruginous Lake Matano

(Crowe et al., 2008), and microaerophilic iron oxidizers are likely important in the production of IF-like sediments on the seafloor, such as the Loihi hydrothermal field (Emerson and Moyer, 2002). Metabolic iron oxidation thus appears to be common in modern iron-replete aquatic systems. It follows that these processes likely were common in iron-rich water columns in ancient oceans.

Numerous studies have documented a fossil record of microbially mediated iron oxidation in Proterozoic and younger, iron oxide-rich sedimentary rocks (Grenne and Slack, 2003; Juniper and Fouquet, 1988; Lager, 2001; Little et al., 2004; Planavsky et al., 2009; Slack et al., 2007) but not in Archean IFs. Microaerophilic Fe(II) oxidizers produce distinctive oxide-coated structures that have been found in jaspers and IF dating back to the Paleoproterozoic (Lager, 2001; Planavsky et al., 2009; Slack et al., 2007). *Gallionella*-type or *Mariprofundus*-like oxidizers are bean-shaped cells that grow at the terminus of a helical structure called a stalk, which is composed largely of polysaccharides typically encrusted by ferrihydrite (Comolli et al., 2011), whereas *Leptothrix*-type oxidizers produce an iron-encrusted sheath. The apparent absence of these fossil remains in the Archean, contrasted to their local abundance in younger iron oxide-rich rocks, might be a signal of a temporal increase in the involvement of microaerophilic oxidizers. However, it has been demonstrated that *G. ferruginea* does not form a stalk under the lower range of oxygen conditions at which these organisms can thrive (Hallbeck and Pedersen, 1990). Therefore, generally more reducing conditions in the Archean may have precluded template-mediated oxide formation (i.e., formation of oxide-coated sheaths and helical structures), but might not necessarily have excluded microaerophilic oxidizers.

It may be possible to use geochemical tools rather than the fossil record to pinpoint oxidation mechanisms. For instance, the REE signature of IFs through time indicates the lack of a discrete redoxcline prior to ~2.4 Ga in most sedimentary basins where IFs were deposited. This is consistent with a role for anoxic or microaerophilic iron-oxidizers in IF deposition (Planavsky et al., 2010a,b).

9.18.6.2.3 Ultraviolet photooxidation of Fe(II)

As an alternative to biological models for Fe(II) oxidation, Cairns-Smith (1978) proposed that ferrous iron was photooxidized by the high flux of ultraviolet (UV) photons that would have reached Earth's surface prior to the rise of atmospheric oxygen and the subsequent development of a protective ozone layer (**Figure 13(c)**). This reaction proceeds readily in acidic waters exposed to wavelengths in the 200–300 nm range:

$$2Fe^{2+}{}_{(aq)} + 2H^{+} + h\nu \rightarrow 2Fe^{3+}{}_{(aq)} + H_2$$

Braterman et al. (1983) and Anbar and Holland (1992) further explored the viability of the photochemical oxidation model at circumneutral pH over a range of UV wavelengths (217–406 nm). Based on a quantum yield determined from proton flux, they suggested that at pH > 6.5 the presence of the dissolved ferrous iron species $Fe(OH)^{+}$ is important because it is oxidized by photons having λ=300–450 nm, a wavelength region where the solar flux is more intense and where seawater is more transparent as compared to λ<300 nm. The dissolved ferric iron formed is subsequently hydrolyzed and precipitated as ferric oxyhydroxide. Extrapolating from these experiments, a mean photochemical oxidation rate of 0.5 mol Fe(II) m^{-2} $year^{-1}$ has been estimated at rapid upwelling rates (4000 m $year^{-1}$), indicating that this process alone could have accounted for deposition of as much as 1.8×10^{14} mol Fe(III) annually (François, 1986). Other estimates place the total amount of Fe(II) photooxidized annually at 2.3×10^{13} mol (Braterman and Cairns-Smith, 1986). These rates are much greater than the annual rates inferred during deposition of the largest Archean and Paleoproterozoic BIF (Pickard, 2002, 2003), although, as mentioned above, it is difficult to constrain maximum sedimentation rates for IFs.

Importantly, the earlier photochemical models focused on determining the rates of Fe(II) photooxidation at, or close to, thermodynamic equilibrium with 0.02 mM Fe and under rather simplistic geochemical conditions in which other ions were unavailable for reaction with dissolved Fe(II). In this regard, Konhauser et al. (2007a) performed a series of experiments designed to mimic conditions in a photic zone proximal to a seamount-type vent system effusing elevated concentrations of Fe(II) into seawater that was saturated with respect to amorphous silica and calcite. Under those conditions, the photochemical contribution to solid-phase precipitation was negligible compared to the formation of the ferrous silicate mineral, greenalite, or the ferrous carbonate, siderite. Many IFs are composed predominantly of iron carbonates or iron silicates, both of which have been widely suggested to be abiotic marine precipitates (e.g., Ohmoto et al., 2004). However, as discussed above, based on petrographic and isotopic constraints, siderite in most IFs is an early diagenetic, or later, mineral phase. In experiments where Fe(II) was exposed to either phototrophic Fe(II)-oxidizing bacteria or dioxygen, ferric oxyhydroxide formed considerably faster than by UV-photooxidation.

As an alternative to these classical models, Foustoukos and Bekker (2008) argued that some deep-water, volcanic-hosted IFs deposited in association with VMS deposits could have formed by oxidation during phase separation in the subsurface into vapor and brine, with hydrogen and HCl being removed into the vapor phase, generating oxidizing and alkaline conditions in the brine. During this process, transition metals would form chloro-complexes and would then be enriched in the brine, which would be expelled from magmatic chambers during large eruptions. This hypothesis, although not yet supported by either detailed modeling or empirical data, warrants serious consideration because it has the potential to explain the enigmatic association of Archean jasper and oxide-facies IF with some Cu-rich VMS deposits that formed in deep-water settings.

9.18.7 Secular Trends for Exhalites, IFs, and VMS Deposits

9.18.7.1 Relationships among Mantle Plumes, IF Deposition, and VMS Mineralization

Secular trends in the distribution of Precambrian IFs and VMS deposits (**Figure 14**) have been discussed previously by many authors (e.g., Bekker et al., 2010; Groves et al., 2005; Huston and Logan, 2004; Huston et al., 2010; Isley and Abbott, 1999;

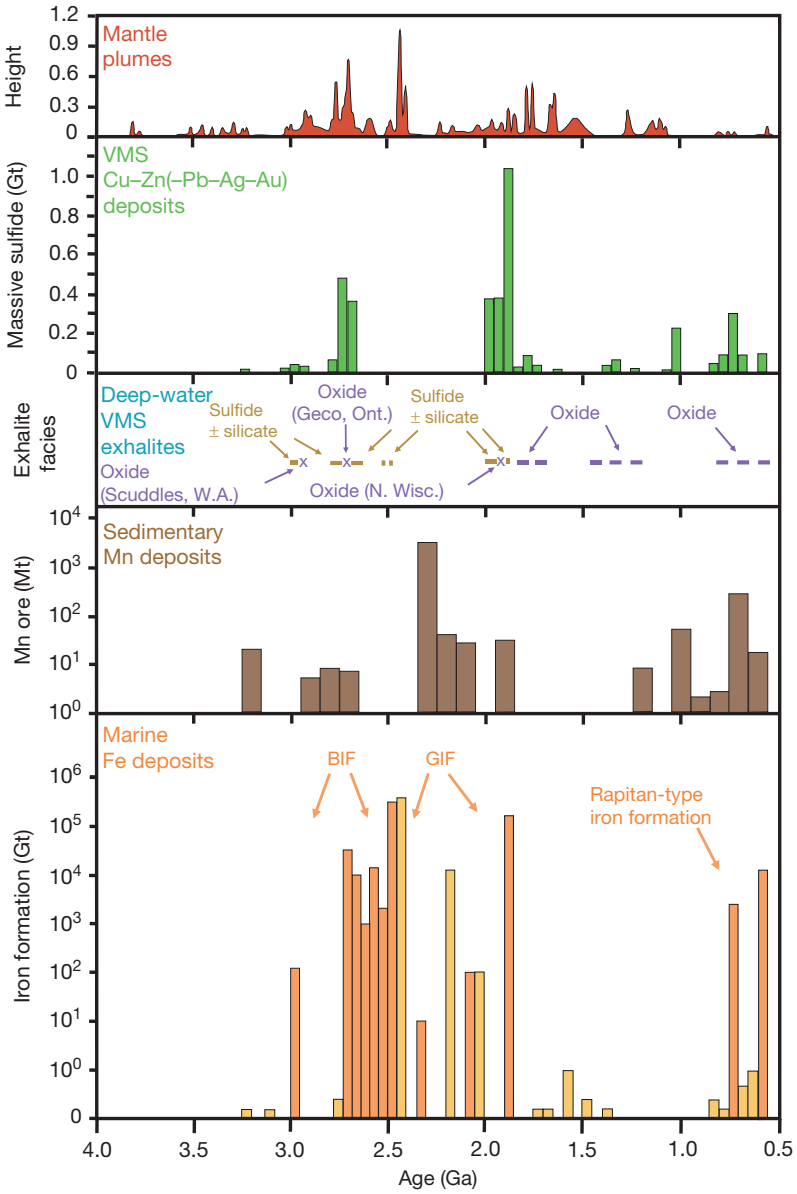

Figure 14 Secular distributions of mantle superplume breakout events and selected marine mineral deposits during the Precambrian. Distribution of mantle superplumes is from Abbott and Isley (2002) in which the *y*-axis (height) is the sum of Gaussian time series for high-Mg intrusive rocks and layered intrusions, flood basalts, and dikes. Distribution of marine Fe deposits is plotted as amount of iron formation in billion metric tons (Gt), integrated over time intervals of 50 Ma (data in **Appendix 2**); apparently small deposits that lack published tonnage data are assigned a size of 0.2 Gt; deposits having poor age control are included as pale orange bars. Distribution of marine Mn deposits is plotted in million metric tons (Mt) of Mn from Maynard (2010). Time periods dominated by banded iron formation (BIF), granular iron formation (GIF), and Rapitan-type iron formation are shown schematically (see text). Distribution of VMS deposits is similarly plotted in Gt for time intervals of 50 Ma (data in Franklin et al., 2005; Appendix A2). Secular facies variation of exhalites associated with deep-water, Cu-rich VMS deposits is from Slack and Cannon (2009). Modified from Bekker A, Slack J, Planavsky N, et al. (2010). Iron formation: The sedimentary product of a complex interplay among mantle, tectonic, oceanic, and biospheric processes. *Economic Geology* 105: 467–508, with data for Mn deposits added from Maynard, 2010. With permission from the Society of Economic Geologists.

James, 1983; Meyer, 1988; Veizer, 1976). Although the deposition of IFs has been genetically linked to mantle plume breakout events and mafic volcanism (Isley and Abbott, 1999), the largest VMS deposits are instead generated in arc settings marked by bimodal volcanism (Franklin et al., 2005). Given that IFs were likely precipitated from hydrothermal plumes and that iron in hydrothermal plumes was released by submarine hydrothermal alteration of volcanic rocks in the deeper part of the ocean, large VMS deposits should have formed contemporaneously near the volcanic sources. Exhalites that formed in stratigraphic association with Cu-rich VMS deposits provide a unique record of deep-water ocean redox

state (Slack et al., 2007). The following sections explore secular trends in seafloor-hydrothermal exhalites and IFs to infer the ocean redox state during their deposition.

9.18.7.2 Secular Patterns in Precambrian VMS-Related Exhalites

There is consensus that the source of iron in Precambrian IFs was in hydrothermal fluids that vented into the deep ocean during submarine volcanism (Bekker et al., 2010, and references therein). Because the generation and transport of this iron are believed to be linked to hydrothermal processes and anoxic conditions, secular trends of IFs, VMS deposits, and the redox state of coeval deep seawater aid in understanding of episodic IF deposition during Precambrian time (**Figure 14**). Insights into ancient deep-ocean redox states come from diverse proxies, one of which is the nature of exhalites that formed by precipitation from hydrothermal vents and plumes as parts of Cu-rich VMS systems. Cu-rich VMS deposit formation is restricted to settings with fluids having temperatures $\geq$300 °C and water depths of >850 m, which permit the precipitation of relatively abundant Cu (>1wt%) in sulfides on or near the seafloor. At shallower depths, hydrothermal fluids at this temperature, assuming present seawater salinity (3 M NaCl), boil in the subsurface and do not produce Cu-rich massive sulfide (Slack et al., 2007).

The exhalites occur as stratiform layers or lenses, up to several meters thick, typically in the hanging wall above VMS deposits or at the same stratigraphic level for hundreds of meters or more along strike (Spry et al., 2000). Given abundant evidence of exhalite mineralization on the modern seafloor (Hannington et al., 1995; also see **Chapter 8.7**), ancient exhalites are widely interpreted as precipitates from spatially associated VMS systems (e.g., Grenne and Slack, 2005; Isley, 1995; Peter, 2003). The mineralogy and geochemistry of exhalites in the geological record vary widely (Spry et al., 2000), but mainly consist of fine-grained quartz (chert) and one or more Fe-rich minerals including hematite, magnetite, greenalite, stilpnomelane, grunerite, siderite, ankerite, pyrite, or pyrrhotite; some exhalites have abundant Mn (in rhodochrosite, kutnahorite, and spessartine), Ba (in barite, hyalophane, and celsian), P (in apatite), F (in fluorite), or B (in tourmaline). In addition to the requirement of a Cu-rich mineralogy in related VMS deposits, several other limitations exist for using exhalites as a paleoredox proxy (see Bekker et al., 2010; Slack et al., 2007).

Mineralogical data for 45 Precambrian exhalites linked to Cu-rich VMS deposits (**Figure 14**; **Appendix 2**) show a secular pattern in which exhalites older than ~1.85 Ga mainly comprise Fe-silicates, sulfide, sulfidic shale, pyritic chert, or pyritic tuff. In contrast, exhalites younger than ~1.85 Ga typically have abundant iron oxides in jasper, hematitic IF, or magnetitic IF as well as Fe-silicates in some cases. Occurrence of the former group of reduced-facies exhalites, which predominates in the Archean and early Paleoproterozoic, suggests deposition on the seafloor under anoxic and possibly sulfidic bottom waters, based on geochemical and thermodynamic arguments (Huston and Logan, 2004; Ohmoto et al., 2006). Younger Precambrian exhalites that contain abundant hematite and magnetite have relatively high Fe(III)/Fe(II) ratios that rule out sulfidic bottom waters during mineralization, assuming no oxidation took place during postdepositional alteration, diagenesis, metamorphism, or weathering (Slack et al., 2009). The presence of hematite or magnetite in these exhalites requires at least suboxic conditions (<5 μM O_2) in coeval deep seawater, in order to permit the precipitation of ferric oxyhydroxide precursors as documented in modern seafloor-hydrothermal vents and plumes (Grenne and Slack, 2005; Slack et al., 2007). It is possible that magnetite in ancient exhalites had a mixed ferrous–ferric 'green rust' precursor such as $Fe(OH)_2$, which in theory could have formed in anoxic seawater (Murray, 1979). This precursor is unlikely, however, because Archean and Paleoproterozoic seawater, as well as diagenetic pore fluids, probably were saturated in $FeCO_3$ prior to $Fe(OH)_2$ saturation, owing to high atmospheric pCO_2 during this time period and resulting bicarbonate saturation in coeval seawater and shallow pore waters (Slack et al., 2009, and references therein). Fully oxic conditions for contemporaneous deep seawater are also discounted, based on REE data on late Paleoproterozoic hematite- and magnetite-rich exhalites that have small negative to small positive shale-normalized Ce anomalies, in contrast to the larger negative Ce anomalies that characterize modern iron oxyhydroxide deposits (Slack et al., 2007, 2009).

There are several exceptions to the patterns of Fe-silicate and sulfide exhalites that are genetically linked to Archean and early Paleoproterozoic Cu-rich VMS deposits (**Figure 14**). These exceptions, which include magnetite IF, hematite IF, or jasper, occur at the following deposits: 2960 Ma Scuddles, Western Australia; 2720 Ma Geco and Willroy, Ontario, Canada; ~2530 Ma Wutai, Shanxi Province, China; and ~1870 Ma Bend and Eisenbrey, Wisconsin, USA. The presence of abundant Fe(III) in hematite and/or magnetite within these >1850 Ma deposits (Slack and Cannon, 2009) should be further evaluated to constrain their origin.

The absence of Cu-rich VMS deposits during some periods of Earth history precludes the use of exhalites for evaluating the redox state of coeval deep oceans. For example, several VMS deposits have been documented in sequences >3000 Ma, including the oldest (3465 Ma) deposits at Big Stubby and Lennons Find in the Pilbara craton of Western Australia. These deposits contain abundant Zn and Pb with little or no elevated Cu (Franklin et al., 2005; Huston et al., 2002; **Appendix 2**), and hence could have formed at relatively shallow depths of a few hundred meters. The oldest Cu-rich VMS deposit with a genetically linked exhalite unit is the ~2.97 Ga Miranda deposit in South Africa (Slack and Cannon, 2009). A long gap of ~620 Ma in exhalite data exists from ~2530 to 1910 Ma, during which 16 VMS deposits are known (Franklin et al., 2005; **Appendix 2**), but none has a reported exhalite. Additional long gaps in the record of Precambrian deep-marine exhalite mineralization of this type are from ~1700–1400 Ma and ~1000–770 Ma. The emerging record of deep-ocean redox state from studies of exhalites associated with VMS deposits is entirely consistent with other geochemical and geological proxies for the rise of atmospheric oxygen in the early Paleoproterozoic and suboxic deep-ocean redox state in the late Paleoproterozoic and Mesoproterozoic.

9.18.7.3 Secular Patterns in Sedimentary Iron Deposits

In order to evaluate a secular pattern in sedimentary iron deposits, we divide Earth history into time intervals characterized by different redox states of the atmosphere–ocean system. The following discussion begins with the Eoarchean and progresses sequentially toward the modern iron cycle.

9.18.7.3.1 Eoarchean IFs

In the Isua greenstone belt of western Greenland, ~3.8 Ga chert and BIF at amphibolite facies metamorphic grade are tectonically interleaved with amphibolite that locally preserves pillow structures (Myers, 2001). The BIF consists predominantly of quartz and magnetite, with minor cummingtonite/grunerite, actinolite, hornblende, and calcite (Dymek and Klein, 1988). Polat and Frei (2005) observed significant enrichments of Fe in Isua pillow basalts, which they attributed to leaching from oceanic crust and precipitation on the seafloor from hydrothermal fluids, suggesting that high-temperature hydrothermal alteration of the immediate substrate might have played an important role in deposition of the Isua BIF.

In the ~4.3–3.8 Ga Nuvvuagittuq greenstone belt of the northeastern Superior Province of Canada, quartz–magnetite–grunerite BIF, as much as 30 m thick, and other siliceous rocks are intercalated with metasomatized amphibolite (Dauphas et al., 2007; Mloszewska et al., 2012; O'Neil et al., 2007). The REE+Y profiles and Fe isotope compositions of this BIF are consistent with its origin as marine exhalite. Low Al_2O_3, TiO_2, and high field strength element (HFSE) concentrations show that it is relatively detritus-free. There are distinctly seawater-like REE+Y profiles and consistently positive Eu anomalies. These features suggest that the rocks preserved some of their primary composition despite metamorphic overprint (Mloszewska et al., 2012).

9.18.7.3.2 Paleoarchean IFs

Paleoarchean IFs are intercalated with bedded chert in ultramafic to felsic volcanic successions in greenstone belts of the Kaapvaal and Pilbara cratons. Bedded cherts consist, to a large extent, of silicified sedimentary and volcaniclastic rocks. Although silicification is common in modern and ancient low-temperature hydrothermal systems in both continental and oceanic settings, the abundance of chert in the Paleoarchean is striking. In contrast, IFs are relatively rare in the >3.0 Ga record, despite evidence for widespread leaching of iron from seafloor rocks during hydrothermal alteration (Hofmann and Harris, 2008). It is possible that the absence of widespread IF deposition during this time period reflects preservational bias. However, many cherts of this age range are uniformly underlain by zones of low-temperature seafloor alteration up to several tens of meters thick (Duchac and Hanor, 1987; Hofmann and Harris, 2008; Hofmann and Wilson, 2007), which suggests the predominance of low-temperature hydrothermal processes at this time. These zones are characterized by silicification and depletion of many elements, including Fe, Mg, and some transition and base metals, which were likely exhaled by hydrothermal systems to the Paleoarchean ocean, thus providing a source of dissolved iron (Hanor and Duchac, 1990; Hofmann and Harris, 2008).

The Onverwacht Group of the Barberton greenstone belt, South Africa, records a time interval of ~240 My, but contains only a single stratigraphic unit that includes IF. The ~3.4 Ga Buck Reef Chert is an unusually thick sequence of predominantly black and white banded chert that contains a 100-m-thick unit of banded ferruginous chert, in which siderite is regarded to be the main iron-bearing mineral at depth (Tice and Lowe 2004). Also in the Barberton greenstone belt, jaspilitic IF units, several tens of meters thick, are intercalated with ferruginous shale of the 3.26–3.23 Ga Fig Tree Group (Heinrichs, 1980; Hofmann, 2005). Felsic volcanic detritus and evidence for hydrothermal activity in rocks interlayered with the IF are widespread (Hofmann, 2011). Two thin jaspilitic units interbedded with ferruginous shale also occur at the top of fining-upward sequences within the ~3.23 Ga Moodies Group of the Barberton greenstone belt and in association with volcanic rocks (Eriksson, 1983).

The Iron Ore Group of the Singhbhum craton in India contains economically important BIF deposits that likely represent different stratigraphic units (e.g., Banerji, 1977). In the southern part of the craton, a low-metamorphic grade, 120-m-thick BIF overlies a sequence of basalts and felsic volcanic rocks dated at 3.51 Ga, possibly indicating a Paleoarchean age for this BIF (Mukhopadhyay et al., 2008), although contact relationships with the underlying dated succession are unclear. In the western part of the craton, BIFs are intercalated with shales that are likely Meso- to Neoarchean in age. Absolute age constraints are not available, highlighting the need for high-precision geochronological studies of the Iron Ore Group in this region.

Amphibolite- to granulite-facies grade BIFs associated with amphibolites, calc-silicate rocks (carbonate-altered mafic rocks), talc-carbonate schists, and metacherts are present in a number of Paleoarchean high-grade remnants of greenstone belts in South Africa (e.g., Assegaai–De Kraalen granitoid-greenstone terrane; Saha et al., 2010), Zimbabwe (e.g., Sebakwean Group; Wilson, 1968), India (e.g., Sargur Group; Naqvi and Rogers, 1987), and elsewhere. Strong deformation and metamorphism make their paleoenvironmental significance unclear. The close spatial association with siliceous and carbonate-bearing metasomatized lithologies suggests a strong hydrothermal influence on the formation of these BIF.

9.18.7.3.3 Neoarchean to Mesoarchean IFs

BIFs are a distinct component of Neo- to Mesoarchean greenstone belts. These BIFs are either intercalated with submarine volcanic rocks or associated with sedimentary strata of continental-shelf environments. Good examples of continental shelf BIF deposits are found on several cratons that experienced transient crustal stability prior to the global magmatic event at 2.7 Ga. The 2.83–2.70 Ga Manjeri Formation of the Zimbabwe craton is a fluvial to shallow-marine succession that was deposited unconformably on older greenstones and granitoids (Hofmann and Kusky, 2004; Hunter et al., 1998). The IF of this unit is intercalated with quartz arenite, shale, and carbonate strata, and lacks obvious links to coeval volcanic rocks. Lithologically similar sequences include the ~2.8 Ga Central Slave Cover Group (Bleeker et al., 1999) of the Slave craton, the ~2.7 Ga Steep Rock Group in the Wabigoon greenstone belt and correlative sequences in Canada (Stone, 2010; Tomlinson

et al., 2003; Wilks and Nisbet, 1988), and the ~2.7 Ga Bababudan Group of the Dharwar craton in India (Srinivasan and Ojakangas, 1986; Trendall et al., 1997).

IFs interlayered with volcanic rocks can be found in most Mesoarchean and Neoarchean greenstone belts. They are commonly thin, less than 20 m thick, and laterally discontinuous. The volcanic components typically consist of mafic–ultramafic or bimodal volcanic rocks that erupted in relatively deep-water, oceanic settings. In several cases, a direct genetic relationship has been documented between volcanic activity and deposition of IF, reflecting volcanic and hydrothermal activity both proximal and distal to volcanic centers (Chown et al., 2000; Fyon et al., 1992).

Mesoarchean IFs that developed in cratonic cover successions between 3.0 and 2.9 Ga are well documented in the Witwatersrand and Pongola basins in the southeastern part of the Kaapvaal craton in South Africa (Beukes and Cairncross, 1991; Smith, 2007). These IFs are laterally extensive, but thin (~10 m thick), and commonly are interbedded with ferruginous shales deposited during marine transgressions. There are no direct relationships with volcanic rocks or volcanism at that time, in accord with trace element and Nd isotope data on the oldest IF of the Mozaan Group in the Pongola basin (Alexander et al., 2008), which indicate a strong continental contribution to the trace element inventory of these IFs.

9.18.7.3.4 Neoarchean IFs

IFs of 2.7–2.45 Ga age are the most laterally extensive and economically valuable of any time in Earth's history. The oldest extensive and thick sediment-hosted BIF is the ~2.60 Ga Marra Mamba Formation of the Hamersley Province in Western Australia. It was deposited in a deep-water basinal setting on a passive continental margin during sea-level highstand of the Marra Mamba Supersequence, and has an average thickness of about 210 m (Krapež et al., 2003; Trendall and Blockley, 1970). This BIF carries a pronounced positive Eu anomaly (Alibert and McCulloch, 1993), suggesting a strong hydrothermal imprint on REE systematics of the global ocean during its deposition. Although the Hamersley and Transvaal successions are equivalent in age and are correlative based on sequence stratigraphy, only ankerite-banded chert of the Campbellrand succession in South Africa corresponds to the Marra Mamba BIF (Beukes and Gutzmer, 2008). A mantle plume breakout event comparable in age to that of the Marra Mamba Formation is unknown.

Only one IF (Bruno's Band) occurs on the Pilbara and Kaapvaal cratons stratigraphically between the ~2.60 Ga Marra Mamba IF and the overlying major 2.50–2.45 Ga IFs (Beukes and Gutzmer, 2008; Krapež et al., 2003). This younger episode of IF deposition closely corresponds with volcanism during the 2.50–2.45 Ga series of mantle plume breakout events of global extent (e.g., Heaman, 1997) and immediately preceded a supercontinent assembly (Barley et al., 2005). Deposition of these IFs occurred on a reactivated continental margin (Krapež et al., 2003), during a rise in sea level. In addition to these well-dated, time-equivalent IFs, those in the Quadrilátero Ferrífero region in Brazil, Middleback Ridge (Gawler craton) in South Australia, Krivoy Rog area in Ukraine, and KMA region in Russia are broadly similar in age based on available geochronological and chemostratigraphic constraints, as well as on similar patterns of megabanding (Bekker et al., 2003; Kulik and Korzhnev, 1997; Prilutzky et al., 1992; Spier et al., 2007; Szpunar et al., 2011). These giant IFs were also deposited on reactivated continental margins and are separated from overlying Paleoproterozoic sequences by a prominent unconformity. The unconformities correspond to a long gap in sedimentation following supercontinent assembly at ~2.4 Ga. Assuming that these IFs are similar in age, more than 70 wt% of the total original iron resources in Precambrian IFs was deposited during the time interval 2.60–2.40 Ga. Surprisingly, a coeval peak in VMS deposition is absent from the geologic record (**Figure 14**); in fact, no VMS deposits are known to have formed within this age range (Franklin et al., 2005; **Appendix 2**). Texturally, these IF deposits differ from the older BIF because they contain intervals having granular textures as well as micro- and nanospheres of hematite (Ahn and Buseck, 1990; Ayres, 1972; Beukes and Klein, 1990; Simonson and Goode, 1989; Spier et al., 2007). However, most granules consist of iron silicates and carbonates with only rare hematite granules; no hematite-coated grains have been documented (Beukes and Klein, 1990; Simonson and Goode, 1989; Spier et al., 2007). Such features are important because deposition of these IFs directly preceded the GOE, and post-GOE GIFs predominantly contain hematite as the iron-bearing mineral within granules and on coated grains. This observation implies that processes responsible for IF deposition before and after the rise of atmospheric oxygen were different, requiring more than one model to explain their formation.

9.18.7.3.5 IFs deposited after the GOE and before ~1.93 Ga

Giant IFs were not deposited between ~2.4 and 1.88 Ga. Nonetheless, sediment-hosted and volcanic-hosted IFs are known from this time period. Shortly after the rise of atmospheric oxygen at ~2.4 Ga (e.g., Bekker et al., 2004), oolitic hematitic ironstone of the lower Timeball Hill Formation, South Africa, was deposited in shallow water above fair-weather wave base (Dorland, 1999; Schweigart, 1965). Its deposition at ~2316 Ma (Hannah et al., 2004) may coincide with a magmatic event at ~2.32 Ga (e.g., Berman et al., 2005; Eriksson et al., 1994a,b; Fetter et al., 2000; Hartlaub et al., 2007). The significance of this event and whether it is related to mantle processes are unknown. Correlative IFs are not documented on other continents.

The slightly younger ~2.22 Ga Hotazel Formation, also in South Africa, contains IF interlayered with manganese-rich sedimentary rocks; this is the largest manganese deposit in the world (Tsikos et al., 2003). The iron and manganese formation lies above, and is most likely genetically related to, the submarine-emplaced Ongeluk Lavas of mafic to intermediate composition that are coeval with a ~2.22 Ga mantle plume breakout event (Ernst and Buchan, 2001). Although volcanic rocks and dikes related to this event are developed on nearly all continents, other iron and manganese formations of this age are unknown. Iron- and manganese-rich strata of the Hotazel Formation consist of three upward-shallowing sequences deposited in a slope environment (Schneiderhan et al., 2006). Significantly, the deposit lacks positive Eu anomalies, but has pronounced negative Ce anomalies, indicating an oxygenated state of at least the upper part of the ocean (Tsikos and Moore,

1997). The absence of a positive Eu anomaly is also important because it indicates that the global ocean was not dominated by a high-temperature, hydrothermal flux at that time and that Fe and Mn were likely derived locally, within the basin, by low-temperature, shallow-water alteration of the underlying thick (≥1 km) sequence of volcanic rocks. Considering that the 2.22 Ga mantle plume breakout event coincides with a positive carbon isotope excursion in seawater composition, the Lomagundi Event, related to high relative burial rates of organic carbon (e.g., Bekker et al., 2001; Karhu and Holland, 1996; Schidlowski et al., 1976), this REE pattern may indicate that significant parts of the oceans were already oxygenated by that time and that Fe and Mn were soluble only in isolated to semi-isolated basins overwhelmed by a hydrothermal flux of reductants.

Hematitic oolites and hematite-rich sandstones continued to be deposited in shallow-marine environments during the Lomagundi carbon isotope excursion in South Africa (e.g., Silverton Formation; Schweigart, 1965) and on the Kola Peninsula, Russia (Kuetsjärvi Sedimentary Formation; Akhmedov, 1972a). IFs deposited during the Lomagundi excursion are developed within the Lomagundi Group of the ~2.2–2.1 Ga Magondi belt, Zimbabwe (Master, 1991). In West Africa, they are present in the Ijil Group, Mauritania (Bronner and Chauvel, 1979) and the Nigerian schist belts (Mücke, 2005), both in the 2.2–2.1 Ga Birimian basin. Iron- and manganese-rich strata are also developed in West Africa in the Francevillian basin, Gabon (Leclerc and Weber, 1980). Volcanic-hosted IFs deposited during the Lomagundi carbon isotope excursion are also known in Brazil (e.g., Aimbé Formation, Guarinos Group; Resende and Jost, 1995; Itapicuru Complex of the Rio Itapicuru greenstone belt; Dalton de Souza et al., 2003) and Norway (Iddjajav'ri Group, Karasjok greenstone belt; Often, 1985). Considering uncertainty in the ages of these IFs, it is difficult to relate them to a specific mantle plume breakout event. However, several such events occurred between 2.2 and 2.1 Ga (Ernst and Buchan, 2001) and thus it seems likely that the deep-ocean redox state was too high, rather than the strength of mantle plume events being too low, to form giant sedimentary iron deposits during this time interval.

Following the end of the Lomagundi carbon isotope excursion at 2.1–2.0 Ga, small, volcanic-hosted IFs were deposited in several basins in North America (e.g., Homestake Iron Formation, Black Hills, South Dakota; Frei et al., 2008) and Finland (Laajoki and Saikkonen, 1977; Paakola, 1971). Oolitic hematitic ironstone is also present in the Kolasjoki Sedimentary Formation, Kola Peninsula, Russia (Akhmedov, 1972b), which was deposited during this time. Combined, these data suggest that dynamic ocean redox conditions were re-established in the aftermath of the GOE, characterized by periodic upwelling of iron into shallow-water settings above storm and wave base in association with mantle plume breakout events. A number of mantle plume events are recognized during this time interval, the most prominent being the ~2069–2053 Ma event that led to the emplacement of the Bushveld Complex in South Africa, and a number of mafic to ultramafic dikes and intrusions on the Superior and Sarmatia cratons (Chernyshov et al., 1998; Elming et al., 2010; Ernst and Bleeker, 2010). The absence of contemporaneous large accumulations of sedimentary iron is puzzling. However, considering that this event immediately followed the Lomagundi excursion, during which large amounts of oxygen were released to the atmosphere–ocean system, it is possible that the ocean redox state was buffered to change by a hydrothermal flux of reductants, preventing anoxia and significant Fe transport to sites favorable for IF accumulation.

9.18.7.3.6 C.1.93–1.85 Ga IFs coeval with large VMS deposits

Extensive and large IFs reappear after an approximately 500 My gap, at about 1.88 Ga. These are predominantly GIFs and are most common in North America at the margins of the Superior craton (Simonson, 2003), and in Western Australia (Goode et al., 1983; Rasmussen et al., 2012). They are coeval with emplacement of the ~1.88 Ga ultramafic LIP (Heaman et al., 1986, 2009; Hulbert et al., 2005) that is potentially related to a mantle plume breakout event (Hamilton et al., 2009; see for a different view Heaman et al., 2009) during the early stage in the assembly of Laurentia. These IFs are now recognized to be correlative, based on high-precision geochronology (Findlay et al., 1995; Fralick et al., 2002; Machado et al., 1997; Schneider et al., 2002; Stott et al., 2010). IFs extend discontinuously for more than 3000 km along the southern and eastern margins of the Superior craton, from Minnesota, Wisconsin, and Michigan, to Quebec (Mistassini basin), and northward to the Labrador Trough. Correlative and texturally similar GIFs also occur in the center of the Superior craton in the Hudson Bay region (Richmond Bay and Belcher Islands) and in Sutton Inliers, NW part of Ontario (Chandler, 1984; Hamilton et al., 2009; Hawley, 1926; Stott et al., 2010). This group of IFs is considered to have been deposited in extensional settings with coeval submarine mafic volcanism (Fralick et al., 2002; Ricketts et al., 1982; Schulz and Cannon, 2007). A back-arc basinal setting for the IFs has been proposed by these workers, whereas a foreland basin setting was advocated by others (e.g., Hoffman, 1987; Ojakangas et al., 2001; Schneider et al., 2002).

An intriguing question is whether deposition of these IFs represents either local, basin-scale conditions or the composition and redox state of the global ocean. This is a critical issue because occurrences and ages of these IFs have been used by some workers to infer deep-water anoxic conditions in the coeval global ocean (e.g., Poulton et al., 2004; Slack and Cannon, 2009); if these IFs instead reflect more restricted, basin-scale conditions, our understanding of the global ocean redox state might be incorrect. Paleogeographic reconstructions are not adequately detailed to answer this question; however, tidal signatures have been observed in IFs and interbedded sedimentary rocks of this age in Minnesota and the Hudson Bay region (Ojakangas, 1983; Chandler, 1984), which are consistent with at least episodically open-marine conditions during IF deposition. Two independent questions can be asked as a basis to address this issue. First, do sedimentary successions of similar age on the margins of other cratons provide evidence for high concentrations of iron in seawater? Second, do iron-oxide exhalites occur in association with coeval, deep-water (Cu-rich) VMS deposits?

The ~1.88 Ga Frere Iron Formation along the northern margin of the Yilgarn craton of Western Australia (Goode et al., 1983; Rasmussen et al., 2012) and IF of the Gibraltar Formation in the Kahochella Group along the southeastern

margin of the Slave craton in North America (Bowring et al., 1984; Hoffman et al., 2011; Roscoe et al., 1987) are granular and likely equivalent in age to the Animikie IFs. In addition, the presence of the ~1.88 Ga Rochford Formation along the eastern margin of the Wyoming craton, although poorly dated and not granular (Frei et al., 2008), supports synchronous deposition of IFs on several cratons. On the other hand, a ~20-m-thick magnetite–hematite oolitic iron formation in the middle member of the Watterson Formation (Hurwitz Group) on the Hearne craton of Canada (Miller and Reading, 1993) is most likely older than the 1.88 Ga IFs on the margins of the Superior craton. The age of this oolitic unit is not well constrained, but detrital zircon geochronology for several units within the Hurwitz Group, including the Watterson Formation, suggests that it is ~1.93 Ga (Davis et al., 2005). In contrast, the precisely dated (1882 ± 3.5 Ma) lower part of the Recluse Group in the Kilohigok basin on the Slave craton, northwestern Canada, lacks IF (Bowring and Grotzinger, 1992). Instead, organic matter-rich and sulfidic shales are present at this stratigraphic level (Bowring and Grotzinger, 1992). Iron speciation and sulfur isotope systematics of these shales might help constrain the local redox state. However, coeval euxinic and ferruginous conditions are expected when there is an anoxic deep ocean (e.g., Planavsky et al., 2011; Reinhard et al., 2009).

Deposition of IFs on the Superior craton was synchronous with a peak in tonnages of VMS deposits (**Figure 14**), some of which were generated in arcs adjacent to the craton. VMS deposits of this age are known in the hinterland to the south of the Animikie basin (Schulz and Cannon, 2007), in the Labrador Trough (Barrett et al., 1988), and in the Trans-Hudson orogen (Syme and Bailes, 1993). Recent geochronological studies of the host metavolcanic rocks to VMS deposits in the Pembine-Wausau terrane of northern Wisconsin indicate that these deposits formed at ~1875 Ma, contemporaneously with GIF of the Animikie basin (Schulz and Cannon, 2008). These data also suggest that the hydrothermal systems were the source of iron for the IFs, consistent with earlier models (e.g., Isley, 1995). However, laterally continuous iron-oxide exhalites are absent at or near these deep-water VMS deposits that formed presumably in open-marine conditions. This observation is unlikely to reflect preservational bias, because slightly younger 1.84, 1.79, and 1.78 Ga Cu-rich VMS deposits that similarly formed in arc settings contain abundant hematite and magnetite exhalites, jasper, and IF (Slack and Cannon, 2009; Slack et al., 2007). This analysis points toward an anoxic and ferruginous composition of deep waters in open-marine settings at ~1.93–1.88 Ga.

The Animikie basin of the Lake Superior region contains another stratigraphic level with regionally extensive IFs. This level is stratigraphically above the 1850 Ma Sudbury impact ejecta layer and is older than the ~1830 Ma regional metamorphic event related to the Penokean orogeny (Cannon et al., 2010). These IFs are mineralogically and texturally different from the ~1880 Ma IFs of the Animikie basin, and were likely deposited in deeper waters, below fair-weather and, probably, storm-wave base. They are present in the: (1) Marquette Iron Range, Michigan (~60-m-thick Bijiki Iron Formation Member of the Michigamme Slate containing siderite, chert, iron oxides and silicates; Cannon et al., 2010; Ojakangas, 1994; Ojakangas et al., 2001), (2) Iron River-Crystal Falls Iron Ranges (~15-m-thick chert–siderite slate of the Stambaugh Formation; James et al., 1968), (3) Gogebic Iron Range, Wisconsin (~47-m-thick IF of the Tyler Formation consisting of chert and siderite; Cannon et al., 2008; Schmidt, 1980), and (4) Mesabi Iron Range, Minnesota (~27-m-thick chert–siderite IF in the lower part of the Virginia Formation; Lucente and Morey, 1983). Deposition of these IFs might be genetically linked with submarine mafic volcanism in the Animikie basin based on spatial association with, for example, the Badwater Greenstone, but this relationship has not been documented in detail. The IFs commonly are interbedded with, or overlain by, black sulfidic shales, which likely record the development of euxinic conditions in the basin (cf. Poulton et al., 2004). Despite poor exposure, these iron deposits are easily traceable by magnetic anomalies. Their deposition indicates that anoxic and ferruginous seawater redox conditions were re-established in the Animikie basin after 1850 Ma, in association with mafic volcanism, although evidence for a shallow redoxcline in this case is absent and duration of these conditions was likely short and the extent of iron deposition probably was limited.

Thinly banded, silicate-facies IF of similar age, or slightly older, is present in the Pipe Formation of the Thompson nickel belt, Manitoba (Bleeker and Macek, 1996). However, GIFs are absent along the western and northern margins of the Superior craton, whereas they are developed continuously along the eastern and southern margins. Considering the

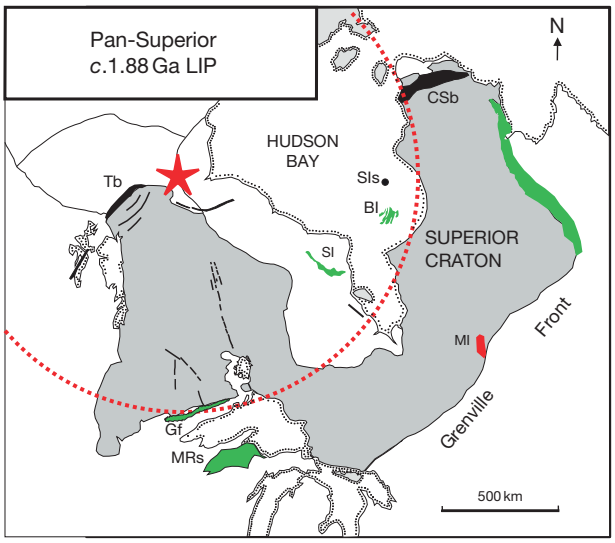

Figure 15 Distribution of iron formations and magmatic occurrences of the ~1880 Ma Circum-Superior event on the Superior craton. CSb, Cape Smith belt with ~1870 Ma volcanics of the Chukotat Formation; SIs, Sleeper Island sills; BI, Belcher Group; SI, Sutton Inlier with metasediments and sills; Tb, Thompson belt; Gf, Gunflint Iron Formation with volcanics; MRs, Marguette Range Supergroup with iron formation, volcanics, and sills; MI, Upper Albanel Group of the Mistassini basin with iron formation. Red star and circle locate inferred center and 1000 km radius of underlying mantle plume ~1880 Ma. Paleoproterozoic basins that contain 1.88 Ga iron formation and volcanics are shown in green, those that contain only iron formation are in red, and those that contain only volcanic units of this age as well as dikes and sills of this age in the interior of the craton are shown in black. Modified from Ernst RE and Bell K (2010) Large igneous provinces (LIPs) and carbonatites. *Mineralogy and Petrology* 98: 55–76.

occurrence of similar facies IFs in the Hudson Bay area and Sutton Inliers, it is plausible that a significant part of the Superior craton was submerged and sloped to the south during deposition of the Animikie IFs, due to uplift caused by the mantle plume then centered on the northwestern corner of the Superior craton (cf. Ernst and Bell, 2010). In this interpretation, IFs in the Sutton Inliers and the Hudson Bay area represent thin, shallow-water facies of the intracratonic basin extending to the southern and eastern margins of the Superior craton (**Figure 15**).

A key unresolved question is why the ~1.88 Ga magmatism led to extensive deposition of IFs on several continents given that the long time intervals preceding and following this event had minimal IF deposition despite being similarly affected by mantle plume activity. In terms of simple mass balance, it might be that the flux of hydrothermally derived reductants (e.g., Fe, H_2S, and H_2) at 1.88 Ga was capable of overwhelming the redox state of the ambient deep ocean. Therefore, the volume of magma and the rate at which it was added by mantle plumes to the oceanic realm at this time could be a critical factor. If so, the question can be rephrased: what processes were responsible for generating the unique strength of the ~1.88 Ga mantle plume event? We emphasize here that this event corresponds with the early stage in supercontinent assembly, a topic discussed in more detail below.

9.18.7.3.7 Proterozoic age gap in major IF deposition

It is generally assumed that after ~1.85 Ga, major sediment-hosted IFs were not deposited for approximately 1.1 Gy (Huston and Logan, 2004; Isley and Abbott, 1999; Klein, 2005; Slack and Cannon, 2009). This distinctive pattern in the secular trend for IFs has been explained by a change in the deep ocean redox state from anoxic to oxygenated (Holland, 1984) or sulfidic (Canfield, 1998) conditions. In contrast, it has been recently proposed that the deep ocean was anoxic but not sulfidic (Planavsky et al., 2011; Poulton et al., 2010), or suboxic (Slack et al., 2007, 2009). The earlier suggestion by Holland (1984) for oxygenated deep-ocean conditions after ~1.88 Ga has fallen out of favor, but (arguably) the model has not been ruled out. An alternative model, suggesting that deep-ocean conditions were predominantly sulfidic over ~1.1 Ga of the Middle Proterozoic history (e.g., Canfield, 1998; Poulton et al., 2004), also has lost favor recently because practically all evidence for this model can be satisfied with locally developed euxinic conditions on continental shelves and in intracratonic basins (e.g., Planavsky et al., 2011; Scott et al., 2008; Slack et al., 2007). The emerging consensus is that the redox state of the deep ocean was variable over the time interval of ~1.85–0.75 Ga, but distinctly more reducing than that characteristic of the Phanerozoic (Planavsky et al., 2011; Poulton et al., 2010; Slack et al., 2007). The terms 'ferruginous' and 'suboxic' are not ideal for defining the redox state of the deep ocean during this period since the first was widely used for the Archean and the second has been used in different ways for modern and ancient conditions (Canfield and Thamdrup, 2009). More importantly, higher hydrothermal fluxes of metals, including Fe and Mn, should be expected if the oceans were at a low oxidation state and had a higher content of dissolved organic carbon (cf., Rothman et al., 2003) to effectively ligate metals.

The record of this hydrothermal flux might be found in Fe and base metal contents of mid-Proterozoic shales and in their isotope signatures. Poulton et al. (2010) argued that euxinic shales deposited on continental margins (possibly in areas corresponding to modern oxygen-minimum zones) and in intracratonic basins could have been a major sink for the hydrothermal iron flux to the Middle Proterozoic oceans, and were thus responsible for the absence or scarcity of Middle Proterozoic IFs. At present, this suggestion has not yet been quantitatively evaluated, but it would require a higher total Fe content in average shale during this time interval. Data in Kump and Holland (1992) do show that the average Proterozoic shale has more Fe than the average Phanerozoic shale but less than the average Archean shale. Considering that giant IFs were also deposited during the Archean, this trend in iron content of average shale seems to suggest that other factors besides the presence of marginal euxinia controlled the abundance of IFs in the Middle Proterozoic. It has also been proposed that a rise in seawater sulfate level after ~1.88 Ga led to a decrease in the flux of the hydrothermal iron – shutting off the deposition of major IF (Kump and Seyfried, 2005). However, seawater sulfate levels decreased rather than increased in the Middle Proterozoic after the ~2.22–2.1 Ga Lomagundi carbon isotope excursion (Bekker and Holland, 2012), thus challenging this model.

Although large sedimentary IFs during the Middle Proterozoic (1.85–0.75 Ga) are indeed absent, several small IFs and iron-rich lithologies in sedimentary rock-dominated successions are known outside of the Animikie basin (see **Appendix 1**). Magnetite and siderite IFs of the Aok Formation in the Neoproterozoic Shaler Supergroup in the Duke of York and Brock Inliers of Victoria Island, northern Canada, were deposited at ~840 Ma before the onset of the oldest Neoproterozoic glacial events (Rainbird et al., 1994; Young, 1981). Older examples within this age range include the ~1.70 Ga Freedom Formation of the Lower Baraboo Series, Wisconsin, which contains in the lower part banded ferruginous chert interlayered with sideritic and kaolinitic slate 60–160 m thick (Leith, 1935; Van Wyck and Norman, 2004; Weidman, 1904) and the likely correlative magnetite–chert IF of the Tomiko terrane in Ontario (Easton, 2005). Additionally, the Chuanlinggou IF on the North China craton, a classic GIF deposit, also appears to be latest Paleoproterozoic in age (~1.7 Ga; Dai et al., 2004; Wan et al., 2003).

Noteworthy examples of small iron deposits that formed during this time gap in shallow-water settings occur in northern Australia in the Sherwin Formation and the Munyi Member of the Corcoran Formation, both within the ~1.49 Ga Maiwok Subgroup of the Roper basin, Northern Territory (Abbott and Sweet, 2000; Canavan, 1965) and the correlative Constance Range ironstone of the Train Range Member of the Mullera Formation in the South Nicholson basin, Queensland (Harms, 1965; Jackson et al., 1999). These iron-rich units consist of oolitic, pisolitic, and peloidal, trough cross-stratified ironstone and ferruginous siliciclastic rocks as much as 23 m thick (Abbott and Sweet, 2000; Harms, 1965). Unweathered samples show grapestones and ooids as much as 8 mm in diameter (**Figure 5(b)**) composed of hematite and magnetite with nuclei of quartz or oolitic intraclasts; chamosite and greenalite are present locally in a secondary siderite matrix (Abbott and Sweet, 2000). Beds within the ironstone units are bounded by

erosional surfaces with sharp compositional contrast between ooidal ironstones and overlying quartz-rich sandstones. The presence of intraclasts and peloids of iron-rich sediment in quartz-rich sandstone and clasts of ironstone within intraformational conglomerate (**Figure 5(b)**) strongly suggests that the sediments were originally iron-rich. Many ironstone intraclasts have a pisolitic coating, testifying to the primary deposition of iron oxyhydroxides in the sedimentary environment. The ooids and peloids likely formed at the redox boundary between shallow, oxidized and deep, anoxic waters. Notably, the Sherwin Formation and Munyi Member of the Corcoran Formation enclose black shales of the Velkerri Formation that were used previously to infer a long-term sulfidic state of the coeval deep ocean, based on sulfur isotope composition, iron speciation, and molybdenum isotope composition (Arnold et al., 2004; Shen et al., 2003). Leaving aside arguments whether available geochemical and geological evidence for the ocean redox state during the Mesoproterozoic is consistent with a pervasively euxinic deep ocean (e.g., Meyer and Kump, 2008; Poulton et al., 2010; Slack et al., 2007, 2009), this intricate relationship between ironstones and euxinic black shales strongly suggests that ferruginous and euxinic conditions alternated in the Mesoproterozoic intracratonic Roper and South Nicholson basins on geologically short timescales.

Oolitic ironstones are also developed in the ~1.38 Ga Xiamaling Formation of the Xiahuayuan region in Hebei Province of North China (Su et al., 2010) and in the poorly dated, late Neoproterozoic (but preglacial) Nizhne–Angara Formation of the Angara-Pit area, Siberia, Russia. IFs deposited at ~1490, 1368, and 767 Ma (see **Appendix 1**) broadly – within analytical error – correspond with ages for emplacement of LIPs at ~1460, 1380, and either 780 or 755 Ma (Ernst et al., 2008). Poor age constraints presently available for other IFs deposited during this time interval make it difficult to test their possible relationship with mantle plume events.

In addition to shallow-water, sediment-hosted IFs, numerous shallow-water exhalites are associated with sedimentary exhalative (SEDEX) and VMS deposits that formed during the late Paleoproterozoic and Mesoproterozoic. These deposits contain jasper, hematite, and magnetite layers having positive Eu and negative Ce anomalies (e.g., Hatton and Davidson, 2004; Lottermoser, 1989; Lottermoser and Ashley, 1996; Strydom et al., 1987). Although these VMS and exhalite deposits commonly formed within isolated to semi-isolated basins and thus should not be used to infer the redox state of the coeval deep ocean, they do provide strong evidence that shallow-water settings were oxygenated at that time. In contrast, mineralogical and geochemical data for deep-water, open-marine exhalites provide strong evidence for a low-oxygen (suboxic) state of the deep ocean during their deposition (Slack et al., 2007, 2009). Interestingly and surprisingly, large Mn deposits are absent during this time period with the single exception of the ~1.44 Ga Wafangzi Mn deposit in NE China (Maynard, 2010; Su et al., 2010). This trend, if real, suggests that a strong oxic sink for Mn might not exist during this time period in the oceans.

Even though IFs of this age range are of minor economic importance, their existence suggests that from ~1.85 to 0.75 Ga hydrothermal iron from deep-water oceanic settings was episodically delivered, although in rare cases and in generally small amounts, to shallow-water environments for the deposition of IF, ironstone, and iron-rich shale. In addition, within isolated to semi-isolated basins having strong volcanic and hydrothermal activity, the flux of reductants was strong enough to locally overwhelm the water-column redox state, thus leading to iron transport on a local scale. Open-marine, deep-water environments were in general sufficiently oxidized for iron to precipitate from hydrothermal plumes as iron oxyhydroxide. Combined, this record of the iron cycle is very similar to that in the Phanerozoic. Although it does not provide rigorous quantitative constraints on the deep-ocean redox state, the record challenges models for persistently oxic, fully anoxic, or sulfidic conditions within open-marine, deep-water settings. In summary, a low and yet variable redox state of the deep ocean is most consistent with this record.

9.18.7.3.8 Neoproterozoic manganese deposits and IFs

Manganese deposits and IFs of Neoproterozoic age are extensively but discontinuously developed in association with glacial deposits. In addition, iron-rich shales are relatively common in contemporaneous, glacially influenced successions (e.g., Young, 2002). The latter relationship was reemphasized by Canfield et al. (2008) to infer a return during the late Neoproterozoic to Archean-style anoxic, ferruginous ocean conditions. Significant iron and manganese accumulations in association with glacial deposits are present in a number of Neoproterozoic successions worldwide, although for other Neoproterozoic IFs a clear stratigraphic or temporal relationship with ice ages has not been established (e.g., Cabral et al., 2011; see also **Appendix 1**).

Presently available geochronological constraints and stratigraphic correlations imply that IFs are at least temporally related to the Sturtian (~715 Ma) and Marinoan (~635 Ma) glaciations, although some uncertainty exists regarding a number of Neoproterozoic glacial events, their ages and duration, and chemostratigraphically based correlations (e.g., Kendall et al., 2009). The Rapitan IF and Franklin igneous event on Victoria Island in Canada are both ~715 Ma (Heaman et al., 1992; Macdonald et al., 2010), supporting a genetic relationship among volcanism, mantle processes, and deposition of IF at least on the basin scale. Neoproterozoic IFs are typically enriched in Mn and P and have high Co, Ni, and Cu contents (Halverson et al., 2011; Klein and Beukes, 1993; Planavsky et al., 2010a,b; see also **Chapter 9.11**). Highly positive sulfur isotope values in shales and manganese formations overlying Neoproterozoic glacial diamictites have been related to Rayleigh distillation in low-sulfate oceans, which were highly susceptible to the development of anoxic ferruginous conditions and hydrothermal delivery of iron and manganese into shallow basins during mantle plume breakout events (Liu et al., 2006). Importantly, IFs were deposited during deglaciation as indicated by the presence of dropstones in IFs and interlayering with tillites. Poor age constraints for other Neoproterozoic IFs do not warrant correlation with Neoproterozoic mantle plume events, although several such events occurred during the late Neoproterozoic (e.g., Ernst and Buchan, 2001). However, almost all Neoproterozoic IFs are spatially and temporally linked with submarine mafic and felsic volcanic units. Some basins hosting IFs of this age also contain coeval VMS deposits (e.g., Buhn et al., 1992; Cabral et al., 2011), suggesting a proximal hydrothermal source of metals. Most of these IFs were

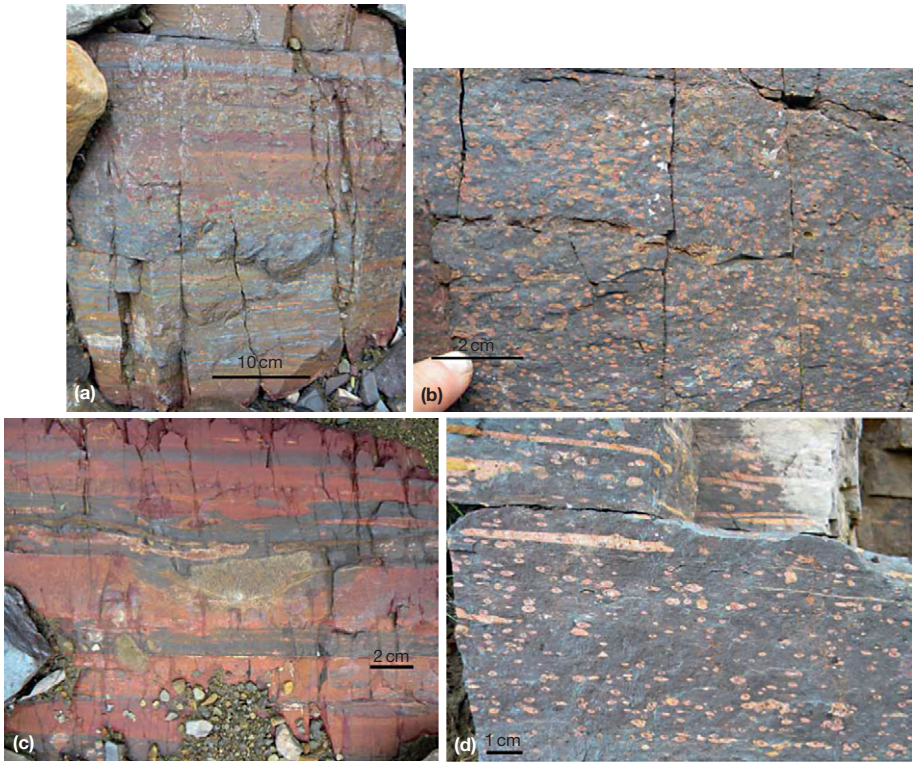

Figure 16 Rapitan Iron Formation at Cranswick River, Mackenzie Mountains, Northwestern Territories, Canada. (a) Nodular and banded jasper interlayered with hematite bands and overprinted by anastomosing hematite. (b) Jasper nodules and lenses in massive hematite. (c) Banded jasper–hematite iron formation with dropstone overprinted by anastomosing hematite. (d) Jasper nodules and lenses in massive hematite. Photographs are courtesy of E. Turner.

deposited either in closed rift basins or on reactivated continental margins (e.g., Trompette et al., 1998).

Neoproterozoic IFs generally comprise laminated and nodular hematite, massive magnetite, hematitic mudstone, and jasper (**Figure 16**). Lenticular and nodular chert and jasper are less common, but are present within laminated jasper beds (Yeo, 1981). Banded cherts, similar to those in Archean and Paleoproterozoic IFs, are absent. Furthermore, the thickness of Neoproterozoic IFs is highly variable over relatively short distances. GIFs and intraformational conglomerates containing hematite pebbles developed locally at the top of the Rapitan Iron Formation and in the Jacadigo Group, Brazil, but coated grains are uncommon (Klein and Beukes, 1993a; Klein and Ladeira, 2004). REE patterns for Neoproterozoic IFs have either no or slightly positive Eu anomalies, and either no or slightly negative Ce anomalies (Derry and Jacobsen, 1990; Fryer, 1977; Halverson et al., 2011; Klein and Beukes, 1993a; Klein and Ladeira, 2004; Liu et al., 2006; Lottermoser and Ashley, 2000), likely indicating a high degree of dilution of locally derived, hydrothermal fluid by mildly oxidized seawater. Models that are generally accepted for Phanerozoic manganese deposits (see **Chapter 9.11**) are probably also applicable to the origin of Neoproterozoic IFs. These models infer anoxic conditions with enhanced submarine volcanism in the deeper parts of isolated to semi-isolated basins and manganese precipitation occurring at the redox boundary on the shallow margins of the basins. Another factor, in addition to mantle plume events and tectonics, which could have contributed to deposition of IF, is dramatic sea-level fall during ice ages. Sea-level fall would decrease the overlying hydrostatic pressure and shift equilibrium in the seafloor hydrothermal systems toward higher Fe/H_2S ratios, thus promoting larger Fe fluxes into the oceans (Kump and Seyfried, 2005). In sum, although the occurrence of Neoproterozoic IFs supports long durations of glaciations and the existence of redox-stratified basins, they do not require extreme snowball Earth conditions in order to form.

9.18.7.3.9 Phanerozoic ironstones, anoxic events, and VMS deposits

The most prominent peaks in deposition of Phanerozoic ironstones occur in the Ordovician–Devonian and Jurassic–Paleogene (**Figure 17**). The ironstones generally are only several meters thick, rarely reach 25 m in thickness, and extend for over 1000 km along ancient continental margins in Fennoscandia and the Himalayas where they demarcate areas of past upwelling (e.g., Garzanti, 1993; Sturesson, 2003). The ironstones are composed largely of iron oxide ooids (goethite and limonite), with smaller amounts of Fe-silicates (chamosite, berthierite, and glauconite) and Fe-carbonates (siderite), typically as cements. In contrast to most Proterozoic IFs and early Paleozoic hydrothermal deposits, ironstones have very little chert, but commonly are

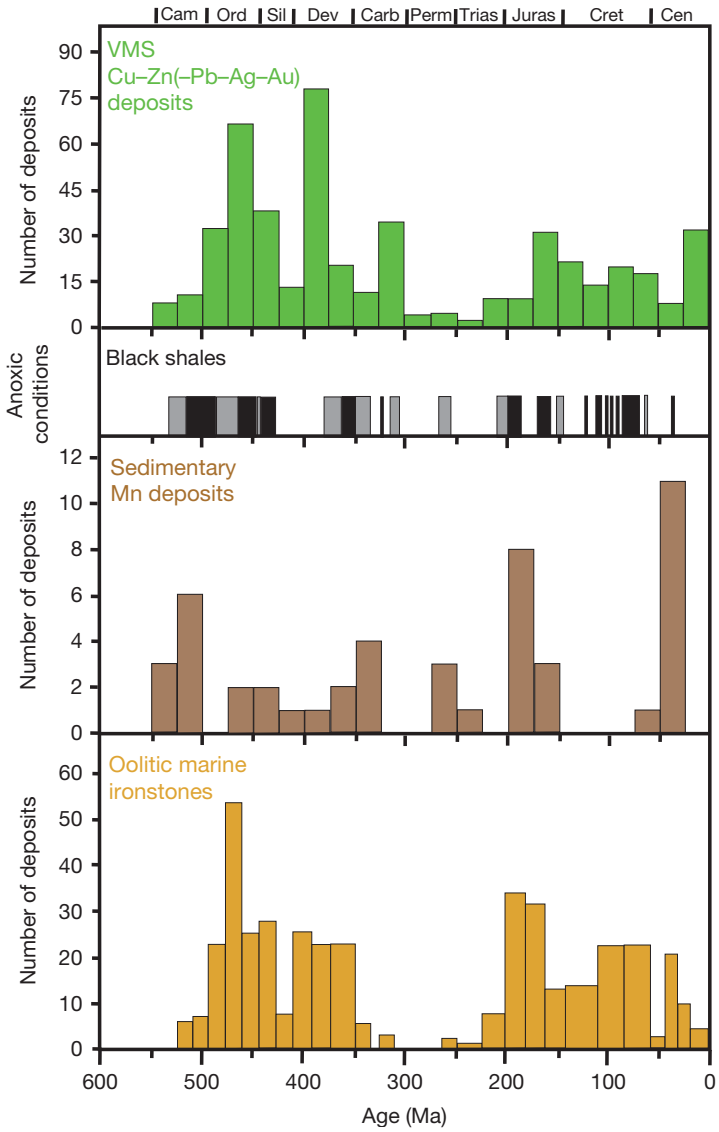

Figure 17 Secular distribution of Phanerozoic oolitic marine ironstones (from Petranek and Van Houten, 1997) compared to those of marine anoxic conditions and VMS deposits (from Bekker et al., 2010) and a number of sedimentary Mn deposits (from Maynard, 2010). Data for VMS deposits and for sedimentary Mn deposits are compiled for time intervals of 25 Ma. Marine anoxic conditions are shown for inferred global periods of anoxia by black bars and more limited periods of anoxia by gray bars; the latter reflecting less-widespread, regional black shale facies. Data for anoxic conditions during Cambrian through Jurassic periods are from Arthur and Sageman (1994), for Cretaceous from Leckie et al. (2002), and for Cenozoic from Jacobs and Lindberg (1998).

enriched in manganese and phosphorus. However, in some cases, ironstones are associated with chert deposits (Borchert, 1965; Franceschelli et al., 2000; Glenn and Arthur, 1990). Many ironstone deposits contain stilpnomelane, volcanic glass shards, and other tuffaceous material implying contemporaneous volcanism. Typically, bulk analyses of oolitic ironstone, when normalized to shale composites or local shale, have minor negative to positive Ce anomalies, are enriched in light REE with respect to heavy REE, and lack significant Eu anomalies (e.g., Bhattacharyya and Crerar, 1993; Sturesson, 2003).

Ironstones are common to time intervals characterized by negative seawater Sr isotope excursions (Sturesson, 2003), peaks in the formation of VMS deposits (cf. Franklin et al., 2005; Peter, 2003), large volcanic- and sediment-hosted Mn deposits (Maynard, 2010), extensive ocean anoxia, greenhouse conditions, volcanic events, emplacement of LIPs, and quiescence in Earth's magnetic field (e.g., Garzanti, 1993; Sturesson, 2003; Van Houten and Arthur, 1989). Ironstones are typically thought to have been deposited during periods with low sedimentation rates at the beginning of a sea-level rise, as suggested by their position in Transgressive System Tracts (**Figure 6(b)**; Burkhalter, 1995; Maynard and Van Houten, 1992; Taylor et al., 2002) and commonly are topped by hardgrounds, thought to represent the maximum

flooding surface. They are also common to upwelling areas where phosphates were deposited. Collectively, these diverse associations have been linked with mantle superplume events (e.g., Garzanti, 1993). Furthermore, ironstones are related to time periods when seawater was saturated with calcite, rather than with aragonite or high-Mg calcite, and when the so-called 'calcite seas' developed, which correspond with times of rapid seafloor spreading and high rates of Mg removal from seawater (Maynard, 1986; Stanley and Hardie, 1998). The formation of berthierite and siderite in shallow, well-agitated marine environments requires weakly reducing but non-sulfidic conditions in the water column and sediment pore waters. However, berthierite and hematite ooids co-occur in ironstones, even forming discrete laminae within individual ooids, thus indicating fluctuating redox conditions during either deposition or early diagenesis, but prior to compaction. In addition, glauconite, an abundant sedimentary aluminosilicate mineral with Fe(III) substituting for Al(III) and lower Eh requirements for precipitation than berthierite, is virtually absent in oolitic ironstones (Maynard, 1986) and does not co-exist with chamosite but occurs in deeper-water facies equivalents (e.g., green shales; Hunter, 1970). Where sedimentary facies analysis has been performed, the following sequence of facies and mineralogical changes from shallow, oxidized waters to deep, reduced waters is evident: hematitic oolitic ironstone; chamositic oolitic ironstone; glauconitic, illitic, and chloritic green shales; and, finally, organic matter-rich, sulfidic shales.

The genesis of Phanerozoic ironstones and the iron source for these deposits remains controversial. Extreme degrees of weathering on peneplained continents linked with high sea-level stands during dispersion of supercontinents are commonly inferred (e.g., Van Houten and Arthur, 1989). However, neither sea-level highstand nor supercontinent dispersal seems to be a prerequisite for the deposition of Phanerozoic ironstones (Van Houten, 1985). Furthermore, because iron is highly insoluble in the presence of even traces of dissolved oxygen, this model implies that iron was delivered from the continents in solution with slightly acidic river waters or groundwaters, in colloidal form, or complexed with organic ligands, and the iron was precipitated in deltas or along shorelines on mixing with seawater having higher pH and ionic strength (Castano and Garrels, 1950; Huber and Garrels, 1953). However, considering the fast rate of iron precipitation on mixing with seawater, a corollary of this model is that ironstone deposition should be centered on a point source as commonly found in subterranean estuaries showing a well-defined 'iron curtain' near the sediment–seawater interface (Charette and Sholkovitz, 2002; Rouxel et al., 2008a,b), rather than along the full extent of the shoreline with little variation in thickness. An alternative model relates ironstones to submarine weathering of volcanic ash (e.g., Sturesson, 2003), even though many ironstone-bearing units lack volcanic ash beds. Reworking of pedogenic ferruginous pisoids into the marine environment has also been suggested, but it does not explain their restricted stratigraphic position, global secular trend, low Al content in goethitic and hematitic oolites (e.g., Maynard, 1986), or $\varepsilon_{Nd}(t)$ values above those of proximal crustal sources (Sturesson et al., 1999), indicating some contribution to REE budget from juvenile sources.

Aller et al. (1986) developed a model of an early diagenetic iron source from anoxic sediments into the water column as originally advocated by Borchert (1965). Aller et al. (1986) proposed a model for ironstone deposition based on modern Amazon deltaic sediments in which high amounts of organic matter loading, anoxia at the sediment–water interface, and intense physical reworking promote the re-oxidation of pore-water iron. These processes in the Amazon River allow for significant burial rates of reactive iron phases, such as ferric and mixed-valence authigenic iron minerals, despite the presence of abundant dissolved sulfate (Aller et al., 1986). The model is consistent with the depositional setting of ironstones, although it does not explain their episodic secular distribution or much more pronounced iron enrichments relative to modern Amazonian deltaic sediments. Nonsteady diagenetic reworking of preexisting metal-enriched (anoxic) shales is a potential mechanism for ironstone deposition that has not been explored in any detail, but would provide an explanation for the close association of ironstones with periods of marine anoxia.

Cotter and Link (1993) were among the first workers to suggest that iron was supplied from deep-water, anoxic settings. Broad correspondence of the secular distribution of Phanerozoic ironstones with that of VMS and volcanic- and sediment-hosted Mn deposits (**Figure 17**) offers additional insight into ironstone deposition and suggests that the iron originated in coeval seafloor-hydrothermal systems. Along these lines, we suggest that deposition of major Phanerozoic ironstones is mechanistically linked to times of global ocean anoxia during mantle superplume events. Enhanced volcanic and hydrothermal activity led to extensive formation of VMS deposits, higher sea level, and contributed to short-term, ocean-wide anoxia. Under anoxic conditions, hydrothermal and diagenetic iron could have been transported by upwelling currents, together with phosphorus and manganese, onto the shelf where the iron was oxidized biologically or abiologically at a shallow-water dynamic redoxcline. Cretaceous anoxic events also have been genetically linked to extensive submarine magmatism based on geochemical evidence (Turgeon and Creaser, 2008) and geological arguments (Kerr, 1998; Sinton and Duncan, 1997). The model implies that even if sulfidic conditions persisted throughout the oceans, more hydrothermal iron than in the modern ocean was transported from the deep ocean, as either ligand bound or nanoparticulate phases. However, even under widespread anoxic conditions, sulfide formation in the deep oceans could have been limited by organic matter availability. Anoxic conditions with low sulfide levels could have allowed for transport of dissolved iron onto the continental shelves. This model is supported by iron isotope data that point toward hydrothermal iron delivery onto the portions of the upper slope in the Atlantic Ocean during Cretaceous OAE 2A (Owens et al., 2012).

9.18.8 Controls on IF Deposition

The above discussion allows us to discriminate the major controls on IF deposition. Although in some cases it is difficult to resolve whether an IF was deposited proximally or distally to submarine volcanism, IFs hosted in volcanic-dominated successions are in general more common during Earth's early

history (>2.5 Ga) and probably reflect a higher mantle heat flux. As time progressed, relatively small sediment-hosted IFs appeared (or were preserved) in the geologic record starting around 3.2 Ga, but did not reach significant thickness and extent until 2.6 Ga. An intriguing cause-and-effect relationship underlies fundamental environmental changes between 2.5 and 2.3 Ga including emplacement of the first true LIP, a peak in the deposition of distal, sediment-hosted IFs, atmospheric oxidation, and Paleoproterozoic glaciations. The response of the biosphere to the superplume event may have led to changes in surface environments. Following atmospheric oxidation at ~2.4 Ga, iron and manganese deposition was localized in basins characterized by restricted circulation and intense submarine volcanism.

The later peak in IF deposition at ~1.88 Ga was also closely linked in time with a significant mantle plume breakout event that affected the Superior craton, among others. We infer that at least on the scale of basins that surrounded the Superior and Yilgarn cratons, the redox state and sulfate content of seawater were sufficiently low that the hydrothermal flux of iron and other reductants (e.g., Mn, H_2S, and H_2) overwhelmed the oxidizing potential of seawater. It is likely that very low marine sulfate concentrations at this time, similar to those during the Archean, would have increased the iron/sulfide ratio in emanating hydrothermal fluids, which also would have promoted iron-replete conditions in the ocean (Kump and Seyfried, 2005) and deposition of major IFs at the dynamic redoxcline in shallow waters (Planavsky et al., 2009). High atmospheric pCO_2 and, consequently, surface temperatures during the mantle plume breakout event could have led to stagnant circulation and the decreased solubility of dissolved oxygen in surface waters, resulting in anoxic conditions within these basins, if not in the global ocean. In addition, mantle plume breakout events generate higher sea level (Condie et al., 2001), leading again to sluggish ocean circulation promoting anoxia on a basin to global scale.

Our analysis agrees with previous studies (e.g., Isley and Abbott, 1999) that the deposition of giant IFs corresponded closely in time with major mantle plume events. Therefore, rather than linking the termination of deposition of large, economic IFs at ~1.85 Ga and the expansion of sulfidic conditions to changes in surface conditions (e.g., Poulton et al., 2004), we propose that these secular changes, at least in the Animikie basin, were a consequence of several contemporaneous processes but foremost the waning of a mantle plume event and a decrease in the hydrothermal iron flux.

Recurrent associations in the Precambrian between superplume events and IF deposition have been known for some time (Barley et al., 2005; Condie et al., 2001; Isley, 1995). Recently, their secular relationship in the Precambrian and Phanerozoic with VMS deposits was also established (Bekker et al., 2010). The link is obvious: hydrothermal systems were more extensive, vigorous, reducing, and metal-rich during LIP emplacement. As a result, larger volumes of metals were leached from submarine volcanic rocks and vented to the ocean floor, where massive sulfide deposits formed; consequently, ocean redox state was lowered by an enhanced flux of hydrothermally derived reductants and Fe with Mn were delivered by plumes to shallow-water settings where they precipitated, forming iron- and manganese-rich sediments. Peaks in the tonnage of VMS deposits are typically associated with time intervals when supercontinents were assembled, because VMS mineralization hosted by bimodal volcanic rocks in back-arc basins has a high preservation potential in the rock record. Considering that mantle plumes are relatively common throughout Earth's history, it remains uncertain why superplumes and associated peaks in diverse mineral deposits are genetically linked with the early stages in the supercontinent assembly. The association is, however, striking and repetitive at ~2.74–2.69, 2.5–2.45, 2.05–2.06, 1.88, 1.1, and 0.5 Ga when the Kenorland, Vaalbara, Nuna, Zimvaalbara-São Francisco, Rodinia, and Gondwana supercontinents were assembled, respectively (cf. Huston et al., 2010). It is proposed herein that external ocean closure during the early stage of supercontinent amalgamation dramatically changed the heat budget of the mantle, leading to mantle overturn, superplume events, and eventually the development of a new mantle convection pattern (**Figure 18**). As a result, superplume-initiated rifting at the time of external ocean contraction allows plate tectonics to persist without interruption in the aftermath of the supercontinent assembly.

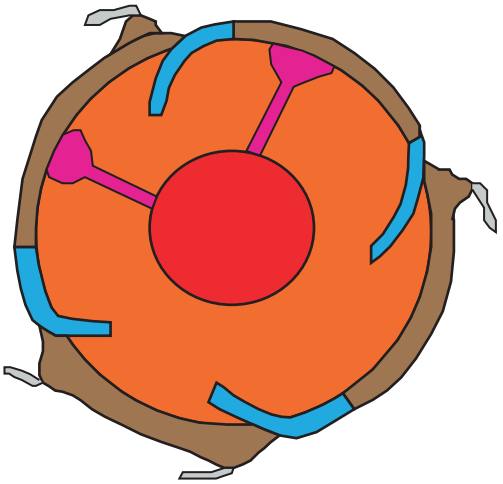

Figure 18 Hypothetical relationship during the early stage of supercontinent assembly between supercontinent amalgamation leading to external ocean closure and changes in the heat budget of the mantle, leading to mantle overturn, superplume events, and, eventually, the development of a new mantle convection pattern. See text for discussion.

Whereas Fe–Si compounds, the likely protolith for pre-GOE IFs, formed predominantly in the deeper parts of basins and were widely redistributed by density currents, post-GOE IFs record the upwelling and oxidation of ferrous iron, precipitation on the shelf and, later, transport by storm events and wave currents back into the basin. GIF first appeared at ~2.6 Ga or earlier, but their predominant mineralogy was not iron oxides until shortly after the GOE.

Whereas VMS deposits show a peak in global tonnage at ~1.88 Ga, coeval with the peak in deposition of GIF, VMS deposits are puzzlingly absent during the 2.50–2.45 Ga mantle plume event when large tonnages of IF accumulated (**Figure 14**). Potentially, long-term global tectonic processes played a role. The hydrothermal flux of iron likely was derived predominantly from mid-ocean ridges at that time and corresponding

VMS deposits that formed in this setting were likely recycled to the mantle. Differences between IFs deposited before and after the GOE, in terms of original textures and depositional settings, imply potentially different mechanisms for iron precipitation. Similarly, assembly of the supercontinent Rodinia at ~1.2–1.1 Ga, corresponding with a small peak in VMS tonnage and a massive mantle plume event that affected North America, southern Africa, and western and central Australia (Ernst et al., 2008), is not reflected in the record of IFs. Open-marine, sedimentary successions of this age are rare, which could at least partially explain the lack of IFs of this age in the rock record. As stressed above, the development of a more sulfate-rich ocean with respect to that during the Archean and early Paleoproterozoic would have lowered iron/sulfide ratios in hydrothermal fluids (Kump and Seyfried, 2005), decreasing the potential for deposition of massive iron deposits.

Reasons for the 1.1 Gy gap in the deposition of large IFs in the Proterozoic remain uncertain. Although we note several exceptions to this IF hiatus, these are small units that predominantly occur within restricted basins. If the temporary cessation of plate tectonics (cf., Silver and Behn, 2008) was responsible for the gap, why did major mantle plume events and, more importantly, VMS deposits formed during this time period (**Figure 14**)? Mantle plume events do not necessarily require plate tectonic processes, but VMS mineralization does need a submarine heat source in an oceanic environment, or at least marine basins that developed on rifted continental or oceanic crust (e.g., Franklin et al., 2005; Huston et al., 2010).

The secular distribution of IFs clearly deserves more attention. Although precise geochronology has been very successful in dating Precambrian successions, including host strata to IFs and VMS ores, some major economic iron deposits are still poorly dated; knowing their ages might critically influence our understanding of past oceanic and atmospheric redox states, as well as large-scale evolution of the Earth system. Among these poorly dated deposits (**Appendix 1**) critically in need of high-precision geochronology, are Paleoproterozoic examples including Krivoy Rog in Ukraine, the KMA in Russia, and the Cauê Iron Formation in Brazil; a number of Mesoproterozoic and Neoproterozoic IFs in Russia, China, and Australia; and Archean IFs in India.

Neoproterozoic IFs are interbedded with glacial deposits, but it is unlikely that snowball Earth conditions alone led to their deposition. Long-term ice cover likely played an important role in lowering the redox state of deep seawater and decreasing marine sulfate concentrations, by inhibiting or slowing down atmosphere–ocean exchange, continental pyrite oxidation, and riverine transport of sulfate to the oceans. However, the geological setting of the giant Rapitan Iron Formation, as well as other Neoproterozoic IFs (**Appendix 1**), provides a strong case for temporal and genetic connection to submarine volcanism. Therefore, at least three factors were likely critically important in the genesis of Neoproterozoic IFs: (1) seawater redox state, (2) an enhanced hydrothermal flux of iron during mantle plume breakout events, and (3) basin configuration including at least partial physical separation from the global ocean.

Close relationships among IFs, VMS deposits, seawater anoxia, and mantle plume events during the Precambrian provide a key framework for interpreting the origin of Phanerozoic ironstones. In contrast to many of the previous studies of ironstones, we emphasize similarity in the secular trends of ironstones, VMS, and sediment-hosted Mn deposits, organic matter-rich shales, and intervals of enhanced submarine volcanism during mantle plume breakout events in the Phanerozoic (**Figure 17**). We propose that some Phanerozoic ironstones formed during anoxic events when hydrothermal iron was delivered to shallow shelf settings either in isolated basins or on open continental margins.

The biosphere also played an important role in the genesis of IFs. Not only was biotic activity involved in direct or indirect precipitation of iron, but it also influenced the seawater redox state and composition. For example, emergence and evolution of the biological silica sink during the Precambrian and Phanerozoic influenced scavenging efficiency of phosphorus and metals onto ferric oxyhydroxides. However, even precipitation and oxidation mechanisms for iron-rich compounds that were the precursor sediments of Archean IFs are not unequivocally established. The problem remains that it is neither obvious what the texture and mineralogical composition of those sediments were, nor where and how the original sediments were deposited prior to their resedimentation into the basin realm. Certainly, the widespread presence of graded beds within BIF supports a model in which some of the original sediments were granular, as it is seemingly impossible to produce graded beds from amorphous iron-rich clays, iron-rich gels, or chemically deposited varves – the traditionally inferred precursor sediments to BIF. Whereas recognition that classic BIF of the Dales Gorge Member, in the Hamersley Province of Western Australia, are density-current deposits is significant, that recognition has made interpretation of the precursor sediments even more difficult, because the original depositional site is unknown. The same problem exists for GIFs, because they are essentially clastic sedimentary rocks.

More broadly, our model for IF genesis provides a new perspective on the secular evolution of the ocean redox state. We suggest that submarine volcanism was episodically responsible for generating extensive ocean- and basin-scale anoxia by the hydrothermal venting of significant fluxes of reductants such as H_2, H_2S, Fe(II), and Mn(II). This perspective applies to both Precambrian and Phanerozoic environments, and provides a framework for better understanding ocean evolution and the origin of sedimentary mineral deposits.

9.18.8.1 Influence of Hydrothermal Processes on Ocean Composition and Organic Productivity

Late Archean and Paleoproterozoic IFs are commonly interbedded with or adjacent to organic matter-rich, sulfidic shales. Similar shale facies appear to be underrepresented in the Archean record, beyond stratigraphic intervals that were deposited during mantle plume breakout events (Condie et al., 2001). This association to date has not been explained satisfactorily. During the Phanerozoic, the link between black shales and mantle plume

events commonly has been explained by sea-level rise and a higher flux of reductants into the ocean. The reductant flux is tied to anoxia, which favors organic matter preservation. This explanation does not apply, however, to the Archean oceans that were persistently anoxic (e.g., Planavsky et al., 2010a,b).

An important perspective is provided by considering the carbon isotope mass balance relevant to Archean surface anoxic conditions (e.g., Bekker and Holland, 2012). In the modern world, when the sedimentary cover is recycled to the oceans, organic carbon is oxidized and inorganic carbon is dissolved, making both available for biological processing. However, under anoxic surface conditions in the Archean, organic carbon was likely redeposited and hence was not biologically recycled. Including this aspect into the carbon isotope mass balance (cf. Bekker and Holland, 2012) requires that burial of 'new' organic carbon was less than 5% of the modern burial rate of organic carbon. As a result, the amount of oxygen released by the biological carbon cycle was also very low. We infer that restricted availability of critical nutrients, such as Mo, could have limited biological productivity and consequently organic carbon burial to these low levels.

In order to explain the origin of organic matter-rich shales associated with IFs, we infer high primary productivity that was driven by high nutrient fluxes, sourced from either the deep ocean or the continents. In nearly all modern aquatic systems, primary production of organic matter is limited by phosphorus or bioavailable nitrogen (e.g., Redfield, 1958), but trace metals can be also colimiting or even limiting. Phosphorus was asserted to be the ultimate limiting nutrient in the Archean oceans, given a high flux of iron oxides that removed phosphate (Bjerrum and Canfield, 2002). However, during the Archean and Paleoproterozoic, especially during peak times of IF deposition, high dissolved silica concentrations could have prevented iron oxyhydroxides from being a major dissolved phosphate sink (Konhauser et al., 2007b). Additionally, high levels of bicarbonate during the Precambrian (cf. Grotzinger, 1990) would have inhibited the precipitation of carbonate fluorapatite (CFA) by greatly increasing its solubility. The possibility of inhibited CFA formation is particularly important; in the modern oceans, this flux accounts for the vast majority (60–80%) of phosphorus burial (e.g., Ruttenberg and Berner, 1993). Furthermore, low burial rates of 'new' organic matter and high efficiency of its remineralization in an anoxic ocean lacking mechanisms for adequate export of organic carbon to sediments likely resulted in a low burial flux of phosphorus with organic carbon. Combined, these factors point toward a dramatically different Archean than the modern phosphorus cycle and relatively higher, rather than lower, dissolved phosphorus concentrations in Archean seawater with respect to modern seawater (Planavsky et al., 2010a,b).

If phosphorus content was not the controlling factor for Archean primary productivity, could nitrogen be the culprit? In the Archean anoxic ocean, dinitrogen was seemingly fixed by diazotrophic cyanobacteria and ammonium assimilation was also likely common (Garvin et al., 2009; Glass et al., 2009; Godfrey and Falkowski, 2009). Both nitrogen fixation and ammonium assimilation are operated by enzymes, which are dependent on bioessential trace metals such as Fe, V, and Mo, as metal cofactors (Glass et al., 2009). Both the V and Mo dissolved loads were generally low or negligible in early oceans (Lalonde et al., 2011; Scott et al., 2008), because under an essentially anoxic atmosphere these metals are insoluble. Thus, Mo limitation was likely in the Archean oceans due to anoxic redox conditions on land, just as iron is locally limiting in the modern oceans because of a predominance of the oxic water column. Iron concentrations, in contrast, were high and iron was likely utilized by diazotrophs on early Earth for nitrogen fixation and ammonium assimilation (Glass et al., 2009). Iron availability enhances nitrogen fixation and photosynthesis in modern environments (e.g., Berman-Frank et al., 2001, 2007); however, Fe–Mo nitrogenase is 100 times as efficient as Fe–Fe nitrogenase in dinitrogen fixation (Zerkle et al., 2006). Therefore, nitrogen limitation (via trace metal colimitation) of primary productivity was much more important than phosphorus limitation in the early oceans. It is possible that nitrogen stress was partially alleviated during mantle plume breakout events when IFs were deposited, since bioessential trace metals (e.g., Mo and V) can be sourced from hydrothermal fluids (e.g., Kuhn et al., 2003; also see **Chapter 8.7**). It is difficult to quantitatively estimate an increased level of organic productivity due to enhanced hydrothermal metal delivery to the Archean oceans during mantle plume events, considering the absence of positive carbon isotope excursions in the Archean carbonate record.

Related changes in the atmosphere and terrestrial settings are also relevant. The volcanism that occurred during mantle plume events delivered large amounts of CO_2 to the atmosphere, and enhanced chemical weathering under resulting greenhouse conditions would have generated a large flux of dissolved bicarbonate and nutrients, such as phosphorus and, to a lesser extent, nitrogen, to the oceans. This flux, by itself, might account for high organic productivity and high absolute burial rates of organic carbon, while the relative burial rate of organic carbon remained constant (cf. Aharon, 2005). Volcanic SO_2 flux to the atmosphere was also scaled up during the mantle plume breakout events, and a larger sulfur flux was delivered to shallow-marine environments. As a result, iron oxyhydroxides precipitated in deeper-water environments and carbonate-facies IFs mark a transition zone to highly productive shelves on which organic matter-rich and sulfidic shales were deposited, utilizing reactive iron delivered by iron-depleted hydrothermal plumes (**Figure 19**; Bekker et al., 2009; Rouxel et al., 2005). These sulfidic shales could have scavenged seawater Mo that was delivered to the oceans hydrothermally or, possibly, through oxidative weathering, providing an explanation for Mo enrichments observed in the 2.5 Ga Mount McRae Shale (Anbar et al., 2007) and shales proximal to the ~2.7 Ga Kidd Creek VMS deposit (Watanabe, 2002). Some of the hydrothermally delivered Mo was likely coprecipitated with iron oxyhydroxides in IFs, contributing to Mo isotope fractionations observed in the Mount McRae Shale (Duan et al., 2010). The carbonate-facies IFs reflect diagenetic reactions in settings where microbial Fe(III) reduction was coupled with

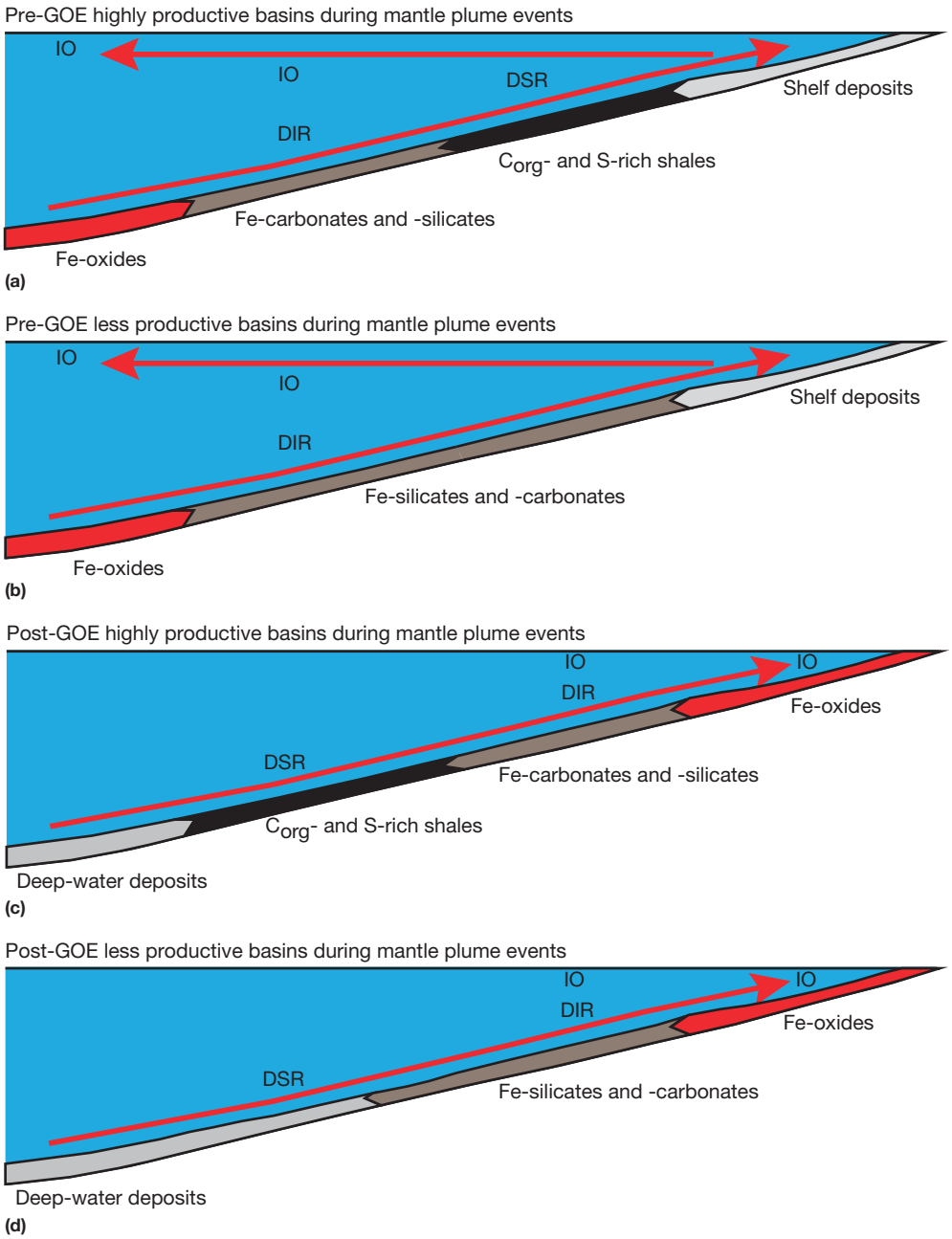

Figure 19 Schematic diagram of iron formation facies in high and low productivity basins before and after the GOE. Red arrows indicate iron fluxes with upwelling and offshelf currents. Before the GOE, iron was upwelled onto the shelves during mantle plume events, partially oxidized while the remaining iron was transported in solution back to the deeper part of the basin by offshore currents. Iron oxidation (IO) in the upper part of the water column delivered iron oxyhydroxides to the deeper part of the water column and sediments, where dissimilatory iron reduction (DIR) with organic matter as electron donor took place. Dissimilatory sulfate reduction (DSR) occurred in organic matter-rich shales and any other facies that contained abundant organic matter. In contrast, after the GOE, iron was quantitatively oxidized in shallow-water settings where it was upwelled during the mantle plume events.

remineralization of organic matter (Walker, 1984). Less productive shallow-water shelves in the Archean oceans were depositional sites for carbonates as well as silicate- and carbonate-facies GIFs during the mantle plume events (Beukes and Klein, 1990).

In contrast, post-GOE Paleoproterozoic IFs are predominantly granular, shallow-water, oxide-facies IFs that grade to finely laminated, sub-storm base (but still shelfal) Fe-silicate and carbonate-facies types. These extensive GIFs are related to rapid oxidation of iron delivered by upwelling iron-rich waters

to nearshore, high-energy environments and to subsequent sedimentary reworking of these precipitates. Deeper, in areas of high organic productivity on shelf, organic matter-rich and sulfidic shales were deposited in association with GIF during mantle plume events after the GOE (Figure 19).

Combined, these data suggest that after the GOE, there was a dynamic redoxcline between continuously oxic shallow waters and ferruginous deeper waters on the continental shelves, which was the typical depositional site for IFs (Bekker et al., 2010). In contrast, pre-GOE IFs were predominantly deposited in deeper-water settings having either a dynamic chemocline separating anoxic ferruginous deep waters from anoxic sulfidic shallow waters where black shales were deposited on highly productive shelves or a gradual transition to shallow-water, reduced-facies GIF in low productivity areas around submerged cratons (Figure 19). This fundamental difference in the distribution of IF facies is linked to oxygenation of the shallow ocean and the formation of a discrete redoxcline. The difference between pre- and post-GOE IFs is recorded not only in their sedimentary facies, but also in a much larger range of iron isotope fractionations in pre-GOE IFs (Planavsky et al., 2012; Rouxel et al., 2005). Without a fully oxygenated surface layer, partial oxidation was common in upwelling water masses during the Archean, resulting in Rayleigh fractionation during Fe removal and consequently a much larger range of sedimentary iron isotope values.

9.18.8.2 Implications for Atmospheric Oxidation

The emerging view is one of coupled enhanced primary productivity and deposition of IFs initiated by mantle plume events. If this model is valid, then it has implications for the rise of atmospheric oxygen. Once extensive oxidative continental weathering began, it provided abundant Mo to the oceans to activate the much more efficient Mo-nitrogenase enzyme (with respect to Fe–Fe nitrogenase enzyme). In addition, an enhanced hydrothermal Mo flux was likely delivered to the oceans during deposition of IFs at ~2.48–2.45 Ga. With more Mo available, nitrogen fixation would have flourished, leading to increased primary productivity by photosynthetic cyanobacteria. In turn, higher net oxygen production not only would have provided the oxygen required to remove iron from seawater, but also would have increased the terrestrial flux of dissolved Mo to the oceans. Under these conditions, Fe–Mo-nitrogenase would have replaced the less-efficient Fe–Fe nitrogenase, removing nitrogen limitation and leading to irreversible atmospheric oxidation. Paradoxically, in this model the rise of atmospheric oxygen is brought on by an enhanced flux of reductants from the mantle. Although IFs were deposited and LIPs emplaced before then, both processes are not comparable in scale or extent with those at 2.5–2.45 Ga (Barley et al., 2005; Condie et al., 2001; Heaman, 1997; Isley and Abbott, 1999).

Consistent with the above model, the oldest positive carbon isotope excursion is found in carbonates of the ~2.48 Ga Tongwane Formation, South Africa, which sits above an IF (Bekker et al., 2001). Mass-independent sulfur isotope fractionations, a proxy for the atmospheric redox state, declined shortly after deposition of the ~2.5–2.45 Ga IFs. Coincident with this shift is the onset of glaciations related to the GOE and the oxidation of atmospheric methane, which was an important greenhouse gas during the Archean (Bekker and Kaufman, 2007).

9.18.9 Euxinic Conditions Induced by Shift in Dissolved Fe/S Ratio of Seawater due to Iron Oxidation

Although ferruginous conditions appear to have been dominant in Archean oceans, there are several documented cases of euxinia or free sulfide existing in the coeval water column (e.g., Anbar et al., 2007; Kendall et al., 2010; Reinhard et al., 2009; Scott et al., 2008, 2011). Evidence for euxinia indicates that total dissolved S/Fe ratios commonly were greater than the pyrite stoichiometry of two (FeS_2). These results seem surprising, given a general acceptance of low sulfate and high iron concentrations in Archean seawater. However, even at very low sulfate concentrations it might be possible to develop euxinia. Low-sulfate, iron-rich oceans having spatial heterogeneities in dissolved S/Fe ratios are prone to locally establish euxinic conditions. Euxinia can develop in such oceans where Fe(II) oxidation effectively strips dissolved Fe^{2+}, creating a water mass with a relatively high S/Fe ratio. This water mass might retain a high dissolved S/Fe ratio when it later feeds a coastal setting, assuming the common case where rates of isopycnal mixing are much greater than those of diapycnal mixing. Because microbial Fe(III) reduction requires particulate contact, the reaction is expected to be very sluggish in the water column and therefore allows iron oxyhydroxides to sink. Ferric–ferrous iron interactions, Si coatings on Fe oxyhydroxides, and low C_{org} content in the water column also likely prevented Fe(III) reduction above the sediment–water interface. If a water mass in the photic zone has relatively high S/Fe ratios, it would become euxinic given a sufficient organic matter flux to fuel sulfate reduction. This scenario, in light of modern circulation patterns such as that feeding the Peru upwelling zone, could develop in an equivalent position to the modern OMZ euxinia in a low-sulfate, low-oxygen ocean regardless of the dissolved sulfate/Fe^{2+} ratios in deep waters. Although the Archean oceans are typically envisioned to be iron-replete and sulfide-poor, euxinia was likely relatively common in many settings having high rates of sulfate reduction. This is also consistent with the highly negative Fe isotope values in sulfidic black shales, which suggest extensive iron depletion through partial oxidation in the water column (Rouxel et al., 2005).

Changes in the atmosphere and in terrestrial settings linked with mantle plume events were also likely relevant to the local development of euxinic conditions in Archean oceans. Associated volcanism would have supplied large amounts of H_2S/SO_2 and CO_2 to the atmosphere and to marine environments. Enhanced chemical weathering under greenhouse conditions likely delivered nutrients to the oceans and, at the same time, sulfur compounds to shallow marine environments. As a result, iron oxyhydroxides would precipitate in deeper-water environments, whereas sulfidic conditions would develop in shallow-water environments where iron-depleted hydrothermal plumes delivered reactive iron (Figure 19(a); Bekker et al., 2009; Rouxel et al., 2005). A dynamic chemocline would therefore exist between anoxic ferruginous deep waters and anoxic sulfidic shallow waters, persisting until hydrothermal iron and atmospheric/terrestrial sulfur fluxes subsided, which would have

switched the ocean back to an unstratified, anoxic state. Expansion of the mixing zone between hydrothermally derived metal and atmospherically derived sulfur compounds during superplume events would have generated a high productivity zone ideally suited for increased burial of organic carbon.

9.18.10 Research Perspectives and Future Directions

Progress in research on IFs is closely linked to advancements in the understanding of surface and submarine-hydrothermal processes in the Precambrian and advances in geochronology, petrology, analytical geochemistry, and chemical oceanography. Early studies from the 1940s to the 1960s were directed mainly to map the distribution of this newly recognized iron resource in Precambrian terranes, and to provide age constraints and a stratigraphic framework. The discovery of Precambrian IFs immediately initiated speculations among geochemists about the mode of their origin based largely on application of thermodynamics to aqueous chemistry of the ancient oceans. Classical petrographic and metamorphic petrology studies focused on establishing paragenesis and mineral composition of the protolith sediments of IFs. Starting in the early 1970s, sedimentological facies analysis followed by basin analysis and sequence stratigraphy were incorporated into studies of IFs. The latter two aspects provide relatively recent and still underexplored directions for future research, with the goal of linking IF origin to plate tectonics and supercontinent cycles.

Progress since the late 1970s in the understanding of chemical oceanography and hydrothermal processes in the modern ocean has certainly influenced studies of IFs, although progress has been limited largely because direct comparison with modern hydrothermal analogues may not be directly applicable to the processes of IF deposition. Quantitative modeling of hydrothermal processes is needed in order to investigate the possible effects that these processes had on ancient oceans that lacked oxygen and sulfate.

Analyses of REE and Nd isotopes on bulk samples confirmed that hydrothermal processes dominated the chemistry of the early oceans. Once the role of hydrothermal processes in the origin of IFs and their links with submarine volcanism were appreciated, geochronology was employed to provide a test for synchronicity or diachronicity of IFs in unrelated basins on different cratons. This work helped establish a temporal and genetic link between IF deposition and mantle plume events. Although this work led to precise ages and revealed episodicity in deposition of major IFs, some giant IFs are still undated and their ages, once available, may dramatically impact our understanding of surface processes on early Earth.

Biological influences on the deposition of IFs were considered by Precambrian geologists and paleontologists for some time. However, only since the 1990s, with advances in the field of geomicrobiology, has the full potential of anaerobic photochemical iron oxidation as a driver for IF precipitation been realized. Models and experimental work on modern anaerobic iron-oxidizing communities have not yet been coupled fully with the rock record, in the sense that a direct proxy for this process in IFs is so far unknown. In fact, although models for iron oxidation have advanced significantly, it remains uncertain what signature in the rock record can discriminate among various mechanisms for iron oxidation.

Advances in analytical techniques have further broadened the field of geochemical investigation of IFs. New inductively coupled plasma mass-spectrometry (ICP-MS) instrumentation allows fast analysis of major and trace elements, including REE, as well as nontraditional stable isotopes (e.g., Fe, Cr, Si, and Ni). In situ laser-ablation techniques coupled with multicollector inductively coupled plasma mass-spectrometry (MC-ICP-MS) instrumentation and secondary ion mass spectroscopy (SIMS) provide an incredible level of spatial resolution ($\sim$10–20 μm) with a precision and accuracy approaching those of more time-consuming techniques using mineral separates and column chemistry, which provide limited spatial resolution. However, as discussed above, the absence of primary minerals in IF makes this direction of research, ultimately focused on the isotope and trace element composition of ancient seawater, likely to fail. Bulk sample analysis might provide a better way to characterize the composition of primary precipitates because the postdepositional redistribution of elements and intermineral isotopic fractionations will likely have a minimal effect on the scale of a hand specimen. However, in situ analysis still has a high potential when it is closely linked with detailed petrographic work. For example, the high preservation potential of primary textures in silicified layers and chert nodules is still largely unexplored, as are intra- and intergrain isotopic and trace element compositional heterogeneity in GIF. Data on these types of material might provide a better insight into seawater composition as well as mixing rates and element residence times in ancient oceans.

Field and detailed petrographic studies of Precambrian IFs rarely have been undertaken since the early 1990s and many IFs located in remote areas or areas having logistically difficult access were not investigated until the recent boom in iron ore prices. Industrial support during the last two decades was also mainly directed toward understanding how high-grade iron ores formed. As a result, recent state-of-the-art geochemical work has been done mainly on random or old grab samples without detailed geological control. Until now, no study has attempted to compare deep-water and shallow-water, or proximal and distal, sections of the same IF in the same depositional basin despite the obvious appeal of this approach.

Future progress in the study of IFs depends largely on careful integration of field-based and petrographic studies together with advanced geochemical analyses. Further, close links with geomicrobiology, chemical oceanography, and an understanding of submarine-hydrothermal processes are essential for deciphering the origin and evolution of IFs through time. The prospect is bright, but the burden of interaction and collaborative research is on participants, because each of these fields is in a rather advanced stage. However, as elsewhere in modern science, major breakthroughs are at the interface of fields and sciences rather than within established disciplines. Integration thus is needed among traditional, 'old-fashioned' disciplines and new advanced fields; the outcome of this research and training will likely lead to a well-rounded new generation of Precambrian geologists.

Appendix 1 Precambrian Banded Iron Formations, Granular Iron Formations, and Rapitan-Type Iron Formations[a]

Formation/group/deposit	*Location*	*Age (Ma)*	*Size (Gt)*	*Reference(s)*
1. *Maly Khinghan Formation*	Far East, Russia	~560	10 000	4, 6
2. Yerbel Formation	Southeastern Uruguay	~560	Unknown	7, 8
3. *Jacadigo Group* (*Urucum district*)	Mato Grosso do Sul State, Brazil	~600	1000	4, 9–11
4. *Bisokpabe Group*	Togo, West Africa	~600	Unknown	12, 13
5. Chestnut Hill Formation	New Jersey Highlands, New Jersey, USA	~600	Unknown (small)	14, 15
6. *Holowilena Ironstone*	South Australia, Australia	~650	Unknown (small)	16–18
7. *Braemar Iron Formation*	South Australia, Australia	~650	Unknown (small)	18–20
8. *Vil'va and Koyva Formations*	Western slope of Middle Ural Mountains, Russia	~650	Unknown (small)	21–24
9. Bakeevo (Tolparovo) Formation	Southern Ural Mountains, Russia	~650	Unknown (small)	22
10. *Dzhetymtau Suite*	Middle Tian-Shan, Kyrgyzstan	~650	Unknown (small)	25–28
11. UK Formation	Southern Ural Mountains, Russia	~700(?)	Unknown	22
12. Yamata Formation	East Siberia, Russia	~700(?)	Unknown	6
13. Lake Khanka Formation	Far East, Russia	~700(?)	Unknown	6
14. *Rapitan Formation*	Yukon Territory and Northwest Territories, Canada	715	1000	4, 29–32
15. *Chuos Formation*	Northern Namibia	~715	Unknown	4, 12, 33, 34
16. *Tindir Group*	Alaska, USA	715	Unknown (small)	35, 36
17. *Fulu Formation*	Jiangxi Province, China	~741	1000 (estimated)	6, 37
18. *Medvezhevo Formation*	Patom uplift, Siberia, Russia	~700–750	Unknown (small)	38, 39
19. *Kingston Peak Formation*	California, USA	~700–750	Unknown (small)	40, 41
20. *Numees Formation*	Southern Namibia	~700–750	Unknown (small)	12, 33, 34, 42
21. *Mugur Formation*	Tuva, Russia and Mongolia	767 ± 15	Unknown	6
22. Nizhne-Angara Formation	Angara-Pit area, Enisey Ridge, Siberia, Russia	~800	Unknown	43
23. Aok Formation (Shaler Supergroup)	Northwest Territories, Canada	~840	Unknown (small)	44, 45
24. Xiamaling Formation	Xiahuayuan region, Hebei Province, North China	1368 ± 12 Ma	Unknown (small)	46, 47
25. Roper Group (Corcoran and McMinn Formations)	Northern Territory, Australia	~1490	Unknown (small)	48, 49
26. South Nicholson Group (Mullera Formation)	Queensland, Australia	~1500	Unknown (small)	50, 51
27. Shoshong Formation	Eastern Botswana	~1600	1	4, 52, 53
28. Chuanlinggou Iron Formation	Hebei Province, China	~1650–1600	Unknown (small)	54, 55
29. Pike's Peak Iron Formation	Arizona, USA	~1728(57)	Unknown (small)	57–59
30. Gibraltar Formation	Northwest Territories, Canada	~1880	Unknown	60–62
31. Frere Formation	Western Australia, Australia	~1890	10 000	4, 63–66
32. Alwar Group (North Delhi fold belt)	Rajasthan and Haryana Provinces, India	~1850–2000	Unknown (small)	67–69
33. Lake Superior region	USA and Canada		10 000 (region total)	4

(*Continued*)

Appendix 1 (Continued)

Formation/group/deposit	*Location*	*Age (Ma)*	*Size (Gt)*	*Reference(s)*
Gunflint Iron Formation	Ontario, Canada	$<1878 \pm 2$ (71) to 1850 ± 1 (72)	(See above)	72–74
Negaunee Iron Formation	Michigan, USA	$<1874 \pm 9$ (71) to $>1850 \pm 1$ (72)	(See above)	75–77
Biwabik Iron Formation	Minnesota, USA	<1880 to $>1850 \pm 1$ (72)	(See above)	74, 75, 78
Ironwood Iron Formation	Michigan and Wisconsin, USA	<1880 to $>1850 \pm 1$ (72)	(See above)	75, 77, 79
Riverton Iron Formation	Michigan, USA	<1880 to $>1850 \pm 1$ (72)	(See above)	75, 77, 80
34. Sokoman Iron Formation	Labrador and Quebec, Canada	1877.8 ± 1.3	100 000	4, 81, 82
35. Rochford Formation	South Dakota, USA	1884 ± 29	Unknown (small)	75, 83
36. Basile Formation	Northwest Territories, Canada	1930	Unknown	84, 85
37. Liaohe Group	Liaoning Province, China	$\sim$1950–2050	100 (estimated)	86, 87
38. Estes Formation	South Dakota, USA	2020–2100	Unknown (small)	75, 83
39. Pääkkö Iron Formation	Central Finland	2080 ± 45	100	4, 88, 89
40. Glen Township Formation	Minnesota, USA	$\sim$2100	Unknown (small)	75, 90
41. Lomagundi Group	Northern Zimbabwe	$\sim$2100–2200	Unknown (small)	91, 92
42. Caldeirão belt	Bahia State, Brazil	>2078 to <2687	Unknown (small)	93, 94
43. Malumfashi, Maru, Birnin Gwari, Kushaka, Muro, Egbe-Isanlu, and Obajana schist belts	Northern and southern parts of West-Nigeria	$\sim$2100	Unknown (small)	95
44. Ijil Group	Western Mauritania	$\sim$2200	100	4, 96, 97
45. Nimba Itabirite	Liberia, West Africa	>2100 to <2615	10 000	4, 98–100
46. Hotazel Iron Formation	Northern Cape Province, South Africa	$\sim$2200	150 (calculated; 101)	102–105
47. Timeball Hill Formation	Gauteng and North West Provinces, South Africa	$\sim$2320	10	106–108
48. Kursk Supergroup	Western Russia	$\sim$2450	300 000(109)	4, 110, 111
49. Krivoy Rog Supergroup	Eastern Ukraine	$\sim$2450	50 000	4, 110, 112, 113
50. Transvaal Province	Northern Cape Province, South Africa		100 000(114)	4
Griquatown Iron Formation	Northern Cape Province, South Africa	2431 ± 31	(See above)	4, 115, 116
Kuruman Iron Formation	Northern Cape Province, South Africa	2465 ± 7	(See above)	115, 117
Penge Iron Formation	North West Province, South Africa	2480 ± 6	(Included above; 118)	119, 120
51. Hamersley Basin	Western Australia, Australia		100 000(121)	4
Boolgeeda Iron Formation	Western Australia, Australia	2445 ± 5	19 000	122, 123
Weeli Wolli Formation	Western Australia, Australia	2449 ± 3	19 000	122–124
Brockman Iron Formation (Joffre Mbr)	Western Australia, Australia	2461 ± 6	30 000	122–124
Brockman Iron Formation (Dales Gorge Mbr)	Western Australia, Australia	2461 ± 6 to 2495 ± 16	13 000	122, 124, 125

(*Continued*)

Appendix 1 (Continued)

Formation/group/deposit	*Location*	*Age (Ma)*	*Size (Gt)*	*Reference(s)*
Mt. Sylvia Formation	Western Australia, Australia	~2505	3000	122–124
Marra Mamba Iron Formation	Western Australia, Australia	2597 ± 5	17 000	122, 126
52. Cauê Formation	Minas Gerais State, Brazil	~2450	100 000	4, 127, 128
53. Indian Creek Metamorphic Suite	Montana, USA	2470–2750	1	4, 129–131
54. Ruker Series	Prince Charles Mountains, East Antarctica	2450–2480	Unknown	132–134
55. Benchmark Iron Formation	South Dakota, USA	2480–2560	Unknown (small)	76, 84
56. Hutchison Group (Middleback Ranges)	Cleve domain, South Australia, Australia	~2500	1000	4, 135–137
57. Nemo Iron Formation	South Dakota, USA	2560–2890	Unknown (small)	76, 84
58. Chitradurga Group	Karnataka Province, southern India	2614 ± 8	1000 (estimated)	138–140
59. Beardmore-Geraldton assemblage	Ontario, Canada	~2700	Unknown (small)	141, 142
60. Anshan Iron Formation	Liaoning Province, China	~2700	10 000 (estimated) (143)	144–146
61. Manjeri Iron Formation	Southern Zimbabwe	~2700–2830	Unknown	147–149
62. Bababudan Group	Karnataka Province, southern India	2720 ± 7	1000 (estimated)	150–152
63. Central Slave Cover Group	Nunavut, Canada	2730–2920	Unknown	153
64. Carajás Formation	Pará State, Brazil	~2740–2750	50 000 (estimated)	154, 155
65. West Rand Group	Gauteng Province, South Africa	~2960	10	4, 156–158
66. Pongola Supergroup	KwaZulu-Natal Province, South Africa	~2960	100	4, 159, 160
67. Jack Hills belt	Western Australia, Australia	>3080 ± 20	Unknown (small)	161, 162
68. Moodies Group	Barberton, South Africa	~3230	Unknown (small)	163–165

[a]Most iron formations ~2.4 Ga and older consist largely of banded iron formation (BIF); those ~2.3–0.8 Ga are predominantly granular iron formation (GIF); Neoproterozoic Rapitan-type iron formation (0.80–0.56 Ga) associated with glacial deposits are in italics. Several ironstones of Mesoproterozoic age are included in this compilation (see text). Algoma-type iron formation, which occurs in or is closely associated stratigraphically with volumetrically abundant volcanic rocks (1–3), is excluded because this generally smaller type of iron deposit, relative to predominantly sediment-hosted iron formation, does not inform the redox state of deep seawater on a large scale (2). Sizes of BIFs are estimated amounts of originally deposited iron formation (4), and are much greater than those of reported ore reserves or resources, which are affected by extent of erosional preservation, mining practices, economics, and other factors. This compilation does not include numerous (mostly small) sediment-hosted iron formations in China and elsewhere in Far East Asia (5), for which geologic, geochronologic, and tonnage data are difficult to obtain.

1. Gross GA (1995) Algoma-type iron-formation. In: Eckstrand OR, Sinclair WD, and Thorpe RI (eds.) *Geology of Canadian Mineral Deposit Types*: *Geological Survey of Canada*, pp. 66–73. Geology of Canada, No. 8.
2. Huston DL and Logan GA (2004) Barite, BIFs and bugs: Evidence for the evolution of the Earth's early hydrosphere. *Earth and Planetary Science Letters* 220: 41–55.
3. Klein C (2005) Some Precambrian banded iron-formations (BIFs) from around the world: Their age, geologic setting, mineralogy, metamorphism, geochemistry, and origin. *American Mineralogist* 90: 1473–1499.
4. James HL (1983) Distribution of banded iron-formations in space and time. In: Trendall AF and Morris RC (eds.) *Iron-formation*: *Facts and problems*. *Developments in Precambrian Geology*, vol. 6, pp. 471–490. Amsterdam: Elsevier.
5. Rodionov SM, et al. (2003) Preliminary metallogenic belt and mineral deposit maps for northeast Asia. *U.S. Geological Survey Open-File Report 03-204*, 104 p.
6. Ilyin AV (2009) Neoproterozoic banded iron formations. *Lithology and Mineral Resources* 44: 78–86.
7. Aubet NR, Pecoits E, Bekker A, Gingras MK, Zwingmann H, Veroslavsky G, de Santa Ana H, Konhauser KO (2012) Chemostratigraphic constraints on early Ediacaran carbonate ramp dynamics, Río de la Plata craton (Uruguay). Gondwana Research 22: 1073–1090.
8. Pecoits E, Gingras M, Aubet N, and Konhauser K (2008) Ediacaran in Uruguay: Palaeoclimatic and palaeobiological implications. *Sedimentology* 55: 689–719.
9. Urban H, Stribrny B, and Lippolt HJ (1992) Iron and manganese deposits of the Urucum district, Mato Grosso do Sul, Brazil. *Economic Geology* 87: 1375–1392.
10. Trompette R, Alvarenga CJS, and Walde D (1998) Geological evolution of the Neoproterozoic Corumba graben system (Brazil): Depositional context of the stratified Fe and Mn ores of the Jacadigo Group. *Journal of South American Earth Sciences* 11: 587–597.
11. Klein C and Ladeira EA (2004) Geochemistry and mineralogy of Neoproterozoic banded iron-formations and some selected, siliceous manganese formations from the Urucum district, Mato Grosso do Sul, Brazil. *Economic Geology* 99: 1233–1244.
12. Beukes NJ (1973) Precambrian iron-formations of southern Africa. *Economic Geology* 68: 960–1004.
13. Simpara N, Sougy J, and Trompette R (1985) Lithostratigraphie et structure du Buem unité externe de la chaine panafricaine des Dahomeyides dans la region de Bassar (Togo). *Journal of African Earth Sciences* 3: 479–486.

14. Volkert RA (2001) Geologic setting of Proterozoic iron, zinc, and graphite deposits, New Jersey Highlands. In: Slack JF (ed.) *Proterozoic Iron and Zinc Deposits of the Adirondack Mountains and the New Jersey Highlands*. *Society of Economic Geologists Field Trip Guidebook Series*, Vol. 35, Part 1, pp. 59–73.
15. Volkert RA, Monteverde DH, Friehauf KC, Gates AE, Dalton RF, and Smith RC II (2010) Geochemistry and origin of Neoproterozoic ironstone deposits in the New Jersey Highlands and implications for the eastern Laurentian rifted margin in the north-central Appalachians, USA. In: Tollo RP, Bartholomew MJ, Hibbard JP, and Karabinos PM (eds.) *From Rodinia to Pangea*: *The Lithotectonic Record of the Appalachian Region*. *Geological Society of America Memoir* 206: 283–306.
16. Dalgarno CR and Johnson JE (1965) The Holowilena ironstrone, a Sturtian glacigene unit. *Quarterly Notes of the Geological Survey of South Australia* 13: 2–4.
17. Preiss WV (2006) Old Boolcoomata Conglomerate Member of the Benda Siltstone—Neoproterozoic glacial sedimentation in terrestrial and marine environments in an active rift basin. *MESA Journal* 41: 15–23.
18. Kendall B, Creaser RA, Calver CR, Raub TD, and Evans DAD (2009) Correlation of Sturtian diamictite successions in southern Australia and northwestern Tasmania by Re-Os black shale geochronology and the ambiguity of "Sturtian"-type diamictite-cap carbonate pairs as chronostratigraphic marker horizons. *Precambrian Research* 172: 301–310.
19. Whitten GF (1970) The investigation and exploitation of the Razorback Ridge iron deposit. *Geological Survey of South Australia*, *Report of Investigations 33*, 165 p.
20. Lottermoser BG and Ashley PM (2000) Geochemistry, petrology and origin of Neoproterozoic ironstones in the eastern part of the Adelaide Geosyncline, South Australia. *Precambrian Research* 101: 49–67.
21. Ablizin BD, Klyuzhina ML, Kurbatskaya FA, and Kurbatskiy AM (1982) *Upper Riphean and Vendian of the West Slope of the Middle Ural*, 140 p. Moscow: Nayka [in Russian].
22. Bekker YuR (1988) *Precambrian Molasses*, 288 p. Leningrad: Nedra [in Russian].
23. Chumakov NM (1992) The problems of old glaciations (pre-Pleistocene glaciogeology in the USSR). *Soviet Scientific Reviews*, *Section G*. *Geology Reviews* 1(pt 3): 1–208.
24. Chumakov NM (2011) Late Proterozoic African glacial era. *Stratigraphy and Geological Correlation* 19: 1–20.
25. Zubtsov YI (1972) Precambrian tillites in the Tien Shan, and their stratigraphic value. *Byulleten' Moskovskogo Obshchestva Ispytateley Prirody*, *Otdel Geologicheskiy* 47: 42–56 [in Russian].
26. Korolev VG and Maksumova RA (1984) *Precambrian Tillites and Tilloides of Tian Shan*, 189 p. Frunze: Ilim Publishing House [in Russian].
27. Sagandykov KS and Sudorgin AA (1984) *Dzhetym Iron-Bearing Basin of Tien Shan*, 216 p. Frunze: Ilim Publishing House [in Russian].
28. Chumakov NM (2009) The Baykonurian glaciohorizon of the Late Vendian. *Stratigraphy and Geological Correlation* 17: 373–381.
29. Young GM (1976) Iron-formation and glaciogenic rocks of the Rapitan Group, Northwest Territories, Canada. *Precambrian Research* 3: 137–158.
30. Yeo GM (1986) Iron-formation in the Late Proterozoic Rapitan Group, Yukon and Northwest Territories. In: Morin JA (ed.) *Mineral Deposits of Northern Cordillera*, Special Volume 37, pp. 142–153. Cassiar, BC: Canadian Institute of Mining and Metallurgy.
31. Klein C and Beukes NJ (1993) Sedimentology and geochemistry of the glaciogenic Late Proterozoic Rapitan iron-formation in Canada. *Economic Geology* 88: 542–565.
32. Macdonald FA, Schmitz MD, Crowley JL, et al. (2010) Calibrating the Cryogenian. *Science* 327: 1241–1243.
33. Roesener H and Schreuder CP (1992) Iron. In: *Mineral Resources of Namibia*, pp. 2.4-1–2.4-14. Namibia: Geological Survey of Namibia. Special Publication.
34. Hoffmann K-H, Condon DJ, Bowring SA, and Crowley JL (2004) U–Pb zircon date from the Neoproterozoic Ghaub Formation, Namibia: Constraints on Marinoan glaciation. *Geology* 32: 817–820.
35. Young GM (1982) The Late Proterozoic Tindir Group, east-central Alaska: Evolution of a continental margin. *Geological Society of America Bulletin* 93: 759–783.
36. Kaufman AJ, Knoll AH, and Awramik SM (1992) Biostratigraphic and chemostratigraphic correlation of Neoproterozoic sedimentary successions: Upper Tindir Group, northwestern Canada, as a test case. *Geology* 20: 181–185.
37. Tang J-F, Fu H-Q, and Yu Z-Q (1987) Stratigraphy, type and formation conditions of the Late Precambrian banded iron ores in South China. *Chinese Journal of Geochemistry* 6: 331–341 [in English].
38. Ivanov AI, Lifshits VI, Perevalov OV, et al. (1995) *Precambrian of the Patoma Uplift*, 353 p. Moscow: Nedra [in Russian].
39. Chumakov NM (2011) The Neoproterozoic glacial formations of the North and Middle Urals. In: Arnaud E, Halverson GP, and Shields-Zhou G (eds.) *The Geological Record of Neoproterozoic Glaciations*, pp. 289–296. London: Geological Society of London. Memoir 36.
40. Miller JMG (1985) Glacial and syntectonic sedimentation: The Upper Proterozoic Kingston Peak Formation, southern Panamint Range, eastern California. *Geological Society of America Bulletin* 96: 1537–1553.
41. Condon DJ, Prave AR, and Benn DI (2002) Neoproterozoic glacial-rainout intervals: Observations and implications. *Geology* 30: 35–38.
42. van Staden A, Naidoo T, Zimmermann U, and Germs GJB (2006) Provenance analysis of selected clastic rocks in Neoproterozoic to lower Paleozoic successions of southern Africa from the Gariep Belt and the Kango Inlier. *South African Journal of Geology* 109: 215–232.
43. Yudin NI (1968) *Lithology of Iron Ore Deposits of the Angara-Pitsk Basin*, 152 p. Moscow: Laboratory of Sedimentary Ore Deposits, Nauka [in Russian].
44. Rainbird RH, Jefferson CW, Hildebrand RS, and Worth JK (1994) The Shaler Supergroup and revision of Neoproterozoic stratigraphy in the Amundsen basin, Northwest Territories. *Geological Survey of Canada*, *Current Research*, *Paper 94-1A*, pp. 61–70.
45. Rainbird RH, Jefferson CW, and Young GM (1996) The early Neoproterozoic sedimentary succession B of northwest Laurentia: Correlations and paleogeographic significance. *Geological Society of America Bulletin* 108: 454–470.
46. Song C and Zhang Z (1983) Xiamaling Formation and its depositional environments in Xiahuayuan region, Hebei Province, North China. *Journal of Stratigraphy* 7: 104–111 [in Chinese].
47. Su W, Zhang S, Huff WD, et al. (2008) SHRIMP U–Pb ages of K-bentonite beds in the Xiamaling Formation: Implications for revised subdivision of the Meso- to Neoproterozoic history of the North China Craton. *Gondwana Research* 14: 543–553.
48. Canavan F (1965) Iron ore deposits of Roper Bar. In: McAndrew J (ed.) *Geology of Australian Ore Deposits*: *Melbourne*, *Australasian Institute of Mining and Metallurgy*, *Eighth Commonwealth Mining and Metallurgical Congress of Australia and New Zealand*, pp. 212–215.
49. Kendall B, Creaser RA, Gordon GW, and Anbar AD (2009) Re–Os and Mo isotope systematics of black shales from the Middle Proterozoic Velkerri and Wollogorang Formations, McArthur basin, northern Australia. *Geochimica et Cosmochimica Acta* 73: 2534–2558.
50. Harms JE (1965) Iron ore deposits of Constance Range. In: McAndrew J (ed.) *Geology of Australian ore deposits*: *Melbourne*, *Australasian Institute of Mining and Metallurgy*, *Eighth Commonwealth Mining and Metallurgical Congress of Australia and New Zealand*, pp. 264–269.
51. Page RW and Sweet IP (1998) Geochronology of basin phases in the western Mt Isa inlier and correlation with the McArthur basin. *Australian Journal of Earth Sciences* 45: 219–232.
52. Ermanovics IF, Key RM, and Jones MT (1978) The Palapye Group, central-eastern Botswana. *Transactions of the Geological Society of South Africa* 81: 61–73.
53. Mapeo RBM, Ramokate LV, Armstrong RA, and Kampunzu AB (2004) U–Pb zircon age of the upper Palapye group (Botswana) and regional implications. *Journal of African Earth Sciences* 40: 1–16.
54. Wan Y-S, Zhang Q-D, and Song T-R (2003) SHRIMP ages of detrital zircons from the Changcheng System in the Ming Tombs area, Beijing: Constraints on the protolith nature and maximum depositional age of the Mesoproterozoic cover of the North China craton. *Chinese Science Bulletin* 48: 2500–2506 [in English].

55. Dai Y-D, Song H-M, and Shen J-Y (2004) Fossil bacteria in Xuanlong iron ore deposits of Hebei Province. *Science in China*, *Series D* 47: 347–356 [in English].
56. This age is problematic because the contact between the dated felsic metavolcanic unit and the Pike's Peak Iron-Formation is a fault.
57. Slatt RM, Heintz GM, Lowry PH, and O'Hara PF (1978) *Precambrian Pike's Peak Iron-Formation*, *Central Arizona*. Arizona Bureau of Geology and Mineral Technology, Special Paper 2, pp. 73–82.
58. Burr JL (1991) Proterozoic stratigraphy and structural geology of the Hieroglyphic Mountains, central Arizona. *Arizona Geological Society Digest* 19: 117–133.
59. Burr JL (1994) Constraints on timing of Early Proterozoic deformation and metamorphism in the Hieroglyphic Mountains, central Arizona [abs.]. *Geological Society of America Abstracts with Programs* 26: 405.
60. Bowring SA, Van Schmus WR, and Hoffman PF (1984) U–Pb zircon ages from Athapuscow aulacogen, East Arm of Great Slave Lake, N.W.T. *Canadian Journal of Earth Sciences* 21: 1315–1324.
61. Roscoe SM, Gandhi SS, Charbonneau BW, Maurice YT, and Gibb RA (1987) Mineral resource assessment of the area in the East Arm (Great Slave Lake) and Artillery Lake region, N.W.T., proposed as a national park (NTS 75 J,K, L, N, O). Geological Survey of Canada, Open File 1434, 92 p.
62. Hoffman PF, Bowring SA, Buchwaldt R, and Hildebrand RS (2011) Birthdate for the Coronation paleocean: Age of initial rifting in Wopmay orogen, Canada. *Canadian Journal of Earth Sciences* 48: 281–293.
63. Goode ADT, Hall WDM, and Bunting JA (1983) The Nabberu basin of Western Australia. In: Trendall AF and Morris RC (eds.) *Iron-Formation*: *Facts and Problems*. *Developments in Precambrian Geology*, vol. 6, pp. 295–323. Amsterdam: Elsevier.
64. Rasmussen B and Fletcher IR (2002) Indirect dating of mafic intrusions by SHRIMP U–Pb analysis of monazite in contact metamorphosed shale: An example from the Palaeoproterozoic Capricorn orogen, Western Australia. *Earth and Planetary Science Letters* 197: 287–299.
65. Pirajno F, Hocking RM, Reddy SM, and Jones AJ (2009) A review of the geology and geodynamic evolution of the Palaeoproterozoic Earaheedy Basin, Western Australia. *Earth-Science Reviews* 94: 39–77.
66. Rasmussen B, Fletcher IR, Bekker A, Muhling JR, Gregory CJ, and Thorne AM (2012) Deposition of 1.88-billion-year-old iron formations as a consequence of rapid crustal growth. *Nature* 484: 498–501.
67. Patwardhan AM, Patil DN, and Sukhtankar RK (1987) On magnetite quartizites occurring around Narnaul, Haryana, India. In: Appel PWU and LaBerge GL (eds.) *Precambrian Iron-Formations*, pp. 513–537. Athens: Theophrastus Publications.
68. Biju-Sekhar S, Yokoyama K, Pandit MK, Okudaira T, Yoshida M, and Santosh M (2003) Late Paleoproterozoic magmatism in Delhi fold belt, NW India and its implication: Evidence from EPMA chemical ages of zircons. *Journal of Asian Earth Sciences* 22: 189–207.
69. Deb M and Thorpe RI (2004) Geochronological constraints in the Precambrian geology of Rajasthan and their metallogenic implications. In: Deb M and Goodfellow WD (eds.) *Sediment-Hosted Lead-Zinc Sulphide Deposits*, pp. 246–263. New Delhi: Narosa Publishing.
70. Radiometric age within iron formation.
71. Minimum age from occurrence of Sudbury impact layer at top of iron formation.
72. Floran RJ and Papike JJ (1978) Mineralogy and petrology of the Gunflint Iron Formation, Minnesota-Ontario: Correlation of compositional and assemblage variations at low to moderate grade. *Journal of Petrology* 19: 215–288.
73. Fralick P, Davis DW, and Kissin SA (2002) The age of the Gunflint Formation, Ontario, Canada: Single zircon U–Pb age determinations from reworked volcanic ash. *Canadian Journal of Earth Sciences* 39: 1085–1091.
74. Addison WD, Brumpton GR, Valini DA, et al. (2005) Discovery of distal ejecta from the 1850 Ma Sudbury impact event. *Geology* 33: 193–196.
75. Bayley RW and James HL (1973) Precambrian iron-formations of the United States. *Economic Geology* 68: 934–959.
76. Schneider DA, Bickford ME, Cannon WF, Schulz KJ, and Hamilton MA (2002) Age of volcanic rocks and syndepositional iron formations, Marquette Range Supergroup: Implications for the tectonic setting of Paleoproterozoic iron formations of the Lake Superior region. *Canadian Journal of Earth Sciences* 39: 999–1012.
77. Cannon WF, Schulz KJ, Horton JW Jr., and Kring DA (2010) The Sudbury impact layer in the Paleoproterozoic iron ranges of northern Michigan, USA. *Geological Society of America Bulletin* 122: 50–75.
78. Perry EC, Tan FC, and Morey GB (1973) Geology and stable isotope geochemistry of Biwabik Iron Formation, northern Minnesota. *Economic Geology* 68: 1110–125.
79. Cannon WF, LaBerge GL, Klasner JS, and Schulz KJ (2008) The Gogebic Iron Range – A sample of the northern margin of the Penokean fold and thrust belt. *U.S. Geological Survey Professional Paper 1730*, 44 p.
80. James HL, Dutton CE, Pettijohn FJ, and Wier KL (1968) Geology and ore deposits of the Iron River-Crystal Falls district, Iron County, Michigan. *U.S. Geological Survey Professional Paper 570*, 134 p.
81. Klein C and Fink RP (1976) Petrology of the Sokoman Iron-Formation in the Howells River area, at the western edge of the Labrador Trough. *Economic Geology* 71: 453–487.
82. Findlay JM, Parrish RR, Birkett TC, and Watanabe DH (1995) U–Pb ages from the Nimish Formation and Montagnais glomeroporphyritic gabbro of the central New Quebec orogen, Canada. *Canadian Journal of Earth Sciences* 32: 1208–1220.
83. Frei R, Dahl PS, Duke EF, et al. (2008) Trace element and isotopic characterization of Neoarchean and Paleoproterozoic iron formations in the Black Hills (South Dakota, USA): Assessment of chemical change during 2.9–1.9 Ga deposition bracketing the 2.4–2.2 Ga first rise of atmospheric oxygen. *Precambrian Research* 162: 441–474.
84. Bowring SA, Van Schmus WR, and Hoffman PF (1984) U–Pb zircon ages from Athapuscow aulacogen, East Arm of Great Slave Lake, N.W.T. *Canadian Journal of Earth Sciences* 21: 1315–1324.
85. Johnson BJ (1990) Stratigraphy and structure of the Early Proterozoic Wilson Island Group, East Arm thrust-fold belt, N.W.T. *Canadian Journal of Earth Sciences* 27: 552–569.
86. Zhang Q-S (1987) Banded iron formations in China. In: Appel PWU and LaBerge GL (eds.) *Precambrian Iron-Formations*, pp. 423–448. Athens: Theophrastus Publications.
87. Luo Y, Sun M, Zhao G-C, Li S-Z, Xu P, Ye K, and Xia X-P (2004) LA-ICP-MS U–Pb zircon ages of the Liaohe Group in the eastern block of the North China craton: Constraints on the evolution of the Jiao-Liao-Ji belt. *Precambrian Research* 134: 349–371.
88. Sakko M and Laajoki K (1975) Whole rock Pb–Pb isochron age for the Pääkkö iron formation in Väyrylänkylä, South Puolanka area, Finland. *Bulletin of the Geological Society of Finland* 47: 113–116.
89. Laajoki K and Saikkonen R (1977) On the geology and geochemistry of the Precambrian iron formations in Väyrylänkylä, South Puolanka area, Finland. *Bulletin of the Geological Survey of Finland* 292: 137.
90. Morey GB and Southwick DL (1995) Allostratigraphic relationships of Early Proterozoic iron-formations in the Lake Superior region. *Economic Geology* 90: 1983–1993.
91. Master S (1991) Stratigraphy, tectonic setting, and mineralization of the Early Proterozoic Magondi Supergroup, Zimbabwe: A review. Economic Geology Research Unit Information Circular 238, 75 p. Johannesburg: University of Witwatersrand.
92. Mapeo RBM, Armstrong RA, and Kampunzu AB (2001) SHRIMP U–Pb zircon geochronology of gneisses from the Gweta borehole, northeast Botswana: Implications for the Palaeoproterozoic Magondi belt in southern Africa. *Geological Magazine* 138: 299–308.
93. Jordan VH (1972) Die Minas-Gruppe in Nordost-Bahia, Brasilien. *Geologische Rundschau* 61: 441–469.

94. Oliveira EP, Mello EF, and McNaughton N (2002) Reconnaissance U–Pb geochronology of Precambrian quartzites from the Caldeirão belt and their basement, NE São Francisco craton, Bahia, Brazil: Implications for the early evolution of the Paleoproterozoic Itabuna-Salvador-Curaçá orogen. *Journal of South American Earth Sciences* 15: 349–362.
95. Mücke A (2005) The Nigerian manganese-rich iron-formations and their host rocks – From sedimentation to metamorphism. *Journal of African Earth Sciences* 41: 407–436.
96. Bronner G and Chauvel J-J (1979) Precambrian banded iron-formations of the Ijil Group (Kediat Ijil, Reguibat Shield Mauritania). *Economic Geology* 74: 77–94.
97. Bronner G, Chauvel J-J, and Triboulet C (1992) Les formations ferrifères du Précambrien de Mauritanie: Origine et evolution des quartzites ferrugineux. *Chronique de la Récherche Minière* 508: 3–27.
98. Berge JW (1974) Geology, geochemistry, and origin of the Nimba itabirite and associated rocks, Nimba County, Liberia. *Economic Geology* 69: 80–92.
99. Berge JW, Johansson K, and Jack J (1977) Geology and origin of the hematite ores of the Nimba Range, Liberia. *Economic Geology* 72: 582–607.
100. Billa M, Feybesse J-L, Bronner G, et al. (1999) Les formations à quartzites rubanés ferrugineux des Monts Nimba et du Simandou: Des unités empilées tectoniquement, sur un "soubassement" plutonique Archéen (craton de Kénéma-Man), lors de l'orogène Éburnéen. *Comptes Rendus de l'Académie des Sciences*, *Series IIA* 329: 287–294.
101. Tonnage figure excludes Mn-rich units.
102. Tsikos H and Moore JM (1997) Petrography and geochemistry of the Paleoproterozoic Hotazel Iron-Formation, Kalahari manganese field, South Africa: Implications for Precambrian manganese metallogenesis. *Economic Geology* 92: 87–97.
103. Tsikos H, Beukes NJ, Moore JM, and Harris C (2003) Deposition, diagenesis, and secondary enrichment of metals in the Paleproterozoic Hotazel Iron Formation, Kalahari manganese field, South Africa. *Economic Geology* 98: 1449–1462.
104. Cornell DH, Schütte SS, and Eglington BL (1996) The Ongeluk basaltic andesite formation in Griqualand West, South Africa: Submarine alteration in a 2222 Ma Proterozoic sea. *Precambrian Research* 79: 101–123.
105. Dorland HC (2004) *Provenance Ages and Timing of Sedimentation of Selected Neoarchean and Paleoproterozoic Successions on the Kaapvaal Craton*. Unpublished PhD Thesis, Rand Afrikaans University, Johannesburg, 326 p.
106. Schweigart H (1965) Genesis of the iron ores of the Pretoria Series, South Africa. *Economic Geology* 60: 269 – 298.
107. Dorland HC (1999) *Paleoproterozoic Laterites*, *Red Beds and Ironstones of the Pretoria Group with Reference to the History of Atmospheric Oxygen*. Unpublished MSc Thesis, Rand Afrikaans University, South Africa, 147 p.
108. Hannah JL, BekkerA, Stein HJ, Markey RJ, and Holland HD (2004) Primitive Os and 2316 Ma age for marine shale: Implications for Paleoproterozoic glacial events and the rise of atmospheric oxygen. *Earth and Planetary Science Letters* 225: 43–52.
109. Size of original iron formation unit is estimated based on tonnage data for Fe (4).
110. Alexandrov EA (1973) The Precambrian banded iron-formations of the Soviet Union. *Economic Geology* 68: 1035–1062.
111. Belykh VI, Dunai EI, and Lugovaya IP (2007) Physicochemical formation conditions of banded iron formations and high-grade iron ores in the region of the Kursk magnetic anomaly: Evidence from isotopic data. *Geology of Ore Deposits* 49: 147–159.
112. Belevtsev YN, Belevtsev RY, and Siroshtan RI (1983) The Krivoy Rog basin. In: Trendall AF and Morris RC (eds.) *Iron-Formation*: *Facts and Problems*. *Developments in Precambrian Geology*, vol. 6, pp. 211–251. Amsterdam: Elsevier.
113. Kulik DA and Korzhnev MN (1997) Lithological and geochemical evidence of Fe and Mn pathways during deposition of Lower Proterozoic banded iron formation in the Krivoy Rog Basin (Ukraine). *Geological Society Special Publication* 119: 43–80.
114. Tonnage total for region includes Penge Iron Formation in North West Province, South Africa (4).
115. Beukes NJ (1980) Lithofacies and stratigraphy of the Kuruman and Griquatown iron-formations, northern Cape Province, South Africa. *Transactions of the Geological Society of South Africa* 83: 69–86.
116. Barton ES, Altermann W, Williams IS, and Smith CB (1994) U–Pb zircon age for a tuff in the Campbell Group, Griqualand West Sequence, South Africa: Implications for Early Proterozoic rock accumulation rates. *Geology* 22: 343–346.
117. Pickard AL (2003) SHRIMP U–Pb zircon ages for the Palaeoproterozoic Kuruman Iron Formation, northern Cape Province, South Africa: Evidence for simultaneous BIF deposition on Kaapvaal and Pilbara cratons. *Precambrian Research* 125: 275–315.
118. Tonnage data are included in the total for the Griquatown-Transvaal region (4).
119. Miyano T and Beukes NJ (1997) Mineralogy and petrology of the contact metamorphosed amphibole asbestos-bearing Penge Iron Formation, Eastern Transvaal, South Africa. *Journal of Petrology* 38: 651–676.
120. Nelson DR, Trendall AF, and Altermann W (1999) Chronological correlations between the Pilbara and Kaapvaal cratons. *Precambrian Research* 97: 165–189.
121. Regional total; tonnages for individual iron formations in the Hamersley Basin are estimated using relative stratigraphic thicknesses compared to the total tonnage for the basin.
122. Trendall AF (1983) The Hamersley Basin. In: Trendall AF and Morris RC (eds.) *Iron-Formation*: *Facts and Problems*. *Developments in Precambrian Geology*, vol. 6, pp. 69–130. Amsterdam: Elsevier.
123. Trendall AF, Compston W, Nelson DR, De Laeter JR, and Bennett VC (2004) SHRIMP zircon ages constraining the depositional chronology of the Hamersley Group, Western Australia. *Australian Journal of Earth Sciences* 51: 621–644.
124. Barley ME, Pickard AL, and Sylvester PJ (1997) Emplacement of a large igneous province as a possible cause of banded iron formation 2.45 billion years ago. *Nature* 385: 55–58.
125. Taylor D, Dalstra HJ, Harding AE, Broadbent G, and Barley ME (2001) Genesis of high-grade hematite orebodies of the Hamersley Province, Western Australia. *Economic Geology* 96: 837–873.
126. Trendall AF, Nelson DR, De Laeter JR, and Hassler SW (1998) Precise zircon U–Pb ages from the Marra Mamba Iron Formation and Wittenoom Formation, Hamersley Group, Western Australia. *Australian Journal of Earth Sciences* 45: 137–142.
127. Spier CA, de Oliveira SMB, Sial AN, and Rios FJ (2007) Geochemistry and genesis of banded iron formations of the Cauê Formation, Quadrilátero Ferrífero, Minas Gerais, Brazil. *Precambrian Research* 152: 170–206.
128. Noce CM, Tassinari C, and Lobato LM (2007) Geochronological framework of the Quadrilátero Ferrífero, with emphasis on the age of gold mineralization hosted in Archean greenstone belts. *Ore Geology Reviews* 32: 500–510.
129. Immega IP and Klein C (1976) Mineralogy and petrology of some metamorphic Precambrian iron-formations in southwestern Montana. *American Mineralogist* 61: 1117–1144.
130. Harms TA, Brady JB, Burger HR, and Cheney JT (2004) Advances in the geology of the Tobacco Root Mountains, Montana, and their implications for the history of the northern Wyoming province. In: Brady JB, Burger HR, Cheney JT, and Harms TA (eds.) *Precambrian Geology of the Tobacco Root Mountains*, *Montana*, pp. 227–243. Boulder, CO: Geological Society of America. Special Paper 377.
131. Roberts H, Dahl P, Kelley S, and Frei R (2002) New ^{207}Pb–^{206}Pb and ^{40}Ar–^{39}Ar ages from SW Montana, USA: Constraints on the Proterozoic and Archaean tectonic and depositional history of the Wyoming Province. *Precambrian Research* 117: 119–143.
132. Grew ES (1982) Geology of southern Prince Charles Mountains, East Antarctica. In: Craddock C (ed.) *Antarctic Geoscience*, pp. 473–478. Madison: University of Wisconsin Press.

133. Rowley PD, Ford AB, Williams PI, and Pride DE (1983) Metallogenic provinces of Antarctica. In: Oliver RL, James PR, and Jago JB (eds.) *Antarctic Earth Science*, pp. 414–419. Cambridge: Cambridge University Press.
134. Phillips G, Wilson CJL, Campbell LH, and Allen CM (2006) U–Th–Pb detrital zircon geochronology from the southern Prince Charles Mountains, East Antarctica – Defining the Archaean to Neoproterozoic Ruker Province. *Precambrian Research* 148: 292–306.
135. Yeates G (1990) Middleback Range iron ore deposits. In: Hughes FE (ed.) *Geology of the Mineral Deposits of Australia and Papua New Guinea*. Australasian Institute of Mining and Metallurgy Monograph 14, pp. 1045–1048.
136. Fanning CM, Reid AJ, and Teale GS (2007) A geochronological framework for the Gawler craton, South Australia. *South Australia Geological Survey Bulletin* 55: 80.
137. Szpunar M, Hand M, Barovich K, Jagodzinski E, and Belousova E (2011) Isotopic and geochemical constraints on the Paleoproterozoic Hutchinson Group, southern Australia: Implications for Paleoproterozoic continental reconstructions. *Precambrian Research* 187: 99–126.
138. Gnaneshwar Rao T and Naqvi SM (1995) Geochemistry, depositional environment and tectonic setting of the BIF's of the Late Archaean Chitradurga Schist Belt, India. *Chemical Geology* 121: 217–243.
139. Khan RMK and Naqvi SM (1996) Geology, geochemistry and genesis of BIF of Kushtagi schist belt, Archaean Dharwar craton, India. *Mineralium Deposita* 31: 123–133.
140. Nutman AP, Chadwick B, Krishna Rao B, and Vasudev VN (1996) SHRIMP U/Pb zircon ages of acid volcanic rocks in the Chitradurga and Sandur Groups, and granites adjacent to the Sandur Schist belt, Karnataka. *Journal of the Geological Society of India* 47: 153–164.
141. Barrett TJ and Fralick PW (1989) Turbidites and iron formation, Beardmore-Geraldton, Ontario: Application of a combined ramp/fan model to Archean clastic and chemical sedimentation. *Sedimentology* 36: 221–234.
142. Fralick PW and Pufahl PK (2006) Iron formation in Neoarchean deltaic successions and the microbially mediated deposition of transgressive systems tracts. *Journal of Sedimentary Research* 76: 1057–1066.
143. Excludes Algoma-type iron formation in the Benxi region.
144. Sills JD, Wang K-Y, Windley BF, Yan Y-H, and Zhai M-G (1987) Banded iron formations in the Early Precambrian of NE China. In: Appel PWU and LaBerge GL (eds.) *Precambrian Iron-Formations*, pp. 449–465. Athens: Theophrastus Publications.
145. Zhai M-G and Windley BF (1990) The Archaean and Early Proterozoic banded iron formations of North China: Their characteristics, geotectonic relations, chemistry and implications for crustal growth. *Precambrian Research* 48: 267–286.
146. Hou K-J, Li Y-H, and Wan D-F (2007) Constraints on the Archean atmospheric oxygen and sulfur cycle from mass-independent sulfur records from Anshan-Benxi BIFs, Liaoning Province, China. *Science in China Series D (Earth Sciences)* 50: 1471–1478 [in English].
147. Hunter MA, Bickle MJ, Nisbet EG, Martin A, and Chapman HJ (1998) Continental extensional setting for the Archean Belingwe greenstone belt, Zimbabwe. *Geology* 26: 883–886.
148. Hofmann A and Kusky TM (2004) The Belingwe greenstone belt: Ensialic or oceanic? In: Kusky TM (ed.) *Precambrian Ophiolites and Related Rocks*. *Developments in Precambrian Geology*, Vol. 13, pp. 487–537. Amsterdam: Elsevier.
149. Wilson JF, Nesbitt RW, and Fanning CM (1995) Zircon geochronology of Archaean felsic sequences in the Zimbabwe craton: A revision of greenstone stratigraphy and a model for crustal growth. In: Coward MP and Ries AC (eds.) *Early Precambrian Processes*, pp. 109–126. London: Geological Society. Special Publication 95.
150. Naqvi SM, Sawkar RH, Subba Rao DV, Govil PK, and Gnaneshwar Rao T (1988) Geology, geochemistry and tectonic setting of Archaean greywackes from Karnataka nucleus, India. *Precambrian Research* 39: 193–216.
151. Arora M, Govil PK, Charan SN, et al. (1995) Geochemistry and origin of Archean banded iron-formation from the Bababudan Schist belt, India. *Economic Geology* 90: 2040–2057.
152. Trendall AF, de Laeter JR, Nelson DR, and Mukhopadhyay D (1997) A precise zircon U–Pb age for the base of the BIF of the Mulaingiri Formation (Bababudan Group, Dharwar Supergroup) of the Karnataka craton. *Journal of the Geological Society of India* 50: 161–170.
153. Bleeker W, Ketchum JWF, Jackson VA, and Villeneuve ME (1999) The central Slave basement complex, Part I: Its structural topology and autochthonous cover. *Canadian Journal of Earth Sciences* 36: 1083–1109.
154. Klein C and Ladeira EA (2002) Petrography and geochemistry of the least altered banded iron-formation of the Archean Carajás Formation, northern Brazil. *Economic Geology* 97: 643–651.
155. Trendall AF, Basei MAS, de Laeter JR, and Nelson DP (1998) SHRIMP zircon U–Pb constraints on the age of the Carajás Formation, Grão Pará Group, Amazon craton. *Journal of South American Earth Sciences* 11: 265–277.
156. Frimmel HE (1996) Witwatersrand iron-formations and their significance for gold genesis and the composition limits of orthoamphibole. *Mineralogy and Petrology* 56: 273–295.
157. Kositcin N and Krapež B (2004) Relationship between detrital zircon age-spectra and the tectonic evolution of the Late Archaean Witwatersrand Basin, South Africa. *Precambrian Research* 129: 141–168.
158. Smith AJB, Beukes NJ, and Gutzmer J (in review) The composition and depositional environments of Mesoarchean iron formations of the West Rand Group, Witwatersrand Supergroup, South Africa. *Economic Geology* 108(1): 111–134.
159. Beukes NJ and Cairncross B (1991) A lithostratigraphic-sedimentological reference profile for the Late Archaean Mozaan Group, Pongola Sequence: Application to sequence stratigraphy and correlation with the Witwatersrand Supergroup. *South African Journal of Geology* 94: 44–69.
160. Hegner E, Kröner A, and Hunt P (1994) A precise U–Pb zircon age for the Archaean Pongola Supergroup volcanics in Swaziland. *Journal of African Earth Sciences* 18: 339–341.
161. Spaggiari CV, Pidgeon RT, and Wilde SA (2007) The Jack Hills greenstone belt, Western Australia. Part 2: Lithological relationships and implications for the deposition of $\geq$4.0 Ga detrital zircons. *Precambrian Research* 155: 261–286.
162. Rasmussen B, Fletcher IR, Muhling JR, and Wilde SA (2010) In situ U–Th–Pb geochronology of monazite and xenotime from the Jack Hills belt: Implications for the age of deposition and metamorphism of Hadean zircons. *Precambrian Research* 180: 26–46.
163. Anhaeusser CR (1976) The geology of the Sheba Hills area of the Barberton Mountain Land, South Africa, with particular reference to the Eureka syncline. *Transactions of the Geological Society of South Africa* 79: 253–280.
164. Eriksson KA (1983) Siliciclastic-hosted iron-formations in the Early Archean Barberton and Pilbara sequences. *Journal of the Geological Society of Australia* 30: 473–482.
165. Huebeck C and Lowe DR (1994) Depositional and tectonic setting of the Archean Moodies Group, Barberton greenstone belt, South Africa. *Precambrian Research* 68: 257–290.

Appendix 2 Exhalites Associated with Precambrian Deep-Water (Cu-Rich) Volcanogenic Massive Sulfide Deposits[a]

VMS deposit (District)	*Location*	*Age (Ma)*	*VMS (Mt)*	*Exhalite type(s)*	*Reference(s)*
Keete Inlet	Alaska, USA	~554–600	<1	Magnetite IF	9, 10
Jingtieshan	Gansu Province, China	586–670	<1	Hematite–magnetite–siderite IF, jasper	11, 12
Um Samiuki	Eastern Desert, Egypt	~750	<1	Magnetite IF	13–15
Matchless	Central Namibia	760–780	2.5	Magnetite IF	16–18
Otjihase	Central Namibia	760–780	15.4	Magnetite IF	16, 19, 20
Xiqiu	Zhejiang Province, China	~900	31.0	Jasper	21–23
Altîn-Tepe	Eastern Romania	~1000	10.9	Magnetite IF	24
Palmeiropolis	Tocantins State, Brazil	1170–1270	5.0	Magnetite IF	25, 26
Boksputs	Cape Province, South Africa	1275 ± 7	1.7	Magnetite IF	27, 28
Itaberaba	São Paulo State, Brazil	1395 ± 10	None (29)	Magnetite and hematite IF	30, 31
Bon Ton	Colorado, USA	~1700	<1	Magnetite IF	32, 33
Jones Hill	New Mexico, USA	1720 ± 15	11.0	Magnetite IF, spessartine-rich IF (coticule)	34–36
Old Dick/Bruce (Bagdad)	Arizona, USA	1721 ± 6	~2	Hematitic chert	37–39
United Verde (Jerome)	Arizona, USA	1738.5 ± 0.5	>30	Jasper, hematite IF	5, 40, 41
Copper Chief (Jerome)	Arizona, USA	1738.5 ± 0.5	<1	Jasper, magnetite, and hematite IF	5, 40, 42
Miguela	Eastern Bolivia	1765–1690	1.6	Magnetite and hematite IF	43, 44
Gunnison (Gunnison)	Colorado, USA	1776 ± 7	<1	Magnetite IF, hematitic chert	33, 45, 46
Encampment/Pearl	Wyoming, USA	1792 ± 15	<1	Magnetite IF, silicate IF, ferruginous chert	47, 48
San Diego	Western Australia, Australia	1843 ± 2	2.3	Magnetite IF; sulfide–silicate IF	49, 50
Sherritt Gordon	Manitoba, Canada	~1860	7.0	Sulfidic chert and schist	51, 52
Crandon	Wisconsin, USA	1869 ± 6	63.5	Pyritic argillite/tuff; pyritic chert	53–55
Eisenbrey/Thornapple	Wisconsin, USA	~1870	3.0	Magnetite IF; silicate IF	56, 57
Bend	Wisconsin, USA	~1870	3.7	Jasper, magnetite, and hematite IF	56, 58
Soucy	Québec, Canada	~1880	5.5	Sulfide–silicate IF	59, 60
Ruttan	Manitoba, Canada	1883 ± 2	82.8	Pyritic chert, sulfide IF	61–63
Anderson Lake (Snow Lake)	Manitoba, Canada	1892 ± 3	3.4	Sulfide IF	64, 65
Spruce Point (Snow Lake)	Manitoba, Canada	1892 ± 3	1.9	Sulfide IF	65, 66
Bigstone (Snow Lake)	Manitoba, Canada	1892 ± 3	1.5	Sulfidic tuff	65, 66
Aijala	Southwestern Finland	~1895	<1	Silicate IF, oxide IF	67, 68
Flin Flon (Flin Flon)	Manitoba, Canada	1903 ± 7	62.9	Sulfide IF, magnetite IF	69, 70
Wutai	Shanxi Province, China	~2530	Unknown	Sulfide IF, magnetite IF	71, 72
Ingladhal	Mysore State, India	2614 ± 8	~1	Pyritic IF	73–75
Izok	Nunavut, Canada	2681 ± 7	16.5	Sulfide–silicate IF	76
Corbet (Noranda)	Québec, Canada	2700.8 ± 2.6	2.8	Pyritic IF	77, 78
Millenbach (Noranda)	Québec, Canada	2700.8 ± 2.6	3.6	Sulfide IF	78–80
High Lake	Nunavut, Canada	2705 ± 1	15.6	Pyritic IF, carbonate IF	81
Geco (Manitouwadge)	Ontario, Canada	2720 ± 2	58.4	Magnetite IF; sulfide–silicate IF	82–84
Willroy (Manitouwadge)	Ontario, Canada	2723 ± 2	4.0	Magnetite IF; sulfide–silicate IF	82–84
Bell Allard (Matagami)	Québec, Canada	2724.5 ± 1.8	3.2	Sulfidic chert and tuff; silicate IF	85–88
Orchan (Matagami)	Québec, Canada	2724.5 ± 1.8	3.5	Sulfidic chert and tuff; silicate IF	85–88
Selbaie	Québec, Canada	2729 ± 3	29.9	Pyritic IF	89, 90
Sturgeon Lake (Sturgeon Lake)	Ontario, Canada	2735.5 ± 1.5	4.0	Pyritic tuff	91–94
Lyon Lake (Sturgeon Lake)	Ontario, Canada	2735.5 ± 1.5	3.2	Pyritic tuff	91–94
Scuddles (Golden Grove)	Western Australia, Australia	2960 ± 6	10.5	Sulfidic chert; magnetite IF; jasper	95, 96
Maranda (Murchison)	North West Province, South Africa	2966.5 ± 1.6	<1	Pyritic chert	97, 98

[a]Exhalites are chemical sedimentary rocks that formed on the sea floor by precipitation from submarine-hydrothermal fluids, generally as fallout from nonbuoyant plumes either proximal or distal to volcanogenic massive sulfide (VMS) deposits (1–4). Occurrences compiled here are restricted to VMS deposits having ≥1% Cu, which implies formation from high-temperature (>300 °C) fluids in relatively deep seawater at depths of >850 m (5). Excluded from this compilation are exhalites that occur within the same volcanic or volcanosedimentary sequence as the VMS deposit(s), but are at different (or unknown) stratigraphic levels (6). Exhalites associated with Zn–Pb deposits are also excluded, because they could have formed from low-temperature fluids in shallow restricted basins, within oxic seawater above the chemocline. Similarly excluded are magnetite-rich lenses that formed by subseafloor replacement and not as true exhalites, such as in the Gossan Hill VMS deposit in Western Australia (7), and epigenetic magnetite-rich bodies belonging to the iron oxide–copper–gold (IOCG) class of deposits that formed in continental, not submarine, settings (8). With few exceptions, ages of the VMS deposits are based on high-precision U–Pb zircon geochronology of felsic metavolcanic host rocks. Abbreviations: Ma, million years; Mt, million metric tons; IF, iron formation.

1. Spry PG, Peter JM, and Slack JF (2000) Meta-exhalites as exploration guides to ore. *Reviews in Economic Geology* 11: 163–201.
2. Peter JM, Kjarsgaard IM, and Goodfellow WD (2003) Hydrothermal sedimentary rocks of the Heath Steele belt, Bathurst mining camp, New Brunswick: Part 1. Mineralogy and mineral chemistry. In: Goodfellow WD, McCutcheon SR, and Peter JM (eds.) *Massive Sulfide Deposits of the Bathurst Mining Camp*, *New Brunswick*, *and Northern Maine*. *Economic Geology Monograph* 11: 361–390.
3. Grenne T and Slack JF (2005) Geochemistry of jasper beds from the Ordovician Løkken ophiolite, Norway: Origin of proximal and distal siliceous exhalites. *Economic Geology* 100: 1511–1527.
4. Franklin JM, Gibson HL, Jonasson IR, and Galley AG (2005) Volcanogenic massive sulfide deposits. In: Hedenquist JW, Thompson JFH, Goldfarb RJ, and Richards JP (eds.) *Economic Geology One Hundredth Anniversary Volume 1905–2005*, pp. 523–560. Littleton, CO: Society of Economic Geologists.
5. Slack JF, Grenne T, Bekker A, Rouxel OJ, and Lindberg PA (2007) Suboxic deep seawater in the late Paleoproterozoic: Evidence from hematitic chert and iron formation related to seafloor-hydrothermal sulfide deposits, central Arizona, USA. *Earth and Planetary Science Letters* 255: 243–256.
6. Sangster DF (1978) *Exhalites Associated with Archaean Volcanogenic Massive Sulphide Deposits*, pp. 70–81. University of Western Australia, Geology Department and Extension Service Publication 2.
7. Sharpe R and Gemmell JB (2002) The Archean Cu–Zn magnetite-rich Gossan Hill volcanic-hosted massive sulfide deposit, Western Australia: Genesis of a multistage hydrothermal system. *Economic Geology* 97: 517–539.
8. Williams PJ, Barton MD, Johnson DA, et al. (2005) Iron oxide copper–gold deposits: Geology, space-time distribution, and possible modes of origin. In: Hedenquist JW, Thompson JFH, Goldfarb RJ, and Richards JP (eds.) *Economic Geology One Hundredth Anniversary Volume 1905–2005*, pp. 371–405. Littleton, CO: Society of Economic Geologists.
9. Maas KM, Still JC, Clough AH, and Oliver LK (1991) Mineral investigations in the Ketchikan mining district, Alaska, 1990: Southern Prince of Wales Island and vicinity. *U.S. Bureau of Mines Open File Report 33-91*, 138 p.
10. Slack JF, Shanks WC III, Karl SM, Gemery PA, Bittenbender PE, and Ridley WI (2007) Geochemical and sulfur-isotopic signatures of volcanogenic massive sulfide deposits on Prince of Wales Island and vicinity, Southeastern Alaska. U.S. Geological Survey Professional Paper 1732-C, 37 p.
11. Sun H, Wu J, Yu P, and Li J (1998) Geology, geochemistry and sulfur isotope composition of the Late Proterozoic Jingtieshan (superior-type) hematite–jasper–barite iron ore deposits associated with stratabound Cu mineralization in the Gansu Province, China. *Mineralium Deposita* 34: 102–112.
12. Mao J, Zhang Z, Yang J, Song B, Wu M, and Zuo G (1998) Single-zircon dating of Precambrian strata in the west sector of the northern Qilian Mountains and its geological significance. *Chinese Science Bulletin* 43: 1289–1294 [in English].
13. Shukri NM and Mansour MS (1980) Lithostratigraphy of Um Samiuki district, Eastern Desert, Egypt. *Jeddah University Institute of Applied Geology Bulletin* 4: 83–93.
14. Helmy HM, Kamel OA, and El-Mahallawi MM (1999) Silver- and silver-bearing minerals from the Precambrian volcanogenic massive sulfide deposit, Um Samiuki, Eastern Desert, Egypt. In: Stanley CJ (ed.) *Mineral Deposits*: *Processes to Processing*, pp. 163–166. Rotterdam: Balkema.
15. Ali KA, Stern RJ, Manton WI, Kimura JI, and Khamees HA (2009) Geochemistry, Nd isotopes and U–Pb SHRIMP zircon dating of Neoproterozoic volcanic rocks from the central Eastern Desert of Egypt: New insights into the ~750 Ma crust-forming event. *Precambrian Research* 171: 1–22.
16. Porada H (1985) Stratigraphy and facies in the Upper Proterozoic Damara Orogen, Namibia, based on a geodynamic model. *Precambrian Research* 29: 235–264.
17. Klemd R, Maiden KJ, and Okrusch M (1987) The Matchless copper deposit, South West Africa/Namibia: A deformed and metamorphosed massive sulfide deposit. *Economic Geology* 82: 587–599.
18. Hawkesworth CJ, Kramers JD, and Miller RMcG (1981) Old model Nd ages in Namibian Pan-African rocks. *Nature* 289: 278–282.
19. Goldberg I (1976) A preliminary account of the Otjihase copper deposit, South West Africa. *Economic Geology* 71: 384–390.
20. Hartmann KG (1994) *Tectonic and Structural Aspects at the Otjihase Mine*, *Matchless Belt*, *Namibia*. Unpublished MSc Thesis, Rhodes University, Grahamstown, South Africa, 101 p.
21. Sun H-T (1992) A general review of volcanogenic massive sulphide deposits in China. *Ore Geology Reviews* 7: 43–71.
22. Hou Z-Q, Deng J, Sun H-T, and Song S-H, (1999) Volcanogenic massive sulfide deposits in China: Setting, feature, and style. *Exploration and Mining Geology* 8: 149–175.
23. Xu Y-T, Han M, Shang S-C, Zhou C, Li H-M, and Wu Y-F (2000) Evidence for metallogenic geochemistry of volcano-hot spring deposition in Xiqiu copper deposit, Zhejiang Province, China. *Chinese Journal of Geochemistry* 19: 250–260 [in English].
24. Ianovici V and Borcoş M (1982) Romania. In: Dunning FW, Mykura W, and Slater D (eds.) *Mineral Deposits of Europe*, *Volume 2*: *Southeast Europe*, pp. 55–142. London: The Mineralogical Society and The Institution of Mining and Metallurgy.
25. Araujo SM (1986) *Petrologia e mineralizações sulfetadas da seqüência vulcano-sedimentar de Palmeirópolis-Goiás*. Unpublished MSc Thesis, Universidade de Brasília, Brasília, 196 p.
26. Araujo SM, Scott SD, and Longstaffe FJ (1996) Oxygen isotope composition of alteration zones of highly metamorphosed volcanogenic massive sulfide deposits: Geco, Canada, and Palmeirópolis, Brazil. *Economic Geology* 91: 697–712.
27. Geringer GJ, Pretorius JJ, and Cilliers FH (1987) Strata-bound copper–iron sulfide mineralization in a Proterozoic front arc setting at Boksputs, northwest Cape Province, South Africa—A possible Besshi-type deposit. *Mineralium Deposita* 22: 81–89.
28. Cornell DH and Pettersson A (2007) Ion probe zircon dating of metasediments from the Areachap and Kakamas terranes, Namaqua-Natal Province and the stratigraphic integrity of the Areachap Group. *South African Journal of Geology* 110: 575–584.
29. No massive sulfide occurs in this area but geochemical and oxygen isotope data suggest high-temperature, VMS-type alteration prior to regional metamorphism (23).
30. Pérez-Aguilar A, Juliani C, Monteiro LVS, Fallick AE, and Bettencourt JS (2005) Stable isotope constraints on Kuroko-type paleohydrothermal systems in the Mesoproterozoic Serra do Itaberaba Group, São Paulo State, Brazil. *Journal of South American Earth Sciences* 18: 305–321.
31. Juliani C, Hackspacher P, Dantas EL, and Fetter AH (2000) The Mesoproterozoic volcano-sedimentary Serra do Itaberaba Group of the central Ribeira belt, São Paulo State, Brazil: Implications for the age of the overlying São Roque Group. *Revista Brasil Geociencias* 30: 82–86.
32. Knight DC (1981) *Stratigraphy and Mineralogy of a Zinc-Rich Sillimanite Gneiss near Maysville*, *Chaffee County*, *Colorado*. Unpublished MSc Thesis, University of Manitoba, Winnipeg, 94 p.
33. Bickford ME, Shuster RD, and Boardman SJ (1989) U–Pb geochronology of the Proterozoic volcano-plutonic terrane in the Gunnison and Salida areas, Colorado. In: Grambling JA and Tewksbury BJ (eds.) *Proterozoic Geology of the Southern Rocky Mountains*, pp. 33–48. Boulder, CO: Geological Society of America. Special Paper 235.
34. Riesmeyer WD (1978) *Precambrian Geology and Ore Deposits of the Pecos Mining District*, *San Miguel and Santa Fe Counties*, *New Mexico*. Unpublished MS Thesis, University of New Mexico, Albuquerque, 215 p.
35. Robertson JM and Condie KC (1989) Geology and geochemistry of Early Proterozoic volcanic and subvolcanic rocks of the Pecos greenstone belt, Sangre de Cristo Mountains, New Mexico. In: Grambling JA and Tewksbury BJ (eds.) *Proterozoic Geology of the Southern Rocky Mountains*, pp. 119–146. Boulder, CO: Geological Society of America. Special Paper 235.

36. Slack JF, Grenne T, and Bekker A (2009) Seafloor-hydrothermal Si–Fe–Mn exhalites in the Pecos greenstone belt, New Mexico, and the redox state of ca.1720 Ma deep seawater. *Geosphere* 5: 302–314.
37. Conway CM (1986) Early Proterozoic geology and massive sulfide deposits, Jerome and Bagdad, Arizona; field guide to Early Proterozoic strata that host massive sulfide deposits at Bagdad, Arizona. In: Nations JD, Conway CM, and Swann GA (eds.) *Geology of Central and Northern Arizona*, pp. 140–157. Flagstaff: Northern Arizona University. Field Trip No. 8.
38. Connelly TJ and Conway CM (1987) Massive sulfide deposits at Bagdad, Arizona: End-products of a recurrent Early Proterozoic volcanic hydrothermal system. In: *Society of Economic Geologists Guidebook Series*, vol. 1, pp. 116–123.
39. Bryant B, Wooden JL, and Nealey JD (2001) Geology, geochronology, geochemistry, and Pb-isotopic compositions of Proterozoic rocks, Poachie region, west-central Arizona—A study of the east boundary of the Proterozoic Mojave crustal province. U.S. Geological Survey Professional Paper 1639, 54 p.
40. Lindberg PA and Gustin MS (1987) Field-trip guide to the geology, structure, and alteration of the Jerome, Arizona ore deposits. In: *Arizona Bureau of Mines and Mineral Technology*, vol. 5, pp. 176–181. Geological Survey Branch Special Paper.
41. Gustin MS (1990) Stratigraphy and alteration of the host rocks, United Verde massive sulfide deposit, Jerome, Arizona. *Economic Geology* 85: 29–49.
42. Lindberg PA (1986) Geology of the Copper Chief mine, Jerome district, Arizona. *Arizona Geological Society Digest* 16: 343–349.
43. Biste M and Gourlay AW (2000) Geology and setting of the Miguela A-Zone, Guarayos greenstone belt, eastern Bolivia. In: Sherlock R and Logan MAV (eds.) *VMS Deposits of Latin America*, pp. 359–374. Canada: Geological Association of Canada. Mineral Deposits Division Special Publication 2.
44. Boger SD, Raetz M, Giles D, Etchart E, and Fanning CM (2005) U–Pb age data from the Sunsas region of eastern Bolivia: Evidence for the allochthonous origin of the Paragua block. *Precambrian Research* 139: 121–146.
45. Drobeck PA (1981) Proterozoic syngenetic massive sulfide deposits in the Gunnison gold belt, Colorado. In: *New Mexico Geological Society Guidebook*, vol. 32, pp. 279–286.
46. Nelson CJ and Riesmeyer WD (1983) Geology of the Anaconda–Gunnison mine area, Gunnison County, Colorado. In: Anonymous (ed.) *Gunnison Gold Belt and Powderhorn Carbonatite Field Trip*, pp. 8–18. Denver: Denver Region Exploration Geologists Society.
47. Klipfel PD (1992) *Geology and Metallogeny of the Southern Portion of the Encampment District*, *Colorado and Wyoming*. Unpublished PhD Thesis, Colorado School of Mines, Golden, 244 p.
48. Premo WR and Van Schmus WR (1989) Zircon geochronology of Precambrian rocks in southeastern Wyoming and northern Colorado In: Grambling JA and Tewksbury BJ (eds.) *Proterozoic Geology of the Southern Rocky Mountains*, pp. 13–32. Boulder, CO: Geological Society of America. Special Paper 235.
49. Page RW, Blake DH, Sun Ss, Tyler IM, Griffin TJ, and Thorne AM (1994) New geological and geochronological constraints on volcanogenic massive sulphide prospectivity near Halls Creek (WA). *AGSO Research Newsletter* 20: 4–7.
50. Anglo Australian Resources web site, www.anglo.com.au/koongie.asp.
51. Froese E and Goetz PA (1981) Geology of the Sherridon Group in the vicinity of Sherridon, Manitoba. Geological Survey of Canada Paper 80–21, 20 p.
52. Morelli RM and Creaser RA (2007) Testing the robustness of the Re-Os low-level sulfide chronometers: An example from metamorphosed VMS ores, Trans Hudson orogen, Canada [abs.]. *Geological Society of America Abstracts with Progams* 39: 276.
53. Lambe RN and Rowe RG (1987) Volcanic history, mineralization, and alteration of the Crandon massive sulfide deposit, Wisconsin. *Economic Geology* 82: 1204–1238.
54. Sims PK, Van Schmus WR, Schulz KJ, and Peterman ZE (1989) Tectono-stratigraphic evolution of the Early Proterozoic Wisconsin magmatic terranes of the Penokean orogen. *Canadian Journal of Earth Sciences* 26: 2145–2158.
55. Erickson AJ Jr. and Côté R (1996) Geological summary—Crandon deposit. *Institute on Lake Superior Geology Proceedings* 42: 129–141.
56. DeMatties TA (1996) A geologic framework for Early Proterozoic volcanogenic massive sulfide deposits in Wisconsin: An exploration model. *Institute on Lake Superior Geology Proceedings* 42: 31–65.
57. May ER (1996) Eisenbrey: A structurally complex Proterozoic copper–zinc massive sulfide deposit, Rusk County, Wisconsin. *Institute on Lake Superior Geology Proceedings* 42: 107–128.
58. DeMatties TA and Rowell WF (1996) The Bend deposit: An Early Proterozoic copper–gold VMS deposit. *Institute on Lake Superior Geology Proceedings* 42: 143–159.
59. Barrett TJ, Wares RP, and Fox JS (1988) Two-stage hydrothermal formation of a Lower Proterozoic sediment-hosted massive sulfide deposit, northern Labrador Trough, Quebec. *Canadian Mineralogist* 26: 871–888.
60. Wares RP and Clark T (1994) Geochemical effects of basin evolution on exhalative massive sulfide deposits, northern Labrador Trough [abs.]. *Geological Association of Canada Abstracts with Programs* 19: A118.
61. Speakman DS, Chornoby PJ, Haystead BCW, and Holmes GF (1982) Geology of the Ruttan deposit, northern Manitoba. In: Hutchinson RW, Spence CD, and Franklin JM (eds.) *Precambrian Sulphide Deposits*, pp. 525–555. Canada: Geological Association of Canada. Special Paper 25.
62. Barrie CT and Taylor CF (2001) Geology, alteration mineralogy, geochemistry and volcanogenic massive-sulphide potential of the Ruttan mine area and the southern Rusty Lake volcanic belt (NTS 64B). *Open File Report OF2001-9*, Manitoba Geological Survey, 25 p.
63. Barrie CT, Taylor C, and Ames DE (2005) Geology and metal contents of the Ruttan volcanogenic massive sulfide deposit, northern Manitoba, Canada. *Mineralium Deposita* 39: 795–812.
64. Bailes AH and Galley AG (1996) Setting of Paleoproterozoic volcanic-hosted massive base metal sulfide deposits, Snow Lake. *Geological Survey of Canada Bulletin* 426: 105–138.
65. Bailes AH and Galley AG (1999) Evolution of the Paleoproterozoic Snow Lake arc assemblage and geodynamic setting for associated volcanic-hosted massive sulphide deposits, Flin Flon Belt, Manitoba, Canada. *Canadian Journal of Earth Sciences* 36: 1789–1805.
66. Gale GH, Dabek LB, and Fedikow MAF (1997) The application of rare earth element analyses in the exploration for volcanogenic massive sulfide type deposits. *Exploration and Mining Geology* 6: 233–252.
67. Latvalahti U (1979) Cu–Zn–Pb ores of the Aijala-Orijarvi area, southwest Finland. *Economic Geology* 74: 1035–1059.
68. Väisänen M and Mänttäri I (2002) 1.90-1.88 Ga arc and back-arc basin in the Orijärvi area, SW Finland. *Geological Survey of Finland Bulletin* 74: 185–214.
69. Syme EC and Bailes AH (1993) Stratigraphic and tectonic setting of Early Proterozoic volcanogenic massive sulfide deposits, Flin Flon, Manitoba. *Economic Geology* 88: 566–589.
70. Stern RA, Machado N, Syme EC, Lucas SB, and David J (1999) Chronology of crustal growth and recycling in the Paleoproterozoic Amisk collage (Flin Flon belt), Trans-Hudson Orogen, Canada. *Canadian Journal of Earth Sciences* 36: 1807–1827.
71. Li J, Kusky T, Niu X, Jun F, and Polat A (2004) Neoarchean massive sulfide of Wutai Mountain, North China: A black smoker chimney and mound complex within 2.50 Ga-old oceanic crust. In: Kusky TM (ed.) *Precambrian Ophiolites and Related Rocks*. *Developments in Precambrian Geology* 13: 339–362.
72. Kröner A, Wilde SA, Li J-H, and Wang K-Y (2005) Age and evolution of a Late Archean to Paleoproterozoic upper to lower crustal section in the Wutaishan/Hengshan/Fuping terrain of northern China. *Journal of Asian Earth Sciences* 24: 577–595.

73. Bhattacharyay HN, Mukherjee AD, and Bhattacharyay PK (1993) Rock-water interaction and evolution of sulphide ores in the Late Archaean Chitradurga greenstone belt of southern India. *Mineralium Deposita* 28: 303–309.
74. Raghu Nandan KR, Vidyadharay KT, Murthy VS, and Naik RH (1995) Base metal and precious metal mineralisation in Ingaldhalu area, Chitradurga greenstone belt, Karnataka. *Records of the Geological Survey of India* 120: 68–82.
75. Nutman AP, Chadwick B, Rao BK, and Vasudev VN (1996) SHRIMP U/Pb zircon ages of acid volcanic rocks in the Chitradurga and Sandur Groups, and granites adjacent to the Sandur Schist belt, Karnataka. *Journal of the Geological Society of India* 47: 153–164.
76. Morrison IR (2004) Geology of the Izok massive sulfide deposit, Nunavut Territory, Canada. *Exploration and Mining Geology* 13: 25–36.
77. Knuckey MJ and Watkins JJ (1982) The geology of the Corbet massive sulphide deposit, Noranda district, Quebec, Canada. In: Hutchinson RW, Spence CD, and Franklin JM (eds.) *Precambrian Sulphide Deposits*, pp. 297–317. Canada: Geological Association of Canada. Special Paper 25.
78. Mortensen JK (1993) U–Pb geochronology of the eastern Abitibi Subprovince. Part 2: Noranda-Kirkland Lake area. *Canadian Journal of Earth Sciences* 30: 29–41.
79. Knuckey MJ, Comba CDA, and Riverin G (1982) Structure, metal zoning and alteration at the Millenbach deposit, Noranda, Quebec. In: Hutchinson RW, Spence CD, and Franklin JM (eds.) *Precambrian Sulphide Deposits*, pp. 255–295. Canada: Geological Association of Canada. Special Paper 25.
80. Kalogeropoulos SI and Scott SD (1989) Mineralogy and geochemistry of an Archean tuffaceous exhalite: The main contact tuff, Millenbach mine area, Noranda, Quebec. *Canadian Journal of Earth Sciences* 26: 88–105.
81. Petch CA (2004) The geology and mineralization of the High Lake volcanic-hosted massive sulfide deposit, Nunavut. *Exploration and Mining Geology* 13: 37–47.
82. Sangster DF and Scott SD (1976) Precambrian, strata-bound, massive Cu–Zn–Pb sulfide ores of North America. In: Wolf KH (ed.) *Handbook of Strata-Bound and Stratiform Ore Deposits*, vol. 6, pp. 129–222. Amsterdam: Elsevier.
83. Friesen RG, Pierce GA, and Weeks RM (1982) Geology of the Geco base metal deposit. In: Hutchinson RW, Spence CD, and Franklin JM (eds.) *Precambrian Sulphide Deposits*, pp. 343–363. Canada: Geological Association of Canada. Special Paper 25.
84. Zaleski E, van Breemen O, and Peterson VL (1999) Geological evolution of the Manitouwadge greenstone belt and Wawa–Quetico subprovince boundary, Superior Province, Ontario, constrained by U–Pb zircon dates of supracrustal and plutonic rocks. *Canadian Journal of Earth Sciences* 36: 945–966.
85. Costa UR, Barnett RL, and Kerrich R (1983) The Mattagami Lake mine Archean Zn–Cu sulfide deposit, Quebec: Hydrothermal coprecipitation of talc and sulfides in a sea-floor brine pool—Evidence from geochemistry, $^{18}O/^{16}O$, and mineral chemistry. *Economic Geology* 78: 1144–1203.
86. Liaghat S and MacLean WH (1992) The Key Tuffite, Matagami mining district: Origin of the tuff components and mass changes. *Exploration and Mining Geology* 1: 197–207.
87. Piche M, Guha J, and Daigneault R (1993) Stratigraphic and structural aspects of the volcanic rocks of the Matagami mining camp, Quebec: Implications for the Norita ore deposit. *Economic Geology* 88: 1542–1558.
88. Mortensen JK (1993) U–Pb geochronology of the eastern Abitibi Subprovince. Part 1: Chibougamau–Matagami–Joutel region. *Canadian Journal of Earth Sciences* 30: 11–28.
89. Barrie CT and Krogh TE (1996) U–Pb zircon geochronology of the Selbaie Cu–Zn–Ag–Au mine, Abitibi subprovince, Canada. *Economic Geology* 91: 563–575.
90. Taner MF (2000) The geology of the volcanic-associated polymetallic (Zn, Cu, Ag and Au) Selbaie deposits, Abitibi, Quebec, Canada. *Exploration and Mining Geology* 9: 189–214.
91. Davis DW, Krogh TE, Hinzer J, and Nakamura E (1985) Zircon dating of polycyclic volcanism at Sturgeon Lake and implications for base metal mineralization. *Economic Geology* 80: 1942–1952.
92. Shegelski RJ (1987) The depositional environment of Archean iron formations, Sturgeon-Savant greenstone belt, Ontario, Canada. In: Appel PWU and LaBerge GL (eds.) *Precambrian Iron-Formations*, pp. 329–344. Athens: Theophrastus Publications S.A.
93. Koopman ER, Patterson MR, Franklin JM, and Poulsen KH (1991) Stratigraphic and structural geology of the Lyon Lake massive sulphide deposit, Sturgeon Lake, Ontario. In: Franklin JM, Schnieders BR, and Koopman ER (eds.) *Mineral Deposits in the Western Superior Province*, *Ontario* (*Field Trip 9*), pp. 95–104. Geological Survey of Canada Open File 2164.
94. Hudak GL, Morton RL, Franklin JM, and Peterson DM., 2003, Morphology, distribution, and estimated eruption volumes for intracaldera tuffs associated with volcanic-hosted massive sulfide deposits in the Archean Sturgeon Lake Caldera complex, northwestern Ontario. In: White J, Smellie J, and Clague D (eds.) *Explosive Subaqueous Volcanism*, pp. 345–360. Geophysical Monograph 140.
95. Ashley PM, Dudley RJ, Lesh RH, Marr JM, and Ryall AW (1988) The Scuddles Cu–Zn prospect, an Archean volcanogenic massive sulfide deposit, Golden Grove district, Western Australia. *Economic Geology* 83: 918–951.
96. Wang Q, Schiøtte L, and Campbell IH (1998) Geochronology of supracrustal rocks from the Golden Grove area, Murchison province, Yilgarn craton, Western Australia. *Australian Journal of Earth Sciences* 45: 571–577.
97. Vearncombe JR, Barton JM, Cheshire PE, De Beer JH, Stettler EH, and Brandl G (1992) Geology, geophysics and mineralisation of the Murchison schist belt, Rooiwater Complex and surrounding granitoids. South African Geological Survey Memoir 81, 139 p.
98. Brandl G, Jaeckel P, and Kroner A (1996) Single zircon age for the felsic Rubbervale Formation, Murchison greenstone belt, South Africa. *South African Journal of Geology* 99: 299–234.

References

Abbott DH and Isley AE (2002) The intensity, occurrence, and duration of superplume events and eras over geological time. *Journal of Geodynamics* 34: 265–307.

Abbott ST and Sweet IP (2000) Tectonic control on third-order sequences in a siliciclastic ramp-style basin: An example from the Roper Superbasin (Mesoproterozoic), northern Australia. *Australian Journal of Earth Sciences* 47: 637–657.

Abraham K, Hofmann A, Foley SF, et al. (2011) Coupled silicon–oxygen isotope fractionation traces Archaean silicification. *Earth and Planetary Science Letters* 301: 222–230.

Aharon P (2005) Redox stratification and anoxia of the early Precambrian oceans: Implications for carbon isotope excursions and oxidation events. *Precambrian Research* 137: 207–222.

Ahn JH and Buseck PR (1990) Hematite nanospheres of possible colloidal origin from a Precambrian banded iron formation. *Science* 250: 111–113.

Akhmedov AM (1972a) Hematite oolites in sedimentary rocks of the Pechenga Complex. In: Belkov IV (ed.) *Materials on Mineralogy of the Kola Peninsula*, pp. 135–137. Leningrad: Nauka (in Russian).

Akhmedov AM (1972b) Iron-rich metasedimentary rocks of the Pechenga Complex and their genesis In: Belkov IV (ed.) *Materials on Geology and Metallogeny of Kola Peninsula*, pp. 125–131. Apatity: Kola Science Centre (in Russian).

Alexander BW, Bau M, and Andersson P (2009) Neodymium isotopes in Archean seawater and implications for the marine Nd cycle in Earth's early oceans. *Earth and Planetary Science Letters* 283: 144–155.

Alexander BW, Bau M, Andersson P, and Dulski P (2008) Continentally-derived solutes in shallow Archean seawater: Rare earth element and Nd isotope evidence in iron

formation from the 2.9 Ga Pongola Supergroup, South Africa. *Geochimica et Cosmochimica Acta* 72: 378–394.
Alibert C and McCulloch MT (1993) Rare earth element and neodymium isotopic compositions of the banded iron-formations and associated shales from Hamersley, Western Australia. *Geochimica et Cosmochimica Acta* 57: 187–204.
Aller RC, Mackin JE, and Cox RT (1986) Diagenesis of Fe and S in Amazon inner shelf muds – apparent dominance of Fe reduction and implications for the genesis of ironstones. *Continental Shelf Research* 6: 263–289.
Aller RC, Madrid V, Chistoserdov A, Aller JY, and Heilbrun C (2010) Unsteady diagenetic processes and sulfur biogeochemistry in tropical deltaic muds: Implications for oceanic isotope cycles and the sedimentary record. *Geochimica et Cosmochimica Acta* 74: 4671–4692.
Alt JC (1988) Hydrothermal oxide and nontronite deposits on seamounts in the Eastern Pacific. *Marine Geology* 81: 227–239.
Alt JC (2003) Stable isotopic composition of upper oceanic crust formed at a fast spreading ridge, ODP Site 801. *Geochemistry, Geophysics, Geosystems* 4: 8908.
Alt JC, France-Lanord C, Floyd PA, Castillo P, and Galy A (1992) Low-temperature hydrothermal alteration of Jurassic ocean crust, Site 801. *Proceedings of the Ocean Drilling Program, Scientific Results* 129: 415–427.
Altermann W and Nelson DR (1998) Sedimentation rates, basin analysis, and regional correlations of three Neoarchaean and Palaeoproterozoic sub-basins of the Kaapvaal Craton as inferred from precise U–Pb zircon ages from volcaniclastic sediments. *Sedimentary Geology* 120: 225–256.
Amakawa H, Nozakia Y, and Masuda A (1996) Precise determination of variations in the $^{138}Ce/^{142}Ce$ ratios of marine ferromanganese nodules. *Chemical Geology* 131: 183–195.
Anbar AD, Duan Y, Lyons TW, et al. (2007) A whiff of oxygen before the Great Oxidation Event? *Nature* 317: 1903–1906.
Anbar AD and Holland HD (1992) The photochemistry of manganese and the origin of banded iron formations. *Geochimica et Cosmochimica Acta* 56: 2595–2603.
Anbar AD and Rouxel OJ (2007) Metal stable isotopes in paleoceanography. *Annual Review of Earth and Planetary Sciences* 35: 717–746.
Andre L, Cardinal D, Alleman LY, and Moorbath S (2006) Silicon isotopes in 3.8 Ga West Greenland rocks as clues to the Eoarchaean supracrustal Si cycle. *Earth and Planetary Science Letters* 245: 162–173.
Arndt NT, Nelson DR, Compston W, Trendall AF, and Thorne AM (1991) The age of the Fortescue Group, Hamersley Basin, Western Australia, from ion microprobe zircon U–Pb results. *Australian Journal of Earth Sciences* 38: 261–281.
Arnold GL, Anbar AD, Barling J, and Lyons TW (2004) Molybdenum isotope evidence for widespread anoxia in mid-Proterozoic oceans. *Science* 304: 87–90.
Arthur MA and Sageman BB (1994) Marine black shales: Depositional mechanisms and environments of ancient deposits. *Annual Review of Earth and Planetary Sciences* 22: 499–551.
Arvidson RS, Mackenzie FT, and Guidry MW (2006) MAGIC: A Phanerozoic model for the geochemical cycling of major rock-forming components. *American Journal of Science* 306: 135–190.
Ayres DE (1972) Genesis of iron-bearing minerals in banded iron formation mesobands in the Dales Gorge Member, Hamersley Group, Western Australia. *Economic Geology* 67: 1214–1233.
Banerji A (1977) On the Precambrian banded iron formations and the manganese ores of the Singhbhum region, eastern India. *Economic Geology* 72: 90–98.
Barghoorn ES and Tyler SA (1965) Microorganisms from Gunflint Chert. *Science* 147: 563–577.
Barley ME, Bekker A, and Krapež B (2005) Late Archean to early Paleoproterozoic global tectonics, environmental change and the rise of atmospheric oxygen. *Earth and Planetary Science Letters* 238: 156–171.
Barley ME, Pickard AL, and Sylvester PJ (1997) Emplacement of a large igneous province as a possible cause of banded iron formation 2.45 billion years ago. *Nature* 385: 55–58.
Barrett TJ, Wares RP, and Fox JS (1988) Two-stage hydrothermal formation of a Lower Proterozoic sediment-hosted massive sulfide deposit, northern Labrabor Trough, Quebec. *Canadian Mineralogist* 26: 871–888.
Barton ES, Altermann W, Williams IS, and Smith CB (1994) U–Pb zircon age for a tuff in the Campbellrand Group, Griqualand West Sequence, South Africa: Implications for Early Proterozoic rock accumulation rates. *Geology* 22: 343–346.
Basile-Doelsch I (2006) Si stable isotopes in the Earth's surface: A review. *Journal of Geochemical Exploration* 88: 252–256.
Basile-Doelsch I, Meunier J, and Parron C (2005) Another continental pool in the terrestrial silicon cycle. *Nature* 433: 399–402.
Bau M and Dulski P (1996) Distribution of yttrium and rare-earth elements in the Penge and Kuruman iron-formations, Transvaal Supergroup, South Africa. *Precambrian Research* 79: 37–55.
Bau M, Hohndorf A, Dulski P, and Beukes NJ (1997a) Sources of rare-earth elements and iron in Paleoproterozoic iron-formations from the Transvaal Supergroup, South Africa: Evidence from neodymium isotopes. *Journal of Geology* 105: 121–129.
Bau M and Möller P (1993) Rare-earth element systematics of the chemically precipitated component in Early Precambrian iron formations and the evolution of the terrestrial atmosphere–hydrosphere–lithosphere system. *Geochimica et Cosmochimica Acta* 57: 2239–2249.
Bau M, Möller P, and Dulski P (1997b) Yttrium and lanthanides in eastern Mediterranean seawater and their fractionation during redox-cycling. *Marine Chemistry* 56: 123–131.
Baur ME (1979) Thermodynamics of heterogeneous iron—Carbon systems: Implications for the terrestrial primitive reducing atmosphere. *Chemical Geology* 22: 189–206.
Baur ME, Hayes JM, Studley SA, and Walter MA (1985) Millimeter-scale variations of stable isotope abundances in carbonates from banded iron-formations in the Hamersley Group of Western Australia. *Economic Geology* 80: 270–282.
Beal EJ, House CH, and Orphan VJ (2009) Manganese- and iron-dependent marine methane oxidation. *Science* 325: 184–187.
Beard BL, Handler RM, Scherer MM, et al. (2010) Iron isotope fractionation between aqueous ferrous iron and goethite. *Earth and Planetary Science Letters* 295: 241–250.
Beard BL, Johnson CM, Cox L, Sun H, Nealson KH, and Aguilar C (1999) Iron isotope biosignatures. *Science* 285: 1889–1892.
Beard BL, Johnson CM, Skulan JL, Nealson KH, Cox L, and Sun H (2003) Application of Fe isotopes to tracing the geochemical and biological cycling of Fe. *Chemical Geology* 195: 87–117.
Beaumont V and Robert F (1999) Nitrogen isotope ratios of kerogens in Precambrian cherts: A record of the evolution of atmospheric chemistry? *Precambrian Research* 96: 63–82.
Becker RH and Clayton RN (1972) Carbon isotope evidence for the origin of a banded iron-formation in Western Australia. *Geochimica et Cosmochimica Acta* 36: 577–595.
Behrends T and Van Cappellen P (2007) Transformation of hematite into magnetite during dissimilatory iron reduction—conditions and mechanisms. *Geomicrobiology Journal* 24: 403–416.
Bekker A, Barley ME, Fiorentini ML, Rouxel OJ, Rumble D, and Beresford SW (2009) Atmospheric sulfur in Archean komatiite-hosted nickel deposits. *Science* 326: 1086–1089.
Bekker A and Holland HD (2012) Oxygen overshoot and recovery during the Early Paleoproterozoic. *Earth and Planetary Science Letters* 317–318: 295–304.
Bekker A, Holland HD, Wang P-L, et al. (2004) Dating the rise of atmospheric oxygen. *Nature* 427: 117–120.
Bekker A, Karhu JA, Eriksson KA, and Kaufman AJ (2003) Chemostratigraphy of Paleoproterozoic carbonate successions of the Wyoming Craton: Tectonic forcing of biogeochemical change? *Precambrian Research* 120: 279–325.
Bekker A and Kaufman AJ (2007) Oxidative forcing of global climate change: A biogeochemical record across the oldest Paleoproterozoic ice age in North America. *Earth and Planetary Science Letters* 258: 486–499.
Bekker A, Kaufman AJ, Karhu JA, et al. (2001) Chemostratigraphy of the Paleoproterozoic Duitschland Formation, South Africa: Implications for coupled climate change and carbon cycling. *American Journal of Science* 301: 261–285.
Bekker A, Krapež B, Slack JF, et al. (2012) Iron formation: The sedimentary product of the complex interplay among mantle, tectonic, oceanic, and biospheric processes – a reply. *Economic Geology* 107: 379–380.
Bekker A, Slack JF, Planavsky N, et al. (2010) Iron formation: The sedimentary product of a complex interplay among mantle, tectonic, oceanic, and biospheric processes. *Economic Geology* 105: 467–508.
Bennett SA, Rouxel OJ, Schmidt K, Garbe-Schonberg D, Statham PJ, and German CR (2009) Iron isotope fractionation in a buoyant hydrothermal plume, 5°S Mid-Atlantic Ridge. *Geochimica et Cosmochimica Acta* 73: 5619–5634.
Berman RG, Sanborn-Barrie M, Stern RA, and Carson CJ (2005) Tectonometamorphism at ca. 2.35 and 1.85 Ga in the Rae Domain, western Churchill Province, Nunavut, Canada: Insight from structural, metamorphic, and *in situ* geochronologic analysis of the southwestern Committee Bay Belt. *Canadian Mineralogist* 43: 409–442.
Berman-Frank I, Cullen JT, Shaked Y, Sherrell RM, and Falkowski PG (2001) Iron availability, cellular iron-quotas, and nitrogen fixation in *Trichodesmium*. *Limnology and Oceanography* 46: 1249–1260.
Berman-Frank I, Quigg A, Finkel ZV, Irwin AJ, and Haramaty L (2007) Nitrogen-fixation strategies and Fe requirements in cyanobacteria. *Limnology and Oceanography* 52: 2260–2269.
Beukes NJ (1973) Precambrian iron-formations of southern Africa. *Economic Geology* 68: 960–1004.
Beukes NJ and Cairncross B (1991) A lithostratigraphic–sedimentological reference profile for the Late Archaean Mozaan Group, Pongola Sequence: Application to

sequence stratigraphy and correlation with the Witwatersrand Supergroup. *South African Journal of Geology* 94: 44–69.
Beukes NJ and Gutzmer J (2008) Origin and paleoenvironmental significance of major iron formations at the Archean-Paleoproterozoic boundary. *Reviews in Economic Geology* 15: 5–47.
Beukes NJ and Klein C (1990) Geochemistry and sedimentology of a facies transition—from microbanded to granular iron-formation—in the early Proterozoic Transvaal Supergroup, South Africa. *Precambrian Research* 47: 99–139.
Beukes NJ, Klein C, Kaufman AJ, and Hayes JM (1990) Carbonate petrography, kerogen distribution, and carbon and oxygen isotope variations in an early Proterozoic transition from limestone to iron-formation deposition, Transvaal Supergroup, South Africa. *Economic Geology* 85: 663–690.
Beukes NJ, Mukhopadyay J, and Gutzmer J (2008) Genesis of high-grade iron ores of the Archean iron ore group around Noamundi, India. *Economic Geology* 103: 365–386.
Bhattacharyya DP and Crerar DA (1993) Genetic model for the Phanerozoic oolitic ironstones and some speculations about its implications for the deposition of banded iron formation. *Proceedings of the National Academy of Sciences, India* 63: 48–72.
Bjerrum CJ and Canfield DE (2002) Ocean productivity before about 1.9 Ga ago limited by phosphorus adsorption onto iron oxides. *Nature* 417: 159–162.
Bleeker W, Ketchum JWF, Jackson VA, and Villeneuve ME (1999) The Central Slave Basement Complex, Part I: Its structural topology and autochthonous cover. *Canadian Journal of Earth Sciences* 36: 1083–1109.
Bleeker W and Macek J (1996) Evolution of the Thompson nickel belt, Manitoba: Setting of Ni–Cu deposits in the western part of the Circum Superior boundary zone. *Field Trip Guidebook A1, Geological Association of Canada/Mineralogical Association of Canada Annual Meeting*, Winnipeg, Manitoba, 27–29 May 1996. Winnipeg, MB: Geological Association of Canada.
Blothe M and Roden EE (2009) Composition and activity of an autotrophic Fe(II)-oxidizing, nitrate-reducing enrichment culture. *Applied Environmental Microbiology* 75: 6937–6940.
Bolhar R, Hofmann A, Woodhead J, Hergt J, and Dirks P (2002) Pb- and Nd-isotope systematics of stromatolitic limestones from the 2.7 Ga Ngezi Group of the Belingwe Greenstone Belt: Constraints on timing of deposition and provenance. *Precambrian Research* 114: 277–294.
Bolhar R, Kamber BS, Moorbath S, Fedo CM, and Whitehouse MJ (2004) Characterization of Early Archaean chemical sediments by trace element signatures. *Earth and Planetary Science Letters* 222: 43–60.
Borchert H (1965) Formation of marine sedimentary iron ores. In: Riley JP and Skirrow G (eds.) *Chemical Oceanography*, vol. 2, pp. 159–204. New York: Academic Press.
Bowring SA and Grotzinger JP (1992) Implications of new chronostratigraphy for tectonic evolution of Wopmay Orogen, northwest Canadian Shield. *American Journal of Science* 292: 1–20.
Bowring SA, Van Schmus WR, and Hoffman PF (1984) U–Pb zircon ages from Athapuscow aulacogen, East Arm of Great Slave Lake, N.W.T., Canada. *Canadian Journal of Earth Sciences* 21: 1315–1324.
Boyd ES, Anbar AD, Miller S, Hamilton TL, Lavin M, and Peters JW (2011) A late methanogen origin for molybdenum-dependent nitrogenase. *Geobiology* 9: 221–232.
Boyd PW and Ellwood MJ (2010) The biogeochemical cycle of iron in the ocean. *Nature Geoscience* 3: 675–682.
Boyle EA, Bergquist BA, Kayser RA, and Mahowald N (2005) Iron, manganese, and lead at Hawaii Ocean Time-series station ALOHA: Temporal variability and an intermediate water hydrothermal plume. *Geochimica et Cosmochimica Acta* 69: 933–952, 5165–5166.
Boyle EA, Edmond JM, and Sholkovitz ER (1977) Mechanism of iron removal in estuaries. *Geochimica et Cosmochimica Acta* 41: 1313–1324.
Brantley SL, Guynn RL, Liermann LJ, Anbar AD, Barling J, and Icopini G (2004) Fe isotopic fractionation during mineral dissolution with and without bacteria. *Geochimica et Cosmochimica Acta* 68: 3189–3204.
Braterman PS and Cairns-Smith AG (1986) Photoprecipitation and the BIFs—some quantitative aspects. *Origins of Life and Evolution of Biospheres* 16: 190–191.
Braterman PS, Cairns-Smith AG, and Sloper RW (1983) Photooxidation of hydrated Fe^{2+}—significance for banded iron formations. *Nature* 303: 163–164.
Braun J-J, Pagel M, Muller J-P, Bilong P, Michard A, and Guillet B (1990) Cerium anomalies in lateritic profiles. *Geochimica et Cosmochimica Acta* 54: 781–795.
Breitkopf JH (1988) Iron formations related to mafic volcanism and ensialic rifting in the southern margin zone of the Damara Orogen, Namibia. *Precambrian Research* 38: 111–130.
Brocks JJ (2011) Millimeter-scale concentration gradients of hydrocarbons in Archean shales: Live-oil escape or fingerprint of contamination? *Geochimica et Cosmochimica Acta* 75: 3196–3213.
Bronner G and Chauvel JJ (1979) Precambrian banded iron-formations of the Ijil Group (Kediat Ijil, Reguibat Shield, Mauritania). *Economic Geology* 74: 77–94.
Bruland KW and Lohan MC (2006) Controls of trace elements in seawater. In: Elderfield H (ed.) *The Oceans and Marine Geochemistry*, pp. 23–47. Oxford: Elsevier-Pergamon.
Buhn B, Stanistreet IG, and Okrusch M (1992) Late Proterozoic outer shelf manganese and iron deposits at Otjosondu (Namibia) related to the Damaran oceanic opening. *Economic Geology* 87: 1393–1411.
Buick R (1992) The antiquity of oxygenic photosynthesis: Evidence from stromatolites in sulphate-deficient Archaean lakes. *Science* 255: 74–77.
Buick IS, Allen C, Pandit M, Rubatto D, and Hermann J (2006) The Proterozoic magmatic and metamorphic history of the Banded Gneiss Complex, central Rajasthan, India: LA-ICP-MS U–Pb zircon constraints. *Precambrian Research* 151: 119–142.
Bullen TD, White AF, Childs CW, Vivit DV, and Schulz MS (2001) Demonstration of significant abiotic iron isotope fractionation in nature. *Geology* 29: 699–702.
Burkhalter RM (1995) Ooidal ironstones and ferruginous microbialites: Origin and relation to sequence stratigraphy (Aalenian and Bajocian, Swiss Jura Mountains). *Sedimentology* 42: 57–74.
Burton J and Fralick P (2007) Deposition and cementation of Paleoproterozoic Gunflint Formation carbonate: Implications for early hydrosphere chemistry. *Proceedings of the Institute on Lake Superior Geology* 53: 45–46.
Butler IB, Archer C, Vance D, Oldroyd A, and Rickard D (2005) Fe isotope fractionation on FeS formation in ambient aqueous solution. *Earth and Planetary Science Letters* 236: 430–442.
Byrne R and Sholkovitz E (1996) Marine chemistry and geochemistry of the lanthanides. In: Gschneider KA Jr. and Eyring L (eds.) *Handbook on the Physics and Chemistry of Rare Earths*, ch. 158, vol. 23, pp. 497–593. Amsterdam: Elsevier.
Cabral AR, Moore JM, Mapani BS, Koubová M, and Sattler CD (2011) Geochemical and mineralogical constraints on the genesis of the Otjosondu ferromanganese deposit, Namibia: Hydrothermal exhalative versus hydrogenetic (including snowball-Earth) origins. *South African Journal of Geology* 114: 57–76.
Cairns-Smith AG (1978) Precambrian solution photochemistry, inverse segregation, and banded iron formations. *Nature* 276: 807–808.
Cameron EM (1983) Evidence from Early Proterozoic anhydrite for sulfur isotopic partitioning in Precambrian oceans. *Nature* 304: 54–56.
Cameron V, Vance D, Archer C, and House CH (2009) A biomarker based on the stable isotopes of nickel. *Proceedings of the National Academy of Sciences of the United States of America* 106: 10944–10948.
Canavan F (1965) Iron and manganese ore deposits of iron range. In: McAndrew J (ed.) *Geology of Australian Ore Deposits. Eighth Commonwealth Mining and Metallurgical Congress of Australia and New Zealand*, pp. 391–393. Melbourne: Australasian Institute of Mining and Metallurgy.
Canfield DE (1998) A new model for Proterozoic ocean chemistry. *Nature* 396: 450–453.
Canfield DE, Poulton SW, Knoll AH, et al. (2008) Ferruginous conditions dominated later Neoproterozoic deep-water chemistry. *Science* 321: 949–952.
Canfield DE and Teske A (1996) Late Proterozoic rise in atmospheric oxygen concentration inferred from phylogenetic and sulphur-isotope studies. *Nature* 382: 127–132.
Canfield DE and Thamdrup B (2009) Towards a consistent classification scheme for geochemical environments, or, why we wish the term 'suboxic' would go away. *Geobiology* 7: 385–392.
Cannon WF, LaBerge GL, Klasner JS, and Schulz KJ (2008) The Gogebic iron range—a sample of the northern margin of the Penokean fold and thrust belt. *US Geological Survey Professional Paper 1730*. Reston, VA: US Geological Survey.
Cannon WF, Schulz KJ, Horton JW Jr., and Kring DA (2010) The Sudbury impact layer in the Paleoproterozoic iron ranges of northern Michigan, USA. *Geological Society of America Bulletin* 122: 50–75.
Castano JR and Garrels RM (1950) Experiments on the deposition of iron with special reference to the Clinton iron ore deposits. *Economic Geology* 45: 755–770.
Chandler FW (1984) Metallogenesis of an Early Proterozoic foreland sequence, eastern Hudson Bay, Canada. *Journal of the Geological Society* 141: 299–313.
Chandler FW (1986) Sedimentology and paleoclimatology of the Huronian (Early Aphebian) Lorrain and Gordon Lake Formations and their bearing on models for sedimentary copper mineralization. In: *Current Research, Part A. Geological Survey of Canada, Paper 86-1A*, pp. 121–132. Ottawa, ON: Geological Survey of Canada.
Chandler FW and Parrish RR (1989) Age of the Richmond Gulf Group and implications for rifting in the Trans-Hudson Orogen, Canada. *Precambrian Research* 44: 277–288.

Charette MA and Sholkovitz ER (2002) Oxidative precipitation of groundwater-derived ferrous iron in the subterranean estuary of a coastal bay. *Geophysical Research Letters* 29(10): 85-1–85-4.

Chernyshov NM, Albekov AY, and Ryborak MV (2009) On current status of scheme of stratigraphy and magmatism of early Precambrian of Voronezh crystalline massif. *Vestnik* 2: 33–40.

Chernyshov NM, Bayanova TB, Chernyshova MN, and Levkovich NV (1998) Age of norite-diorite intrusions based on geochronologic data for the Yelan nickel-bearing complex and its temporal relationship with gabbro-norites of the Mamon complex of the Voronezh Crystalline Massif. *Geologiya i Geofizika* 39: 1064–1070.

Chown EH, N'Dah E, and Mueller WU (2000) The relation between iron formation and low temperature hydrothermal alteration in an Archaean volcanic environment. *Precambrian Research* 101: 263–275.

Clement JC, Shrestha J, Ehrenfeld JG, and Jaffe PR (2005) Ammonium oxidation coupled to dissimilatory reduction of iron under anaerobic conditions in wetland soils. *Soil Biology and Biochemistry* 37: 2323–2328.

Cloud P (1955) Physical limits of glauconite formation. *American Association of Petroleum Geologists Bulletin* 39: 484–492.

Cloud PE (1965) Significance of Gunflint (Precambrian) microflora. *Science* 148: 27–35.

Cloud P (1973) Paleoecological significance of banded iron-formation. *Economic Geology* 68: 1135–1143.

Clout JM and Simonson BM (2005) Precambrian iron formations and iron-formation hosted iron ore deposits. In: Hedenquist JW, Thompson JFH, Goldfarb RJ, and Richards JP (eds.) *Economic Geology 100th Anniversary Volume, 1905–2005*, pp. 643–679. Littleton, CO: Society of Economic Geologists, Inc.

Cocherie A, Calvez JY, and Oudin-Dunlop E (1994) Hydrothermal activity as recorded by Red Sea sediments: Sr–Nd isotopes and REE signatures. *Marine Geology* 118: 291–302.

Comolli LR, Luef B, and Chan CS (2011) High resolution 2D and 3D cryo-TEM reveals structural adaptations of two stalk-forming bacteria to an Fe-oxidizing lifestyle. *Environmental Microbiology* 12: 2915–2929.

Condie KC (1993) Chemical composition and evolution of the upper continental crust: Contrasting results from surface samples and shales. *Chemical Geology* 104: 1–37.

Condie KC, Des Marais DJ, and Abbott D (2001) Precambrian superplumes and supercontinents: A record in black shales, carbon isotopes and paleoclimates? *Precambrian Research* 106: 239–260.

Corliss JB, Lyle M, Dymond J, and Crane K (1978) The chemistry of hydrothermal mounds near the Galapagos Rift. *Earth and Planetary Science Letters* 40: 12–24.

Cotter E and Link JE (1993) Deposition and diagenesis of Clinton ironstones (Silurian) in the Appalachian foreland basin of Pennsylvania. *Geological Society of America Bulletin* 105: 911–922.

Craddock PR, Bach W, Seewald JS, Rouxel OJ, Reeves E, and Tivey MK (2010) Rare earth element abundances in hydrothermal fluids from the Manus Basin, Papua New Guinea: Indicators of sub-seafloor hydrothermal processes in back-arc basins. *Geochimica et Cosmochimica Acta* 74: 5494–5513.

Craddock PR and Dauphas N (2011) Iron and carbon isotope evidence for microbial iron respiration throughout the Archean. *Earth and Planetary Science Letters* 303: 121–132.

Croal LR, Johnson CM, Beard BL, and Newman DK (2004) Iron isotope fractionation by Fe(II)-oxidizing photoautotrophic bacteria. *Geochimica et Cosmochimica Acta* 68: 1227–1242.

Crosby HA, Johnson CM, Roden EE, and Beard BL (2005) Coupled Fe(II)–Fe(III) electron and atom exchange as a mechanism for Fe isotope fractionation during dissimilatory iron oxide reduction. *Environmental Science & Technology* 39: 6698–6704.

Crowe SA, Jones C, Katsev S, et al. (2008) Photoferrotrophs thrive in an Archean ocean analogue. *Proceedings of the National Academy of Sciences of the United States of America* 105: 15938–15943.

Crowe SA, Katsev S, Leslie K, et al. (2011) The methane cycle in ferruginous Lake Matano. *Geobiology* 9: 61–78.

Cuadros J, Dekov VM, Arroyo X, and Nieto F (2011) Smectite formation in submarine hydrothermal sediments: Samples from the *HMS Challenger* expedition (1872–1876). *Clays and Clay Minerals* 59: 164.

Dai Y-D, Song H-M, and Shen J-Y (2004) Fossil bacteria in Xuanlong iron ore deposits of Hebei Province. *Science China Earth Series* 47: 347–356.

Dalton de Souza J, Kosin M, Melo RC, Oliveira EP, Carvalho MJ, and Leite CM (2003) Guia de excursão—geologia do segmento norte do orógeno Itabuna-Salvador-Curaçá. *Revista Brasileira de Geociências* 33(1-Suplemento): 27–32.

Dauphas N, Cates N, Mojzsis SJ, and Busigny V (2007) Identification of chemical sedimentary protoliths using iron isotopes in the >3750 Ma Nuvvuagittuq supracrustal belt, Canada. *Earth and Planetary Science Letters* 254: 358–376.

Dauphas N and Rouxel OJ (2006) Mass spectrometry and natural variations of iron isotopes. *Mass Spectrometry Reviews* 25: 515–550.

Dauphas N, van Zuilen M, Wadhwa M, Davis AM, Marty B, and Janney PE (2004) Clues from iron isotope variations on the origin of Early Archaean banded iron formations from Greenland. *Science* 306: 2077–2080.

Davis WJ, Rainbird RH, Aspler LB, and Chiarenzelli JR (2005) Detrital zircon geochronology of the Paleoproterozoic Hurwitz and Kiyuk groups, western Churchill Province, Nunavut. *Geological Survey of Canada, Current Research* 2005-F1. Ottawa, ON: Natural Resources Canada.

de Baar HJW, German CR, Elderfield H, and van Gaans P (1988) Rare earth element distributions in anoxic waters of the Cariaco Trench. *Geochimica et Cosmochimica Acta* 52: 1203–1219.

De Carlo EH and Green WJ (2002) Rare earth elements in the water column of Lake Vanda, McMurdo Dry Valleys, Antarctica. *Geochimica et Cosmochimica Acta* 66: 1323–1333.

De Carlo EH, McMurtry GM, and Yeh H-W (1983) Geochemistry of hydrothermal deposits from Loihi submarine volcano, Hawaii. *Earth and Planetary Science Letters* 66: 438–449.

De la Rocha CL, Brzezinski MA, and DeNiro MJ (2000) A first look at the distribution of the stable isotopes of silicon in natural waters. *Geochimica et Cosmochimica Acta* 64: 2467–2477.

Derry LA and Jacobsen SB (1988) The Nd and Sr isotopic evolution of Proterozoic seawater. *Geophysical Research Letters* 15: 397–400.

Derry LA and Jacobsen SB (1990) The chemical evolution of Precambrian seawater: Evidence from REEs in banded iron formations. *Geochimica et Cosmochimica Acta* 54: 2965–2977.

Ding T, Jiang S, Wang D, et al. (1996) *Silicon Isotope Geochemistry*. Beijing: Geological Publishing House.

Dirks PHGM, Jelsma HA, and Hofmann A (2002) Thrust-related accretion of an Archaean greenstone belt in the midlands of Zimbabwe. *Journal of Structural Geology* 24: 1707–1727.

Dorland HC (1999) *Paleoproterozoic Laterites, Red Beds and Ironstones of the Pretoria Group with Reference to the History of Atmospheric Oxygen*. MSc Thesis, Rand Afrikaans University.

Douthitt CB (1982) The geochemistry of the stable isotopes of silicon. *Geochimica et Cosmochimica Acta* 46: 1449–1458.

Douville E, Charlou JL, Oelkers EH, et al. (2002) The rainbow vent fluids (36°14′ N, MAR): The influence of ultramafic rocks and phase separation on trace metal content in Mid-Atlantic Ridge hydrothermal fluids. *Chemical Geology* 184: 37–48.

Duan Y, Anbar AD, Arnold GL, Lyons TW, Gordon GW, and Kendall B (2010) Molybdenum isotope evidence for mild environmental oxygenation before the Great Oxidation Event. *Geochimica et Cosmochimica Acta* 74: 6655–6668.

Duchac KC and Hanor JS (1987) Origin and timing of metasomatic silicification of an Early Archean komatiite sequence, Barberton Mountain Land, South Africa. *Precambrian Research* 37: 125–146.

Dymek RF and Klein C (1988) Chemistry, petrology, and origin of banded iron-formation lithologies from the 3800 Ma Isua Supracrustal belt, West Greenland. *Precambrian Research* 39: 247–302.

Easton RM (2005) The Grenvillian Tomiko quartzites of Ontario: Correlatives of the Baraboo Quartzites of Wisconsin, the Mazatzal orogen of New Mexico, or unique? Implications for the tectonic architecture of Laurentia in the Great Lakes region. *Institute on Lake Superior Geology, Annual Meeting, Proceedings* 51: 15–16.

Edmond JM, Measures C, McDuff RE, et al. (1979) Ridge crest hydrothermal activity and the balances of the major and minor elements in the ocean: The Galapagos data. *Earth and Planetary Science Letters* 46: 1–18.

Edmonds HN and German CR (2004) Particle geochemistry in the Rainbow hydrothermal plume, Mid-Atlantic Ridge. *Geochimica et Cosmochimica Acta* 68: 759–772.

Edwards KJ, Glazer BT, Rouxel OJ, et al. (2011a) Ultra-diffuse hydrothermal venting supports Fe-oxidizing bacteria and massive umber deposition at 5000 m off Hawaii. *ISME Journal* 5: 1748–1758.

Edwards KJ, Rogers DR, Wirsen CO, and McCollom TM (2003) Isolation and characterization of novel psychrophilic, neutrophilic, Fe-oxidizing, chemolithoautotrophic α- and γ-*Proteobacteria* from the deep sea. *Applied and Environmental Microbiology* 69: 2906–2913.

Edwards KJ, Wheat CG, and Sylvan JB (2011b) Under the sea: Microbial life in volcanic oceanic crust. *Nature Reviews In Microbiology* 9: 703–712.

Ehrenreich A and Widdel F (1994) Anaerobic oxidation of ferrous iron by purple bacteria, a new type of phototrophic metabolism. *Applied and Environmental Microbiology* 60: 4517–4526.

Elderfield H, Gass IG, Hammond A, and Bear LM (1972) The origin of ferromanganese sediments associated with the Troodos Massif of Cyprus. *Sedimentology* 19: 1–19.
Elming SA, Shumlyanskyy L, Kravchenko S, Layer P, and Soderlund U (2010) Proterozoic basic dykes in the Ukrainian shield: A palaeomagnetic, geochronologic and geochemical study—The accretion of the Ukrainian shield to Fennoscandia. *Precambrian Research* 178: 119–135.
Elrod VA, Berelson WM, Coale KH, and Johnson KS (2004) The flux of iron from continental shelf sediments: A missing source for global budgets. *Geophysical Research Letters* 31: L12307.
Emerson D and Moyer CL (2002) Neutrophilic Fe-oxidizing bacteria are abundant at the Loihi Seamount hydrothermal vents and play a major role in Fe oxide deposition. *Applied and Environmental Microbiology* 68: 3085–3093.
Eriksson KA (1983) Siliciclastic-hosted iron-formations in the Early Archean Barberton and Pilbara sequences. *Journal of the Geological Society of Australia* 30: 473–482.
Eriksson PG, Engelbrecht JP, Res M, and Harmer RE (1994a) The Bushy Bend lavas, a new volcanic member of the Pretoria Group, Transvaal Sequence. *South Afrian Journal of Geology* 97: 1–7.
Eriksson PG, Reczko BFF, Merkle RKW, et al. (1994b) Early Proterozoic black shales of the Timeball Hill Formation, South Africa: Volcanogenic and palaeoenvironmental influences. *Journal of African Earth Sciences* 18: 325–337.
Ernst RE, Wingate MTD, Buchan KL, and Li ZX (2008) Global record of 1600-700 Ma Large Igneous Provinces (LIPs): Implications for the reconstruction of the proposed Nuna (Columbia) and Rodinia supercontinents. *Precambrian Research* 160: 159–178.
Ernst RE and Bell K (2010) Large igneous provinces (LIPs) and carbonatites. *Mineralogy and Petrology* 98: 55–76.
Ernst R and Bleeker W (2010) Large igneous provinces (LIPs), giant dyke swarms, and mantle plumes: Significance for breakup events within Canada and adjacent regions from 2.5 Ga to the Present. *Canadian Journal of Earth Sciences* 47: 695–739.
Ernst RE and Buchan KL (2001) Large mafic magmatic events through time and links to mantle-plume heads. In: Ernst RE and Buchan KL (eds.) *Mantle Plumes: Their Identification through Time*. *Geological Society of America Special Papers* 352, pp. 483–575. Boulder, CO: Geological Society of America.
Escoube R, Rouxel OJ, Sholkovitz E, and Donard OFX (2009) Iron isotope systematics in estuaries: The case of North River, Massachusetts (USA). *Geochimica et Cosmochimica Acta* 73: 4045–4059.
Evans MJ and Derry LA (2002) Quartz control of high germanium/silicon ratios in geothermal waters. *Geology* 30: 1019–1022.
Evans KA, McCuaig TC, Leach D, Angerer T, and Hagemann SG (2013) Banded iron formation to iron ore: A record of the evolution of Earth environment? *Geology* 41: 99–102.
Ewers WE and Morris RC (1981) Studies of the Dales Gorge Member of the Brockman Iron Formation, Western Australia. *Economic Geology* 76: 1929–1953.
Farquhar J, Bao H, and Thiemens M (2000) Atmospheric influence of Earth's earliest sulfur cycle. *Science* 289: 756–758.
Farquhar J and Wing BA (2005) The terrestrial record of stable sulphur isotopes: A review of the implications for evolution of Earth's sulphur cycle. In: McDonald I, Boyce AJ, Butler IB, Herrington RJ, and Polya DA (eds.) *Mineral Deposits and Earth Evolution*. *Geological Society Special Publication* 248, pp. 167–177. London: Geological Society of London.
Farquhar J, Zerkle AL, and Bekker A (2011) Geological constraints on the origin of oxygenic photosynthesis. *Photosynthesis Research* 107: 11–36.
Feely RA, Trefry JH, Lebon GT, and German CR (1998) The relationship between P/Fe and V/Fe ratios in hydrothermal precipitates and dissolved phosphate in seawater. *Geophysical Research Letters* 25: 2253–2256.
Fetter AH, Van Schmus WR, Santos TJS, Neto JAN, and Henriarthaud M (2000) U–Pb and Sm–Nd geochronological constraints on the crustal evolution and basement architecture of Ceará State, NW Borborema Province, NE Brazil: Implications for the existence of the Paleoproterozoic supercontinent "Atlantica". *Revista Brasileira de Geociências* 30: 102–106.
Findlay JM, Parrish RR, Birkett TC, and Watanabe DH (1995) U–Pb ages from the Nimish Formation and Montagnais glomeroporphyritic gabbro of the central New Quebec Orogen, Canada. *Canadian Journal of Earth Sciences* 32: 1208–1220.
Fischer WW and Knoll AH (2009) An iron shuttle for deepwater silica in Late Archean and Early Paleoproterozoic iron formation. *Geological Society of America Bulletin* 121: 222–235.
Fischer WW, Schroeder S, Lacassie JP, et al. (2009) Isotopic constraints on the Late Archean carbon cycle from the Transvaal Supergroup along the western margin of the Kaapvaal Craton, South Africa. *Precambrian Research* 169: 15–27.
Fitoussi C, Bourdon B, Kleine T, Oberli F, and Reynolds BC (2009) Si isotope systematics of meteorites and terrestrial peridotites: Implications for Mg/Si fractionation in the solar nebula and for Si in the Earth's core. *Earth and Planetary Science Letters* 287: 77–85.
Foustoukos DI and Bekker A (2008) Hydrothermal Fe(II) oxidation during phase separation: Relevance to the origin of Algoma-type BIFs. *Geochimica et Cosmochimica Acta* 72: A280.
Fralick P, Davis DW, and Kissin SA (2002) The age of the Gunflint Formation, Ontario, Canada: Single zircon U–Pb age determinations from reworked volcanic ash. *Canadian Journal of Earth Sciences* 39: 1085–1091.
Fralick PW and Pufahl PK (2006) Iron formation in Neoarchean deltaic successions and the microbially mediated deposition of transgressive systems tracts. *Journal of Sedimentary Research* 76: 1057–1066.
Franceschelli M, Puxeddu M, and Carta M (2000) Mineralogy and geochemistry of Late Ordovician phosphate-bearing oolitic ironstones from NW Sardinia, Italy. *Mineralogy and Petrology* 69: 267–293.
François LM (1986) Extensive deposition of banded iron formations was possible without photosynthesis. *Nature* 320: 352–354.
Franklin JM, Gibson HL, Galley AG, and Jonasson IR (2005) Volcanogenic massive sulfide deposits. In: Hedenquist JW, Thompson JFH, Goldfarb RJ, and Richards JP (eds.) *Economic Geology 100th Anniversary Volume, 1905–2005*, pp. 523–560. Littleton, CO: Society of Economic Geologists, Inc.
Frei R, Dahl PS, Duke EF, et al. (2008) Trace element and isotopic characterization of Neoarchean and Paleoproterozoic iron formations in the Black Hills (South Dakota, USA): Assessment of chemical change during 2.9–1.9 Ga deposition bracketing the 2.4–2.2 Ga first rise of atmospheric oxygen. *Precambrian Research* 162: 441–474.
Frei R, Gaucher C, Poulton SW, and Canfield DE (2009) Fluctuations in Precambrian atmospheric oxygenation recorded by chromium isotopes. *Nature* 461: 225–250.
Froelich PN, Hambrick GA, Andreae MO, Mortlock RA, and Edmond JM (1985) The geochemistry of inorganic germanium in natural waters. *Journal of Geophysical Research* 90(C1): 1133–1141.
Frost CD, von Blanckenburg F, Schoenberg R, Frost BR, and Swapp SM (2007) Preservation of Fe isotope heterogeneities during diagenesis and metamorphism of banded iron formation. *Contributions to Mineralogy and Petrology* 153: 211–235.
Fryer BJ (1977) Rare earth evidence in iron-formations for changing Precambrian oxidation-states. *Geochimica et Cosmochimica Acta* 41: 361–367.
Fürsich FT, Oschmann W, Singh B, and Jaitly AK (1992) Hardgrounds, reworked concretion levels and condensed horizons in the Jurassic of western India: Their significance for basin analysis. *Journal of the Geological Society* 149: 313–331.
Fyon JA, Breaks FW, Heather KB, et al. (1992) Metallogeny of metallic mineral deposits in the Superior Province of Ontario. In: Thurston PC, Williams HR, Sutcliffe RH, and Scott GM (eds.) *Geology of Ontario, Ontario Geological Survey Special Volume 4*, part 2, pp. 1091–1174. Toronto, ON: Ministry of Northern Development and Mines.
Garrels RM, Perry EA, and Mackenzie FT (1973) Genesis of Precambrian iron-formations and development of atmospheric oxygen. *Economic Geology* 68: 1173–1179.
Garvin J, Buick R, Anbar AD, Arnold GL, and Kaufman AJ (2009) Isotopic evidence for an aerobic nitrogen cycle in the latest Archean. *Science* 323: 1045–1048.
Garzanti E (1993) Himalayan ironstones, superplumes, and the breakup of Gondwana. *Geology* 21: 105–108.
German CR and Elderfield H (1990) Application of the Ce anomaly as a paleoredox indicator: The ground rules. *Paleoceanography* 5: 823–833.
German CR, Holliday BP, and Elderfield H (1991) Redox cycling of rare earth elements in the suboxic zone of the Black Sea. *Geochimica et Cosmochimica Acta* 55: 3553–3558.
Glass JB, Wolfe-Simon F, and Anbar AD (2009) Coevolution of metal availability and nitrogen assimilation in cyanobacteria and algae. *Geobiology* 7: 100–123.
Glenn CR and Arthur MA (1990) Anatomy and origin of a Cretaceous phosphorite-greensand giant, Egypt. *Sedimentology* 37: 123–154.
Glenn CR, Föllmi KB, Riggs SR, et al. (1994) Phosphorus and phosphorites – sedimentology and environments of formation. *Eclogae Geologicae Helvetiae* 87: 747–788.
Godfrey LV and Falkowski PG (2009) The cycling and redox state of nitrogen in the Archaean ocean. *Nature Geoscience* 2: 725–729.
Gole MJ and Klein C (1981) Banded iron-formation through much of Precambrian time. *Journal of Geology* 89: 169–183.
Golubic S and Lee SJ (1999) Early cyanobacterial fossil record: Preservation, palaeoenvironments and identification. *European Journal of Phycology* 34: 339–348.
Goode ADT, Hall WDM, and Bunting JA (1983) The Nabberu basin of Western Australia. In: Trendall AF and Morris RC (eds.) *Iron-Formation: Facts and Problems*, pp. 295–323. Amsterdam: Elsevier Science.
Goodwin AM (1973) Archean iron-formations and tectonic basins of Canadian Shield. *Economic Geology* 68: 915–933.

Goodwin AM, Monster J, and Thode HG (1976) Carbon and sulfur isotope abundances in Archean iron-formations and early Precambrian life. *Economic Geology* 71: 870–891.

Grassineau NV, Nisbet EG, Bickle MJ, et al. (2001) Antiquity of the biological sulphur cycle: Evidence from sulphur and carbon isotopes in 2700 million-year-old rocks of the Belingwe Belt, Zimbabwe. *Proceedings of the Royal Society Series B* 268: 113–119.

Grenne T and Slack JF (2003) Paleozoic and Mesozoic silica-rich seawater: Evidence from hematitic chert (jasper) deposits. *Geology* 31: 319–322.

Grenne T and Slack JF (2005) Geochemistry of jasper beds from the Ordovician Løkken ophiolite, Norway: Origin of proximal and distal siliceous exhalites. *Economic Geology* 100: 1511–1527.

Gross GA (1980) A classification of iron-formation based on depositional environments. *Canadian Mineralogist* 18: 215–222.

Grotzinger JP (1990) Geochemical model for Proterozoic stromatolite decline. *American Journal of Science* 290: 80–103.

Groves DI, Condie KC, Goldfarb RJ, Hronsky JMA, and Vielreicher RM (2005) Secular changes in global tectonic processes and their influence on the temporal distribution of gold-bearing mineral deposits. *Economic Geology* 100: 203–224.

Groves DI, Phillips N, Ho SE, Houstoun SM, and Standing CA (1987) Craton-scale distribution of Archaean greenstone gold deposits: Predictive capacity of the metamorphic model. *Economic Geology* 82: 2045–2058.

Gruner JW (1922) The origin of sedimentary iron-formations: The Biwabik Formation of the Mesabi Range. *Economic Geology* 22: 407–460.

Gueguen B, Rouxel O, Ponzevera E, Bekker A, and Fouquet Y (in press) Nickel isotope variations in terrestrial silicate rocks and geological reference materials measured by MC-ICP-MS. *Geostandards and Geoanalytical Research*.

Guilbaud R, Butler IB, and Ellam RM (2011) Abiotic pyrite formation produces a large Fe isotope fractionation. *Science* 332: 1548–1551.

Guo Q, Strauss H, Kaufman AJ, et al. (2009) Reconstructing Earth's surface oxidation across the Archean–Proterozoic transition. *Geology* 37: 399–402.

Habicht KS, Gade M, Thamdrup B, Berg P, and Canfield DE (2002) Calibration of sulfate levels in the Archean ocean. *Science* 298: 2372–2374.

Hallbeck L and Pederson K (1990) Culture parameters regulating stalk formation and growth rates of *Gallionella ferruginea*. *Journal of General Microbiology* 136: 1675–1680.

Hallbeck L and Pedersen K (1991) Autotrophic and mixotrophic growth of *Gallionella ferruginea*. *Journal of Genetic Microbiology* 137: 2657–2661.

Halverson GP, Poitrasson F, Hoffman PF, Nédélec A, Montel J-M, and Kirby J (2011) Fe isotope and trace element geochemistry of the Neoproterozoic syn-glacial Rapitan iron formation. *Earth and Planetary Science Letters* 309: 100–112.

Hamade T, Konhauser KO, Raiswell R, Goldsmith S, and Morris RC (2003) Using Ge/Si ratios to decouple iron and silica fluxes in Precambrian banded iron formations. *Geology* 31: 35–38.

Hamilton MA (2008) The significance of new U/Pb baddeleyite ages from two Paleoproterozoic diabase dikes in northern Ontario. *Summary of Field Work and Other Activities 2008, Ontario Geological Survey Open File Report 6226*, pp. 17-1–17-10.

Hamilton MA, Buchan KL, Ernst RE, and Stott GM (2009) Widespread and short-lived 1870 Ma mafic magmatism along the northern Superior craton margin. *Eos Transactions, American Geophysical Union* 90(22), Joint Assembly Supplement: Abstract GA11A-01.

Han TM (1988) Origin of magnetite in Precambrian iron-formations of low metamorphic grade. In: Zachrisson E (ed.) *Proceedings of the Seventh Quadrennial IAGOD Symposium*, pp. 641–656. Stuttgart: E. Schweizerbart'sche Verlagsbuchhandlung.

Han TM and Runnegar B (1992) Megascopic eukaryotic algae from the 2.1-billion-year-old Negaunee Iron-Formation, Michigan. *Science* 257: 232–235.

Hannah JL, Bekker A, Stein HJ, Markey RJ, and Holland HD (2004) Primitive Os and 2316 Ma age for marine shale: Implications for Paleoproterozoic glacial events and the rise of atmospheric oxygen. *Earth and Planetary Science Letters* 225: 43–52.

Hanert HH (2002) Bacterial and chemical iron oxide deposition in a shallow bay on Palaea Kameni, Santorini, Greece: Microscopy, electron probe microanalysis, and photometry of in situ experiments. *Geomicrobiology Journal* 19: 317–342.

Hannington MD, Jonasson IR, Herzig PM, and Petersen S (1995) Physical and chemical processes of seafloor mineralization at mid-ocean ridges. In: Humphris SE, Zierenberg RA, Mullineaux LS, and Thomson RE (eds.) *Seafloor Hydrothermal Systems: Physical, Chemical, Biological, and Geological Interactions, Geophysical Monograph Series*, vol. 91, pp. 115–157. Washington, DC: American Geophysical Union.

Hanor JS and Duchac KC (1990) Isovolumetric silicification of Early Archean komatiites: Geochemical mass balances and constraints on origin. *Journal of Geology* 98: 863–877.

Haq BU (1991) Sequence stratigraphy, sea-level change, and significance for the deep sea. In: Macdonald DIM (ed.) *Sedimentation, Tectonics and Eustasy: Sea-Level Changes at Active Margins*. *International Association of Sedimentologists Special Publication* 12, pp. 3–39. Oxford: Blackwell Scientific Publications.

Harder EC (1919) Iron-depositing bacteria and their geologic relations. *US Geological Survey Professional Paper* 113. Washington, DC: US Government Printing Office.

Harms JE (1965) Iron ore deposits of Constance Range. In: McAndrew J (ed.) *Geology of Australian Ore Deposits, Eighth Commonwealth Mining and Metallurgical Congress*, pp. 264–269. Melbourne: The Australasian Institute of Mining and Metallurgy.

Hartlaub RP, Heaman LM, Chacko T, and Ashton KE (2007) Circa 2.3-Ga magmatism of the Arrowsmith orogeny, Uranium City region, western Churchill craton, Canada. *Journal of Geology* 115: 181–195.

Hartman H (1984) The evolution of photosynthesis and microbial mats: A speculation on the banded iron formations. In: Cohen Y, Castenholz RW, and Halvorson HO (eds.) *Microbial Mats: Stromatolites*, pp. 449–453. New York: Alan R Liss.

Hatton OJ and Davidson GJ (2004) Soldiers Cap Group iron-formations, Mt Isa Inlier, Australia, as windows into the hydrothermal evolution of a base-metal-bearing Proterozoic rift basin. *Australian Journal of Earth Sciences* 51: 85–106.

Hawley JE (1926) Geology and economic possibilities of Sutton Lake area, District of Patricia. *Ontario Department of Mines, Annual Report* 34.

Hayashi T, Tanimizu M, and Tanaka T (2004) Origin of negative Ce anomalies in Barberton sedimentary rocks, deduced from La–Ce and Sm–Nd isotope systematics. *Precambrian Research* 135: 345–357.

Heaman LM (1997) Global mafic volcanism at 2.45 Ga: Remnants of an ancient large igneous province? *Geology* 25: 299–302.

Heaman LM, Lecheminant AN, and Rainbird RH (1992) Nature and timing of Franklin igneous events, Canada: Implications for a Late Proterozoic mantle plume and the break-up of Laurentia. *Earth and Planetary Science Letters* 109: 117–131.

Heaman LM, Machado N, Krogh TE, and Weber W (1986) Precise U–Pb zircon ages for the Molson dyke swarm and the Fox River sill: Constraints for Early Proterozoic crustal evolution in northeastern Manitoba, Canada. *Contributions to Mineralogy and Petrology* 94: 82–89.

Heaman LM, Peck D, and Toope K (2009) Timing and geochemistry of 1.88 Ga Molson igneous events, Manitoba: Insights into the formation of a craton-scale magmatic and metallogenic province. *Precambrian Research* 172: 143–162.

Heikoop JM, Tsujita CJ, Risk MJ, Tomascik T, and Mah AJ (1996) Modern iron ooids from a shallow-marine volcanic setting: Mahengetang, Indonesia. *Geology* 24: 759–762.

Heimann A, Johnson C, Beard B, et al. (2010) Fe, C, and O isotope compositions of banded iron formation carbonates demonstrate a major role for dissimilatory iron reduction in ~2.5 Ga marine environments. *Earth and Planetary Science Letters* 294: 8–18.

Heinrichs T (1980) Lithostratigraphische Untersuchungen in der Fig Tree Gruppe des Barberton Greenstone Belt zwischen Umsoli und Lomati (Südafrika). *Göttinger Arbeiten zur Geologie und Paläontologie*, vol. 22.

Heising S, Richter L, Ludwig W, and Schink B (1999) *Chlorobium ferrooxidans* sp nov., a phototrophic green sulfur bacterium that oxidizes ferrous iron in coculture with a "*Geospirillum*" sp strain. *Archives of Microbiology* 172: 116–124.

Hekinian R, Hoffert M, Larque P, Cheminee JL, Stoffers P, and Bideau D (1993) Hydrothermal Fe and Si oxyhydroxide deposits from South-Pacific intraplate volcanoes and East Pacific Rise axial and off-axial regions. *Economic Geology* 88: 2099–2121.

Hoffman PF (1987) Early Proterozoic foredeeps, foredeep magmatism, and superior-type iron formations of the Canadian Shield. In: Kröner A (ed.) *Proterozoic Lithospheric Evolution, Geodynamics Series*, vol. 17, pp. 85–98. Washington, DC.: American Geophysical Union.

Hoffman PF (2011) Birthdate for the Coronation paleocean: Age of initial rifting in Wopmay orogen, Canada. *Canadian Journal of Earth Sciences* 48: 281–293.

Hoffman PF and Schrag DP (2002) The snowball Earth hypothesis: Testing the limits of global change. *Terra Nova* 14: 129–155.

Hofmann A (2005) The geochemistry of sedimentary rocks from the Fig Tree Group, Barberton greenstone belt: Implications for tectonic, hydrothermal and surface processes during mid-Archaean times. *Precambrian Research* 143: 23–49.

Hofmann A (2011) Archaean hydrothermal systems in the Barberton greenstone belt and their significance as a habitat for early life. In: Golding S and Glikson M (eds.) *Earliest Life on Earth: Habitats, Environments and Methods of Detection*, pp. 51–78. Berlin: Springer-Verlag.

Hofmann A and Bolhar R (2007) The origin of carbonaceous cherts in the Barberton greenstone belt and their significance for the study of early life in mid-Archaean rocks. *Astrobiology* 7: 355–388.

Hofmann A, Dirks PH, Jelsma HA, and Matura N (2003) A tectonic origin for ironstone horizons in the Zimbabwe craton and their significance for greenstone belt geology. *Journal of the Geological Society* 160: 83–97.

Hofmann A and Harris C (2008) Stratiform alteration zones in the Barberton greenstone belt: A window into subseafloor processes 3.5–3.3 Ga ago. *Chemical Geology* 257: 224–242.

Hofmann A and Kusky TM (2004) The Belingwe greenstone belt: Ensialic or oceanic? In: Kusky TM (ed.) *Precambrian Ophiolites and Related Rocks*, pp. 487–537. Amsterdam: Elsevier.

Hofmann A and Wilson AH (2007) Silicified basalts, bedded cherts and other sea floor alteration phenomena of the 3.4 Ga Nondweni greenstone belt, South Africa. *Developments in Precambrian Geology* 15: 571–605.

Holland HD (1973) The oceans: A possible source of iron in iron-formations. *Economic Geology* 68: 1169–1172.

Holland HD (1984) *The Chemical Evolution of the Atmosphere and Oceans*. Princeton, NJ: Princeton University Press.

Holland HD (2005) Sedimentary mineral deposits and the evolution of Earth's near-surface environments. *Economic Geology* 100: 1489–1509.

Holm NG and Charlou JL (2001) Initial indications of abiotic formation of hydrocarbons in the Rainbow ultramafic hydrothermal system, Mid-Atlantic Ridge. *Earth and Planetary Science Letters* 191: 1–8.

Hotinski RM, Kump LR, and Arthur MA (2004) The effectiveness of the Paleoproterozoic biological pump: A $\delta^{13}C$ gradient from platform carbonates of the Pethei Group (Great Slave Lake Supergroup, NWT). *Geological Society of America Bulletin* 116: 539–554.

Hren MT, Tice MM, and Chamberlain CP (2009) Oxygen and hydrogen isotope evidence for a temperate climate 3.42 billion years ago. *Nature* 462: 205–208.

Huber RW and Garrels RM (1953) Relation of pH and oxidation potential to sedimentary iron ore formation. *Economic Geology* 48: 337–357.

Hulbert LJ, Hamilton MA, Horan MF, and Scoates RFJ (2005) U–Pb zircon and Re–Os isotope geochronology of mineralized ultramafic intrusions and associated nickel ores from the Thompson nickel belt, Manitoba, Canada. *Economic Geology* 100: 29–41.

Hunter JH (1970) Facies of iron sedimentation of the Clinton Group. In: Fisher GW, Pettijohn FJ, Meeb JC, and Weaver KN (eds.) *Studies of Appalachian Geology: Central and Southern*, pp. 101–121. New York: Interscience.

Hunter MA, Bickle MJ, Nisbet EG, Martin A, and Chapman HJ (1998) Continental extensional setting for the Archean Belingwe Greenstone Belt, Zimbabwe. *Geology* 26: 883–886.

Huston DL and Logan BW (2004) Barite, BIFs and bugs: Evidence for the evolution of the Earth's early hydrosphere. *Earth and Planetary Science Letters* 220: 41–55.

Huston DL, Pehrsson S, Eglington BM, and Zaw K (2010) The geology and metallogeny of volcanic-hosted massive sulfide deposits: Variations through geologic time and with tectonic setting. *Economic Geology* 105: 571–591.

Huston DL, Sun SS, Blewett R, et al. (2002) The timing of mineralization in the Archean North Pilbara terrain, Western Australia. *Economic Geology* 97: 733–755.

Hyslop EV, Valley JW, Johnson CM, and Beard BL (2008) The effects of metamorphism on O and Fe isotope compositions in the Biwabik Iron Formation, northern Minnesota. *Contributions to Mineralogy and Petrology* 155: 313–328.

Ilyin AV (2009) Neoproterozoic banded iron formations. *Lithology and Mineral Resources* 44: 78–86.

Isley AE (1995) Hydrothermal plumes and the delivery of iron to banded iron formation. *Journal of Geology* 103: 169–185.

Isley AE and Abbott DH (1999) Plume-related mafic volcanism and the deposition of banded iron formation. *Journal of Geophysical Research* 104: 15461–15477.

Jackson MJ, Sweet IP, Page RW, and Bradshaw BE (1999) South Nicholson basin: Evidence for the early Mesoproterozoic Roper Superbasin. In: Bradshaw BE and Scott DL (eds.) *Integrated Basin Analysis of the Isa Superbasin Using Seismic, Well Log and Geopotential Data: An Evaluation of the Economic Potential of the Northern Lawn Hill Platform*. Australian Geological Survey Record 1999/19.

Jacobs DK and Lindberg DR (1998) Oxygen and evolutionary patterns in the sea: Onshore/offshore trends and recent recruitment of deep-sea faunas. *Proceedings of the National Academy of Sciences of the United States of America* 95: 9396–9401.

Jacobsen SB and Pimentel-Klose MR (1988) Nd isotopic variations in Precambrian banded iron formations. *Geophysical Research Letters* 15: 393–396.

James HL (1954) Sedimentary facies of iron-formation. *Economic Geology* 49: 235–293.

James HL (1983) Distribution of banded iron-formation in space and time. In: Trendall AF and Morris RC (eds.) *Iron-Formation Facts and Problems*, pp. 471–490. Amsterdam: Elsiever.

James HL, Dutton CE, Pettijohn FJ, and Wier KL (1968) Geology and ore deposits of the Iron River-Crystal Falls district, Iron County, Michigan. *US Geological Survey Professional Paper 570*. Washington, DC: US Government Printing Office.

Javaux EJ (2011) Early eukaryotes in Precambrian oceans. In: Gargaud M, López-Garcia P, and Martin H (eds.) *Origins and Evolution of Life: An Astrobiological Perspective*, pp. 414–449. Cambridge: Cambridge University Press.

Jia YF and Kerrich R (2004) Nitrogen 15-enriched Precambrian kerogen and hydrothermal systems. *Geochemisty, Geophysics, Geosystems* 5: Q07005.

Jiang SY, Ding TP, Wan DF, and Li YH (1993) Silicon isotopic compositions of Archean banded Si–Fe formation (BIF) in the Gongchangling ore deposit, Liaoning-Province, China. *Science in China. Series B, Chemistry* 36: 482–489.

Johnson CM, Beard BL, Beukes NJ, Klein C, and O'Leary JM (2003) Ancient geochemical cycling in the Earth as inferred from Fe isotope studies of banded iron formations from the Transvaal craton. *Contributions to Mineralogy and Petrology* 144: 523–547.

Johnson CM, Beard BL, Klein C, Beukes NJ, and Roden EE (2008a) Iron isotopes constrain biologic and abiologic processes in banded iron formation genesis. *Geochimica et Cosmochimica Acta* 72: 151–169.

Johnson CM, Beard BL, and Roden EE (2008b) The iron isotope fingerprints of redox and biogeochemical cycling in the modern and ancient Earth. *Annual Review of Earth and Planetary Sciences* 36: 457–493.

Johnson TM and Bullen TD (2004) Mass-dependent fractionation of selenium and chromium isotopes in low-temperature environments. In: Johnson C, Beard B, and Albarède F (eds.) *Geochemistry of Non-Traditional Stable Isotopes. Reviews in Mineralogy & Geochemistry*, vol. 56, pp. 289–317. Washington, DC: Mineralogical Society of America.

Johnson KS, Gordon RM, and Coale KH (1997) What controls dissolved iron in the world ocean? *Marine Chemistry* 57: 137–161.

Juniper SK and Fouquet Y (1988) Filamentous iron silica deposits from modern and ancient hydrothermal sites. *Canadian Mineralogist* 26: 859–869.

Kappler A, Pasquero C, Konhauser KO, and Newman DK (2005) Deposition of banded iron formations by anoxygenic phototrophic Fe(II)-oxidizing bacteria. *Geology* 33: 865–868.

Karhu JA and Holland HD (1996) Carbon isotopes and the rise of atmospheric oxygen. *Geology* 24: 867–870.

Kato Y, Kano T, and Kunugiza K (2002) Negative Ce anomaly in the Indian banded iron formations: Evidence for the emergence of oxygenated deep-sea at 2.9–2.7 Ga. *Resource Geology* 52: 101–110.

Kato Y, Kawakami T, Kano T, Kunugiza K, and Swamy NS (1996) Rare-earth element geochemistry of banded iron formations and associated amphibolite from the Sargur belts, south India. *Journal of Southeast Asian Earth Sciences* 14: 161–164.

Kato Y, Ohta I, Tsunematsu T, et al. (1998) Rare earth element variations in mid-Archean banded iron formations: Implications for the chemistry of ocean and continent and plate tectonics. *Geochimica et Cosmochimica Acta* 62: 3475–3497.

Kato Y, Yamaguchi KE, and Ohmoto H (2006) Rare earth elements in Precambrian banded iron formations: Secular changes of Ce and Eu anomalies and evolution of atmospheric oxygen. In: Ohmoto H and Kessler SK (eds.) *Chemical and Biological Evolution of Early Earth: Constraints from Banded Iron-Formations. Geological Society of America Memoir* 198, pp. 269–289. Boulder, CO: Geological Society of America.

Kaufman AJ, Hayes JM, and Klein C (1990) Primary and diagenetic controls of isotopic compositions of iron-formation carbonates. *Geochimica et Cosmochimica Acta* 54: 3461–3473.

Kaufman AJ, Johnston DT, Farquhar J, et al. (2007) Late Archean biospheric oxygenation and atmospheric evolution. *Science* 317: 1900–1903.

Kawabe I, Ohta A, Ishii S, Tokumura M, and Miyauchi K (1999) REE partitioning between Fe–Mn oxyhydroxide precipitates and weakly acid NaCl solutions: Convex tetrad effect and fractionation of Y and Sc from heavy lanthanides. *Geochemical Journal* 33: 167–179.

Kendall B, Creaser RA, Calver CR, Raub TD, and Evans DAD (2009) Correlation of Sturtian diamictite successions in southern Australia and northwestern Tasmania by Re–Os black shale geochronology and the ambiguity of "Sturtian"-type diamictite-cap carbonate pairs as chronostratigraphic marker horizons. *Precambrian Research* 172: 301–310.

Kendall B, Reinhard CT, Lyons TW, Kaufman AJ, Poulton SW, and Anbar AD (2010) Pervasive oxygenation along Late Archaean ocean margins. *Nature Geoscience* 3: 647–652.

Kerr AA (1998) Oceanic plateau formation: A cause of mass extinction and black shale deposition around the Cenomanian–Turonian boundary? *Journal of the Geological Society* 155: 619–626.

Khan RMK and Naqvi SM (1996) Geology, geochemistry and genesis of BIF of Kushtagi schist belt, Archaean Dharwar Craton, India. *Mineralium Deposita* 31: 123–133.

Kimberley MM (1989) Exhalative origins of iron formations. *Ore Geology Reviews* 5: 13–145.

Kimberley MM (1994) Debate about ironstone: Has solute supply been surficial weathering, hydrothermal convection, or exhalation of deep fluids? *Terra Nova* 6: 116–132.

Kirschvink JL (1992) Late Proterozoic low-latitude global glaciation: The snowball Earth. In: Schopf JW and Klein C (eds.) *The Proterozoic Biosphere*, pp. 51–52. Cambridge: Cambridge University Press.

Klein C (2005) Some Precambrian banded iron-formations (BIFs) from around the world: Their age, geologic setting, mineralogy, metamorphism, geochemistry, and origin. *American Mineralogist* 90: 1473–1499.

Klein C and Beukes NJ (1989) Geochemistry and sedimentology of a facies transition from limestone to iron-formation deposition in the Early Proterozoic Transvaal Supergroup, South Africa. *Economic Geology* 84: 1733–1774.

Klein C and Beukes NJ (1992) Time distribution, stratigraphy, and sedimentologic setting, and geochemistry of Precambrian iron-formation. In: Schopf JW and Klein C (eds.) *The Proterozoic Biosphere*, pp. 139–146. Cambridge: Cambridge University Press.

Klein C and Beukes NJ (1993) Sedimentology and geochemistry of the glaciogenic Late Proterozoic Rapitan Iron Formation in Canada. *Economic Geology* 88: 542–565.

Klein C and Gole MJ (1981) Mineralogy and petrology of parts of the Marra Mamba Iron Formation, Hamersley Basin, Western Australia. *American Mineralogist* 66: 507–525.

Klein C and Ladeira EA (2004) Geochemistry and mineralogy of Neoproterozoic banded iron-formations and some selected, siliceous manganese formations from the Urucum district, Mato Grosso do Sul, Brazil. *Economic Geology* 99: 1233–1244.

Klinkhammer G, Elderfield H, and Hudson A (1983) Rare-earth elements in seawater near hydrothermal vents. *Nature* 305: 185–188.

Knauth LP (2005) Temperature and salinity history of the Precambrian ocean: Implications for the course of microbial evolution. *Palaeogeography, Palaeoclimatology, Palaeoecology* 219: 53–69.

Knauth LP and Lowe DR (2003) High Archean climatic temperature inferred from oxygen isotope geochemistry of cherts in the 3.5 Ga Swaziland Supergroup, South Africa. *Geological Society of America Bulletin* 115: 566–580.

Knoll AH, Javaux EJ, Hewitt D, and Cohen P (2006) Eukaryotic organisms in Proterozoic oceans. *Philosophical Transactions of the Royal Society Series B* 361: 1023–1038.

Konhauser KO, Amskold L, Lalonde SV, Posth NR, Kappler A, and Anbar A (2007a) Decoupling photochemical Fe(II) oxidation from shallow-water BIF deposition. *Earth and Planetary Science Letters* 258: 87–100.

Konhauser KO, Hamade T, Raiswell R, et al. (2002) Could bacteria have formed the Precambrian banded iron formations? *Geology* 30: 1079–1082.

Konhauser KO, Lalonde SV, Amskold L, and Holland HD (2007b) Was there really an Archean phosphate crisis? *Science* 315: 1234.

Konhauser KO, Lalonde S, Planavsky NJ, et al. (2011) Aerobic bacterial pyrite oxidation and acid rock drainage during the Great Oxidation Event. *Nature* 478: 369–373.

Konhauser KO, Newman DK, and Kappler A (2005) The potential significance of microbial Fe(III) reduction during deposition of Precambrian banded iron formations. *Geobiology* 3: 167–177.

Konhauser KO, Pecoits E, Lalonde SV, et al. (2009) Oceanic nickel depletion and a methanogen famine before the Great Oxidation Event. *Nature* 458: 750–753.

Krapež B, Barley ME, and Pickard AL (2003) Hydrothermal and resedimented origins of the precursor sediments to banded iron formations: Sedimentological evidence from the early Palaeoproterozoic Brockman Supersequence of Western Australia. *Sedimentology* 50: 979–1011.

Kroopnick PM (1985) The distribution of ^{13}C of $\sum CO_2$ in the world oceans. *Deep Sea Research Part A. Oceanographic Research Papers* 32: 57–84.

Kuhn T, Bostick BC, Koschinsky A, Halbach P, and Fendorf S (2003) Enrichment of Mo in hydrothermal Mn precipitates: Possible Mo sources, formation process and phase associations. *Chemical Geology* 199: 29–43.

Kulik DA and Korzhnev MN (1997) Lithological and geochemical evidence of Fe and Mn pathways during deposition of Lower Proterozoic banded iron formation in the Krivoy Rog basin (Ukraine). In: Nicholson K, Hein JR, Bühn B, and Dasgupta S (eds.) *Manganese Mineralization: Geochemistry and Mineralogy of Terrestrial and Marine Deposits. Geological Society Special Publication* 119, pp. 43–80. London: Geological Society of London.

Kump LR and Holland HD (1992) Iron in Precambrian rocks: Implications for the global oxygen budget of the ancient Earth. *Geochimica et Cosmochimica Acta* 56: 3217–3223.

Kump LR and Seyfried WE Jr. (2005) Hydrothermal Fe fluxes during the Precambrian: Effect of low oceanic sulfate concentrations and low hydrostatic pressure on the composition of black smokers. *Earth and Planetary Science Letters* 235: 654–662.

Laajoki K and Saikkonen R (1977) On the geology and geochemistry of the Precambrian iron formations in Väyrylänkylä, south Puolanka area, Finland. *Geological Survey of Finland, Bulletin* 292: 1–137.

LaBerge GL (1964) Development of magnetite in iron-formations of the Lake Superior region. *Economic Geology* 59: 1313–1342.

Lager I (2001) The geology of the Palaeoproterozoic limestone-hosted Dannemora iron deposit, Sweden. *SGU Rapporter och meddelanden* 107. Uppsala, Sweden: Geological Survey of Sweden.

Lalonde S, Planavsky NJ, Rouxel OJ, Pecoits E, and Konhauser KO (2011) Molybdenum and vanadium abundances in banded iron formation and the onset of oxidative continental weathering. *Mineralogical Magazine* 75(3): 1266.

Leckie RM, Bralower TJ, and Cashman R (2002) Oceanic anoxic events and plankton evolution: Biotic response to tectonic forcing during the mid-Cretaceous. *Paleoceanography* 17: 13-1–13-29.

Leclerc J and Weber F (1980) Geology and genesis of the Moanda manganese deposits, Republic of Gabon. In: Varentsov IM and Grasselly G (eds.) *Geology and Geochemistry of Manganese, Proceedings of the 2nd International Symposium on Geology and Geochemistry of Manganese,* Sydney, Australia, 17–24 August 1976, pp. 89–109. Stuttgart: E. Schweizerbart'sche Verlagsbuchhandlung.

Lehours AC, Evans P, Bardot C, Joblin K, and Gerard F (2007) Phylogenetic diversity of archaea and bacteria in the anoxic zone of a meromictic lake (Lake Pavin, France). *Applied and Environmental Microbiology* 73: 2016–2019.

Leith CK (1903) *The Mesabi Iron-Bearing District of Minnesota. US Geological Survey Monograph* 43. Washington, DC: US Government Printing Office.

Leith A (1935) The pre-Cambrian of the Lake Superior region, the Baraboo district, and other isolated areas in the upper Mississippi Valley. *Kansas Geological Society Guide Books* 9: 329–332.

Lemoalle J and Dupont B (1973) Iron-bearing oolites and the present conditions of iron sedimentation in Lake Chad (Africa). In: Bernard GCA (ed.) *Ores in Sediments*, pp. 167–178. Berlin: Springer.

Lepp H and Goldich SS (1964) Origin of Precambrian iron formations. *Economic Geology* 59: 1025–1060.

Li YL, Konhauser KO, Cole DR, and Phelps TJ (2011) Mineral ecophysiological data provide growing evidence for microbial activity in banded-iron formations. *Geology* 39: 707–710.

Lilley MD, Feely RA, and Trefry JH (1995) Chemical and biological transformations in hydrothermal plumes. In: Humphris SE, Zierenberg RA, Mullineaux LS, and Thomson RE (eds.) *Seafloor Hydrothermal Systems: Physical, Chemical, Biological, and Geological, Geophysical Monograph Series*, vol. 91, pp. 369–391. Washington, DC: American Geophysical Union.

Little CTS, Glynn SEJ, and Mills RA (2004) Four-hundred-and-ninety-million-year record of bacteriogenic iron oxide precipitation at sea-floor hydrothermal vents. *Geomicrobiology Journal* 21: 415–429.

Liu T-B, Alten J, and Maynard JB (2006) Superheavy S isotopes from glacial-associated sediments of the Neoproterozoic of South China: Oceanic anoxia or sulfate limitation? In: Kesler SE and Ohmoto H (eds.) *Evolution of Early Earth's Atmosphere, Hydrosphere, and Biosphere—Constraints from Ore Deposits, Geological Society of America Memoirs*, vol. 198, pp. 205–222. Boulder, CO: Geological Society of America.

Lottermoser BG (1989) Rare-earth element study of exhalites within the Willyama Supergroup, Broken Hill block, Australia. *Mineralium Deposita* 24: 92–99.

Lottermoser BG and Ashley PM (1996) Geochemistry and exploration significance of ironstones and barite-rich rocks in the Proterozoic Willyama Supergroup, Olary Block, South Australia. *Journal of Geochemical Exploration* 57: 57–73.

Lottermoser BG and Ashley PM (2000) Geochemistry, petrology and origin of Neoproterozoic ironstones in the eastern part of the Adelaide Geosyncline, South Australia. *Precambrian Research* 101: 49–67.

Lucente ME and Morey GB (1983) Stratigraphy and sedimentology of the Lower Proterozoic Virginia Formation, northern Minnesota. *Minnesota Geological Survey Report of Investigations* 28. St. Paul, MN: Minnesota Geological Survey.

Lyons TW and Severmann S (2006) A critical look at iron paleoredox proxies based on new insights from modern euxinic marine basins. *Geochimica et Cosmochimica Acta* 70: 5698–5722.

Macdonald FA, Schmitz MD, Crowley JL, et al. (2010) Calibrating the Cryogenian. *Science* 327: 1241–1243.

Machado N, Clark T, David J, and Goulet N (1997) U–Pb ages for magmatism and deformation in the New Quebec orogen. *Canadian Journal of Earth Sciences* 34: 716–723.

Maliva RG, Knoll AH, and Simonson BM (2005) Secular change in the Precambrian silica cycle: Insights from chert petrology. *Geological Society of America Bulletin* 117: 835–845.

Marbler H, Koschinsky A, Pape T, et al. (2010) Geochemical and physical structure of the hydrothermal plume at the ultramafic-hosted Logatchev hydrothermal field at 14°45′N on the Mid-Atlantic Ridge. *Marine Geology* 271: 187–197.

Marin-Carbonne J, Chaussidon M, Boiron MC, and Robert F (2011) A combined in situ oxygen, silicon isotopic and fluid inclusion study of a chert sample from Onverwacht Group (3.35 Ga, South Africa): New constraints on fluid circulation. *Chemical Geology* 286: 59–71.

Marin-Carbonne J, Chaussidon M, and Robert FB (2012) Micrometer-scale chemical and isotopic criteria (O and Si) on the origin and history of Precambrian cherts: Implications for paleo-temperature reconstructions. *Geochimica et Cosmochimica Acta* 92: 29–147.

Master S (1991) Stratigraphy, tectonic setting, and mineralization of the Early Proterozoic Magondi Supergroup, Zimbabwe: A review. *Economic Geology Research Unit Information Circular* 238, Johannesburg University of the Witwatersrand.

Maynard JB (1986) Geochemistry of oolitic iron ores: An electron microprobe study. *Economic Geology* 81: 1473–1483.

Maynard JB (2010) The chemistry of manganese ores through time: A signal of increasing diversity of Earth-surface environments. *Economic Geology* 105: 535–552.
Maynard JB and Van Houten FB (1992) Descriptive model of oolitic ironstones. In: Bliss JD (ed.) *Developments in Mineral Deposit Modeling. US Geological Survey Bulletin 2004,* pp. 39–40. Washington, DC: US Government Printing Office.
McAllister SM, Davis RE, McBeth JM, Tebo BM, Emerson D, and Moyer CL (2011) Biodiversity and emerging biogeography of the neutrophilic iron-oxidizing zetaproteobacteria. *Applied and Environmental Microbiology* 77: 5445–5457.
Meyer C (1988) Ore-deposits as guides to geologic history of the Earth. *Annual Review of Earth and Planetary Sciences* 16: 147–171.
Meyer KM and Kump LR (2008) Oceanic euxinia in Earth history: Causes and consequences. *Annual Review of Earth and Planetary Sciences* 36: 251–288.
Miller AR and Reading KL (1993) Iron-formation, evaporite, and possible metallogenetic implications for the Lower Proterozoic Hurwitz Group, District of Keewatin, Northwest Territories. *Current Research, Part C, Geological Survey of Canada, Paper 93-1C*, pp. 179–185. Ottawa, ON: Natural Resources Canada.
Mills RA (1995) Hydrothermal deposits and metalliferous sediments from TAG, 26° N Mid-Atlantic Ridge. In: Parson LM, Walker CL, and Dixon DR (eds.) *Hydrothermal Vents and Processes, Geological Society Special Publication* 87, pp. 121–132. London: Geological Society of London.
Mloszewska AM, Pecoits EP, Cates NL, et al. (2012) The composition of Earth's oldest iron formations: The Nuvvuagittuq Supracrustal belt (Québec, Canada). *Earth and Planetary Science Letters* 317–318: 331–342.
Morey GB (1999) High-grade iron ore deposits of the Mesabi Range, Minnesota—product of a continental-scale Proterozoic ground-water flow system. *Economic Geology* 94: 133–141.
Morris RC (1993) Genetic modelling for banded iron-formations of the Hamersley Group, Pilbara craton, Western Australia. *Precambrian Research* 60: 243–286.
Morris RC (2002) Opaque mineralogy and magnetic properties of selected banded iron-formations, Hamersley Basin, Western Australia—discussion. *Australian Journal of Earth Sciences* 49: 579–581.
Morris RC and Horwitz RC (1983) The origin of the BIF-rich Hamersley Group of Western Australia—deposition on a platform. *Precambrian Research* 21: 273–297.
Mortlock RA and Froelich PN (1987) Continental weathering of germanium—Ge/Si in the global river discharge. *Geochimica et Cosmochimica Acta* 51: 2075–2082.
Mortlock RA, Froelich PN, Feely RA, Massoth GJ, Butterfield DA, and Lupton JE (1993) Silica and germanium in Pacific Ocean hydrothermal vents and plumes. *Earth and Planetary Science Letters* 119: 365–378.
Mottl MJ, Holland HD, and Corr RF (1979) Chemical exchange during hydrothermal alteration of basalt by seawater. 2. Experimental results for Fe, Mn, and sulfur species. *Geochimica et Cosmochimica Acta* 43: 869–884.
Mücke A (2005) The Nigerian manganese-rich iron-formations and their host-rocks-from sedimentation to metamorphism. *Journal of African Earth Sciences* 41: 407–436.
Mücke A, Dzigbodi-Adjimah K, and Annor A (1999) Mineralogy, petrography, geochemistry and genesis of the Paleoproterozoic Birimian manganese-formation of Nsuta/Ghana. *Mineralium Deposita* 34: 297–311.
Muehlenbachs K (1998) The oxygen isotopic composition of the oceans, sediments and the seafloor. *Chemical Geology* 145: 263–273.
Mukhopadhyay J, Beukes NJ, Armstrong RA, Zimmermann U, Ghosh G, and Medda RE (2008) Dating the oldest greenstone in India: A 3.51-Ga precise U–Pb SHRIMP zircon age for dacitic lava of the southern Iron Ore Group, Singhbhum craton. *Journal of Geology* 116: 449–461.
Müller G and Förstner U (1973) Recent iron ore formation in Lake Malawi, Africa. *Mineralium Deposita* 8: 278–290.
Murray JW (1979) Iron oxides. In: Burns RG (ed.) *Marine Minerals, Mineralogical Society of America Short Course Notes*, vol. 6, pp. 47–98. Chantilly, VA: Mineralogical Society of America.
Myers JS (2001) Protoliths of the 3.7–3.8 Ga Isua greenstone belt, West Greenland. *Precambrian Research* 105: 129–141.
Naqvi SM and Rogers JJW (1987) *Precambrian Geology of India*. Oxford: Oxford University Press.
O'Neil J, Maurice C, Stevenson R, Larocque J, Cloquet C, and David JFD (2007) The geology of the 3.8 Ga Nuvvuagittuq (Porpoise Cove) greenstone belt, northeastern Superior Province, Canada. *Developments in Precambrian Geology* 15: 219–250.
Often M (1985) The Early Proterozoic Karasjok greenstone belt, Norway: A preliminary description of lithology, stratigraphy and mineralization. In: *Geology of Finnmark: A collection of papers papers on the geology, geophysics, geochemistry, metallogeny and Quaternary geology of Finnmark, northern Norway, Norges Geologiske Undersøkelse Bulletin* 403, pp. 75–88. Trondheim: Norges Geologiske Undersøkelse.
Ohmoto H, Watanabe Y, and Kumazawa K (2004) Evidence from massive siderite beds for a CO_2-rich atmosphere before ~1.8 billion years ago. *Nature* 429: 395–399.
Ohmoto H, Watanabe Y, Yamaguchi KE, et al. (2006) Chemical and biological evolution of early Earth: Constraints from banded iron-formations. In: Ohmoto H and Kessler SK (eds.) *Evolution of the Atmosphere, Hydrosphere, and Biosphere on Early Earth: Constraints from Ore Deposits. Geological Society of America Memoirs*, vol. 198, pp. 291–331. Boulder, CO: Geological Society of America.
Ojakangas RW (1983) Tidal deposits in the Early Proterozoic basin of the Lake Superior region—the Palms and the Pokegama Formations: Evidence for subtidal shelf deposition of Superior type banded iron formation. In: Medaris LG (ed.) *Early Proterozoic Geology of the Great Lakes Region. Geological Society of America Memoirs*, vol. 160, pp. 49–66. Boulder, CO: Geological Society of America.
Ojakangas RW (1994) Sedimentology and provenance of the Early Proterozoic Michigamme Formation and Goodrich Quartzite, Northern Michigan—Regional stratigraphic implications and suggested correlations. *US Geological Survey Bulletin 1904-R*. Washington, DC: US Government Printing Office.
Ojakangas RW, Marmo JS, and Heiskanen KI (2001) Basin evolution of the Paleoproterozoic Karelian Supergroup of the Fennoscandian (Baltic) Shield. *Sedimentary Geology* 141–142: 255–285.
Owens JD, Lyons TW, Li X, et al. (2012) Iron isotope and trace metal records of iron cycling in the proto-North Atlantic during the Cenomanian-Turonian oceanic anoxic event (OAE-2). *Paleoceanography* 27: PA3223.
Paakola J (1971) The volcanic complex and associated manganiferous iron formation of the Porkonen-Pahtavaara area in Finnish Lapland. *Bulletin de la Commission Géologique de Finlande* 247. Helsinki: Geological Survey of Finland.
Partridge MA, Golding SD, Baublys KA, and Young E (2008) Pyrite paragenesis and multiple sulfur isotope distribution in late Archean and early Paleoproterozoic Hamersley Basin sediments. *Earth and Planetary Science Letters* 272: 41–49.
Perry EC (1967) Oxygen isotope chemistry of ancient cherts. *Earth and Planetary Science Letters* 3: 62–66.
Perry EC, Tan FC, and Morey GB (1973) Geology and stable isotope geochemistry of Biwabik Iron Formation, northern Minnesota. *Economic Geology* 68: 1110–1125.
Peter JM (2003) Ancient iron formations: Their genesis and use in the exploration for stratiform base metal sulphide deposits, with examples from the Bathurst mining camp. In: Lentz DR (ed.) *Geochemistry of Sediments and Sedimentary Rocks, Geological Association of Canada GeoText 4*, pp. 145–176. St. John's, NL: Geological Association of Canada.
Peter JM, Goodfellow WD, and Doherty W (2003) Hydrothermal sedimentary rocks of the Heath Steele Belt, Bathurst mining camp, New Brunswick: Part 2. Bulk and rare earth element geochemistry and implications for origin. *Economic Geology Monographs* 11: 391–415.
Petranek J and Van Houten FB (1997) *Phanerozoic Ooidal Ironstones. Czech Geological Survey Special Paper* 7. Prague: Czech Geological Survey.
Philippot P, Van Zuilen M, Lepot K, Thomazo C, Farquhar J, and Van Kranendonk MJ (2007) Early Archaean microorganisms preferred elemental sulfur, not sulfate. *Science* 317: 1534–1537.
Pickard AL (2002) SHRIMP U–Pb zircon ages of tuffaceous mudrocks in the Brockman Iron Formation of the Hamersley Range, Western Australia. *Australian Journal of Earth Sciences* 49: 491–507.
Pickard AL (2003) SHRIMP U–Pb zircon ages for the Palaeoproterozoic Kuruman Iron Formation, northern Cape Province, South Africa: Evidence for simultaneous BIF deposition on Kaapvaal and Pilbara Cratons. *Precambrian Research* 125: 275–315.
Pickard AL, Barley ME, and Krapež B (2004) Deep-marine depositional setting of banded iron formation: Sedimentological evidence from interbedded clastic sedimentary rocks in the early Palaeoproterozoic Dales Gorge Member of Western Australia. *Sedimentary Geology* 170: 37–62.
Planavsky NJ, Bekker A, Rouxel OJ, Knudsen A, and Lyons TW (2010a) Rare earth element and yttrium compositions of Archean and Paleoproterozoic iron formations revisited: New perspectives on the significance and mechanisms of deposition. *Geochimica et Cosmochimica Acta* 74: 6387–6405.
Planavsky NJ, McGoldrick P, Scott CT, et al. (2011) Widespread iron-rich conditions in the mid-Proterozoic ocean. *Nature* 477: 448–495.
Planavsky NJ, Rouxel OR, Bekker A, Hoffman A, Little C, and Lyons TW (2012) The iron isotope compostion of some banded iron formations. *Geochimica et Cosmochimica Acta* 80: 158–169.
Planavsky NJ, Rouxel O, Bekker A, Shapiro R, Fralick P, and Knudsen A (2009) Iron-oxidizing microbial ecosystems thrived in late Paleoproterozoic redox-stratified oceans. *Earth and Planetary Science Letters* 286: 230–242.
Planavsky NJ, Rouxel OJ, Bekker A, et al. (2010b) The evolution of the marine phosphate reservoir. *Nature* 467: 1088–1090.
Pokrovsky OS, Pokrovski GS, Schott J, and Galy A (2006) Experimental study of germanium adsorption on goethite and germanium coprecipitation with iron hydroxide: X-ray absorption fine structure and macroscopic characterization. *Geochimica et Cosmochimica Acta* 70: 3325–3341.

Polat A, Appel PWU, Frei R, et al. (2007) Field and geochemical characteristics of the Mesoarchean (~3075 Ma) Ivisaartoq greenstone belt, southern West Greenland: Evidence for seafloor hydrothermal alteration in supra-subduction oceanic crust. *Gondwana Research* 11: 69–91.

Polat A and Frei R (2005) The origin of Early Archean banded iron formations and of continental crust, Isua, southern West Greenland. *Precambrian Research* 138: 151–175.

Pope MC and Read JF (1997) High-resolution surface and subsurface sequence stratigraphy of the Middle to Late Ordovician (late Mohawkian–Cincinnatian) foreland basin rocks, Kentucky and Virginia. *American Association of Petroleum Geologists Bulletin* 81: 1866–1893.

Poulton SW and Canfield DE (2006) Co-diagenesis of iron and phosphorus in hydrothermal sediments from the southern East Pacific Rise: Implications for the evaluation of paleoseawater phosphate concentrations. *Geochimica et Cosmochimica Acta* 70: 5883–5898.

Poulton SW, Fralick PW, and Canfield DE (2004) The transition to a sulphidic ocean ~1.84 billion years ago. *Nature* 431: 173–177.

Poulton SW, Fralick PW, and Canfield DE (2010) Spatial variability in oceanic redox structure 1.8 billion years ago. *Nature Geoscience* 3: 486–490.

Prakash HSM and Devapriyan GV (1996) REE enrichment in the oxide facies BIF of Chitradurga schist belt, Karnataka. *Journal of the Geological Society of India* 47: 265.

Prilutzky RE, Suslova SN, and Nalivkina YB (1992) Reconstruction of environmental conditions of Early Proterozoic carbonate deposits of the Ukrainian and Baltic shields based on isotopic studies. *Lithology and Mineral Deposits* 5: 76–88.

Puchelt H (1973) Recent iron sediment formation at the Kameni islands, Santorini (Greece). In: Amstutz GC and Bernard AJ (eds.) *Ores in Sediments*, pp. 227–245. Berlin: Springer.

Pufahl PK and Fralick PW (2004) Depositional controls on Palaeoproterozoic iron formation accumulation, Gogebic Range, Lake Superior region, USA. *Sedimentology* 51: 791–808.

Rai D, Eary LE, and Zachara JM (1989) Environmental chemistry of chromium. *Science of the Total Environment* 86: 15–23.

Rainbird RH, Jefferson CW, Hilderbrand RS, and Worth JK (1994) The Shaler Supergroup and revision of the Neoproterozoic stratigraphy in the Amundsen Basin, Northwest Territories. *Geological Survey of Canada Paper 94–1A*, pp. 61–70. Ottawa, ON: Natural Resources Canada.

Raiswell R (2006) An evaluation of diagenetic recycling as a source of iron for banded iron formations. In: Kesler SE and Ohmoto H (eds.) *Evolution of the Atmosphere, Hydrosphere, and Biosphere on Early Earth: Constraints from Ore Deposits, Geological Society of America Memoirs*, vol. 198, pp. 228–238. Boulder, CO: Geological Society of America.

Rasmussen B, Fletcher IR, Bekker A, Muhling JR, Gregory CJ, and Thorne AM (2012) Deposition of 1.88-billion-year-old iron formations as a consequence of rapid crustal growth. *Nature* 484: 498–501.

Rasmussen B, Fletcher IR, Muhling JR, Thorne WS, and Broadbent GC (2007) Prolonged history of episodic fluid flow in giant hematite ore bodies: Evidence from in situ U–Pb geochronology of hydrothermal xenotime. *Earth and Planetary Science Letters* 258: 249–259.

Redfield AC (1958) The biological control of chemical factors in the environment. *American Scientist* 46: 205–221.

Reinhard CT, Raiswell R, Scott C, Anbar AD, and Lyons TW (2009) A Late Archean sulfidic sea stimulated by early oxidative weathering of the continents. *Science* 326: 713–716.

Resende MG and Jost H (1995) Petrogênese de formações ferríferas e metahidrotermalitos da formação aimbé, grupo guarinos (Arqueano), GOIÁS. *Revista Brasileira de Geociências* 25: 41–50.

Reynolds BC, Frank M, and Halliday AN (2006) Silicon isotope fractionation during nutrient utilization in the North Pacific. *Earth and Planetary Science Letters* 244: 431–443.

Ricketts BD, Ware MJ, and Donaldson JA (1982) Volcaniclastic rocks and volcaniclastic facies in the Middle Precambrain (Aphebian) Belcher Group, Northwest Territories, Canada. *Canadian Journal of Earth Sciences* 19: 1275–1294.

Robert F and Chaussidon M (2006) A palaeotemperature curve for the Precambrian oceans based on silicon isotopes in cherts. *Nature* 443: 969–972.

Robertson A (1975) Cyprus umbers: Basalt-sediment relationships on a Mesozoic ocean ridge. *Journal of the Geological Society* 131: 511–531.

Roh Y, Zhang CL, Vali H, Lauf RJ, Zhou J, and Phelps TJ (2003) Biogeochemical and environmental factors in Fe biomineralization: Magnetite and siderite formation. *Clays and Clay Minerals* 51: 83–95.

Roscoe SM, Gandhi SS, Charbonneau BW, Maurice YT, and Gibb RA (1987) Mineral resource assessment of the area in the East Arm (Great Slave Lake) and Artillery Lake region, N.W.T. proposed as a national park. *Geological Survey of Canada Open File 1434*. Ottawa, ON: Natural Resources Canada.

Rosing MT, Bird DK, Sleep NH, and Bjerrum CJ (2010) No climate paradox under the faint early Sun. *Nature* 464: 744–747.

Rothman DH, Hayes JM, and Summons RE (2003) Dynamics of the Neoproterozoic carbon cycle. *Proceedings of the National Academy of Sciences of the United States of America* 100: 8124–8129.

Rouxel OJ and Auro M (2010) Iron isotope variations in coastal seawater determined by multicollector ICP-MS. *Geostandards and Geoanalytical Research* 34: 135–144.

Rouxel OJ, Bekker A, and Edwards KJ (2005) Iron isotope constraints on the Archean and Paleoproterozoic ocean redox state. *Science* 307: 1088–1091.

Rouxel O, Dobbek N, Ludden J, and Fouquet Y (2003) Iron isotope fractionation during oceanic crust alteration. *Chemical Geology* 202: 155–182.

Rouxel O, Galy A, and Elderfield H (2006) Germanium isotopic variations in igneous rocks and marine sediments. *Geochimica et Cosmochimica Acta* 70: 3387–3400.

Rouxel O, Shanks WC, Bach W, and Edwards KJ (2008a) Integrated Fe- and S-isotope study of seafloor hydrothermal vents at East Pacific rise 9–10°N. *Chemical Geology* 252: 214–227.

Rouxel O, Sholkovitz E, Charette M, and Edwards KJ (2008b) Iron isotope fractionation in subterranean estuaries. *Geochimica et Cosmochimica Acta* 72: 3413–3430.

Ruttenberg KC and Berner RA (1993) Authigenic apatite formation and burial in sediments from non-upwelling, continental-margin environments. *Geochimica et Cosmochimica Acta* 57: 991–1007.

Rye R and Holland HD (2000) Geology and geochemistry of paleosols developed on the Hekpoort basalt, Pretoria Group, South Africa. *American Journal of Science* 300: 85–141.

Sadler PM (1981) Sediment accumulation rates and the completeness of stratigraphic sections. *Journal of Geology* 89: 569–584.

Saha L, Hofmann A, Xie HQ, et al. (2010) Zircon ages and metamorphic evolution of the Archean Assegaai-De Kraalen granitoid-greenstone terrain, southeastern Kaapvaal craton. *American Journal of Science* 310: 1384–1420.

Salama W, Weryer S, Gaupp R, and El Aref M (2011) Iron isotope composition of the Middle Eocene ooidal-oncoidal ironstones and the associated lateritic paleosols from the Bahariya Depression, Western Desert, Egypt. *Mineralogical Magazine* 75: 1783.

Sander S and Koschinsky A (2000) Onboard-ship redox speciation of chromium in diffuse hydrothermal fluids from the North Fiji Basin. *Marine Chemistry* 71: 83–102.

Sander SG and Koschinsky A (2011) Metal flux from hydrothermal vents increased by organic complexation. *Nature Geoscience* 4: 145–150.

Savage PS, Georg RB, Armytage RMG, Williams HM, and Halliday AN (2010) Silicon isotope homogeneity in the mantle. *Earth and Planetary Science Letters* 295: 139–146.

Sawayama S (2006) Possibility of anoxic ferric ammonium oxidation. *Journal of Bioscience and Bioengineering* 101: 70–72.

Schidlowski M, Eichmann R, and Junge CE (1976) Carbon isotope geochemistry of the Precambrian Lomagundi carbonate province, Rhodesia. *Geochimica et Cosmochimica Acta* 40: 449–455.

Schijf J, de Baar HJW, and Millero FJ (1995) Vertical distributions and speciation of dissolved rare earth elements in the anoxic brines of Bannock Basin, eastern Mediterranean. *Geochimica et Cosmochimica Acta* 57: 1419–1432.

Schmidt RG (1980) The Marquette Range Supergroup in the Gogebic Iron District, Michigan and Wisconsin. *US Geological Survey Bulletin 1460*. Washington, DC: US Government Printing Office.

Schneider DA, Bickford ME, Cannon WF, Schulz KJ, and Hamilton MA (2002) Age of volcanic rocks and syndepositional iron formations, Marquette Range Supergroup: Implications for the tectonic setting of Paleoproterozoic iron formations of the Lake Superior region. *Canadian Journal of Earth Sciences* 39: 999–1012.

Schneiderhan EA, Gutzmer J, Strauss H, Mezger K, and Beukes NJ (2006) The chemostratigraphy of a Paleoproterozoic Mn and BIF succession—the Voëlwater Subgroup of the Transvaal Supergroup in Griqualand West, South Africa. *South African Journal of Geology* 109: 63–80.

Schröder S, Bekker A, Beukes NJ, Strauss H, and van Niekerk HS (2008) Rise in seawater sulphate concentration associated with the Paleoproterozoic positive carbon isotope excursion: Evidence from sulphate evaporites in the ~2.2–2.1 Gyr shallow-marine Lucknow Formation, South Africa. *Terra Nova* 20: 108–117.

Schroth AW, Crusius J, Chever F, Bostick BC, and Rouxel OJ (2011) Glacial influence on the geochemistry of riverine iron fluxes to the Gulf of Alaska and effects of deglaciation. *Geophysical Research Letters* 38: L16605.

Schulz KJ and Cannon WF (2007) The Penokean orogeny in the Lake Superior region. *Precambrian Research* 157: 4–25.

Schulz KJ and Cannon WF (2008) Synchronous deposition of Paleoproterozoic Superior-type banded iron-formations and volcanogenic massive sulfides in the Lake Superior region: Implications for the tectonic evolution of the Penokean orogen. *Geological Society of America Abstracts with Programs* 40(6): 387.

Schweigart H (1965) Genesis of the iron ores of the Pretoria Series, South Africa. *Economic Geology* 60: 269–298.
Scott C, Bekker A, Reinhard CT, et al. (2011) Late Archean euxinic conditions before the rise of atmospheric oxygen. *Geology* 39: 119–122.
Scott CT, Lyons TW, Bekker A, et al. (2008) Tracing the stepwise oxygenation of the Proterozoic biosphere. *Nature* 452: 456–459.
Severmann S, Johnson CM, Beard BL, et al. (2004) The effect of plume processes on the Fe isotope composition of hydrothermally derived Fe in the deep ocean as inferred from the Rainbow vent site, Mid-Atlantic Ridge, 36°14′ N. *Earth and Planetary Science Letters* 225: 63–76.
Severmann S, Lyons TW, Anbar A, McManus J, and Gordon G (2008) Modern iron isotope perspective on the benthic iron shuttle and the redox evolution of ancient oceans. *Geology* 36: 487–490.
Shen Y and Bekker A (2006) Paleoproterozoic ocean chemistry: Evidence from the Sengoma Argillite Formation (~2.2 Ga) in Botswana. *Astrobiology* 6: 166–167.
Shen Y, Buick R, and Canfield DE (2001) Isotopic evidence for microbial sulphate reduction in the Early Archean era. *Nature* 410: 77–81.
Shen Y, Farquhar J, Masterson A, Kaufman AJ, and Buick R (2009) Evaluating the role of microbial sulfate reduction in the Early Archean using quadruple isotope systematics. *Earth and Planetary Science Letters* 279: 383–391.
Shen Y, Knoll AH, and Walter MA (2003) Evidence for low sulfate and anoxia in a mid-Proterozoic marine basin. *Nature* 423: 633–635.
Shen Y, Pinti DL, and Hashizume K (2006) Biogeochemical cycles of sulfur and nitrogen in the Archean ocean and atmosphere. In: Benn K, Mareschal JC, and Condie K (eds.) *Archean Geodynamics and Environments, Geophysical Monograph Series*, vol. 164, pp. 305–320. Washington, DC: American Geophysical Union.
Sherrell RM, Field MP, and Ravizza G (1999) Uptake and fractionation of rare earth elements on hydrothermal plume particles at 9°45' N, East Pacific Rise. *Geochimica et Cosmochimica Acta* 63: 1709–1722.
Shimizu H, Amano M, and Masuda A (1991) La–Ce and Sm–Nd systematics of siliceous sedimentary rocks: A clue to marine environment in their deposition. *Geology* 19: 369–371.
Shimizu H, Umemoto N, Masuda A, and Appel PWU (1990) Sources of iron formations in the Archean Isua and Malene supracrustals, West Greenland: Evidence from La–Ce and Sm–Nd isotopic data and REE abundances. *Geochimica et Cosmochimica Acta* 54: 1147–1154.
Sholkovitz ER, Boyle E, Price NB, and Edmond JM (1977) Removal of dissolved material in Amazon estuary. *Eos, Transactions American Geophysical Union* 58: 423.
Siever R (1992) The silica cycle in the Precambrian. *Geochimica et Cosmochimica Acta* 56: 3265–3272.
Silver PG and Behn MD (2008) Intermittent plate tectonics? *Science* 319: 85–88.
Simonson BM (2003) Origin and evolution of large Precambrian iron formations. In: Chan MA and Archer AW (eds.) *Extreme Depositional Environments: Mega End Members in Geologic Time, Geological Society of America Special Papers* 370, pp. 231–244. Boulder, CO: Geological Society of America.
Simonson BM and Goode ADT (1989) First discovery of ferruginous chert arenites in the early Precambrian Hamersley Group of Western Australia. *Geology* 17: 269–272.
Simonson BM and Hassler SW (1996) Was the deposition of large Precambrian iron formations linked to major marine transgressions? *Journal of Geology* 104: 665–676.
Simonson BM, Schubel KA, and Hassler SW (1993) Carbonate sedimentology of the early Precambrian Hamersley Group of Western Australia. *Precambrian Research* 60: 287–335.
Sinton CW and Duncan RA (1997) Potential links between oceanic plateau volcanism and global ocean anoxia at the Cenomanian–Turonian boundary. *Economic Geology* 92: 836–842.
Slack JF and Cannon WF (2009) Extraterrestrial demise of banded iron formations 1.85 billion years ago. *Geology* 37: 1011–1014.
Slack JF, Grenne T, and Bekker A (2009) Seafloor-hydrothermal Si-Fe-Mn exhalites in the Pecos greenstone belt, New Mexico, and the redox state of ca. 1720 Ma deep seawater. *Geosphere* 5: 302–314.
Slack JF, Grenne T, Bekker A, Rouxel OJ, and Lindberg PA (2007) Suboxic deep seawater in the late Paleoproterozoic: Evidence from hematitic chert and iron formation related to seafloor-hydrothermal sulfide deposits, central Arizona, USA. *Earth and Planetary Science Letters* 255: 243–256.
Smith ABJ (2007) *The Paleo-Environmental Significance of the Iron-Formations and Iron-Rich Mudstones of the Mesoarchean Witwatersrand-Mozaan Basin, South Africa*. MSc Thesis, University of Johannesburg.
Söderlund U, Hofmann A, Klausen MB, Olsson JR, Ernst RE, and Persson P-O (2010) Towards a complete magmatic barcode for the Zimbabwe craton: Baddeleyite U–Pb dating of regional dolerite dyke swarms and sill complexes. *Precambrian Research* 183: 388–389.
Søgaard EG, Medenwaldt R, and Abraham-Peskir JV (2000) Conditions and rates of biotic and abiotic iron precipitation in selected Danish freshwater plants and microscopic analysis of precipitate morphology. *Water Research* 34: 2675–2682.
Spier CA, de Oliveira SMB, Sial AN, and Rios FJ (2007) Geochemistry and genesis of the banded iron formations of the Caue Formation, Quadrilatero Ferrifero, Minas Gerais, Brazil. *Precambrian Research* 152: 170–206.
Spry PG, Peter JM, and Slack JF (2000) Meta-exhalites as exploration guides to ore. *Reviews in Economic Geology* 11: 163–201.
Srinivasan R and Ojakangas RW (1986) Sedimentology of quartz pebble conglomerates and quartzites of the Archean Bababudan Group, Dharwar craton, south India: Evidence for early crustal stability. *Journal of Geology* 94: 199–214.
Stanley SM and Hardie LA (1998) Secular oscillations in the carbonate mineralogy of reef-building and sediment-producing organisms driven by tectonically forced shifts in seawater chemistry. *Palaeogeography, Palaeoclimatology, Palaeoecology* 144: 3–19.
Steinhoefel G, Horn I, and von Blanckenburg F (2009) Micro-scale tracing of Fe and Si isotope signatures in banded iron formation using femtosecond laser ablation. *Geochimica et Cosmochimica Acta* 73: 5343–5360.
Steinhoefel G, von Blanckenburg F, Horn I, Konhauser KO, Beukes NJ, and Gutzmer J (2010) Deciphering formation processes of banded iron formations from the Transvaal and the Hamersley successions by combined Si and Fe isotope analysis using UV femtosecond laser ablation. *Geochimica et Cosmochimica Acta* 74: 2677–2696.
Stone D (2010) Precambrian geology of the central Wabigoon Subprovince area, northwestern Ontario. *Ontario Geological Survey Open File Report 5422*. Sudbury, ON: Ministry of Northern Development and Mines.
Stott GM, Hamilton MA, and Kamo SL (2010) Archean granitoid geochronology and interpretations, Hudson Bay lowland; In: *Summary of Field Work and Other Activities 2010, Ontario Geological Survey Open File Report 6260*, pp. 21–27. Sudbury, ON: Ministry of Northern Development and Mines.
Straub KL, Benz M, Schink B, and Widdel F (1996) Anaerobic, nitrate-dependent microbial oxidation of ferrous iron. *Applied Environmental Microbiology* 62: 1458–1460.
Straub KL and Buchholz-Cleven BEE (1998) Enumeration and detection of anaerobic ferrous iron-oxidizing, nitrate-reducing bacteria from diverse European sediments. *Applied Environmental Microbiology* 64: 4846–4856.
Straub KL, Rainey FA, and Widdel F (1999) *Rhodovulum iodosum* sp. nov, and *Rhodovulum robiginosum* sp. nov, two new marine phototrophic ferrous-iron-oxidizing purple bacteria. *International Journal of Systematic Bacteriology* 49: 729–735.
Strydom D, van der Westhuizen WA, and Schoch AE (1987) The iron formations of Bushmanland in the north-western Cape Province, South Africa. In: Uitterdijk Appel PW and LaBerge GL (eds.) *Precambrian Iron-Formations*, pp. 621–634. Athens: Theophrastus.
Stumm W and Morgan JJ (1995) *Aquatic Chemistry*, 3rd edn. New York: John Wiley.
Sturesson U (2003) Lower Palaeozoic iron oolites and volcanism from a Baltoscandian perspective. *Sedimentary Geology* 159: 241–256.
Sturesson U, Dronov A, and Saadre T (1999) Lower Ordovician iron ooids and associated oolitic clays in Russia and Estonia: A clue to the origin of iron oolites? *Sedimentary Geology* 123: 63–80.
Su WB, Li HK, Huff WD, et al. (2010) SHRIMP U–Pb dating for a K-bentonite bed in the Tieling Formation, North China. *Chinese Science Bulletin* 55(29): 3312–3323.
Sverjensky DA (1984) Europium redox equilibria in aqueous solution. *Earth and Planetary Science Letters* 67: 70–78.
Syme EC and Bailes AH (1993) Stratigraphic and tectonic setting of Early Proterozoic volcanogenic massive sulfide deposits, Flin Flon, Manitoba. *Canadian Journal of Earth Sciences* 88: 566–589.
Szpunar M, Hand M, Barovich K, Jagodzinski E, and Belousova E (2011) Isotopic and geochemical constraints on the Paleoproterozoic Hutchison Group, southern Australia: Implications for Paleoproterozoic continental reconstructions. *Precambrian Research* 187: 99–126.
Tagliabue A, Bopp L, Dutay JC, et al. (2010) Hydrothermal contribution to the oceanic dissolved iron inventory. *Nature Geoscience* 3: 252–256.
Taitel-Goldman N and Singer A (2002) Synthesis of clay-sized iron oxides under marine hydrothermal conditions. *Clay Minerals* 37: 719–731.
Tanaka T and Masuda A (1982) The La-Ce geochronometer: A new dating method. *Nature* 300: 515–518.
Taylor D, Dalstra HJ, Harding AE, Broadbent GC, and Barley ME (2001) Genesis of high-grade hematite orebodies of the Hamersley Province, Western Australia. *Economic Geology* 96: 837–873.

Taylor KG, Simo JA, Yakum D, and Leckie DA (2002) Stratigraphic significance of ooidal ironstones from the Cretaceous western interior seaway: The Peace River Formation, Alberta, Canada, and the Castlegate Sandstone, Utah, U.S.A. *Journal of Sedimentary Research* 72: 316–327.

Thode HG and Goodwin AM (1983) Further sulfur and carbon isotope studies of Late Archean iron-formations of the Canadian Shield and the rise of sulfate reducing bacteria. *Precambrian Research* 20: 337–356.

Thomazo C, Ader M, and Philippot P (2011) Extreme ^{15}N-enrichments in 2.72-Gyr-old sediments: Evidence for a turning point in the nitrogen cycle. *Geobiology* 9: 107–120.

Tice MM and Lowe DR (2004) Photosynthetic microbial mats in the 3,416-Myr-old ocean. *Nature* 431: 549–552.

Tomlinson KY, Davis DW, Stone D, and Hart TR (2003) U–Pb age and Nd isotopic evidence for Archean terrane development and crustal recycling in the south-central Wabigoon subprovince, Canada. *Contributions to Mineralogy and Petrology* 144: 684–702.

Tompkins LA and Cowan DR (2001) Opaque mineralogy and magnetic properties of selected banded iron-formations, Hamersley Basin, Western Australia. *Australian Journal of Earth Sciences* 48: 427–437.

Toner BM, Fakra SC, Manganini SJ, et al. (2009) Preservation of iron(II) by carbon-rich matrices in a hydrothermal plume. *Nature Geoscience* 2: 197–201.

Trendall AF (1973) Varve cycles in the Weeli Wolli Formation of the Precambrian Hamersley Group, Western Australia. *Economic Geology* 68: 1089–1097.

Trendall AF (1990) Hamersley Basin, Geology and Mineral Resources of Western Australia. *Geological Survey of Western Australia Memoir* 3: 163–190.

Trendall AF (2002) The significance of iron-formation in the Precambrian stratigraphic record. In: Altermann W and Corcoran PL (eds.) *Precambrian Sedimentary Environments: A Modern Approach to Ancient Depositional Systems*, *International Association of Sedimentologists Special Publication* 33, pp. 33–66. Oxford: Blackwell Publishing Ltd.

Trendall A and Blockley J (1970) The iron formations of the Precambrian Hamersley Group, Western Australia with special reference to the associated crocidolite. *Geological Survey of Western Australia Bulletin* 119. Perth: Geological Survey of Western Australia.

Trendall AF, deLaeter JR, Nelson DR, and Mukhopadhyay D (1997) A precise zircon U–Pb age for the base of the BIF of the Mulaingiri Formation (Bababudan Group, Dharwar Supergroup) of the Karnataka craton. *Journal of the Geological Society of India* 50: 161–170.

Trompette R, De Alvarenga CJS, and Walde D (1998) Geological evolution of the Neoproterozoic Corumba graben system (Brazil): Depositional context of the stratified Fe and Mn ores of the Jacadigo Group. *Journal of South American Earth Sciences* 11: 587–597.

Tsikos H, Beukes NJ, Moore JM, and Harris C (2003) Deposition, diagenesis, and secondary enrichment of metals in the Paleoproterozoic Hotazel Iron Formation, Kalahari manganese field, South Africa. *Economic Geology* 98: 1449–1462.

Tsikos H, Matthews A, Erel Y, and Moore JM (2010) Iron isotopes constrain biogeochemical redox cycling of iron and manganese in a Palaeoproterozoic stratified basin. *Earth and Planetary Science Letters* 298: 125–134.

Tsikos H and Moore JM (1997) Petrography and geochemistry of the Paleoproterozoic Hotazel Iron-Formation, Kalahari manganese field, South Africa: Implications for Precambrian manganese metallogenesis. *Economic Geology* 92: 87–97.

Turgeon SC and Creaser RA (2008) Cretaceous oceanic anoxic event 2 triggered by a massive magmatic episode. *Nature* 454: 323–326.

Valaas Hyslop E, Valley JW, Johnson CM, and Beard BL (2008) The effects of metamorphism on O and Fe isotope compositions in the Biwabik Iron Formation, northern Minnesota. *Contributions to Mineralogy and Petrology* 155: 313–328.

Valeton I, Schumann A, Vinx R, and Wieneke M (1997) Supergene alteration since the Upper Cretaceous on alkaline igneous and metasomatic rocks of the Poços de Caldas ring complex, Minas Gerais, Brazil. *Analytical Geochemistry* 12: 133–154.

van den Boorn SHJM, van Bergen MJ, Nijman W, and Vroon PZ (2007) Dual role of seawater and hydrothermal fluids in Early Archean chert formation: Evidence from silicon isotopes. *Geology* 35: 939–942.

van den Boorn SHJM, van Bergen MJ, Vroon PZ, de Vries ST, and Nijman W (2010) Silicon isotope and trace element constraints on the origin of 3.5 Ga cherts: Implications for Early Archaean marine environments. *Geochimica et Cosmochimica Acta* 74: 1077–1103.

Van Houten FB (1985) Oolitic ironstones and contrasting Ordovician and Jurassic paleogeography. *Geology* 13: 722–724.

Van Houten FB and Arthur MA (1989) Temporal patterns among Phanerozoic oolitic ironstones and oceanic anoxia. In: Young TP and Taylor WEG (eds.) *Phanerozoic Ironstones*. *Geological Society Special Publication* 46, pp. 33–49. London: Geological Society of London.

Van Wyck N and Norman M (2004) Detrital zircon ages from Early Proterozoic quartzites, Wisconsin, support rapid weathering and deposition of mature quartz arenites. *Journal of Geology* 112: 305–315.

Veizer J (1976) Evolution of ores of sedimentary affiliation through geologic history: Relations to the general tendencies in evolution of the crust, hydrosphere, atmosphere, and biosphere. In: Wolf KH (ed.) *Handbook of Strata-Bound and Stratiform Ore Deposits*, vol. 3, pp. 1–41. Amsterdam: Elsevier.

Veizer J and Compston W (1976) ^{87}Sr/^{86}Sr in Precambrian carbonates as an index of crustal evolution. *Geochimica et Cosmochimica Acta* 40: 905–914.

Walker JCG (1984) Suboxic diagenesis in banded iron formations. *Nature* 309: 340–342.

Wan Y-S, Zhang Q-D, and Song T-R (2003) SHRIMP ages of detrital zircons from the Changcheng System in the Ming Tombs area, Beijing: Constraints on the protolith nature and maximum depositional age of the Mesoproterozoic cover of the North China craton. *Chinese Science Bulletin* 48: 2500–2506.

Wang Y, Xu H, Merino E, and Konishi H (2009) Generation of banded iron formations by internal dynamics and leaching of oceanic crust. *Nature Geoscience* 2: 781–784.

Watanabe Y (2002) The ecosystems in submarine hydrothermal environments of the Canadian Shield 2.7 billion years ago. *The Late Archean Biosphere: Implications of Organic and Inorganic Geochemistry of Marine Shales and Terrestrial Paleosols*, pp. 1–87. PhD Thesis, Pennsylvania State University.

Weidman S (1904) The Baraboo iron-bearing district of Wisconsin. *Wisconsin Geological and Natural History Survey Bulletin* 13.

Welch SA, Beard BL, Johnson CM, and Braterman PS (2003) Kinetic and equilibrium Fe isotope fractionation between aqueous Fe(II) and Fe(III). *Geochimica et Cosmochimica Acta* 67: 4231–4250.

Wheat CG, Feely RA, and Mottl MJ (1996) Phosphate removal by oceanic hydrothermal processes: An update of the phosphorus budget in the oceans. *Geochimica et Cosmochimica Acta* 60: 3593–3608.

Whitehouse MJ and Fedo CM (2007) Microscale heterogeneity of Fe isotopes in $>$ 3.71 Ga banded iron formation from the Isua Greenstone belt, southwest Greenland. *Geology* 35: 719–722.

Widdel F, Schnell S, Heising S, Ehrenreich A, Assmus B, and Schink B (1993) Ferrous iron oxidation by anoxygenic phototrophic bacteria. *Nature* 362: 834–836.

Wiesli RA, Beard BL, and Johnson CM (2004) Experimental determination of Fe isotope fractionation between aqueous Fe(II), siderite and "green rust" in abiotic systems. *Chemical Geology* 211: 343–362.

Wilks ME and Nisbet EG (1988) Stratigraphy of the Steep Rock Group, northwestern Ontario: A major Archean unconformity and Archean stromatolites. *Canadian Journal of Earth Sciences* 25: 370–391.

Williams LB and Ferrell REJ (1991) Ammonium substitution in illite during maturation of organic matter. *Clays and Clay Minerals* 39: 400–408.

Wilson JF (1968) The geology of the country around Mashaba. *Rhodesia Geological Survey Bulletin* 62.

Winter BL and Knauth LP (1992) Stable isotope geochemistry of Early Proterozoic carbonate concretions in the Animikie Group of the Lake Superior region: Evidence for anaerobic bacterial processes. *Precambrian Research* 54: 131–151.

WOCE Data (2002) WOCE Global Data, V., WOCE International Project Office, WOCE Report No. 180/02, Southampton, UK.

Wu SY (1991) *The Submarine Hydrothermal Chimney in the Mariana Trough and the Sediments in the Philippine Sea*. Beijing: Oceanic Publishing House (in Chinese).

Wu JF, Wells ML, and Rember R (2011) Dissolved iron anomaly in the deep tropical-subtropical Pacific: Evidence for long-range transport of hydrothermal iron. *Geochimica et Cosmochimica Acta* 75: 460–468.

Yeo GM (1981) The Late Proterozoic Rapitan glaciation in the northern Cordillera. In: Campbell FHA (ed.) *Proterozoic Basins of Canada*. *Geological Survey of Canada Paper 81-10*, pp. 25–46. Ottawa, ON: Geological Survey of Canada.

Young GM (1981) The Amundsen embayment, Northwestern Territories; Relevance to the Upper Proterozoic evolution of North America. In: Campbell FHA (ed.) *Proterozoic Basins of Canada. Geological Survey of Canada, Paper 81-10*, pp. 203–218. Ottawa, ON: Geological Survey of Canada.

Young GM (2002) Stratigraphic and tectonic settings of Proterozoic glaciogenic rocks and banded iron-formations: Relevance to the snowball Earth debate. *Journal of African Earth Sciences* 35: 451–466.

Yucel M, Gartman A, Chan CS, and Luther G (2011) Hydrothermal vents as a kinetically stable source of iron-sulphide-bearing nanoparticles to the ocean. *Nature Geoscience* 4: 367–371.

Zahnle KJ, Claire M, and Catling D (2006) The loss of mass-independent fractionation in sulfur due to a Paleoproterozoic collapse of atmospheric methane. *Geobiology* 4: 271–283.

Zerkle AL, House CH, Cox RP, and Canfield DE (2006) Metal limitation of cyanobacterial N_2 fixation and implications for the Precambrian nitrogen cycle. *Geobiology* 4: 285–297.